BONNER METEOROLOGISCHE ABHANDLUNGEN

Heft 97 (2024) (ISSN 0006-7156)
Herausgeber: Andreas Hense

Maike Hacker

Modelling Fog and Low Stratiform Clouds in the Namib Desert with COSMO-FOG

BONNER METEOROLOGISCHE ABHANDLUNGEN

Heft 97 (2024) (ISSN 0006-7156)

Herausgeber: Andreas Hense

Maike Hacker

Modelling Fog and Low Stratiform Clouds in the Namib Desert with COSMO-FOG

Modelling Fog and Low Stratiform Clouds in the Namib Desert with COSMO-FOG

Dissertation
zur
Erlangung des Doktorgrades (Dr. rer. nat.)
der
Mathematisch-Naturwissenschaftlichen Fakultät
der
Rheinischen Friedrich-Wilhelms-Universität Bonn

vorgelegt von
M.Sc.
Maike Hacker
aus
Andernach

Bonn, Juni, 2024

Diese Arbeit ist die ungekürzte Fassung einer der Mathematisch-Naturwissenschaftlichen Fakultät der Rheinischen Friedrich-Wilhelms-Universität Bonn im Jahr 2024 vorgelegten Dissertation von Maike Hacker aus Andernach.

This paper is the unabridged version of a dissertation thesis submitted by Maike Hacker born in Andernach to the Faculty of Mathematical and Natural Sciences of the Rheinische Friedrich-Wilhelms-Universität Bonn in 2024.

Anschrift des Verfassers: Address of the author:

Maike Hacker
Institut für Geowissenschaften, Abt. Meteorologie
Universität Bonn
Auf dem Hügel 20
D-53121 Bonn

Gutachter/Betreuer: Prof. Dr. Andreas Bott,
Rheinische Friedrich-Wilhelms-Universität Bonn
Gutachterin: Dr. Lisa Schielicke,
Rheinische Friedrich-Wilhelms-Universität Bonn

Tag der Promotion: 30. Juli 2024

Danksagung

Sehr herzlich bedanke ich mich bei meinem Betreuer, Prof. Dr. Andreas Bott, für die Unterstützung und Begleitung in den letzten Jahren. Er ermöglichte mir, an dem Projekt NaFoLiCA mitzuarbeiten und motivierte mich zu der vorliegenden Arbeit. Im Rahmen zahlreicher Sitzungen und Einzelgespräche sorgte er für einen soliden Zugang zur wissenschaftlichen Projektarbeit und legte die notwendigen Grundlagen für die anschließende Forschungsarbeit. Von dem weltweit führenden Experten in Nebelmodellierung konnte ich durch seine Förderung viel lernen. Dafür bin ich Prof. Bott sehr dankbar. Vielen Dank auch für das Verständnis bei Unsicherheiten und Problemen und die klare Führung während der gemeinsamen Zeit.

Mein ganz besonderer Dank gilt Dr. Astrid Kerkweg. Ihre großen Programmierkenntnisse und zahlreichen Ideen zu vielen technischen Problemen waren mir eine sehr große Hilfe. Die Eingliederung von PAFOG in COSMO/MESSy wurde von ihr unterstützt und begleitet. Sie hat sich sehr viel Zeit genommen und hatte immer ein offenes Ohr für meine Sorgen und Zweifel. Das hat mir sehr gut getan. In unserer gemeinsamen Zeit als Zimmerkolleginnen verschafften mir zahlreiche Gespräche und Beratungen einen schnellen Zugang zur wissenschaftlichen Arbeit. Sehr dankbar bin ich ihr für die Lektüre der kompletten Arbeit und viele hilfreiche Tipps.

Großer Dank gilt dem Leiter des HRZ, Dr. Rainer Bockholt, und meinem Abteilungsleiter, Fabian Prante, für ihr Verständnis während meiner Doppelbelastung. Durch Teilzeit, flexible Arbeitszeiten und Homeoffice hatte ich die Möglichkeit, meine Tätigkeit im HRZ mit meiner Promotion zu kombinieren. Meine Kolleginnen und Kollegen des HRZ, insbesondere Arthur Lackner und Daniel Meyer, haben mich mit großer Geduld und Rücksichtnahme tatkräftig unterstützt – Euch allen vielen Dank.

Vielen Dank der Projektgruppe NaFoLiCA für die Bereitstellung von Messdaten und Satellitenbildern, sowie den kollegialen Austausch und die anregenden Diskussionen anlässlich der gemeinsamen Projekttreffen. Vielen Dank auch an Dr. Ulrich Schättler vom DWD für die technische Unterstützung zu COSMO.

Bedanken möchte ich mich bei Dr. Volker Küll und Dr. Michael Langguth für die Lektüre und hilfreichen Tipps zu Vorgehen, Methodik und Programmierung in den letzten Jahren.

Weiterhin danke ich Dr. Alexander Kelbch für die synoptische Beratung und Einordnung und Marc Mertes für die wertvolle Administration der IT-Systeme.

Zusammenfassung

Die Wüste Namib – eine der trockensten Regionen der Erde – ist eine typische Küstenwüste mit sehr geringen Niederschlägen und regelmäßig auftretendem Nebel. Der Wassereintrag durch Nebel übersteigt häufig die Niederschlagsmenge, so dass Nebelwasser eine wichtige Wasserquelle für das Ökosystem ist und außerdem eine Wasserquelle für die menschliche Nutzung sein kann. Deshalb ist hier ein besseres Verständnis der Prozesse, die die Entstehung von Nebel und dessen räumlich-zeitliche Verteilung steuern, wichtig.

Zur Untersuchung der Nebelausdehnung und der daran beteiligten Prozesse wird das dreidimensionale Nebelmodell COSMO-FOG entwickelt. Zu diesem Zweck wird die mikrophysikalische Parametrisierung des eindimensionalen Nebel- und Grenzschichtmodells PAFOG in das dreidimensionale numerische Wettervorhersagemodell COSMO implementiert. Um Zugang zu zusätzlichen Diagnosewerkzeugen zu haben, wird nicht das reine COSMO-Modell, sondern COSMO/MESSy (COSMO mit dem Modular Earth Submodel System), verwendet. Die Prozesse, die das Auftreten von Nebel und seine räumliche Variabilität in der Namib-Region steuern, werden mit COSMO-FOG unter Verwendung des MESSy-Submodells TENDENCY analysiert.

Zunächst wird das Modellverhalten und die Konsistenz von COSMO-FOG in einer idealisierten Umgebung für eine horizontal homogene marine Stratuswolke untersucht. Es wird eine Sensitivitätsstudie für COSMO und COSMO-FOG und für unterschiedliche vertikale Modellgitterabstände durchgeführt. Die Simulationen mit COSMO-FOG ergeben einen realistischeren Flüssigwassergehalt für die marine Stratuswolke im Vergleich zum COSMO-Modell. Die Simulationen mit verschiedenen vertikalen Gittern zeigen, dass ein feines vertikales Gitter notwendig ist, um scharfe Gradienten an der Wolkenobergrenze aufzulösen.

Um die räumlich-zeitliche Ausdehnung, die täglichen Lebenszyklusphasen und die dazu beitragenden atmosphärischen Prozesse von Nebel und niedrigen stratiformen Wolken in der Wüste Namib zu untersuchen, werden einzelne Fallstudien im Frühling der südlichen Hemisphäre 2017 mit COSMO-FOG simuliert. Am Nachmittag sind stratiforme Wolken häufig über dem Atlantik und in Küstennähe vorhanden. Am Abend breiten sich diese Wolken landeinwärts aus und bilden Nebel, wo sie auf das ansteigende Gelände der „Großen Randstufe“ treffen. Die Ausbreitung des Nebels und der stratiformen Wolken wird durch die Advektion kalter und feuchter Luftmassen in Wechselwirkung mit turbulenter Durchmischung verursacht. Die Advektion warmer kontinentaler Luftmassen mit einem östlichen Wind führt zu niedrigeren Wolkenhöhen und geringerer räumlicher Ausdehnung von Nebel und stratiformen Wolken. Groß-skaliges Absinken verstärkt diesen Effekt.

Die mit COSMO-FOG erzielten Ergebnisse werden anhand von Satellitenbeobachtungen und bodengestützten Messungen evaluiert. COSMO-FOG erfasst die räumliche Verteilung von Nebel und niedrigen stratiformen Wolken und die meteorologische Situation weitgehend gut. Insbesondere für die Küstenstationen stimmen der Tagesgang und der Beginn der Nebelereignisse mit den Beobachtungen überein. An Stationen im Landesinneren unterschätzt COSMO-FOG gelegentlich die Nebelausdehnung abhängig von der synoptischen Situation.

Abstract

The Namib Desert – one of the driest regions on earth – is a typical coastal desert with very scarce rainfall and regularly occurring fog. Fog water input often exceeds rainfall and thus fog water deposition is a major source of water for the ecosystem and could be a source of water for human settlements. Therefore, a better understanding of the processes that control fog formation and its spatio-temporal patterns is important.

To investigate the spatio-temporal evolution of fog events and the processes controlling fog occurrence, the three-dimensional fog model COSMO-FOG is developed. For this purpose, the microphysical parametrisation of the one-dimensional fog and boundary layer model PAFOG is implemented into the three-dimensional numerical weather prediction model COSMO. To have access to additional diagnostic tools, COSMO/MESSy (COSMO including the Modular Earth Submodel System) is used instead of the pure COSMO model. The processes controlling fog occurrence and its spatial variability in the Namib region are analysed with COSMO-FOG using the MESSy submodel TENDENCY.

At first the model behaviour and consistency of COSMO-FOG is investigated in an idealised environment for a horizontally homogeneous marine stratus. A sensitivity study for the COSMO model and COSMO-FOG with different vertical model grid spacings is performed. The simulations with COSMO-FOG yield a more realistic cloud water content for the marine stratus compared to the COSMO model. The simulations with different vertical grids show that a fine vertical grid is necessary to resolve sharp gradients at cloud top.

In order to investigate the spatio-temporal patterns, diurnal life cycle phases and contributing atmospheric processes of fog and low stratiform clouds in the Namib Desert, individual case studies in the austral spring season 2017 are simulated with COSMO-FOG. In the afternoon, stratiform clouds are often present above the Atlantic Ocean and close to the coastline. In the evening, these clouds proceed onshore and intercept with the terrain of the ascending "Great Escarpment" thus forming fog. The extension of fog and stratiform clouds is caused by the advection of cold and moist air masses interacting with turbulent mixing. The advection of warm continental air masses with an easterly wind causes lower cloud heights and a smaller spatial extent of fog and stratiform clouds. Large-scale subsidence enhances this effect.

The results obtained with COSMO-FOG are evaluated with satellite retrievals and ground-based measurements. COSMO-FOG largely captures the spatial distribution of fog and low stratiform clouds and the meteorological situation. Especially for coastal stations the diurnal cycle and onset of the fog events are in agreement with the observations. At inland stations COSMO-FOG sometimes underestimates the extension of fog dependent on the synoptic situation.

Contents

1 Introduction

Fog is probably not the first phenomenon associated with a desert. For many, the first thing that comes to mind is a sandy desert with heat and drought, large sand dunes and little vegetation – all in all, a hostile place to live in. Deserts are arid areas with no or sparse vegetation resulting from a deficiency of the received water input relative to the water loss by evapotranspiration (Logan, 1968; Warner, 2004). In the tropics and subtropics an almost paradoxial type of desert develops under the influence of cold ocean currents and large-scale subsidence in the subsiding branch of the Hadley cell circulation - so-called coastal deserts. These deserts are almost totally rainless but characterised by high humidity and moderate temperature despite their location surrounding the tropics (Logan, 1968). Above the cold ocean currents, fog or low stratiform clouds frequently form in the marine boundary layer (MBL) and touch the coast of the continents. This part of the coastal desert is characterised by very few and intermittent precipitation but in contrast many fog days and is also termed fog desert. There are three well-developed coastal (fog) deserts: the Namib on the southwestern coast of Africa, the Atacama and Peruvian Deserts, and the desert on the Pacific coast of southwestern North America. Some marginal cases occur at the northwestern coast of Africa and the easternmost of the Canary Islands, the northwestern coast of Australia and possibly the Somalian coast (Logan, 1968).

Located at the southwestern coast of the African continent adjacent to the cold Benguela current, the Namib Desert is a typical coastal desert. Annual precipitation does not exceed 20 mm along the coast (Eckardt et al., 2013; Lancaster et al., 1984; Seely and Henschel, 1998; Seely, 1978). Fog is a characteristic phenomenon with more than 100 fog days per year along the coast (Olivier, 1995) and water input by fog around 0.1-1.0 $\mathrm{l\,m^{-2}\,day^{-1}}$ (Henschel and Seely, 2008) often exceeds rainfall (Eckardt et al., 2013; Olivier, 1992). One of the first fog climatologies based on station measurements detected a fog zone inland between 25 and 50 km (Lancaster et al., 1984).
Numerous observational studies suggest different types of fog occurring regularly in the Namib Desert, i.e. advection fog, radiation fog and lowering stratus clouds (Hachfeld, Jürgens, et al., 2000; Lancaster et al., 1984; Seely and Henschel, 1998; Taljaard, 1979). Many past and recent studies relate the occurrence of fog in the Namib to the advection of sea fog and low-level clouds from the Atlantic Ocean and their interception with the terrain (Andersen and Cermak, 2018; Andersen et al., 2019, 2020; Lancaster et al., 1984; Olivier, 1992; Spirig et al., 2019; Taljaard, 1979). The onshore advection of cloudy marine air masses is facilitated by the presence of a heat low over continental southern Africa and the modification of local winds by synoptic-scale disturbances (Andersen et al., 2020; Olivier and Stockton, 1989). An

anomalously dry free troposphere causes stronger longwave cooling which increases low-cloud cover.
The advection-dominated fog regime has recently been questioned. Based on isotope analysis of fog water, Kaseke et al. (2017) and Kaseke et al. (2018) found that the majority of their fog water probes originated from mixed or sweet water sources. Interpreting this as indication of radiation fog, they suggested that besides advective fog, radiation and mixed fog occur regularly in the Namib Desert. As a result, the mechanisms influencing fog formation and its evolution are currently a subject of scientific debate. A more detailed description of fog origins and its climatology will be given in Section 2.4.

While fog is typically viewed as a hazardous weather phenomenon which is related to traffic accidents, flight delays and cancellations or health issues in moist climate (e.g. Allan et al., 2001; Bendix et al., 2011; Bergot et al., 2007; Egli et al., 2018; Gultepe et al., 2007; Köhler et al., 2017; Pagowski et al., 2004; Stolaki et al., 2012), the occurrence of fog, dew and atmospheric moisture plays an essential role for the survival of many species and ecosystems in the coastal Namib Desert (e.g. Hachfeld, Jürgens, et al., 2000; Henschel and Seely, 2008; Mitchell et al., 2020; Pietruszka and Seely, 1985; Seely, 1978). Fog water input often exceeds rainfall and thus is an essential either supplementary or even exclusive source of water for many highly adapted species (Hachfeld, Jürgens, et al., 2000; Mitchell et al., 2020; Seely, 1978, 1979; Southgate et al., 1996) and could be a source of water for human settlements (Makuti et al., 2004; Shanyengana et al., 2002).
Methods to use atmospheric moisture sources include seeking moist micro-climates e. g. under stones, drinking from wet surfaces, consuming moist food, collecting water on the body (fog harvesting), and absorbing water vapour (Henschel and Seely, 2008). Many small animal species like beetles, scorpions, lizards and termites drink water drops deposited on stones, plants or their bodies given the opportunity that they find deposited fog or it forms near them (Broza, 1979; Henschel and Seely, 2008; Mitchell et al., 2020; Pietruszka and Seely, 1985; Seely, 1979). Larger animals such as ostrich or springbok, but also some lizards and rodents, consume moist food by feeding during cool and moist hours of the day, especially during fog events. They benefit from the increasing moisture content of dry grass which correlates with air humidity (for further reference see Henschel and Seely (2008) and references therein). Some Namib Desert beetles climb the dunes and go into a head-stand position (Fig. 1.1 (a)). This posture allows for the fog water to condense at their carapace and run to the beetle's mouth under gravitiy where it is consumed (Hamilton and Seely, 1976; Nørgaard et al., 2012; Seely, 1979). If the fog does not provide enough water or the wind is too strong the beetles leave the fog (Mitchell et al., 2020; Seely, 1979). Another beetle species digs trenches into the dune sand perpendicular to the mean wind direction and extracts the water from the moist sand (Seely and Hamilton, 1976).
Methods of fog water usage are also applied by many plant species. Some lichens, dune succulents or dwarf shrubs directly absorb fog water by their leaves or stems and transport it to their root system (Gottlieb et al., 2019; Henschel and Seely, 2008; Soderberg, 2010). Several succulents gain water by a negative water vapour

gradient established from outside towards the inside of the leaf when the leaf temperature is below ambient air temperature and the stomata are open (see Henschel and Seely, 2008 and references therein). Other plant species take up deposited fog water from the moist sand surface. The wetting of the sand is often enhanced by fog water dripping from leaves or running off the stems of plants (Fig. 1.1 (b)) (Ebner et al., 2011; Roth-Nebelsick et al., 2012).

(a) (b)

Figure 1.1: Fog-basking Namib Desert beetle (a), drop of fog water collected on a plant (b), from Mitchell et al. (2020)

Inspired by these highly specialised species, fog water can also be used as an artificial supplementary water source for human consumption or irrigation of plants (Park and Kim, 2019; Yu et al., 2021). Recently, even beer is brewed from collected fog water e.g. in Chile (Weiss, 2014) and Gran Canaria. The basic idea is to set up fine mesh nets perpendicular to the main wind direction as artificial fog collectors (Fig. 1.2) (Fessehaye et al., 2014; Shanyengana et al., 2002). The wind blows the fog through the mesh, so the water droplets condense at the mesh and water drips into containers below (Gultepe et al., 2007). One fog collector is the so-called Standard Fog Collector (SFC) developed by Schemenauer and Cereceda (1994). The SFC is a $1\,\mathrm{m}^2$ frame with a double layer of mesh.
Fog collectors have been set up worldwide e.g. in Chile, Peru, Guatemala, South Africa, Eritrea, Yemen, Nepal, Portugal, and on the Canary Islands (Eckardt et al., 2013; Fessehaye et al., 2014; Verbrugghe and Khan, 2023). Despite of its importance as a water resource for human consumption, fog collection projects sometimes fail due to insufficient maintenance combined with extreme weather resulting in damaged collectors (Verbrugghe and Khan, 2023). One of the first operational fog water collection systems in Chile was composed of 100 fog collectors with a total mesh area of $4800\,\mathrm{m}^2$ and able to produce $15000\,\mathrm{l}$ per day on average which means approximately $3\,\mathrm{l}\,\mathrm{m}^{-2}$ per day (Carvajal et al., 2022; Eckardt et al., 2013; Fessehaye et al., 2014; Verbrugghe and Khan, 2023). In 2020, the largest operational fog harvesting project in southwest Morocco provided 16 villages with water for drinking and domestic use (Farnum, 2022).

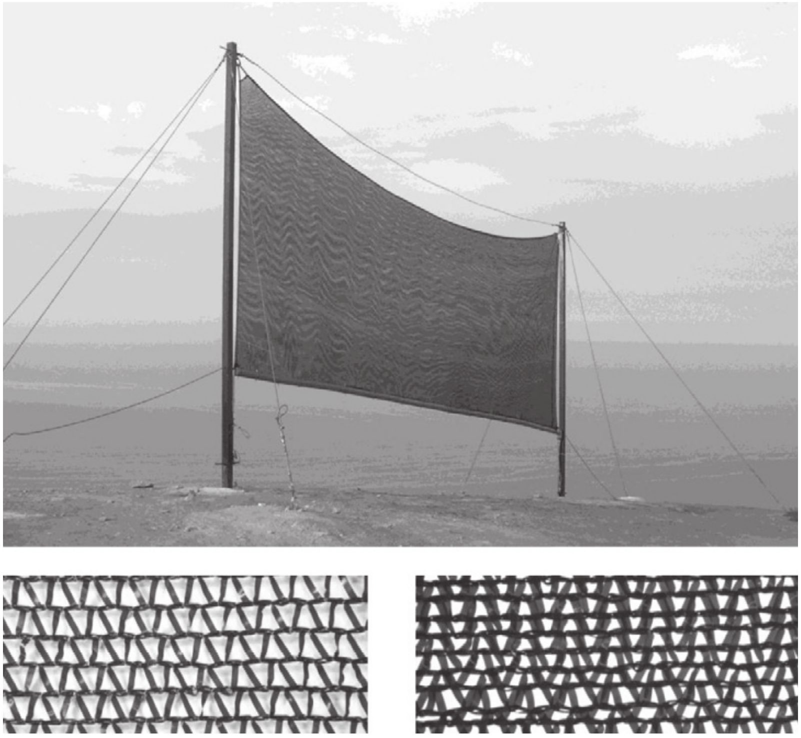

Figure 1.2: Example of a large fog collector at Alto Patache in Chile (top), single (bottom left) and double layer (bottom right) Raschel mesh, from Holmes et al. (2015)

On the banks of the Kuiseb river in Namibia, the mean quantity of collected fog water was $1\,\mathrm{l\,m^{-2}}$ per day which is a low but useful rate which is sufficient for the installation of a fog collection system, especially given that alternative water sources are urgently needed (Eckardt et al., 2013; Henschel et al., 1998). Upscaled to a mesh area of $1200\,\mathrm{m}^2$, the collected fog water would theoretically meet the minimum daily requirement of 1200 l for a village with 13 people, 50 goats, 20 donkeys, 16 cattle, 7 dogs and 30 chickens (Eckardt et al., 2013; Henschel et al., 1998).

Due to the ecological and socioeconomic relevance of fog in the Namib Desert, a better understanding of the local mechanisms that control its formation and spatio-temporal patterns holds large potential. The knowledge of the coherent spatio-temporal development and the microphysical properties of fog events is not only necessary for the construction of fog water collectors but also to comprehend the ecosystems living from fog water input whose protection is important to preserve the biodiversity of many arid environments (Cereceda et al., 2002).
In the central Namib Desert, fog research by means of ground-based measurements and satellite retrievals has a long tradition and many studies have dealt with its climatology (Cermak, 2012; Lancaster et al., 1984; Nagel, 1959; Olivier, 1995; Seely and Henschel, 1998), its relevance as a water source (Hachfeld, Jürgens, et al., 2000; Hamilton and Seely, 1976; Henschel and Seely, 2008; Seely, 1979), its reliability (Pietruszka and Seely, 1985), and its potential for water harvesting (Henschel et al.,

1998; Shanyengana et al., 2002). However, little is still known about the processes which control the formation and spatio-temporal patterns of fog and low stratiform clouds (FLCs) in the Namib Desert, despite their importance.
Previous studies dealing with the spatial patterns and processes involved in fog formation in the Namib frequently focused on fog climatology. The analysis of fog climatology is indeed important but it does neither describe the exact inland extent of the stratiform clouds nor the varying conditions on the ground. Single fog events are more complex than climatology makes them appear and are still poorly understood (Spirig, 2020).
Current knowledge of fog origins in the Namib mainly originates from ground-based measurements and satellite retrievals. However, ground-based measurements are limited in their spatio-temporal extent providing isolated insides. Satellite observations provide spatially coherent information of fog and cloud cover extent but they provide only rare insights into the processes contributing to the formation of that cloud cover. Fog and low clouds are difficult to distinguish in a satellite retrieval, since satellites only see the top of clouds or fog.
Recently, the Namib Fog Life Cycle Analysis (NaFoLiCA) project used the benefits from all these approaches for fog investigation by a combination of remote sensing, in-situ ground-based observations and numerical modelling to further understand the local mechanisms leading to fog occurrence and the spatio-temporal evolution of fog events in the Namib Desert. An analysis of the spatio-temporally coherent development of fog events and the processes responsible for the fog life cycle can be obtained by means of detailed three-dimensional numerical simulations. The numerical modelling of individual fog events in the present study combines process insight with spatial information and is considered to bridge the gap between point measurements and satellite observations on the one hand and fog climatology and single case studies on the other hand.

Numerical atmospheric models determine the state and evolution of the atmosphere using a set of differential equations which are based on the conservation of mass, energy and momentum. The numerical solution of these equations requires the definition of a spatial grid. Current operational numerical weather prediction (NWP) models use grid spacings $\Delta x \sim 1$–$10\,\text{km}$ (Bauer et al., 2015). In contrast to that, the formation and evolution of fog and clouds results from various microphysical processes which take place at micrometre-scale (cloud-scale). Consequently, microphysical processes are still entirely parametrised in NWP models with grid spacing at kilometre-scale (Boutle et al., 2022).
For fog and cloud prediction, the parametrisation of the microphysical processes is essential (Koračin, 2017). The development (Boutle et al., 2022) and the dissipation phase (Lin et al., 2017; Steeneveld et al., 2015) are dependent on the microphysical parametrisation, determining the quality of the fog forecast as a whole. There are basically two differing approaches for microphysical parametrisations: spectral and bulk parametrisations. In spectral schemes, each type of cloud or precipitation particle (e.g. cloud droplets, rain drops, cloud ice, snow, ...) is subdivided according to its size and a separate prognostic equation is solved for each particle type and each size class (e.g. Feingold et al., 1998; Khain et al., 2004; Kogan, 1991; Lynn et al.,

2005; Stevens et al., 1996). Consequently, the number of prognostic equations to be solved increases depending on the complexity of the parametrisation regarding the inclusion of liquid water or ice particles and the numbers of size classes taken into account.
Bulk schemes describe the behaviour of the overall ensemble of cloud particles. They simulate the temporal evolution of bulk cloud characteristics such as the total mass fraction thus minimizing the total number of equations and calculations considerably compared to spectral schemes (e.g. Hong et al., 2004; Kessler, 1969; Lang et al., 2014; Lin et al., 1983). Double-moment or two-moment bulk schemes often use the droplet number concentration in a water category as additional prognostic variable besides the mass fraction of that water category (e.g. Ferrier, 1994; Lim and Hong, 2010; Seifert and Beheng, 2001, 2006).
Spectral modelling of clouds seems an attractive alternative to bulk schemes or multi-moment bulk schemes since less assumptions have to be made in the parametrisation. However, spectral cloud models are computationally very expensive for the application in a three-dimensional numerical model, especially if also ice particles are considered (Seifert and Beheng, 2001). Currently, one- or two-moment microphysical bulk parametrisations still are the workhorses of numerical weather prediction and climate modelling (Grabowski et al., 2019). A comprehensive overview on cloud microphysical parametrisation schemes is given in Grabowski et al. (2019) and Khain et al. (2015).

A fog forecast depends not only on the microphysical parametrisation, but also on the parametrisations of turbulent mixing, atmospheric radiative transfer, as well as heat and moisture fluxes at the Earth's surface since fog formation and its evolution result from complex interactions between microphysical, dynamical, turbulent, surface and radiative processes (Bott, 2021; Ducongé et al., 2020). Modelling of fog and low stratiform clouds with models of various complexity has a long tradition. First approaches to simulate fog and low stratiform clouds relied on one-dimensional models which allow for high vertical resolution and detailed parametrisation schemes. One-dimensional or so-called single column models are computationally cheap compared to three-dimensional models. They locate a vertical column of boxes at one geographical location. This is equivalent to assuming horizontal homogeneity. The complexity of one-dimensional models ranges from very simple models to models with complex parametrisations of microphysical processes. In the single column model developed by Zdunkowski and Nielsen (1969) the sedimentation of cloud water was neglected and turbulence was parametrised using exchange coeffcients constant in time and only varying with height. Zdunkowski and Barr (1972) added the calculation of exchange coefficients as a function of stability, wind shear and height to this model. In the one-dimensional model by Duynkerke (1991) a parametrisation of vegetation was included. Bott et al. (1990) developed the one-dimensional fog model MIFOG with a spectral cloud microphysical parametrisation. Since models with spectral microphysical parametrisations are computationally very expensive, the spectral microphysical parametrisation was replaced by a two-moment bulk parametrisation in the fog model PAFOG to obtain a computationally efficent model suitable for operational fog forecasts (Bott and Trautmann, 2002). Comparing re-

fined versions of both microphysical cloud schemes, Bott (2020) revealed that the parametrised microphysical cloud scheme is capable to simulate the characteristics of the cloud-topped MBL quite well although the effects of single processes differ considerably from the spectral microphysical cloud scheme.
One-dimensional models cannot simulate the full three-dimensional structure of atmospheric processes (Koračin, 2017). Due to the assumption of horizontal homogeneity any types of heterogeneities in surface characteristics or atmospheric variables and three-dimensional advection processes cannot be considered by these models. This may be justified if horizontal advection is of minor importance for the investigated phenomenon which is considered to be valid e.g. for radiation fog (Bott, 2021). If the investigated phenomenon depends on advection or surface heterogeneities, the assumption of horizontal homogeneity is no longer justified and three-dimensional models are necessary. Only three-dimensional models are able to simulate a realistic flow and horizontal heterogeneity. One of the first approaches to use a three-dimensional operational forecast model for fog prediction was made by Ballard et al. (1991) to simulate sea fog highlighting the effect of initial conditions and vertical grid spacings. Nakanishi (2000) was one of the first using a large eddy simulation to study the internal three-dimensional structure of radiation fog. Boutle et al. (2016) presented a version of the Unified Model (UM) with a very high horizontal resolution at 333 m covering a small area around London and found a positive effect of a small horizontal grid spacing on fog forecasts. A model with a similar horizontal grid spacing has also been tested for Delhi (Jayakumar et al., 2018). Despite of horizontal resolution, also the vertical resolution is important to obtain reasonable fog forecasts (Philip et al., 2016; Tardif, 2007). With increasing computer power, it has become feasible to include spectral microphysical parametrisation schemes into three-dimensional models (Iguchi et al., 2012).
Despite of these advances which have been made over the past years fog remains difficult to forecast with numerical models (Boutle et al., 2022; Steeneveld et al., 2015). Holtslag et al. (2010) found that even an empirical method developed in the 60s and 70s by the US Air Force (Fog Stability Index) performed better in terms of forecast skill than the fog forecast of a three-dimensional meso-scale model at 9 km horizontal resolution. Some of the shortcomings of three-dimensional models are the often inadequate and insufficient horizontal and vertical resolution and simplified physical parametrisation schemes (Gultepe et al., 2007; Koračin, 2017). These simplifications are nowadays still necessary to obtain fog forecasts with adequate computational effort.
To overcome some of these shortcomings and use the advantages of both approaches, one-dimensional and three-dimensional models have been coupled. The three-dimensional model provides the vertical profiles of all thermodynamic variables as forcing to run the one-dimensional fog model. This method is computationally rather efficient (e.g. Bartok et al., 2012; Chen et al., 2021; Stolaki et al., 2012). Kim et al. (2020b) and Kim et al. (2020a) used meteorological fields from the three-dimensional Weather Research and Forecasting (WRF) model and from UM as external forcing for PAFOG showing improvements of the coupled model systems compared to WRF and UM alone for the simulation of sea fog.
An alternative approach to coupling one-dimensional and three-dimensional mo-

dels is the implementation of the microphysical parametrisation of one-dimensional fog models into three-dimensional meso-scale models. This approach was first realised by Masbou (2008) implementing the microphysical parametrisation of the one-dimensional fog model PAFOG into the meso-scale Lokal Modell (LM) which yielded promising results. Müller et al. (2010) implemented the PAFOG microphysical parametrisation scheme into the WRF non-hydrostatic meso-scale model (WRF-NMM) and obtained a better representation of the spatial distribution of fog in complex terrain than for WRF-NMM with the standard cloud scheme.

The major objective of the present thesis is to investigate the processes controlling fog occurrence and the spatio-temporal evolution of fog events in the hyper-arid[1] Namib Desert. For this purpose, the three-dimensional numerical fog model COSMO-FOG is developed. Following the approach of Masbou (2008) and Müller et al. (2010), COSMO-FOG is developed based on the implementation of the two-moment microphysical parametrisation of PAFOG into the former operational NWP model COSMO (Consortium for Small-Scale Modeling). However, to have access to additional diagnostic tools, not the pure COSMO model, but COSMO/MESSy (Kerkweg and Jöckel, 2012), i.e. COSMO including the Modular Earth Submodel System (MESSy, Jöckel et al., 2005) is used. For simplicity the model will be called anyhow COSMO-FOG in the remainder of this thesis. Applying the three-dimensional fog model COSMO-FOG in the Namib region, the following scientific questions will be answered:

Q1 Is the three-dimensional fog model COSMO-FOG able to reasonably simulate the time evolution of the cloud-topped marine boundary layer?

Q2 What are the temporal and spatial patterns of coastal fog occurrence in the Namib region?

Q3 What are typical life cycle phases of Namib region fog?

Q4 What factors determine the development, persistence and properties of the fog?

To address these research questions, individual case studies in the austral spring season in September 2017 are simulated with COSMO-FOG, in order to investigate the spatio-temporal patterns, diurnal life cycle phases and contributing atmospheric processes of fog types in the Namib region. All case studies are selected from a field campaign which has been performed in the framework of the **Na**mib **Fo**g **Li**fe **C**ycle **A**nalysis (**NaFoLiCA**) project in early austral spring 2017, when the frequency of inland reaching fog events is highest (Spirig et al., 2019).
The mechanisms controlling fog occurrence and its spatial variability in the Namib region are analysed with COSMO-FOG using the MESSy submodel TENDENCY (Eichinger and Jöckel, 2014) which provides the contributions of individual processes to the total tendency within a model time step. The knowledge of the individual contributions offers new insights into the development of spatio-temporal patterns

[1] Hyper-arid are regions where precipitation is less than 5 % of the potential evapotranspiration (United Nations, 2011).

of FLCs and the processes contributing to the cloud evolution in the Namib region. The spatially coherent process insight provided by the numerical simulations of COSMO-FOG will be important to understand the processes influencing fog evolution in the Namib region. The model results are evaluated by satellite and ground observations obtained during the field campaign in September 2017. The model results are placed in the context of previous related work on FLCs in the Namib region. Thereby, hypotheses regarding the dominant physical mechanisms that control this fog are refined.

This thesis is organised as follows: Chapter 2 starts with an overview on the nature of fog and low stratiform clouds in general before the focus will be put on the Namib Desert. In Chapter 3 the NWP model COSMO is introduced with a focus on its microphysical parametrisation. Afterwards the microphysical scheme of the one-dimensional fog model PAFOG is described in detail. The remaining part of Chapter 3 deals with the implementation of the PAFOG microphysical scheme into the COSMO model. The MESSy submodel TENDENCY is introduced as additional diagnostic tool.
To investigate the model behaviour of COSMO-FOG, a sensitivity study for both microphysical parametrisation schemes (standard COSMO scheme and PAFOG) and different vertical resolutions is performed in a highly idealised environment for a horizontally homogeneous marine stratus, which is presented in Chapter 4. Chapter 5 reports on the simulation of selected case studies from the NaFoLiCA field campaign with COSMO-FOG. The spatial and temporal patterns of Namib fog occurrence and the atmospheric conditions influencing these patterns are investigated exemplarily for one case study. Afterwards the other case studies are analysed with a focus on phenomena and processes that differ from the first case study. Finally, the accuracy of model simulations is evaluated by comparison to ground-based observations. Chapter 6 summarises the results of this thesis and outlines key opportunities for further scientific work.

2 Fog and low stratiform clouds in the Namib Desert

The investigation of FLCs in the Namib requires to address the physical processes involved in fog and cloud formation in general and with emphasis on the special conditions in the Namib Desert.
The processes involved in fog and cloud formation are manifold. The transitions among different fog types and between fog and low stratiform clouds are often fluent. In principle, fog is a cloud that touches the ground while low stratiform clouds are elevated (Warren et al., 2015). On occasion low stratiform clouds might touch the ground on an elevation thus forming fog there (Houze, 2014).
This chapter provides an overview about fog and low stratiform cloud formation and related processes. After introducing the physical basics for fog and cloud formation in Section 2.1, properties and the formation of fog and low stratiform clouds are described in Section 2.2 and Section 2.3, respectively. The special conditions and fog origins in the Namib Desert are described in Section 2.4.

2.1 Physical basics for fog and cloud formation

Fog and low stratiform clouds consist of small water droplets suspended in the air (American Meteorological Society, 2024; World Meteorological Organization, 2017). A necessary prerequisite for the formation of water droplets by condensation is saturation of the air with respect to water vapour. The air reaches saturation if the water vapour pressure e equals the saturation water vapour pressure e_{sat}. The air temperature T equals the dew point temperature T_d and the relative humidity reaches 100 %. A further increase of the water vapour pressure results in condensation.
A slight supersaturation is required for condensation (Roach, 1994). The necessary supersaturation for fog and cloud formation can be reached by three different mechanisms (Roach, 1994):

- cooling of the air, e.g. by adiabatic ascent or longwave radiative cooling
- increase of moisture, e.g. by evaporation
- mixing of undersaturated air parcels with different temperature and humidity.

The effect of temperature and specific humidity changes on the relative humidity can be determined with the following formula (see Babić et al. (2019) for derivation):

$$\frac{\partial RH}{\partial t} = \frac{p}{e_{sat}} \frac{0.622}{(0.378q^v + 0.622)^2} \frac{\partial q^v}{\partial t} - \frac{p}{e_{sat}} \frac{q^v L_v}{(0.378q^v + 0.622) R_v T^2} \frac{\partial T}{\partial t}. \tag{2.1}$$

Here, RH is the relative humidity, t the time, p the pressure, q^v the specific humidity, and T the air temperature. L_v denotes the latent heat of vaporisation and R_v the gas constant of water vapour, respectively. The first term on the right hand side represents the contribution from specific humidity changes and the second term denotes the contribution from temperature changes.

In addition to supersaturation, the formation of fog or cloud droplets in the air requires the availability of sufficient aerosol particles to be activated as cloud condensation nuclei (CCN). Without sufficient cloud condensation nuclei, droplets can only form by the collision of pure water molecules which is called homogeneous nucleation. This requires an enormous supersaturation of several hundred per cent (Mölders and Kramm, 2014; Pruppacher and Klett, 2010; Roach, 1994). The supersaturation at cloud level is typically between 0.2 and 2 %. Fog forms at an even lower supersaturation between 0.02 and 0.2 % (Pruppacher and Klett, 2010). The mean supersaturation in the atmosphere seldom exceeds 1 % (Mölders and Kramm, 2014). Therefore homogeneous nucleation plays no role in natural clouds (Mölders and Kramm, 2014).

In natural clouds, droplets usually form on aerosol particles by heterogeneous nucleation. Aerosol particles are usually sufficiently present and thus no limiting factor for cloud or fog formation. In polluted air more condensation nuclei are available resulting in clouds and fog consisting of more small droplets. These small droplets settle more slowly thus increasing the liquid water content (Roach, 1994).

An aerosol particle is usually composed of water insoluble material and water soluble salts. Therefore a cloud droplet is an aqueous solution impured with water insoluble material. The supersaturation necessary for the droplet formation on aerosol particles depends on the chemical properties of the condensation nucleus and the droplet's curvature. This is described by the Köhler theory (see e.g. Pruppacher and Klett, 2010). The saturation vapour pressure decreases with increasing radius of the droplet. Therefore larger droplets grow while smaller droplets evaporate at a given supersaturation. Higher salt concentration decreases the saturation vapour pressure. For very small drops this allows for the existence of droplets in a undersaturated environment. For larger droplets the influence of salt concentration decreases and the effect of droplet size dominates.

To grow further, droplets have to reach a critical radius which depends on the supersaturation. Once a droplet has exceeded the critical radius it continues to grow by water vapour diffusion as long as the relative humidity exceeds 100 %. When a particle passes the critical radius this is called activation of a cloud droplet.

The number of aerosol particles being activated N_{CCN} can often be approximated by a relation of the form

$$N_{CCN} = C\ S^k \tag{2.2}$$

where S is the supersaturation in % and C and k are constants for a given air mass (e.g. continental or maritime air masses) (Pruppacher and Klett, 2010; Twomey, 1959).

Droplets grow further towards precipitation particles with radii $\geq 100\,\mu\text{m}$ by interparticle collision and coalescence (Pruppacher and Klett, 2010).

2.2 Fog

2.2.1 Definition and properties of fog

Fog is defined as “a suspension of very small, usually microscopic water droplets in the air, reducing visibility at the Earth’s surface” to less than 1000 m (American Meteorological Society, 2024; Roach, 1994; World Meteorological Organization, 2017). However, various other definitions of fog exist (Tardif and Rasmussen, 2007). Since the temperature in the Namib Desert is usually high enough to prevent the formation of ice particles in the planetary boundary layer (PBL), in the following only fog built by liquid water droplets is discussed.
The reduction of the visibility by fog results from Mie scattering on fog droplets (Gultepe et al., 2007). The strength of the extinction by scattering depends on the relation between volume and surface of the droplets. Smaller droplets have a larger extinction coefficient. Therefore, small droplets yield a stronger reduction of the visibility than larger droplets.
Fog consists of droplets with a diameter between 2.5 µm and a few tens of microns with a typical mean diameter between 10 and 20 µm (Pruppacher and Klett, 2010; Roach, 1994). Fog droplets settle with a mean velocity below 1 cm s^{-1} (Roach, 1995). Fog usually holds some tens to few hundred water droplets per cm^3 of air. The water content in fog reaches between 0.05–0.5 g m^{-3} (Pruppacher and Klett, 2010).

2.2.2 Classification of fog

Various classifications have been developed to distinguish between fog types. Classifications of fog types are either based on the meteorological processes dominating its formation and weather scenarios often associated with fog: radiation fog, advection fog, cloud-base lowering fog, precipitation fog, morning evaporation fog (Tardif and Rasmussen, 2007) or they are based on the geographical location: coastal fog, valley fog, mountain fog, urban fog (Bruijnzeel et al., 2006).

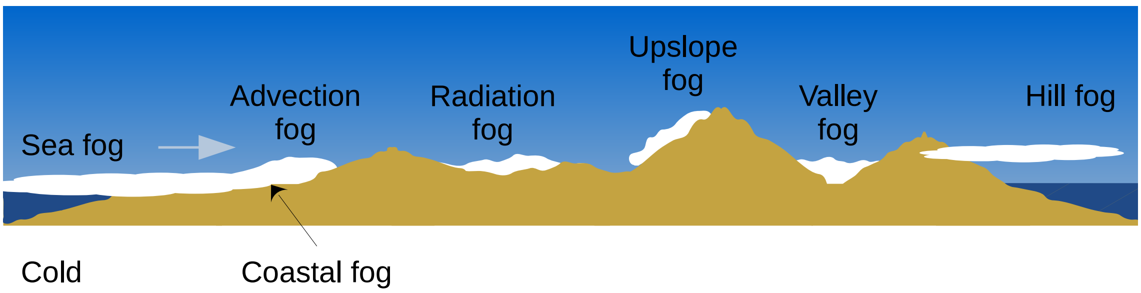

Figure 2.1: Illustration of the most common fog types (not complete), figure adapted from Bruijnzeel et al. (2006).

The World Meteorological Organization (2017) differentiates the following categories of fog: radiation fog, advection fog, evaporation fog, upslope fog, hill fog, frontal fog and freezing fog. However, there is no general nomenclature (Bruijnzeel et al., 2006) and the borders are often fluent. Sometimes there are several expressions referring to basically the same special type of fog, e.g. advection fog - marine fog - sea fog, ground fog - radiation fog, raised fog - stratus, offshore fog - sea fog (Bruijnzeel et al., 2006). In some cases the nomenclature differs also regionally. Hill fog is e.g. termed cloud interception fog (e.g. Spirig et al., 2019) or high fog (e.g. Seely and Henschel, 1998) in Namibia, while it is called Garua fog in Peru and camanchaca fog in Chile (Hesse, 2012). Some examples of the most commonly used fog types which are illustrated in Figure 2.1 are briefly described below. Alternative expressions for the respective fog type are given in parentheses:

Radiation fog forms if the supersaturation develops due to cooling of the atmospheric surface layer by the emission of infrared longwave radiation from the surface (Bruijnzeel et al., 2006; Price et al., 2018). Under clear sky conditions after sunset, a strong radiation deficit develops when the outgoing emitted longwave radiation of the ground is no more balanced by incoming solar radiation resulting in cooling of the atmospheric surface layer. Radiation fog frequently forms in continental regions during night under high pressure with weak wind and no or only few clouds. Clouds emit infrared radiation to the ground, thus reducing the radiative cooling of the surface.
If the air in the lowest atmospheric layers is cooled to the dew point temperature, radiation fog forms. The radiation fog can remain shallow (less than 50 m deep) and optically thin. Often the intensity and vertical extent of radiation fog increase during the night and a deep (100 m or more), optically thick fog develops with a saturated adiabatic temperature profile (Price et al., 2018; Price, 2019). Radiation fog often reaches its maximum extent shortly before sunrise when the temperature is at its diurnal minimum (Bruijnzeel et al., 2006). Fog top often coincides with the top of a nocturnal temperature inversion. Radiation fog is the most typical fog type occurring inland (Bruijnzeel et al., 2006). A special type of radiation fog is valley fog (see below) (Bruijnzeel et al., 2006).

Advection fog (sea fog) forms if warm, moist air is advected over a cooler surface. The temperature of the air decreases over the cool surface until it reaches the dewpoint resulting in saturation. This fog type frequently forms in coastal regions with low sea surface temperature (SST) especially over cold ocean currents like the Humboldt current off the coast of Chile, the Benguela current offshore of Namibia, the California current offshore the west coast of the USA and the Labrador current off the coast of Newfoundland. The fog formed over the ocean can be advected onshore with the sea breeze (grey arrow in Fig. 2.1) and is often termed coastal fog (Bruijnzeel et al., 2006).

Valley fog is basically a radiation fog forming in a valley (Bruijnzeel et al., 2006). It forms frequently under high pressure conditions with clear sky and weak wind. Under these conditions the longwave radiative cooling of the surrounding slopes of the valley results in katabatic winds down the slopes. The cold air accumulates in the valley and fog forms consequently in the cold air pool. This fog is often confined to the dendrite pattern of the valley. Dissipation often includes a stage in which the fog lifts from the ground forming a stratus (Whiteman, 2000).

Upslope fog (mountain fog or orographic fog) forms by adiabatic cooling of moist near-surface air when the air is lifted up over terrain slopes. If the lifting condensation level is below the terrain height and the temperature is cooled to the dewpoint temperature, fog forms at the mountain slope. The upslope flow can be triggered by differential heating of the elevated surface and the resulting mountain-valley circulation (Bott, 2016). Widespread upslope fog forms when moist air is lifted up gently rising terrain (Whiteman, 2000). The distinction of upslope fog from hill fog is difficult or even impossible. Viewed from below upslope fog can appear as stratus. Upslope fog is also termed orographic fog (Bott, 2016) or mountain fog (Bruijnzeel et al., 2006).

Hill fog occurs if the cloud base is lower than the terrain height or the cloud base lowers such that the clouds intersect with the terrain. Sometimes hill fog is also referred to as cloud interception fog or high fog. Hill fog does not necessarily require upslope motion. When viewed from below, it appears as stratus cloud.

According to previous studies, the most common fog types in the Namib Desert are advection fog and cloud interception fog (Andersen et al., 2020; Seely and Henschel, 1998; Spirig et al., 2019).

Fog can dissolve if it is advected over a warm surface. Mixing of a fog layer with undersaturated air can also cause fog dissolution. Incoming solar radiation can cause fog dissolution but not by warming of the fog layer itself but heating of the ground. The fog is then dissolved from below by surface heat fluxes and resulting turbulent mixing (Bott, 2016). Strong radiative cooling of the upper fog layer generates turbulence and thus facilitates the entrainment of dry air drying and thus dissolving the fog.
Many processes occurring in the foggy boundary layer apply also for the cloud-topped boundary layer and will therefore be detailed in the next section.

2.3 Low stratiform clouds

The two most common types of low stratiform clouds are stratus and stratocumulus (Wood, 2015). Above the eastern parts of the subtropical oceans, e.g. above the southeastern Atlantic Ocean west of Namibia, extremely persistent and horizontally extensive fields of stratiform clouds occur (Warren et al., 2015). In these regions the annual mean coverage of stratocumulus is between 40 and 60 % (Wood, 2012, 2015). These cloud fields are called semipermanent subtropical marine stratocumulus sheets.

2.3.1 Definition and properties of stratocumulus and stratus

Stratocumulus and stratus clouds are generally shallow stratiform clouds with low vertical extension (less than 1 km) which occur in the upper few hundred metres in the PBL (Rangno, 2015; Wood, 2012). They are both composed of water droplets given that the temperature at cloud top is larger than -5 to -10 °C, otherwise ice crystals may form (Rangno, 2015).

Stratocumulus is a low-level cloud which appears as a patchy grey and whitish layer with darker and lighter regions if seen from below. The darker regions represent higher amounts of liquid water and give stratocumulus clouds a mosaic-like appearance (Rangno, 2015). The patchy and mosaic-like appearance originates from individual convective elements which are often arranged in groups (American Meteorological Society, 2024). Stratocumulus is basically a convective cloud whose dynamics is driven by convective instability caused by radiative cooling at cloud top (Wood, 2012). Their convective character and the presence of rounded masses and rolls giving them their patchy and mosaic-like appearance distinguishes them from pure stratus (World Meteorological Organization, 2017). In addition, the cloud base height of stratocumulus clouds is often higher and more irregular in height than those of stratus clouds (Rangno, 2015). Stratocumulus is composed of small water droplets and, if so, only produces precipitation in the form of drizzle (Wood, 2012) or light rain (World Meteorological Organization, 2017).

Stratus clouds are homogeneous low-level clouds in the form of a grey layer with a rather uniform base (American Meteorological Society, 2024; Rangno, 2015; World Meteorological Organization, 2017). Stratus lacks the wave pattern of stratocumulus (American Meteorological Society, 2024) since stratus clouds lack the convective elements which distinguishes them from stratocumulus (Warren et al., 2015). Stratus clouds are usually associated with a stable temperature profile in the PBL (Wood, 2015). If at all, stratus produces precipitation in the form of light drizzle, some ice crystals, or snow grains (American Meteorological Society, 2024). Stratus is often located closer to the surface with lower cloud top height than stratocumulus (Wood, 2015).

The liquid water mixing ratio in stratus and stratocumulus clouds increases linearly with height (Wood, 2012). Typical values of the cloud water content in stratus and stratocumulus clouds are around 0.1 to 0.5 $\mathrm{g\,m^{-3}}$ (Pruppacher and Klett, 2010). The mean of the vertically integrated liquid water content (liquid water path (LWP)) for regions to the west of the continents with predominantly low stratiform clouds ranges from 50-80 $\mathrm{g\,m^{-2}}$ (Wood et al., 2002). Since the cloud cover is not equal to 100 %, the LWP of the stratiform clouds may be higher (Wood, 2012). Stratocumulus clouds are usually 200-400 m thick (Lee, 2018; Wood, 2015). Cloud thickness is, among others, regulated by negative feedbacks with drizzle formation and cloud top entrainment. Thicker clouds produce more drizzle which reduces the cloud water and, thus, is a negative feedback on cloud thickness. Cloud top entrainment of dry and warm air from the free troposphere causes evaporation of cloud water and, thus, thins the cloud (Wood, 2015).

The droplet number concentration N_c in stratocumulus clouds reaches values from less than 10 $\mathrm{cm^{-3}}$ to more than 500 $\mathrm{cm^{-3}}$ dependent on the aerosol concentrations

(Wood, 2012). A higher aerosol concentration favours more and smaller cloud droplets yielding higher albedo, less drizzle and sedimentation. There is a large contrast between oceanic and continental regions. Over the ocean high values of $N_c > 200\,\mathrm{cm}^{-3}$ occur mostly downwind of continental regions, e.g. off the Southern California coast or off the coast of Chile. Low values around $50\,\mathrm{cm}^{-3}$ or less typically appear over remote ocean areas (Wood, 2012). In continental areas cloud droplet concentrations exceed values of $200\,\mathrm{cm}^{-3}$ although there are also regions like northern Amazonia or central Africa with lower droplet concentrations (Wood, 2012).
As outlined in Section 2.1, cloud droplet formation in the atmosphere occurs on aerosol particles by heterogeneous nucleation. The number of aerosol particles activated as CCN is dependent on the aerosol size, chemical properties of the aerosol and environmental supersaturation (cf. Sec. 2.1). Over ocean areas CCN usually range from few tens to few hundreds cm^{-3}. Over the continents CCN ranges from a few hundred to few thousand cm^{-3} (Albrecht et al., 1995; Pruppacher and Klett, 2010). The number of activated aerosol is expected to be most sensitive on mean aerosol radius in stratocumulus clouds. Chemical effects like e.g. solubility or surface-tension changes are often less important than aerosol radius (Wood, 2012).
The concentration of aerosol particles influences processes and properties (esp. radiative and chemical) of stratocumulus clouds. This includes e.g. an increased albedo due to increased droplet concentration and reduced droplet surface area, precipitation suppression, and changes to evaporation and condensation rates due to decreased droplet radii (Wood, 2012). Thus, anthropogenic emissions impact on clouds. The aerosol cloud interactions are a difficult subject in cloud-climate research and subject of ongoing research (e.g. Formenti et al., 2019; Haywood et al., 2021; Redemann et al., 2021; Zhang et al., 2024).

2.3.2 Stratiform cloud formation

In general, stratiform clouds such as stratus or stratocumulus clouds form in case of cooling or moistening of the PBL (Wood, 2015). Moistening or cooling of the boundary layer decreases the surface-based level of condensation resulting in cloud formation and an increasing cloud depth if the surface-based level of condensation falls below the inversion and the inversion layer does not change. Cooling of the boundary layer by about 1 K or moistening by 0.2–0.6 $\mathrm{g\,kg}^{-1}$ can lower the surface-based level of condensation by 100 m (Wood, 2012).
As for fog formation, the air must first become supersaturated to initiate cloud formation. This can either be achieved by adiabatic or diabatic cooling towards the dew point temperature, mixing or by an increase of moisture. Stratiform clouds can form by radiative cooling of a moist boundary layer, meso-scale vertical ascent in frontal systems, over orography or in small-scale buoyant systems (Doms et al., 2018). Since marine stratiform clouds play an important role for fog in the Namib region (Seely and Henschel, 1998; Spirig et al., 2019), the following discussion focuses on these.
Marine stratiform clouds can form when the MBL moistens and gets neutrally stratified by turbulent mixing (Boutle and Abel, 2012; Paluch and Lenschow, 1991). Starting from clear sky, initial turbulence is generated by vertical shear of the ho-

rizontal wind or buoyancy (Wood, 2012). Condensation and thus cloud formation typically starts in a thin layer near the top of the boundary layer where saturation is reached if the lifting condensation level is located below the inversion (Wood, 2012, 2015). The initial cloud is often a stratus. Stratus may also form if the temperature stratification is stable, e.g. by advection of warmer air masses over a cold ocean surface. In this case, moisture accumulates near the surface and sea fog may form (Paluch and Lenschow, 1991; Wood, 2012, 2015). Turbulent mixing induced by fog top radiative cooling or wind shear can lift the fog base from the ground, thus forming a stratus (Paluch and Lenschow, 1991; Wood, 2015).
Stratus often transforms into stratocumulus when it is sufficiently thick to become emissive in thermal infrared. The thermal infrared radiative cooling drives convective overturning commonly occurring in stratocumulus (Paluch and Lenschow, 1991; Wood, 2015). The cloud top might increase up to the inversion base height and is typically at 500 to 2000 m above sea level (Wood, 2015).
Stratocumulus and stratus can also develop from many other cloud types, e.g. stratus frequently develops from rising fog (World Meteorological Organization, 2017). Stratus can also develop from stratocumulus when the stratocumulus cloud descends or for any reason loses its patchy and mosaic-like appearance (American Meteorological Society, 2024; World Meteorological Organization, 2017).

2.3.3 Vertical structure of the cloud-topped marine boundary layer

With cloud formation, the neutrally-stratified MBL is decomposed into the lower cloud-free subcloud layer and the above lying cloud layer (Kraus, 2008). In the sub-cloud layer, the profiles of potential temperature θ and water vapour mixing ratio q^v are nearly constant with height and temperature approximately follows the dry adiabat. In the cloud layer above, latent heat release by condensation yields an increase of θ and the loss of water vapour by condensation results in a decrease of q^v (Fig. 2.2). Within the cloud layer temperature decreases with a moist-adiabatic lapse rate (Kraus, 2004; Wood, 2012).
In the cloud-topped MBL, conserved variables are the total water content q^t

$$q^t = q^v + q^c \tag{2.3}$$

and the equivalent potential temperature θ_e

$$\theta_e \approx \theta \exp\left(\frac{L_v r^v_{sat}}{c_p T}\right). \tag{2.4}$$

q^c is the mass fraction of cloud water, r^v_{sat} the saturation mixing ratio of water for a given temperature, and T the air temperature. L_v denotes the latent heat of evaporation and c_p the specific heat capacity at constant pressure.
The cloud-topped MBL is often rather shallow with a boundary layer height between 0.5–1 km. The horizontal wind is approximately constant with height in the well-mixed cloud-topped MBL except for very close to the ocean surface (Wood, 2012). In the transition layer from the cloud-topped MBL to the free troposphere strong

gradients of temperature, humidity, cloud water, tracers, and radiative cooling rates exist. Across the inversion the wind speed sometimes changes several metres per second or the wind direction changes several or tens of degrees (Wood, 2012).
The strength of the inversion is usually around 8 K (Pilié et al., 1979; Riehl et al., 1951) but can reach up to 10–20 K (Lilly, 1968; Wood, 2012) and sometimes exceeds $1\,\mathrm{K\,m^{-1}}$ (Wood, 2012). The inversion layer is often only tens of metres thick (Roach et al., 1982; Wood, 2012).

2.3.4 Processes in the cloud-topped marine boundary layer

Stratiform clouds are controlled by the interaction of radiation, turbulence, surface fluxes, latent heat release, entrainment at cloud top, large-scale subsidence, and microphysical processes (Paluch et al., 1994; Wood, 2012). Figure 2.2 summarises key processes which determine the cloud-topped MBL.

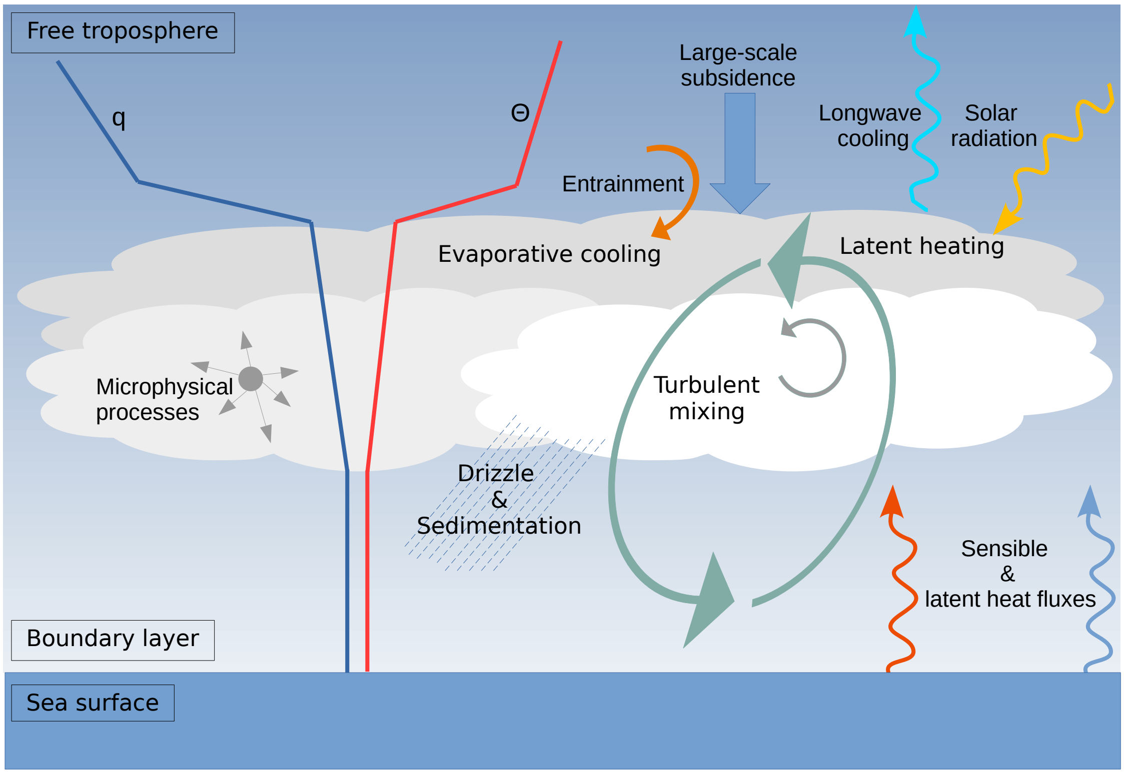

Figure 2.2: Schematic overview of the main processes in the well-mixed cloud-topped MBL, figure adapted from Wood (2012).

Longwave cooling occurs in the most upper part (only a few metres) of the cloud. Cloud droplets are very efficient at absorbing and emitting longwave radiation, so a little way into the cloud layer, upwelling and downwelling longwave radiative fluxes are balanced (Lee, 2018). In the top 10–30 m of the cloud layer, the upwelling longwave radiative flux is stronger than the downwelling longwave radiative flux under a very dry troposphere. So in the upper metres of the cloud, a longwave radiative flux divergence of typically 50–90 $\mathrm{W\,m^{-2}}$ (Roach et al., 1982; Wood, 2012) leads to a strong radiative cooling rate of about 5–10 K h^{-1} (Koračin et al., 2001; Roach et al., 1982) which enhances the temperature inversion.

This net longwave radiative cooling by the emission of thermal infrared radiation at cloud top is the main driver for **latent heating** by condensation and for convective instability resulting in **turbulent mixing** in the boundary layer (Bott et al., 1996; Duynkerke et al., 2004; Ghonima et al., 2016; Lee, 2018; Wood, 2012; Zheng et al., 2018). In the cloud-topped MBL, the surface **sensible heat flux** plays only a minor role for the generation of turbulence compared to longwave cooling at cloud top (Wood, 2012). The strong thermal infrared cooling at cloud top drives negatively buoyant plumes descending through the cloud layer. Thus, the cloud develops its own turbulent structure with turbulent circulations (Boutle and Abel, 2012). The turbulent circulations, also called overturning convective circulations, are the main dynamical feature of stratocumulus clouds (Lilly, 1968; Wood, 2012). The convective circulations are intensified by **latent heating** in updraughts and **evaporative cooling** in downdraughts. The turbulent mixing homogenises the cloud layer. Often the radiative cooling and resulting turbulent mixing are sufficiently strong with negatively buoyant plumes spanning the entire boundary layer depth, so the cloud-topped MBL stays well-mixed (Duynkerke et al., 2004; Nicholls and Leighton, 1986). In this case the cloud layer is coupled to the surface moisture supply thus inhibiting cloud dissipation (Boutle and Abel, 2012; Wood, 2012).

The most important source of moisture is the surface **latent heat flux** which is regulated by relative humidity, temperature and wind speed at the surface (Wood, 2012). Without the moisture supply by the surface latent heat flux, the **entrainment** of warm and dry air from the troposphere would dissipate the cloud (Lee, 2018; Nicholls, 1984). The entrainment of tropospheric air into the boundary layer is further enhanced by turbulent mixing in the cloud-topped MBL generated by cloud top radiative cooling (e.g. Ghonima et al., 2016; Nicholls, 1984; Nicholls and Turton, 1986; Randall et al., 1984). The entrainment of warm and dry air in turn amplifies the cooling at cloud top by evaporation of cloud droplets (Nicholls and Turton, 1986).

Processes changing the inversion base height will also impact the cloud. The dominating processes controlling the height of the inversion layer are turbulent mixing in the boundary layer and subsidence in the lower troposphere (Kraus, 2004). Stronger mixing increases the height of the boundary layer and rises the inversion.

Large-scale subsidence over low SSTs creates a shallow MBL capped by a strong temperature inversion reducing cloud top entrainment of warm and dry air form the troposphere and inhibiting a cloud development in vertical direction beyond the PBL (Andersen et al., 2022; Eckardt et al., 2013; Ghonima et al., 2016; Lee, 2018; Wood, 2012, 2015). The shallow MBL is often well-mixed and the cloud is coupled to the surface moisture supply. A strong temperature inversion at the top of the PBL and the availability of sufficient moisture are important factors for the formation and maintenance of stratocumulus clouds (Duynkerke et al., 2004). Therefore, persistent stratus and stratocumulus clouds frequently occur at the top of a shallow PBL below a strong subsidence inversion associated with strong static stability of the lower troposphere (Andersen et al., 2022). These conditions are typically found above the cool regions of the subtropical oceans off continental west coasts in the descending

branches of the Hadley and Walker circulations, e.g. above the southeastern Atlantic (Duynkerke et al., 2004; Lee, 2018). Above the cold Benguela current and below the large-scale subsidence of warm and dry air from the South Atlantic Anticyclone, the southeastern Atlantic region offers ideal conditions for stratus and stratocumulus formation. Similar circumstances are found at the west coasts of North and South America above the cold water of the Humboldt current and the California current (e.g. Böhm, 2020; Klein and Hartmann, 1993; Lilly, 1968; Luccini and Rivas, 2021; Wood, 2012).
If the cloud-topped MBL becomes deeper than about 1 km due to the entrainment of free tropospheric air into the cloud-topped MBL or due to weak large-scale subsidence, the negative buoyancy of eddies resulting from longwave cooling at cloud top is not strong enough for the eddies to penetrate the subcloud layer. In this case the cloud layer can be decoupled from the surface moisture supply. This results in increased stratification of conserved variables and less cloud cover since the stratiform clouds are cut from surface moisture supply. The layer closest to the surface can however be well mixed by surface generated turbulence due to turbulent fluxes of latent and sensible heat at the sea surface.

The formation and evolution of clouds results from **microphysical processes** (e.g. diffusional particle growth and interparticle collection). A cloud droplet grows by water vapour diffusion if the relative humidity exceeds 100 % (cf. Sec. 2.1). With increasing droplet radius the diffusional growth becomes less efficient and droplets grow towards precipitation particles by interparticle collision and coalescence (Pruppacher and Klett, 2010).
With increasing cloud thickness and LWP, stratocumulus clouds, especially in the MBL, often produce **drizzle** (Wood, 2012). Drizzle occurs $20 - 40\,\%$ of the time in the regions of marine stratocumulus (Wood, 2012). Drizzle drops have diameters from 50 (Khain et al., 2015; Wood, 2015) to 100 µm (Wood, 2012). Their droplet diameter is between that of cloud droplets (2 to 50 µm) and raindrops with a diameter larger than 100 µm (Khain et al., 2015). Drizzle formation is initialised by collision and coalescence of cloud droplets (Pruppacher and Klett, 2010), also called autoconversion (Seifert and Beheng, 2006; Wood, 2012). Below cloud base, drizzle drops evaporate, thus, cooling, moistening, and destabilising the subcloud layer (Wood, 2012, 2015). Observational studies revealed that drizzle rate at cloud base increases with cloud thickness and LWP (Pawlowska and Brenguier, 2003; VanZanten et al., 2005; Wood, 2012). Drizzle occurs most frequently in the early morning hours before sunrise (Wood, 2012) when cloud thickness and LWP reach their maximum. Drizzle can reduce the cloud thickness by drying out the cloud-topped MBL (Wood, 2012).
In addition to drizzle, **sedimentation** of cloud droplets, i.e. the fallout due to gravitational settling, has to be taken into account as a sink for cloud water and droplets. The absorption of incoming **solar radiation** near cloud top is the main driver of the daily cycle of stratocumulus clouds. The heating by solar absorption is strongest at cloud top since scattering of solar radiation at cloud top inhibits solar absorption lower in the cloud layer. The proportion of solar radiation being absorbed by a stratocumulus cloud amounts up to 15 % dependent on the solar zenith angle and the cloud optical depth. The main absorbers in the cloud are water

vapour (roughly 50 % of solar absorption), droplets containing absorbing material, and aerosols (Wood, 2012).
Many complex interactions and feedbacks can change drizzle, cloud water, droplet size, turbulence, and radiation in a stratocumulus cloud. For further details on the feedback mechanisms between microphysical processes, radiation, turbulence and entrainment the reader is referred to Wood (2012) and references therein.

2.3.5 Diurnal cycle of low stratiform clouds

Low stratiform clouds often exhibit a strong diurnal cycle which is mainly driven by the absorption of solar radiation at cloud top. The absorption of solar radiation partly compensates the radiative cooling which is the main driver of turbulent mixing and condensation (Duynkerke et al., 2004). That way, the absorption of solar radiation weakens the turbulent mixing in the cloud-topped MBL and, thus, the ability of the stratocumulus to maintain a well-mixed boundary layer. Due to the reduced mixing during daytime, the cloud might get decoupled from its surface moisture source (Duynkerke et al., 2004). The entrainment continuously supplies warm and dry air from above the inversion into the boundary layer. This results in a thinning of the cloud, lifting of cloud base or even break-up of the cloud (Duynkerke et al., 2004). Since radiative cooling at cloud top drives condensation in the cloud, this is also reduced resulting in fewer droplets and lower liquid water content. If fewer cloud droplets are transported downward by turbulent mixing, the evaporative cooling in the lower part of the cloud decreases.
As a result of reduced driving during daytime, stratocumulus clouds reach their maximum with respect to cloud cover, LWP and cloud thickness shortly before sunrise. Since drizzle increases with cloud thickness and LWP, it also reaches its maximum before sunrise. The minimum in cloud coverage, thickness, and LWP is reached in the early afternoon (Ghonima et al., 2016).

2.3.6 Dissipation of low stratiform clouds

Low stratiform clouds can dissipate in different ways: they can become thinner and disappear as a whole or they can transform into a different cloud type (Wood, 2012). The thinning of a stratiform cloud layer can result from strong subsidence which lowers the inversion (Randall and Suarez, 1984). Alternatively, thinning of stratiform clouds can result from warming or drying of the PBL by heat fluxes and solar radiation, drizzle removing moisture from the cloud layer and entrainment of warm and dry air at cloud top (Wood, 2012). Stratiform clouds can also dissolve by processes including the transition to a stratified and intermittently coupled boundary layer by the reduction of turbulent mixing (Paluch et al., 1994). The reduction of turbulent mixing can result from shortwave solar heating during daytime or from evaporation of precipitation below cloud base. Both processes stabilise the temperature profile (Paluch et al., 1994). Consequently, the marine stratiform cloud is cut off from surface moisture supply and the entrainment of warm and dry air dissipates the cloud (Nicholls, 1984).
The decoupling of the cloud from the surface can be accompanied by the formation

of cumuli below the marine stratiform cloud. This often occurs if air masses are advected over warmer water, e.g. if air masses move towards the equator around the eastern side of subtropical oceanic anticyclones (Wood, 2012). Due to increased surface fluxes over the warmer water, the cloud-topped MBL deepens and warms. This leads to more warm air entrainment at cloud top and a decoupling of the cloud layer from the surface.

2.4 The Namib Desert

The Namib Desert is one of the driest deserts on earth and stretches along the entire Atlantic coast of Namibia (Goudie and Viles, 2015; United Nations, 2011). The Namib Desert gave its name to the state of Namibia. In the local Nama language, "Namib" means "an area where there is nothing" (Westberg and Westberg, 2013). But the Namib Desert is far from being empty and lifeless. Despite of the extreme aridity and despite of temperature that can reach up to 45 °C during the day and can drop below freezing point at night (Lancaster et al., 1984), several species have adapted to this life-hostile place. Life in the Namib Desert depends on two sources of moisture: fog and rain (Eckardt et al., 2013; Hachfeld, Jürgens, et al., 2000; Henschel and Seely, 2008; Lindesay and Tyson, 1990b; Pietruszka and Seely, 1985) The central coastal area receives very few rain with less than 20 mm per year (Eckardt et al., 2013). In contrast, fog occurs on more than 100 days per year (Olivier, 1995; Shanyengana et al., 2002).

2.4.1 Topography of the Namib Desert

The Namib Desert is located at the southwestern coast of the African continent. It spans the length of the Namibian coast extending more than 2000 km from 14 °S to 32 °S from the Carunjamba River in Angola to the Olifants River in South Africa. Bounded by the Atlantic Ocean in the west and the ragged mountain range of the Great Escarpment in the east the Namib Desert reaches 120-200 km inland (Goudie and Viles, 2015).

120-200 km east from the coast the ground rises to an average altitude of 1500 m reaching locally up to more than 2000 m forming the mountain range of the Great Escarpment (Lindesay and Tyson, 1990a; Taljaard, 1979; Tyson and Seely, 1980). The Great Escarpment runs almost parallel to the Atlantic coast and separates the coastal plain including the Namib Desert in the west from the elevated inner plateau in the east whose height ranges between 900 and 1300 m above sea level (Fig. 2.3). Especially in central and southern Namibia altitudes rise several hundred metres over short distances (Mendelsohn et al., 2002).

North of a line from Swakopmund to Windhoek the mountain range of the Great Escarpment is interrupted by the so-called Escarpment Gap which is some hundreds of kilometres wide (Fig. 2.3). The landscape in the area of the Escarpment Gap is characterised by a slowly sloping terrain with gravel covered surfaces and large, free-standing mountains, the so-called inselbergs. Amongst them is the Brandberg massif (2579 m), which is the most impressive inselberg including the highest peak in Namibia (Goudie and Viles, 2015).

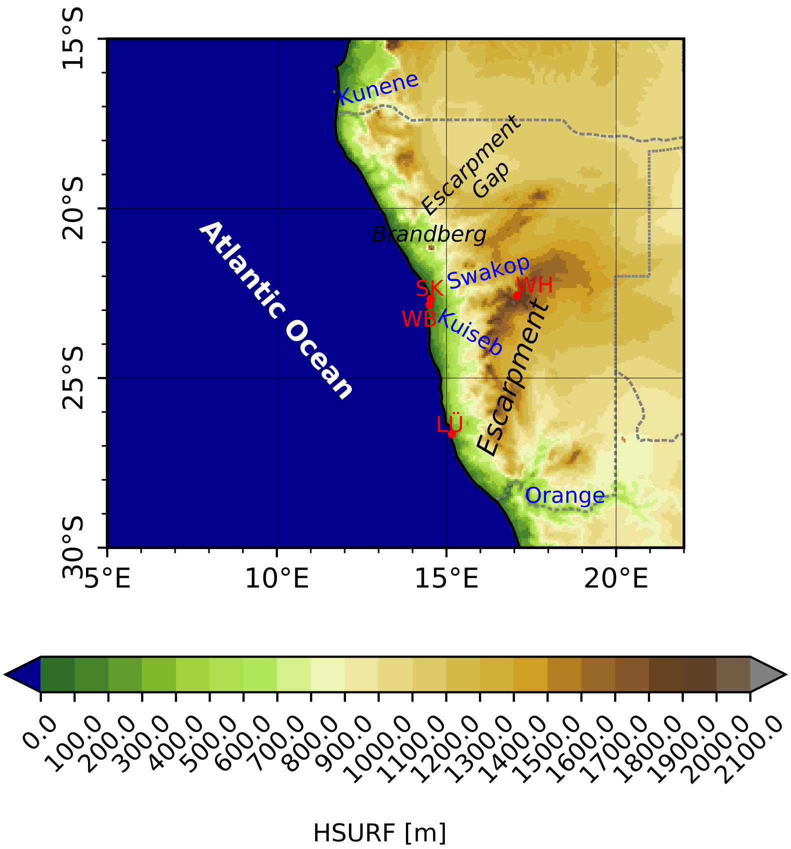

Figure 2.3: Topographic height of the surface *HSURF* [m] in the Namib region. Data is from a COSMO-FOG simulation with a horizontal grid spacing of $\Delta x \simeq 7$ km. The cities are Windhoek (WH), Swakopmund (SK), Walvis Bay (WB) and Lüderitz (LÜ).

The Great Escarpment is traversed by valleys of mostly impermanent ephemeral rivers which flow toward the coast, but only temporarily reach the ocean after precipitation has occurred. The only perennial rivers in the Namib Desert flow at the Namibian borders with Angola and South Africa, namely the Kunene and the Orange. Examples of ephemeral rivers are the Swakop, which enters the Atlantic Ocean just south of Swakopmund and the Kuiseb about midway between the Kunene River and the Orange River (Fig. 2.3). In the Kuiseb valley approximately 56 km inland from the coast, a research station is located at Gobabeb (Lindesay and Tyson, 1990a).
The Kuiseb marks a major landscape change in the desert between the bare rocks of the gravel plains in the north and coast parallel shifting sand dunes in the south (Lindesay and Tyson, 1990a).

2.4.2 Climatic setting of the Namib Desert

Located at the southwestern coast of the African continent in the proximity of the cold Benguela current, the hyper-arid Namib is a typical coastal desert. The coastal aridity is typical of subtropical locations at the subsiding branch of the Hadley cell circulation with dry descending air masses.
Due to the large-scale subsidence, semi-persistent surface anticyclones prevail, forming the subtropical high-pressure belt. This includes the South Atlantic Anticyclone. Southerly and southeasterly winds at the eastern side of the South Atlantic Anticyclone exert stress on the sea surface pushing the coastal water away from the coast. This drives near coastal upwelling of deep ocean water decreasing the SST of the Benguela Current (Goudie and Viles, 2015; Olivier and Stockton, 1989). The largest upwelling region is off the coast from Lüderitz yielding SSTs of approximately 14 °C throughout the year being 5–7 °C colder than the surrounding water of the southern Atlantic Ocean (Goudie and Viles, 2015; Mendelsohn et al., 2002; Olivier and Stockton, 1989). The Benguela current and its upwelling are further enhanced by the presence of the Great Escarpment leading to increased near coastal winds (Jung et al., 2014).
The strong temperature contrast between the low SST and the subsiding warm air leads to a strong temperature inversion capping the shallow well-mixed MBL. Within the inversion layer, the temperature increases 5 to 10 °C on average (Taljaard, 1979). This stable stratification effectively suppresses convection thus inhibiting convective precipitation and separates the MBL from the free troposphere (Eckardt et al., 2013; Lancaster et al., 1984). Turbulent mixing within the MBL creates an approximately adiabatic temperature profile and a specific humidity profile which is nearly constant with height. Under these conditions, low stratiform clouds frequently form below the base of the inversion above the cold ocean current.
As is typical of a coastal desert, the temperature varies less near the coast where the minimum temperature is around 5–10 °C and the maximum temperature is around 25–30 °C. Inland maximum temperatures around 40 °C and minimum temperatures below 0 °C have been measured (Lancaster et al., 1984).

Depending on its position, the South Atlantic Anticyclone causes southwesterly or southerly winds close to the Nambian coast. Thermally and topographically driven wind systems modify the large-scale circulation patterns. The topographic characteristics of the Namib Desert with a moderate slope, bounded by the cold waters of the Benguela current to the west and the deeply dissected Great Escarpment to the east provide ideal conditions for the development of thermally and topographically driven circulations (Taljaard, 1979). The regional airflow in the central Namib Desert results from the interaction of the sea- and land-breeze system induced by the thermal contrast between the cold ocean current and diabatically heated land surface, the mountain-valley wind system in the deep valleys of rivers incised into the Great Escarpment and the plain-mountain wind system between desert and plateau surfaces separated by the Great Escarpment (Lindesay and Tyson, 1990a; Tyson and Seely, 1980). A comprehensive overview on the circulation systems is given in Lindesay and Tyson (1990a,b), Taljaard (1979), and Tyson and Seely (1980).

A southwesterly sea breeze in the range of 5–10 $m\,s^{-1}$ occurs regularly throughout the year with peaks in September and March transporting moist air from the Atlantic inland (Seely and Henschel, 1998). It starts at the coast shortly after sunrise and advances inland across the entire Namib by evening. At nightfall the southwesterly sea breeze typically decays. The strength depends on the distance from the coast (Seely and Henschel, 1998).
A thermal gradient between the cool coastal area and the hot eastern plateau drives a northwesterly plain-mountain wind around 10–15 $m\,s^{-1}$ starting typically in the late afternoon (Lindesay and Tyson, 1990b; Seely and Henschel, 1998). In austral summer, this plain-mountain wind can even continue during night and the inland airflow of the plain-mountain wind may last continuously for several days. In austral winter, the inland-directed plain-mountain winds are weaker and occur only during the day (Lindesay and Tyson, 1990a). After sunset, the eastern plateau cools more rapidly under a clear sky than the often cloud-covered western part of the Namib and the ocean. The resulting temperature gradient drives a moderate (5–10 $m\,s^{-1}$) southeasterly mountain-plain wind starting at night and peaking at sunrise (Seely and Henschel, 1998). The mountain-plain wind then decays rapidly in the morning (Lindesay and Tyson, 1990a; Seely and Henschel, 1998). Mountain-plain winds are typically stronger in winter (Seely and Henschel, 1998). The sea breeze in the coastal zone is in phase with the plain-mountain wind thus enhancing each other up to 50–100 km from the coast (Taljaard, 1979).
On a more local scale, mountain-valley circulations may develop in the valleys of rivers incised into the Great Escarpment. The sea breeze in the coastal zone interacts with the valley wind in the dissected Great Escarpment, thus enhancing each other (Lindesay and Tyson, 1990a).
Sometimes during winter very strong and dry easterly to northeasterly berg winds interrupt the described circulation pattern (Seely and Henschel, 1998). Such disturbances occur rather seldom. Thus, the near-surface winds of the central Namib are widely controlled by thermally and topographically induced boundary layer circulations (Lindesay and Tyson, 1990b).

The geographical and meteorological situation described above results in on average less than 50 mm of rainfall per year in the Namib Desert. Precipitation is lowest and most variable at the west coast. The hyper-arid west coast of the Namib annually receives an average of 15 mm precipitation making the hyper-arid Namib Desert one of the driest places on Earth (Boss, 1941; Eckardt et al., 2013; Henschel and Seely, 2008; Lancaster et al., 1984; Mendelsohn et al., 2002; Seely, 1978). Approximately 100–120 km towards the Great Escarpment in the east, precipitation increases to 65–100 mm (Boss, 1941; Henschel and Seely, 2008; Lancaster et al., 1984; Seely, 1978). Rainfall in the Namib Desert is spatially and temporally highly variable and intermittent (Hachfeld, Jürgens, et al., 2000; Lancaster et al., 1984). Consecutive years without any rainfall have been recorded, e.g. Swakopmund experienced a period of 10 years without rainfall (Shanyengana et al., 2002).

2.4.3 Fog climatology in the Namib Desert

While rain is an unregular and unreliable source of moisture in the Namib Desert, fog occurs regularly and is more predictable than rain (Eckardt et al., 2013; Lancaster et al., 1984; Pietruszka and Seely, 1985; Seely and Henschel, 1998). Satellite retrievals have shown that the number of fog days is highest near the coast and decreases with distance from the coast (Andersen and Cermak, 2018; Andersen et al., 2019; Cermak, 2012; Olivier, 1995). The annual fog day frequency decreases from more than 100 days close to the coast to 40 days at a distance of 40 km from the coast and to 5-10 days at 100 km inland (Cermak, 2012; Olivier, 1995). The highest fog frequency with more than 100 days per year is limited to the low-lying coastal plains in the central Namib which is below 200 m above sea level (Andersen et al., 2019; Olivier, 1995). Olivier (1995) and Cermak (2012) have shown by use of satellite retrievals that fog and stratus clouds occur most frequently in the Central Namib around Walvis Bay, both over land and sea. However, there is a zone of high occurrence frequency for fog with more than 50 days per year along the whole Namibian coast (Olivier, 1995).
Olivier (1995) supposed a link between topography and fog occurrence frequency: Fog advances farther inland when the limitation by the Great Escarpment is missing (in the Escarpment Gap or in valleys of larger rivers). North of Walvis Bay landward spikes in the fog frequency are oriented along river beds (Cermak, 2012; Olivier, 1995). Where the coastal plain narrows, fog occurrence decreases more quickly with distance from the coast.

The monthly distribution of FLC frequency derived from satellite retrievals reveals a maximum from September to January and a minimum in May, June and July (Fig. 2.4) (Andersen et al., 2019; Cermak, 2012). In contrast, ground-based observations show seasonal fog frequency patterns varying between coastal and inland stations (Fig. 2.4). At coastal stations, the fog frequency peaks between April and September (Lancaster et al., 1984; Seely and Henschel, 1998), while farther inland the peak occurs from August to January (Henschel et al., 1998; Lancaster et al., 1984; Spirig, 2020). Thus, ground-based observations and satellite retrievals of fog frequencies show contrasting seasonal fog patterns at coastal stations while the seasonal patterns agree at inland stations (Cermak, 2012; Nagel, 1959; Olivier, 1995).
Andersen et al. (2019) used a combination of satellite observations and ground-based measurement stations to show that the reason for the discrepancies between ground-based observations and satellite retrievals is due to a seasonality in the vertical structure of FLCs influencing the interception of clouds with the terrain. During summer, cloud top and base heights are higher than in winter, causing the clouds to penetrate further inland where they intercept elevated terrain. The higher cloud bases lead to situations where clouds are disconnected from the surface at the coast from August to March. The clouds are classified as fog and low cloud by satellite, but not observed as fog by station measurements. This explains the discrepancies between measurements at ground-based stations and satellite retrievals for coastal areas. During the southern hemispheric winter, cloud top and base heights are about 100 m lower than in summer. Andersen et al. (2019) suggested that the lower cloud

heights cause the clouds to touch the ground more frequently in the coastal plains during southern hemispheric winter. This explains the peak in fog frequency at the coastal stations between April and September.

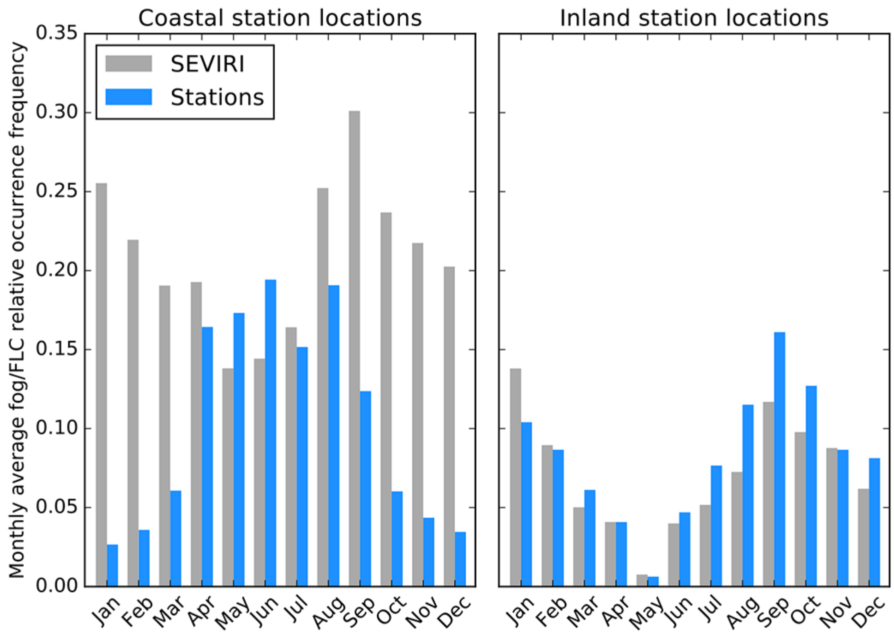

Figure 2.4: Monthly averaged relative FLC occurrence frequency at coastal (left) and inland stations (right). Spinning Enhanced Visible and In- frared Imager (SEVIRI) observations (2004–2017) are illustrated by grey bars; station measurements of ground fog (2015–2017) are in blue. From Andersen et al. (2019).

The onset time of FLCs in the course of the day is strongly related to the distance from the coastline with FLCs appearing significantly earlier at the coast than further inland (Andersen and Cermak, 2018; Andersen et al., 2019). Fog appears shortly after sunset at the lower-lying coastal stations. The onset time of fog varies also in north-south direction. The fog occurs slightly later in the night and the fog event gets shorter the further south the station is located. The investigation of hourly fog precipitation[1] reveals a peak of occurrence in the two hours around sunrise (Spirig, 2020). Most of the FLCs are gone by 14 UTC (Cermak, 2012).
While the number of fog days per year decreases from the coast inland, fog precipitation increases from the coast up to 35-60 km inland and decreases afterwards (Lancaster et al., 1984). Lancaster et al. (1984) measured the highest fog precipitation at two stations 33 km and 60 km from the coast at an altitude of 340 and 500 m (see also Henschel et al., 1998). The increase of fog precipitation is attributable to the increase of the terrain with most precipitation occurring at a height of 300−600 m above sea level. This is related to stratiform clouds below the inversion base at 300

[1]Fog precipitation is measured with a mesh (e.g. a cylindrical wire mesh) installed above a rain gauge (Henschel et al., 1998; Lancaster et al., 1984). The collected water in the rain gauge is often referred to as fog precipitation.

to 600 m which have to travel 20 to 60 km inland to intersect with the terrain (Lancaster et al., 1984).
The number of fog days as defined by non-zero fog precipitation might give a wrong impression about the importance of fog for the ecosystem or the availability for fog harvesting. Not all fogs deposit significant water. Based on non-zero fog precipitation, fog days were more frequently recorded at the most coastal station compared to the station farthest inland. However, at the station farthest inland, the fog precipitation is on average larger. This shows that fogs can be less frequent but produce more fog precipitation when reaching this far inland (Spirig, 2020).

2.4.4 Fog origins in the Namib Desert – Current theories

In the last decades numerous observational studies have dealt with the origin of the frequent fog in the Namib Desert. These observational studies suggest different types of fog regularly occurring in the Namib, i.e. advection fog, radiation fog, frontal fog, and intercepting clouds or lowering stratus clouds (Hachfeld, Jürgens, et al., 2000; Lancaster et al., 1984; Seely and Henschel, 1998; Taljaard, 1979).
Advection fog forms when warm moist air is transported over the cold water of the Benguela current in the Atlantic Ocean by onshore wind (see Sec. 2.2) (Olivier, 1992; Seely and Henschel, 1998). The upwelling and the Benguela current off the Namibian coast create a SST gradient with the coldest water adjacent to the coast. The advection fog is often transported inland with a southerly or southwesterly sea breeze (Olivier, 1992; Seely and Henschel, 1998) and reaches the Namibian coast during the afternoon. On more than 100 days per year this fog penetrates inland approximately 15 km reaching a maximum height usually below 200 m (Seely and Henschel, 1998). The distance from the coast reached by the fog depends on the wind speed and direction at the coast and further inland (Olivier, 1992; Taljaard, 1979). Rarely this fog types reaches as far as Gobabeb (approximately 56 km from the coast) (Seely and Henschel, 1998). Advection fog occurs mainly in austral winter (Andersen et al., 2020).
Radiation fog may form when moist air has been advected inland with the onshore sea breeze at daytime and cools during the night (see Sec. 2.2). This is opposed by observations of very low dewpoint temperatures at Gobabeb hinting at dry katabatic flows during the night obstructive for the formation of radiation fog (Olivier, 1992). Seely and Henschel (1998) suggest the formation of radiation fog when moist coastal air masses mix with a cool easterly mountain-plain wind. Until recently, radiation fog was seen as rare event (Eckardt et al., 2013; Seely and Henschel, 1998).
Frontal fog with drizzle can occur during the passage of a cold front (Seely and Henschel, 1998). This is rarely observed (Seely and Henschel, 1998) and thus not further discussed.

Of great importance in the Namib region is cloud interception fog which frequently occurs in conjunction with a northwesterly breeze (Seely and Henschel, 1998). Extensive and persistent low cloud fields frequently form over the southeastern Atlantic Ocean under the influence of large-scale subsidence from the South Atlantic Anticyclone and the low SST due to the upwelling of the Benguela Current (see Sec. 2.3).

These clouds are located between 100 and 600 m above sea level and are usually topped by a strong capping inversion inhibiting the formation of cumulus clouds (Seely and Henschel, 1998; Taljaard, 1979). These clouds are advected inland and fog forms about 20 to 60 km inland at an altitude of 100 to 600 m above sea level where these clouds intersect terrain (Andersen and Cermak, 2018; Andersen et al., 2019, 2020; Lancaster et al., 1984; Olivier, 1992, 1995; Spirig et al., 2019; Taljaard, 1979). The clouds are advected inland by westerly or northwesterly winds which might be enhanced by a plain-mountain wind or a valley breeze (Olivier, 1992; Seely and Henschel, 1998). The peak seasons of cloud interception fog around September and March are consistent to plain-mountain and mountain-plain winds, because both wind systems are well-developed at that times (Seely and Henschel, 1998). The occurrence of cloud interception fog and advection fog is independent from each other so both fog types can occur at the same time at different altitudes (Seely and Henschel, 1998).
Cloud interception fog and advection fog are of marine advective origin (Andersen et al., 2020). This shows, that fog in the Namib region is strongly related to wind systems. The importance of advective processes for fog in the Namib Desert is further supported by measurements of fog microphysics during the AEROCLO-sA field campaign, which indicate that fog originates from cloudy air masses advected from the ocean (Formenti et al., 2019). The fact that the timing of the onset of FLCs depends on the distance from the coast, with FLCs occurring earlier at the coast than further inland, also points to an advective origin of the fog (Andersen and Cermak, 2018; Andersen et al., 2019, 2020).

The origin of fog from the inland advection of FLCs has recently been questioned. Based on an isotope analysis of fog water, Kaseke et al. (2017) and Kaseke et al. (2018) found that the majority of their fog water probes originated from mixed or sweet water sources. Interpreting this as an indication of radiation fog they suggested a possible shift from an advection-dominated to a radiation-dominated fog regime. As a result, the importance of the various processes leading to fog formation is currently a subject of scientific debate (Andersen et al., 2020).

The importance of the different processes that lead to fog formation and control the spatio-temporal evolution of fog events are still not fully understood (Andersen et al., 2019, 2020; Spirig et al., 2019). For future water resource management in the hyper-arid Namib Desert, it is crucial to understand the mechanisms contributing to fog formation and evolution (Eckardt et al., 2013; Henschel et al., 1998; Shanyengana et al., 2002). Understanding the local mechanisms and thermo-hydrodynamic processes leading to fog formation and the spatio-temporal evolution of fog events in a spatially coherent manner can best be achieved using three-dimensional numerical simulations. To the author's knowledge, there is no modelling study which focuses on understanding the occurrence of FLCs in the Namib Desert.

3 Description of COSMO-FOG

The major objective of this study is the analysis of processes controlling fog occurrence and the spatio-temporal evolution of fog events in the Namib Desert. Therefore, within this thesis the three-dimensional numerical model COSMO-FOG is developed. The COSMO model is not designed for the simulation of fog, but for operational weather forecasting. PAFOG is a one-dimensional forecast model with parametrised cloud microphysics for fog and low stratiform clouds (Bott and Trautmann, 2002).
In this study, the two-moment microphysics scheme of PAFOG is newly implemented into version 5.05 of the meso-scale NWP model COSMO. For the numerical simulation of low-level stratiform clouds, Bott (2020) extended PAFOG by a one-moment bulk parametrisation of drizzle formation. However, to have access to additional diagnostic tools, not the pure COSMO model, but COSMO/MESSy (Kerkweg and Jöckel, 2012), i.e. COSMO including MESSy (Jöckel et al., 2005) is used. For simplicity the model will be called anyhow COSMO-FOG in the remainder of this thesis.
This chapter deals with the implementation of the microphysical parametrisation of PAFOG into the COSMO model. In Section 3.1, the COSMO model is introduced. Afterwards, the microphysical parametrisation scheme of COSMO is described in Section 3.2, before the two-moment microphysical parametrisation scheme of PAFOG is introduced in Section 3.3. The implementation of the PAFOG microphysical parametrisation into COSMO is illustrated in Section 3.4. Finally, additional diagnostics used from MESSy are presented in Section 3.5.

3.1 The numerical weather prediction model COSMO

The COSMO model is a non-hydrostatic limited-area NWP model which can be applied for operational weather prediction, climate simulations and scientific applications on the meso-β and meso-γ scale (Doms and Baldauf, 2018). The basic version of the COSMO model, formerly named Lokal Modell (LM), has been developed by the Deutscher Wetterdienst (DWD, German Meteorological Service). The subsequent improvement and maintainance of the model system has been organised within the framework of the international Consortium for Small-scale Modelling (COSMO) (Doms and Baldauf, 2018).
Since the end of 1999, the COSMO model has been part of the operational NWP system at DWD. Besides the operational NWP application, the COSMO model has been connected to MESSy building a limited-area atmospheric chemistry model (Kerkweg and Jöckel, 2012). Special configurations for regional reanalysis (Bollmeyer et al., 2015; Wahl et al., 2017) and long-term climate simulations (Rockel et al., 2008) have also been developed.

In this study, the COSMO model (version 5.05) is applied in configurations at 7 km and 2.8 km grid spacing. The following model description is mainly based on Doms and Baldauf (2018), Doms et al. (2018) and Baldauf et al. (2011).

3.1.1 The model equations, base state, coordinate system, and time integration

The COSMO model is based on hydro-thermodynamical model equations that describe a non-hydrostatic compressible flow in a moist atmosphere without any scale approximations (Doms and Baldauf, 2018; Schättler et al., 2018; Steppeler et al., 2003). The atmosphere is considered to be composed of dry air, water vapour, liquid water and water in solid state (i.e. frozen state). The prognostic model equations are derived from the budget equations representing the basic conservation laws of mass, momentum and internal energy as well as the ideal gas law.
The solution of prognostic equations in NWP models requires the definition of a spatial and temporal grid. As the spatial and temporal resolution of NWP models is limited by the grid spacing and time step of the model, the model equations have to be averaged. Applying some further simplifications to the hydro-thermodynamic equations (see Doms and Baldauf (2018), their Sec. 2.2 for more details), yields the basic model equations for the relative velocity $\mathbf{v}$, the pressure p, the temperature T, the specific humidity q^v and the specific water content in liquid q^l or optionally frozen form q^f[1,2]:

$$\rho \frac{d\mathbf{v}}{dt} = -\nabla p + \rho \mathbf{g} - 2\boldsymbol{\Omega} \times (\rho \mathbf{v}) - \nabla \cdot \underline{\mathbf{T}}, \tag{3.1}$$

$$\frac{dp}{dt} = -\left(\frac{c_p}{c_v}\right) p \nabla \cdot \mathbf{v} + \left(\frac{c_p}{c_v} - 1\right) Q_h, \tag{3.2}$$

$$\rho c_p \frac{dT}{dt} = \frac{dp}{dt} + Q_h, \tag{3.3}$$

$$\rho \frac{dq^v}{dt} = -\nabla \cdot \mathbf{F}^v - \left(I^l + I^f\right), \tag{3.4}$$

$$\rho \frac{dq^{l,f}}{dt} = -\nabla \cdot \left(\mathbf{P}^{l,f} + \mathbf{F}^{l,f}\right) + I^{l,f}, \tag{3.5}$$

$$\rho = p \left\{ R_d \left\langle 1 + \left(\frac{R_v}{R_d} - 1\right) q^v - q^l - q^f \right\rangle T \right\}^{-1}. \tag{3.6}$$

In equations 3.1–3.6, $\mathbf{g}$ is the acceleration of gravity, $\boldsymbol{\Omega}$ is the constant angular velocity of earth rotation, c_p and c_v are specific heat of dry air at constant pressure and specific heat of dry air at constant volume, respectively. R_d and R_v are the gas constants for dry air and water vapour, respectively. In this system of equations, the continuity equation is replaced by an equation for pressure (Eq. 3.2). The density

[1] Liquid water includes the specific cloud water content and the specific water content of rain. Water in solid form comprises the specific cloud ice content, the specific content of snow and graupel, depending on the scheme used. In the following, the 'specific' will be omitted for convenience for the contents of cloud water, cloud ice, rain, snow, and graupel.

[2] The hat and bar symbols indicating the mean values are omitted for convenience.

of moist air ρ is determined diagnostically from the equation of state.
Equations 3.1–3.6 form a complete set to predict the grid-scale variables of state if the terms describing the contributions from subgrid-scale processes on the grid-scale variables are known. The subgrid-scale processes included in equations 3.1–3.6 are the turbulent transport of momentum (represented by the Reynolds stress tensor $\underline{\mathbf{T}}$), the turbulent fluxes of water vapour $\mathbf{F}^v$, liquid water $\mathbf{F}^l$ and ice $\mathbf{F}^f$, the precipitation fluxes of liquid water $\mathbf{P}^l$ and ice $\mathbf{P}^f$, and the rates of phase transitions of liquid water I^l and ice I^f. Q_h represents all diabatic effects and is given as:

$$Q_h = L_v I^l + L_s I^f - \nabla \cdot (\mathbf{H} + \mathbf{R}) \,. \tag{3.7}$$

Here, L_v and L_s denote the latent heat of vaporisation and sublimation, respectively. $\mathbf{H}$ and $\mathbf{R}$ denote the turbulent flux of sensible heat, and the flux of solar and thermal electromagnetic radiation, respectively.
All terms representing subgrid-scale processes have to be expressed in terms of the grid-scale variables which is called parametrisation. An overview of the physical parametrisation schemes used in the COSMO model is given in Section 3.1.2.

The model equations are numerically solved on an Arakawa-C grid on a rotated spherical coordinate system accounting for the spherical shape of the earth. The geographical coordinates are transformed into rotated coordinates by tilting the north pole in such a way that the equator is close to the centre of the model domain. Thus, effects of the convergence of the meridians are minimized. In vertical direction, a time-independent generalised terrain-following height coordinate ζ is used. The distance between the ζ-surfaces increases with height thus ensuring a finer vertical grid close to the ground.
Due to the fact, that the model atmosphere in the COSMO model is compressible, sound and gravity waves occur in the solution of the model equations. As acoustic sound waves propagate with very fast phase speed, this imposes strong restrictions on the choice of the time step. To solve the model equation system efficiently, a time-splitting approach is applied in the Runge-Kutta integration scheme, splitting the model equations into slow and fast parts. Physical processes, such as advection or the subgrid-scale processes, belong to the slowly varying modes. The fast part consists of the pressure gradient terms, the working terms in the temperature and pressure equation resulting in sound expansion and the buoyancy terms together leading to expansion of gravity waves. The time-splitting method enables the usage of a numerical time step of 40 s or 25 s at grid spacings of 7 km or 2.8 km, respectively.

3.1.2 Parametrisations

As already mentioned above, the set of basic model equations 3.1-3.6 can only be solved with the knowledge of the contributions by subgrid-scale processes to the grid-scale variables. The effect of these subgrid-scale processes on the resolved grid-scale variables is determined by means of physical parametrisations.
In the COSMO model, the parametrisation of radiative processes is based on a δ-two-stream approximation of the radiative transfer equation (Ritter and Geleyn,

1992). Fractional cloud cover for radiative transfer and further applications in post-processing is calculated by an empirical function dependent on the relative humidity, the height of the model layer, and (where necessary) the convective activity (Schättler et al., 2018; Steppeler et al., 2003). Moist convection is parametrised with the mass flux convection scheme of Tiedtke (1989). For shallow convection a simplified version of the mass flux scheme of Tiedtke (1989) is applied. The shallow convection scheme does not form convective precipitation (Doms et al., 2018). The parametrisation of vertical turbulent diffusion is based on a closure according to Mellor and Yamada (1982) at hierarchy level 2.5 as introduced by Mellor and Yamada (1974). The parametrisation uses a prognostic equation for the turbulent kinetic energy (TKE). The turbulent fluxes are parametrised by a traditional K-closure, i.e. the turbulent fluxes are described proportional to the vertical gradient and a factor K which is referred to as turbulent exchange coefficient or turbulent transfer coefficient. The turbulent transfer coefficients are determined in dependence of the vertical wind shear and the stability of the thermal stratification (Baldauf et al., 2011). Departing from the scheme described by Mellor and Yamada (1982), the turbulence parametrisation in the COSMO model uses variables which are conserved under moist adiabatic processes (see Baldauf et al. (2011) for further details). The fluxes of momentum, heat, and moisture at the bottom boundary are parametrised consistently with the turbulence scheme based on a prognostic equation for TKE (Doms et al., 2018). For the calculation of surface fluxes between the surface and the atmosphere, the land surface temperature and specific humidity at the ground are provided by the multi-layer soil model TERRA-ML (Doms et al., 2018). TERRA-ML describes thermal and hydrological processes in the soil (Doms et al., 2018). The microphysical parametrisation is of special importance for the scope of this study and is therefore described more detailed in the following section. Further information on the physical parametrisations can be found in Doms et al. (2018) and references therein.

3.2 Parametrisation for grid-scale clouds and precipitation in the COSMO model

Grid-scale clouds and precipitation including phase changes are parametrised using a one-moment bulk parametrisation in the COSMO model. The prognostic variables in the bulk parametrisation scheme of the COSMO model are the mass fractions q^x of various hydrometeor types x. The general budget equation for the mass fractions q^x is given by equation 3.5, which can be rewritten as (Doms and Baldauf, 2018)

$$\frac{\partial q^{l,f}}{\partial t} + \mathbf{v} \cdot \nabla q^{l,f} - \frac{1}{\rho}\frac{\partial P^{l,f}}{\partial z} = S^{l,f} + M_{q^{l,f}}, \tag{3.8}$$

where the indices l and f mark liquid and solid forms of water substance. The second term on the left hand side describes advection of the mass fractions. The term

$$M_{q^{l,f}} = -\frac{1}{\rho}\nabla \cdot \mathbf{F}^{l,f} \tag{3.9}$$

denotes the source term due to turbulent mixing (Doms and Baldauf, 2018). $P^{l,f}$ are the absolute values of the precipitation fluxes of water (l) and ice (f) which are given as (Doms and Baldauf, 2018)

$$\mathbf{P}^{l,f} = -P^{l,f}\mathbf{e}_z = -\rho q^{l,f}|\mathbf{v}_T^{l,f}|\mathbf{e}_z \tag{3.10}$$

and depend on the mean terminal fall velocities $\mathbf{v}_T^{l,f}$ of the particles being a nonlinear function of the mass fractions $q^{l,f}$. In the bulk parametrisation of the COSMO model, precipitating and non-precipitating categories are distinguished. The bulk microphysical parametrisation of the COSMO model predicts the mass fractions of water vapour, cloud water, rain water, cloud ice, and snow. For high-resolution COSMO simulations, which are expected to explicitly simulate deep moist convection, additionally graupel is considered (Doms et al., 2018; Reinhardt and Seifert, 2006). The mass fractions of cloud water q^c and cloud ice q^i belong to the non-precipitating cloud phase and have a negligible sedimentation velocity. Thus, their precipitation fluxes $\mathbf{P}^{l,f}$ are neglected. Rain, snow and graupel with mass fractions q^r, q^s and q^g belong to the precipitable phase. For the precipitating particles the sedimentation flux is larger than the turbulent fluxes. Therefore, for the precipitating categories rain, snow and graupel, the precipitation fluxes $\mathbf{P}^{l,f}$ are included while the turbulent fluxes $\mathbf{F}^{l,f}$ are neglected.
$S^{l,f}$ represents the cloud microphysical sources and sinks due to phase changes and conversion between different hydrometeor types per unit of moist air (Doms and Baldauf, 2018):

$$S^{l,f} = \frac{1}{\rho}I^{l,f}. \tag{3.11}$$

Examples for these processes are condensation and evaporation of cloud water, autoconversion of cloud water to form rain, evaporation of rain water, melting of cloud ice to form cloud water, ... [3]. A detailed description of the parametrisation of each individual process is beyond the scope of this study. For further information, the reader is referred to Doms et al. (2018).

This study focuses on the numerical simulation of fog and low stratiform clouds, i.e. warm clouds. Fog and low stratiform clouds usually form no precipitation except for drizzle. While graupel often occurs in convective situations with strong updraughts, weather situations with fog and low stratiform clouds are not characterised by strong convective updraughts and a strong temperature inversion suppresses convection in the Namib region (cf. Sec. 2.4). So rain, snow and graupel will not be relevant for the case studies simulated in this study.
For warm clouds, besides the autoconversion from cloud water to rain and drizzle, the condensation and evaporation of cloud water are essential microphysical processes. The condensation or evaporation rates are calculated by a saturation adjustment: If a grid box becomes supersaturated in a numerical time step, the temperature and the mass fractions of cloud water q^c and water vapour q^v will be isobarically adapted to a saturated state taking into account the release of latent heat during condensation. The resulting difference of q^v determines the amount of cloud water

[3] A list of the cloud microphysical processes which are accounted for is given in the appendix.

q^c being condensed. For supersaturation the cloud cover is set to one. If undersaturation occurs in case of $q^c > 0$, the cloud water is evaporated until either saturation with respect to water is reached or all cloud water is evaporated. The nucleation process is encompassed by the saturation adjustment since it is assumed that always enough cloud condensation nuclei are present in case of supersaturation and resulting condensation (Doms et al., 2018). As the condensation rate is calculated by a saturation adjustment, condensation-evaporation is a quasi-reversible process with two thermodynamic states: Either the air in a grid box volume is saturated with respect to water with $q^v = q^v_{sat}$ and $q^c > 0$ or it is undersaturated with $q^v < q^v_{sat}$ and $q^c = 0$. The specific humidity at saturation with respect to water q^v_{sat} is given by (Doms et al., 2018)

$$q^v_{sat}(T,p) = \frac{R_d}{R_v} \frac{e_{sat}(T)}{p - (1 - \frac{R_d}{R_v}) e_{sat}(T)}. \tag{3.12}$$

$e_{sat}(T)$ is the equilibrium vapour pressure over a plane surface of water. It is calculated with the following formula:

$$e_{sat}(T) = p_0^v \exp\left(a_w \frac{T - T_r}{T - b_w} \right) \tag{3.13}$$

using the parameters $p_0^v = 610.78\,\mathrm{Pa}$, $T_r = 273.16\,\mathrm{K}$, $a_w = 17.27$ and $b_w = 35.86\,\mathrm{K}$ (Doms et al., 2018).

The one-moment bulk parametrisation in the COSMO model is not designed for the simulation of fog. It distinguishes condensation and evaporation by a threshold of 100 % relative humidity. A supersaturation cannot occur and is thus neglected. The cloud water content in the COSMO model is treated as a non-precipitating bulk phase without a particle size distribution. The sedimentation flux of cloud water is neglected.
Therefore, in this study, the bulk cloud scheme of the COSMO model is replaced by the two-moment microphyiscal parametrisation scheme of the fog and boundary layer cloud model PAFOG in the lower atmosphere.

3.3 Two-moment microphysical parametrisation in PAFOG

PAFOG is a one-dimensional model which has been developed for the forecast of radiation fog and low-level stratiform clouds (Bott and Trautmann, 2002). PAFOG allows for a fog forecast with a lead time of 24 hours on a standard personal computer within a few minutes. In contrast to the standard microphysical parametrisation of the COSMO model, PAFOG comprises a two-moment microphysical parametrisation which is based on Nickerson et al. (1986) and Chaumerliac et al. (1987).
The two-moment microphysical parametrisation of PAFOG includes modules for the activation of cloud droplets from dry aerosol, a description of the condensation and evaporation process and a module for the sedimentation of cloud droplets (Bott and Trautmann, 2002). All these processes are parametrised dependent on

the droplet number concentration which is treated prognostically in PAFOG. For the simulation of low-level stratiform clouds, PAFOG has recently been extended with a one-moment bulk parametrisation for drizzle formation (Bott, 2020). In the following, the microphysical cloud scheme of PAFOG being relevant for this thesis is described. The description widely follows Nickerson et al. (1986), Chaumerliac et al. (1987), Bott and Trautmann (1997) and Bott (2020).

In contrast to the microphysical parametrisation of the COSMO model, where cloud water is a non-precipitating bulk phase without size distribution, a particle size distribution is assumed for cloud droplets in PAFOG. As in Nickerson et al. (1986), the size distribution of the cloud droplets is assumed to be a log-normal size distribution given as a function of the droplet diameter D by

$$dN^c = \frac{N^c}{\sqrt{2\pi}\sigma_c D} \exp\left[-\frac{1}{2\sigma_c^2} \ln^2\left(\frac{D}{D_0}\right)\right] dD \tag{3.14}$$

with N^c the total number concentration of cloud droplets, D_0 denoting the mean droplet diameter and σ_c the dispersion parameter of the log-normal distribution. σ_c can be prescribed as a function of the aerosol type (maritime: $\sigma_c = 0.28$, continental: $\sigma_c = 0.15$) as in Chaumerliac et al. (1987). Following Bott and Trautmann (2002), $\sigma_c = 0.2$ is used in the present study.

Activation

In a cloud scheme based on a two-moment approach, where the cloud droplet number concentration is a prognostic model variable, the activation of cloud droplets from aerosol particles is an important source term for the droplet number concentration. In PAFOG, the number of activated condensation nuclei at a given grid-scale supersaturation is determined without an explicit calculation of the Köhler theory, instead it is based on Twomey's relation (Twomey, 1959):

$$N_{act} = N^a S^k. \tag{3.15}$$

Here, N_{act} denotes the number of activated condensation nuclei, N^a the number of dry aerosol particles and S the supersaturation. N^a and k are empirical constants depending on the aerosol type. Chaumerliac et al. (1987) define N^a to be $3500\,\mathrm{cm}^{-3}$ and k to be 0.9 for continental clouds, and $N^a = 100\,\mathrm{cm}^{-3}$ and $k = 0.7$ for maritime clouds. In this study the value for N^a is set to $400\,\mathrm{cm}^{-3}$ and $k = 0.7$ as the research area is the Namibian coast which is predominantly influenced by maritime air masses, but sometimes also by continental air masses from the African continent. Currently, N^a is spatially constant over the model domain, although the model domain includes maritime and country seashore parts. Ideally N^a should be a prognostic quantity, however, implementing nucleation, sources and sinks into the model goes beyond the scope of this study and a fixed value of $400\,\mathrm{cm}^{-3}$ must suffice. The effect of the nucleation on the aerosol concentration N^a is neglected.
The increase of the droplet number concentration by activated condensation nuclei is represented as follows:

$$N^c(t + \Delta t) = N^c(t) + \max(N_{act} - N^c(t), 0). \tag{3.16}$$

The above formulation ensures, that the number concentration of cloud droplets increases only for an increase in supersaturation. For constant supersaturation, the already existing cloud droplets grow by condensation and N^c stays constant.

Condensation and evaporation

In the PAFOG microphysical parametrisation, the temporal evolution of the cloud is described by the change of the droplet number concentration and the droplet diameter. The temporal development of the droplet diameter D due to condensation or evaporation is given by

$$\frac{dD}{dt} = G\frac{S}{D} \tag{3.17}$$

where S is the supersaturation and G is the thermodynamic function (Chaumerliac et al., 1987):

$$G = \left(\frac{L_v \rho_w}{KT}\left(\frac{L_v}{R_w T} - 1\right) + \frac{\rho_w R_w T}{e_{sat}(T) D_v}\right)^{-1}. \tag{3.18}$$

Here, L_v is latent heat of vaporisation, ρ_w the density of water, $e_{sat}(T)$ is the saturation vapour pressure over a plane surface of water, R_w the specific gas constant for moist air, D_v the water vapour diffusivity and K the thermal conductivity.
The change of cloud water content q^c by condensation and evaporation, respectively, is given by:

$$\left(\frac{\partial q^c}{\partial t}\right)_{con/eva} = \frac{\rho_w}{\rho}\int\limits_0^\infty \frac{\pi}{2} D^2 \frac{dD}{dt}\frac{dN^c(D)}{dD} dD. \tag{3.19}$$

Inserting the log-normal size distribution and equation 3.17 yields an expression for the change of cloud water content q^c and specific humidity q^v by condensation and evaporation, respectively, as a function of the cloud droplet number concentration N^c, the mean droplet diameter D_0 and the average supersaturation $\overline{S}$:

$$\left(\frac{\partial q^c}{\partial t}\right)_{con/eva} = \frac{\rho_w}{\rho}\frac{\pi}{2} G\overline{S} N^c D_0 \exp\left(\frac{\sigma_c^2}{2}\right) \tag{3.20}$$

$$\left(\frac{\partial q^v}{\partial t}\right)_{con/eva} = -\frac{\rho_w}{\rho}\frac{\pi}{2} G\overline{S} N^c D_0 \exp\left(\frac{\sigma_c^2}{2}\right). \tag{3.21}$$

For further details see Chaumerliac et al. (1987). The change of temperature due to phase changes is given by

$$\left(\frac{\partial T}{\partial t}\right)_{con/eva} = -\frac{L_v}{c_p}\left(\frac{\partial q^v}{\partial t}\right)_{con/eva}. \tag{3.22}$$

The average supersaturation $\overline{S}$ is calculated following Sakakibara (1979) yielding an average supersaturation for a numerical time step in the order of 10 s or even larger (Bott and Trautmann, 2002; Chaumerliac et al., 1987).
The change of the cloud droplet number concentration due to condensation and evaporation is based on the following considerations: For a given supersaturation with $S > 0$ the droplets grow and the cloud water content increases. As long as

no further droplets are activated, the cloud droplet concentration remains constant. In case of undersaturation with $S < 0$, the small droplets evaporate first. Thus, the droplet number concentration and the cloud water content decrease. Assuming, that G and S are constant during the numerical time step Δt, the critical diameter of the largest evaporating droplet can be determined from equation 3.17 as:

$$D_{c,eva} = \sqrt{-2GS\Delta t} \qquad \text{with } S < 0 \tag{3.23}$$

Integration of the log-normal size distribution from the smallest droplet to the critical droplet diameter $D_{c,eva}$ yields the number of evaporating cloud droplets.
For drizzle particles, the condensational growth is neglected (Bott, 2020). In undersaturated air, the evaporation rate is split between drizzle and cloud water depending on the maximum amount of drizzle or cloud water that can evaporate. Due to the larger size and fall speed of the drizzle particles, it is assumed that in a 20 m thick model layer at most 15 % of the total specific drizzle water content[4] can evaporate (Bott, 2020).

Sedimentation

Differing from the standard bulk parametrisation of the COSMO model, the cloud water content has a non-negligible sedimentation velocity in the microphysical parametrisation of PAFOG. The assumption of a droplet size distribution for the cloud droplets allows for the calculation of a sedimentation velocity dependent on the mean droplet diameter D_0. The settling velocity v of the droplets is calculated according to Berry and Pranger (1974) dependent on the Reynolds number Re and the mean droplet diameter D_0:

$$v(D_0) = \frac{\eta Re}{D_0 \rho}, \tag{3.24}$$

where the dynamic viscosity of air η is determined as a function of temperature

$$\eta = 1,496286 \cdot 10^{-6} \frac{T^{1,5}}{T + 120}. \tag{3.25}$$

A more detailed description is given in Bott and Trautmann (1997).
The sedimentation of cloud droplets is numerically solved by the positive definite advection scheme of Bott (1989).

Drizzle

PAFOG has recently been extended by a one-moment bulk parametrisation of drizzle formation (Bott, 2020). The loss of cloud water by the formation of drizzle water is parametrised by

$$\left(\frac{\partial q^c}{\partial t}\right)_{df} = \alpha q^c \tag{3.26}$$

$$\alpha = \frac{q^c}{q^c_{crit}} \frac{1}{3600} \tag{3.27}$$

[4]In the following, the 'specific' will be omitted for convenience.

where α has units of s^{-1} and $q^c_{crit} = 0.5\,\mathrm{g\,kg^{-1}}$. The loss of cloud droplets by the autoconversion process is ignored. Since the drizzle water is a bulk phase without droplet spectrum, assumptions for the diameter have to be made for the parametrisation of drizzle sedimentation. It is assumed that the radius of the drizzle particles increases exponentially between the level where drizzle forms and the surface. The drizzle radius ranges from 70 µm to 90 µm.

Parametrisation of visibility

The reduction of the visibility by fog depends on the number density and size distribution of the droplets. Many small droplets yield a stronger reduction of the visibility than larger droplets. Therefore, the parametrisation of visibility should consider both, the cloud water content and the droplet number concentration. The cloud water content q^c and the droplet number concentration N^c are prognostic variables in the microphysical parametrisation of PAFOG. With these two variables, the visibility is calculated based on the empirical relationship for the calculation of the visibility in warm fogs without ice particles developed from measurements during fog events by Gultepe et al. (2006):

$$VIS = \frac{1.002}{(q^c N^c)^{0.6473}} \qquad \text{if } q^c > 0 \tag{3.28}$$

This relation has been implemented into the PAFOG model by Mohr (2009).

3.4 Implementing PAFOG into the COSMO model – COSMO-FOG

PAFOG and COSMO are both stand-alone models which include a parametrisation scheme for microphysical processes. The one-moment bulk microphysical parametrisation scheme of the COSMO model is replaced by the two-moment microphysical parametrisation of the PAFOG model in the lower atmosphere. So the PAFOG microphysical parametrisation is active in the region of the atmosphere, where FLCs form. All other model components of the COSMO model remain unchanged.
The microphysical parametrisation scheme of the PAFOG model replaces the bulk scheme of the COSMO model in the lower part of the atmosphere extending from the ground up to a prescribed height of 2000 m above ground level. The upper limit of the region, where the PAFOG microphysics is active, is determined in such a way that the distance to the ground is at least 2000 m at every point in the model area. The saturation adjustment of the COSMO model is switched off in that region, since the activation of cloud droplets in the PAFOG microphysics requires a supersaturation which cannot occur with the saturation adjustment.
In this study, COSMO-FOG is applied in midlatitude and subtropical regions, where a strong temperature inversion suppresses the formation of precipitation. The formation of ice phases below 2000 m is not expected. Therefore, below 2000 m a warm-cloud scheme neglecting ice and mixed-phase cloud processes and precipitation except for drizzle is expected to be sufficient in this study. Above 2000 m,

the microphysical parametrisation of the COSMO model remains unchanged. Here, condensation and evaporation are parametrised with the saturation adjustment and in higher regions, where ice clouds can occur, the ice phase can be simulated.
The PAFOG microphysical parametrisation calculates microphysical tendencies of the cloud water content, the droplet number concentration and the drizzle water content. The cloud water content is already a prognostic variable in the COSMO model. In the prognostic equation for the mass fractions q^x (Eq. 3.8) the cloud microphysical sources and sinks $S^{l,f}$ are replaced by the PAFOG processes below 2000 m. Inserting the PAFOG tendencies due to condensation/evaporation $(\partial q^c/\partial t)_{con/eva}$, sedimentation $(\partial q^c/\partial t)_{sed}$ and drizzle formation $(\partial q^c/\partial t)_{df}$ into 3.8 and neglecting the precipitation fluxes, yields the prognostic equation for the cloud water content q^c below 2000 m:

$$\frac{\partial q^c}{\partial t} = \underbrace{-\mathbf{v}\cdot\nabla q^c + M_{q^c}}_{\text{COSMO}} \underbrace{+ \left(\frac{\partial q^c}{\partial t}\right)_{con/eva} - \left(\frac{\partial q^c}{\partial t}\right)_{df} - \left(\frac{\partial q^c}{\partial t}\right)_{sed}}_{\text{PAFOG}}. \tag{3.29}$$

The first two terms on the right hand side ($-\mathbf{v}\cdot\nabla q^c$ and M_{q^c}) represent atmospheric transport by advection and turbulent diffusion, respectively, which are computed by the COSMO model.
Besides the cloud water content q^c, the droplet number concentration N^c and the drizzle water content q^d are prognostic variables in the two-moment scheme of the PAFOG model. Since the COSMO model does neither have drizzle water content nor a cloud droplet number concentration, two additional tracers with associated sources and sinks, among others due to the microphysical processes parametrised in the PAFOG model, are included in the COSMO model. The prognostic equations solved below 2000 m for the droplet number concentration N^c and the drizzle water content q^d can be written as

$$\frac{\partial N^c}{\partial t} = \underbrace{-\mathbf{v}\cdot\nabla N^c + M_{N^c}}_{\text{COSMO}} \underbrace{+\Delta\left(\frac{\partial \overline{S}}{\partial t}\right)\left(\frac{\partial N^c}{\partial t}\right)_{act} + \Delta\left(\overline{S}\right)\left(\frac{\partial N^c}{\partial t}\right)_{eva} - \left(\frac{\partial N^c}{\partial t}\right)_{sed}}_{\text{PAFOG}} \tag{3.30}$$

$$\frac{\partial q^d}{\partial t} = \underbrace{-\mathbf{v}\cdot\nabla q^d + M_{q^d}}_{\text{COSMO}} \underbrace{+ \left(\frac{\partial q^c}{\partial t}\right)_{df} + \Delta\left(\overline{S}\right)\left(\frac{\partial q^d}{\partial t}\right)_{eva} - \left(\frac{\partial q^d}{\partial t}\right)_{sed}}_{\text{PAFOG}}. \tag{3.31}$$

The first two terms on the right hand side represent advection and turbulent diffusion which are determined by the COSMO model. The calculation of the atmospheric tranport processes for the droplet number concentration N^c and the cloud water content q^c by the same routines in the dynamical core of the COSMO model ensures a three-dimensional relation between q^c and N^c.
$(\partial N^c/\partial t)_{act}$ and $(\partial q^c/\partial t)_{df}$ denote the change of the droplet number concentration due to activation and the change of the drizzle water content by the formation of drizzle, respectively. $(\partial\psi/\partial t)_{sed}$ represents the sedimentation of cloud droplets and drizzle water content with $\psi = N^c$ and $\psi = q^d$.

To ensure that the droplet number concentration and the drizzle water content decrease by evaporation ($(\partial\psi/\partial t)_{eva} < 0$) only in case of undersaturation and cloud droplets are only activated if the supersaturation increases, the corresponding tendencies are multiplied by $\Delta\left(\overline{S}\right)$ and $\Delta\left(d\overline{S}/dt\right)$, respectively, which are defined as follows:

$$\Delta\left(\overline{S}\right) = \begin{cases} 1 & \text{for } \overline{S} < 0 \\ 0 & \text{for } \overline{S} > 0 \end{cases} \tag{3.32}$$

$$\Delta\left(\frac{\partial\overline{S}}{\partial t}\right) = \begin{cases} 1 & \text{for } \frac{\partial\overline{S}}{\partial t} > 0 \\ 0 & \text{for } \frac{\partial\overline{S}}{\partial t} < 0. \end{cases} \tag{3.33}$$

The PAFOG microphysics requires the specific humidity q^v, the cloud water content q^c, temperature T and the pressure p as input variables. In addition to those standard model variables, the droplet number concentration N^c and the drizzle water content q^d have to be passed to the microphysical parametrisation of PAFOG. After the inclusion of N^c and q^d as prognostic variables in the COSMO model, the required input can be provided by the COSMO model. The relative humidity which is also needed for the PAFOG microphysics, is calculated from the saturation vapour pressure. The COSMO model receives the prognostic variables updated by PAFOG. At the ground, the sedimentating cloud and drizzle water from PAFOG are treated as grid-scale precipitation.

Due to the formulation of the condensation/evaporation process and the sedimentation based on the droplet number concentration and the mean droplet diameter, the cloud water content q^c always has to be linked to a droplet number concentration N^c. Problems arise for cloud water which has not been formed by the PAFOG microphysics, e.g. cloud water being already present at model initialisation or cloud water being transported into the PAFOG domain from the regions in the model domain, where PAFOG is not active. In this case, the droplet number concentration does not correspond to the cloud water content. As a result, liquid water may accumulate in an undersaturated environment (if no droplets are available) or unrealistically huge droplets form with an enormous settling velocity.
To overcome these problems a boundary condition is necessary linking the cloud water content q^c to a droplet number concentration N^c. One approach for a boundary condition is to relate the cloud water content to the droplet number concentration assuming the log-normal distribution. Integration of the log-normal distribution over the whole droplet spectrum yields for the cloud water content q^c (Chaumerliac et al., 1987):

$$q^c = \frac{N^c}{\rho}\left(\frac{\pi}{6}D_0^3\rho_w\right)\exp\left(\frac{9}{2}\sigma_c^2\right). \tag{3.34}$$

Algebraic operations yield the desired relation between N^c and q^c which is used as a boundary condition in this thesis:

$$N^c = \rho q^c\left(\frac{1}{\frac{\pi}{6}D_0^3\rho_w}\right)\exp\left(-\frac{9}{2}\sigma_c^2\right). \tag{3.35}$$

Here, the mean droplet diameter of the log-normal distribution is set to $D_0 = 10\,\mu m$ and the dispersion parameter is set to $\sigma_c = 0.2$. This relation is applied once for the whole three-dimensional model domain at initialisation. For all other integration steps, it is applied for the lateral boundaries and all layers above the PAFOG domain. That way each cloud entering the PAFOG domain is assigned a predefined droplet size distribution ensuring the treatment of cloud processes by the PAFOG microphysics.

3.5 Additional diagnostics – the MESSy submodel TENDENCY

This study analyses processes contributing to the development and patterns of FLCs in the Namib Desert by means of numerical model simulations. Therefore, it is important to understand the effects of individual processes on the state variables of the model. These are represented by tendencies occurring in the budget equations. In the COSMO model, neither the tendencies including the sum over all simulated processes (e.g. physical, dynamical and chemical) nor the contributions by individual processes are available. These contributions of individual processes to the total tendency within a model time step can be provided by the MESSy submodel TENDENCY (Eichinger and Jöckel, 2014).

MESSy is a multi-institutional project. For further information the reader is referred to Jöckel et al. (2005, 2010) and the MESSy website (http://www.messy-interface.org). The basic idea of MESSy is to connect parametrisations of physical processes, dynamical cores, chemistry packages and diagnostic tools to a base model (e.g. an atmospheric circulation model) by a generalised interface. The specific parametrisation or diagnostic tool is called submodel and is coded completely independent from the underlying base model. MESSy contains submodels for its infrastructure, model physics, atmospheric chemistry and diagnostic tools.

In this study, the basemodel is the NWP model COSMO (see Sec. 3.1) which has been connected to MESSy by Kerkweg and Jöckel (2012). PAFOG is implemented into COSMO/ MESSy (COSMO version 5.05, MESSy version based on tag 2.54.0.3-pre2.55-02). This has the advantage, that the diagnostic features available in the MESSy submodel TENDENCY can be used for the process analysis in the Namib region with COSMO-FOG.

The TENDENCY submodel provides the contributions of individual processes to the total tendency within a model time step. During a model time step, for each of these processes a tendency is calculated for a specific state variable forming pairs of “process-prognostic variable” (Fig. 3.1). This process-prognostic variable pair is passed to the TENDENCY submodel which collects all pairs from all processes and organises the further processing of the tendencies in the model. The process-prognostic variable pairs that have been requested in the namelist (Nml) are saved in TENDENCY for further reference (e.g. output). Thus, the influences of different sources or sinks and transport processes on prognostic variables can be separated.

TENDENCY facilitates sanity checks of the model implementation, e.g. it is straightforward to examine mass conservation or detect unexpected model behaviour. Self-

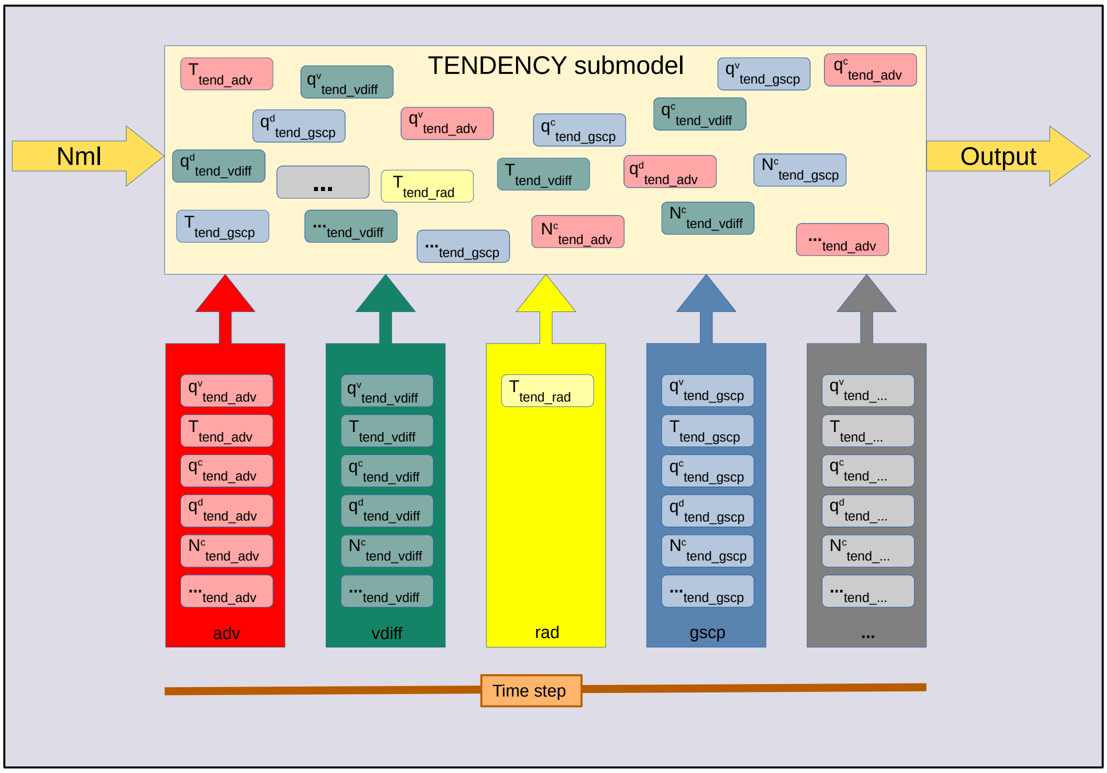

Figure 3.1: Schematic of the MESSy submodel TENDENCY (adapted from Eichinger and Jöckel (2014)). For each process (e.g. advection (adv), turbulent diffusion (vdiff), radiation (rad), grid-scale precipitation (gscp), ...) a tendency is calculated for the state variables (e.g. temperature T, specific humidity q^v, cloud water content q^c, drizzle water content q^d, droplet number concentration N^c, ...) and passed to the submodel TENDENCY.

evidently, TENDENCY enables a better understanding of physical processes on the basis of the budget equations.
For COSMO-FOG the contributions from the PAFOG processes, namely the activation of cloud droplets, the condensation and evaporation, the drizzle formation and the sedimentation occurring in equations 3.29–3.31 are additionally considered.

In this study, TENDENCY is applied to examine how COSMO and COSMO-FOG simulate the major processes occurring in a low-level marine stratiform cloud in an idealised framework. Afterwards, the processes contributing to FLC formation and its development in the Namib Desert will be analysed with the TENDENCY submodel in real case applications.

4 Idealised sensitivity study with COSMO-FOG

After the technical development of the COSMO-FOG model it is necessary to check the coupling and that the new three-dimensional fog model is able to reasonably well simulate the time evolution of the cloud-topped MBL. The model behaviour and consistency of COSMO-FOG is investigated in a highly idealised environment for a horizontally homogeneous marine stratus cloud. A sensitivity study for both microphysical schemes (standard COSMO scheme and PAFOG scheme) with different vertical resolutions is performed. Since the coupling of the COSMO model with the PAFOG model concerns the microphysical parametrisation only and the model dynamics remains unchanged, changes in the results are clearly attributable to the change in the microphysics and respective feedbacks. In order to reduce the complexity of interactions between dynamical and microphysical processes, the originally three-dimensional COSMO model is applied as a quasi one-dimensional model in single column mode. This implies the assumption of horizontal homogeneity for all thermodynamic variables and neglecting advection processes. Although a simulation of realistic fog and stratus is hardly possible with these assumptions, the interaction of different processes occuring in the life cycle of fog or stratus is expected to be simulated reasonably (Smith et al., 2018). It is expected, that findings from the one-dimensional experiment can be transferred to the three-dimensional applications (Bott, 2020).
Bott (2020) simulated a horizontally homogeneous marine stratus cloud and analysed the effects of microphysical parametrisation schemes with different complexity. This approach is taken up here for COSMO and COSMO-FOG using an analogous setup as in Bott (2020).

4.1 Experimental setup

For the simulation of a horizontally homogeneous marine stratus cloud only vertical profiles for the initialisation of the atmosphere and a bottom boundary condition at the sea surface have to be prescribed. Following Bott (2020) the lower boundary is the saturated sea surface at a temperature of 12 °C. The SST stays constant throughout the simulation. The initial profiles of temperature and specific humidity are displayed in Figure 4.1[1]. Below the inversion layer at 900 m, the PBL is neutrally stratified, i.e. the temperature decreases with increasing height with a dry adiabatic lapse rate of $9.8\,°\mathrm{C\,km^{-1}}$. Immediately at the inversion layer height, the tempera-

[1]The initial profiles of temperature, specific humidity and horizontal wind up to 30 000 m are displayed in the appendix.

ture increases by 8 °C. Between the inversion height and 10 000 m the temperature decreases with a lapse rate of 6.5 °C km^{-1}. Between 10 000 m and 20 000 m the temperature is constant with height and above 20 000 m the temperature increases with 1 °C km^{-1}.

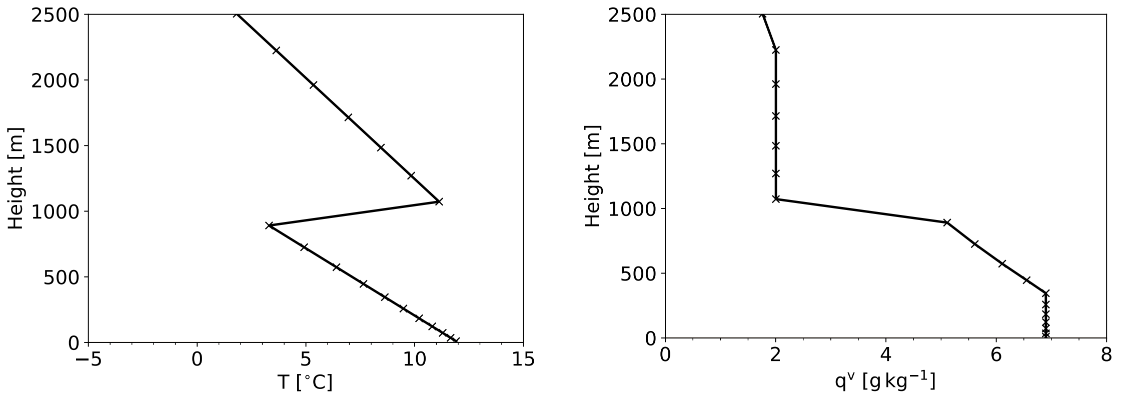

(a) **(b)**

Figure 4.1: Initial profiles of (a) temperature T [°C] and (b) specific humidity q^v [g kg^{-1}] on 15 October, 6 UTC.

The initial specific humidity is vertically constant at 6.9 g kg^{-1} below the inversion. Immediately at the inversion height, specific humidity decreases to 2 g kg^{-1}. Above 2500 m the specific humidity is prescribed by relative humidity. The relative humidity is set to 30 % above 2500 m resulting in a decrease of specific humidity to less than 2 g kg^{-1}. Further above, the relative humidity decreases to 10 % between 10 000 m and 20 000 m and 8 % above 20 000 m. In the PBL, the initial specific humidity is limited such that the relative humidity is lower than 95 %. This limitation is effective between 350 m and the inversion height resulting in a decrease of specific humidity with height. This limitation of specific humidity allows for a cloud-free initialisation so the droplet number concentration does not have to be prescribed based on an assumed mean droplet diameter (cf. Sec. 3.4) but can develop by activation.
The initial horizontal wind profile is set to a vertically constant geostrophic wind u_g=5 m s^{-1} in x-direction which logarithmically decreases to zero at the sea surface. Departing from Bott (2020), no large-scale subsidence is prescribed. At model initialisation, the vertical velocity is set to $w = 0\,\mathrm{m\,s^{-1}}$. In the course of the simulation, the vertical velocity is determined by the dynamical core of COSMO.
The number concentration of the aerosol particles serving as cloud condensation nuclei in the activation parametrisation is held constant throughout the simulation at 400 cm^{-3}.
In terms of solar irradiation, all simulations start on 15 October at 6 UTC and last until 18 October at 18 UTC where local time matches with UTC. The location is at geographical latitude 50 °N and longitude 0.9 °W.

For the simulation of a horizontally homogeneous marine stratus cloud, the COSMO

model is applied in single-column mode using a quasi one-dimensional setup with 7x7 grid points applying double periodic boundary conditions. Thereby only the grid point in the centre of the domain is treated prognostically while the boundary lines are overwritten with the values of the centre grid point (Blahak, 2015). The horizontal grid spacing is 0.025° which is approximately 2.8 km.
The simulations use a stretched vertical grid up to 30 km with varying discretisations[2]. The low resolution (LR) simulations use a stretched vertical grid with the lowest layer above the Earth's surface at 20 m and 57 layers in total which is provided by the Deutscher Wetterdienst (DWD, German Meteorological Service) for the application in the tropics and is very close to the former operational model configuration of COSMO-DE. The grid spacing increases from 20 m in the lowest layer above the surface to $\sim$173 m in the inversion layer. The time step is 25 s.
The simulations with a high resolution (HR) vertical grid use the grid presented by Bott (2020) up to 2440 m and above that height the grid of the LR simulations, thus yielding a grid with 188 layers in total. The lowest layer above the earth's surface is located at 0.5 m above ground and has a thickness of 1 m. With increasing height above ground the layer thickness increases such that at 1000 m a layer depth of approximately 30 m is obtained which is considerably smaller than for the LR simulations.
In the standard COSMO model setup the lowest model layer is usually at 10 m above the surface justifying the approach to treat the canopy as a skin layer without vertical extension being located below the lowest atmospheric model layer. With a layer depth of 1 m, this is no more valid for simulations with larger roughness elements like vegetation, buildings or subgrid-scale orography and the effects of vertically extended canopy could not be neglected any more. However, this is an idealised test case where the single column is placed over the sea surface under idealised conditions. Therefore, the (possible) effect of waves is neglected in the following. Following Bott (2020), the time step is set to 10 s for the HR simulations.
The terrain-following vertical coordinate changes to a height-based coordinate at 15 km height (vcflat). In order to avoid the reflection of vertically propagating waves, a Rayleigh damping layer is applied. In preparation for the simulations in the Namib region and departing from the former operational configuration, the lower boundary of the Rayleigh damping layer is increased from 11 000 m to 18 000 m to place it above the tropopause in the tropics (Panitz et al., 2014).

For the idealised experiments described hereafter, the physical parametrisations are to a great extent adopted from the model configuration of COSMO as detailed in Baldauf et al. (2011) with some modifications. Since convection is not expected to occur due to the strong capping inversion, the convection parametrisation is switched off. The radiation scheme is called every 15 minutes. Fractional cloud cover is neglected so only grid-scale clouds are accounted for by the turbulence and radiation scheme. For the vertical turbulent diffusion, the turbulence scheme based on Mellor

[2]Tables with the height of the model levels and the model layer thicknesses are given in the appendix

and Yamada (1982) is used[3].
In the COSMO turbulence scheme, the turbulent diffusion coefficients for scalars and momentum are limited by a prescribed minimum value (Schättler et al., 2018). The recommended value is $K = 0.75\,\mathrm{m}^2\,\mathrm{s}^{-1}$ (Schättler et al., 2018). This forces continued mixing in order to avoid vanishing mixing and surface fluxes and, thus, a decoupling of surface and atmosphere. For the default value of $K = 0.75\,\mathrm{m}^2\,\mathrm{s}^{-1}$ the inversion at PBL top gradually weakens as the inspection of the liquid water potential temperature and the specific humidity profiles shows (Fig. 4.2 (a) and (b)). The tendencies from TENDENCY reveal that turbulent diffusion erodes the inversion at PBL top. Water vapour is transported into the free troposphere across the inversion layer by turbulent mixing. Dryer and warmer air is entrained into the PBL. The inversion is further weakened by the evaporation of the cloud water transported into the inversion layer by turbulent mixing[4].

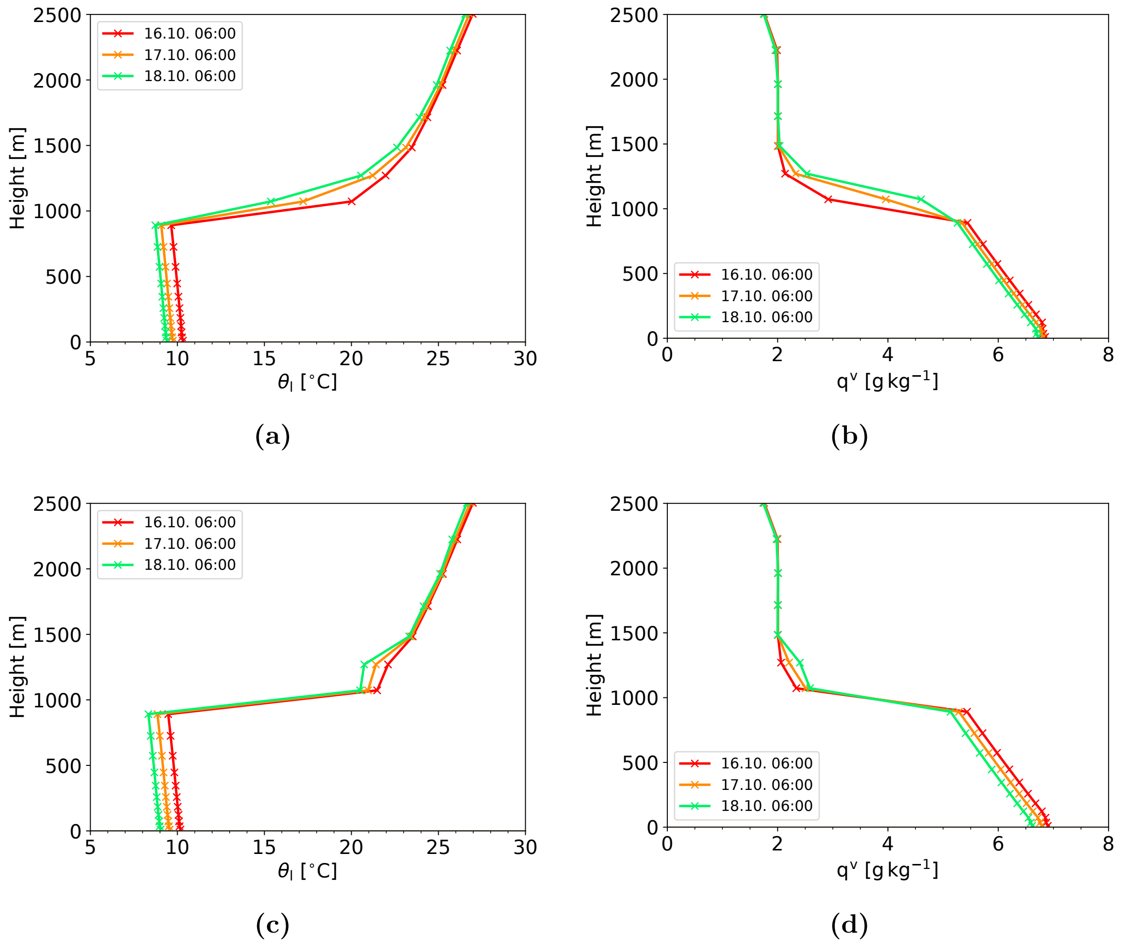

Figure 4.2: Vertical profiles of (a, c) liquid water potential temperature θ_l [°C] and (b, d) specific humidity q^v [$\mathrm{g\,kg^{-1}}$] at different times for (a,b) $K = 0.75\,\mathrm{m}^2\,s^{-1}$ and (c, d) $K = 0.01\,\mathrm{m}^2\,\mathrm{s}^{-1}$.

[3]In this study, a slightly adapted namelist setting for the new setup of the turbulence scheme is used. See Schättler et al. (2018) (their Sec. 6.4) for further details.
[4]Additional figures showing the tendencies are displayed in the appendix.

Similar problems like the underestimation of the thermal inversion amplitude or too fast dissolving of low-level stratus clouds during night have already been reported for the COSMO model (Cerenzia et al., 2014). It is well known that the former operational configurations of COSMO show an excessive mixing in situations with stable atmospheric stratification (Cerenzia et al., 2014). Buzzi (2008) and Buzzi et al. (2011) highlight the disruptive role of the minimum coefficient for vertical diffusion in simulations of the stably-stratified boundary layer. They found that the largest minimum value of the diffusion coefficient not modifying the representation of the stably-stratified boundary layer is $K = 0.01\,\mathrm{m^2\,s^{-1}}$. Sensitivity studies reveal an improvement for the simulation of the marine stratus cloud largely maintaining the inversion for smaller values of K (see Fig. 4.2 (c) and (d) for example with $K = 0.01\,\mathrm{m^2\,s^{-1}}$). Therefore the minimum turbulent diffusion coefficient is set to $K = 0.01\,\mathrm{m^2\,s^{-1}}$ for all following simulations.

In the following, results are presented for the sensitivity study for both microphysical schemes (standard COSMO scheme and PAFOG scheme) with the LR and HR vertical resolutions. For reasons of clarity, identifiers are introduced for the model configurations, which are detailed in Table 4.1.

Table 4.1: Identifiers for model configurations based on the vertical grid and the microphysical parametrisation

Identifier	Vertical Grid	Microphysical Parametrisation
COSMO-LR	**L**ow **R**esolution with 57 levels	standard COSMO
COSMO-FOG-LR		PAFOG
COSMO-HR	**H**igh **R**esolution with 188 levels	standard COSMO
COSMO-FOG-HR		PAFOG

4.2 Sensitivity to microphysical parametrisation

In the following section, results of the idealised sensitivity studies with COSMO-LR and COSMO-FOG-LR will be presented. Both model configurations are identical except for the microphysical parametrisation.

Results for the standard COSMO microphysical parametrisation

Figure 4.3 shows vertical profiles of virtual potential temperature θ_v, liquid water potential temperature θ_l and vertical velocity w at 6 and 14 UTC on 16 and 17 October. The MBL is topped by a strong capping inversion. In the cloud layer beneath the inversion, the virtual potential temperature increases with height while the liquid water potential temperature slightly decreases with height. Thus, the air in the cloud layer is conditionally unstably stratified which is in good agreement to the simulation results obtained by Bott et al. (1996) for a marine stratus cloud.

During daytime the temperature slightly increases by approximately 1 °C due to solar heating. This small daily amplitude results from the large heat capacity of water at the lower boundary of the atmosphere.
Until 6 UTC the temperature in the boundary layer cools by approximately 2 °C. The nighttime cooling is stronger than warming during daytime thus leading to an overall cooling of the atmosphere in the course of the simulation. This is clear from the time of the year well after equinox when nighttime cooling dominates daytime solar heating.

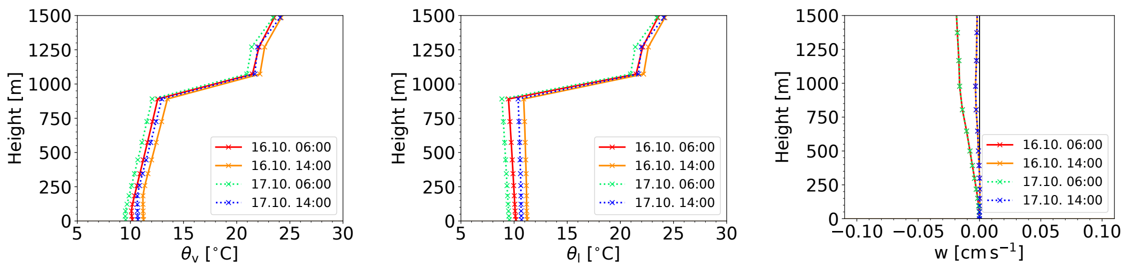

(a) **(b)** **(c)**

Figure 4.3: Vertical profiles of (a) virtual potential temperature θ_v [°C], (b) liquid water potential temperature θ_l [°C] and (c) vertical wind velocity w [m s^{-1}] at different times.

The daily cycle of temperature impacts on the dynamics of the model. In a one-dimensional setup usually no vertical velocity should occur due to mass conservation. As Figure 4.3 (c) reveals, a slight vertical velocity is simulated by the model. During night, COSMO-LR simulates stronger large-scale subsidence than at daytime where subsidence almost vanishes. In the first half of the day the air even slightly lifts (not shown). Due to the one-dimensional setup this lifting and subsiding is global and cannot be compensated by the model. The vertical velocity is nevertheless physically consistent. With the warming during daytime the air in the boundary layer extends and the density decreases. Since the model grid boxes cannot expand this is compensated by a slight upward vertical velocity. At nighttime when the boundary layer cools and density increases the dynamical core of the COSMO model reacts with slight large-scale subsidence to the cooling.
Due to the long night, subsidence prevails in total. Compared to the prescribed subsidence in the setup of Bott (2020), the vertical velocity created by the dynamical core of COSMO is one order of magnitude smaller. COSMO-LR reacts physically consistent for the given boundary conditions.

Figure 4.4 (a) shows a contour plot of the cloud water content as a function of time and height. Following Bott (2020), a cloud layer is defined by the cloud water content exceeding a threshold of 0.01 g kg^{-1}. The COSMO model treats the condensation and evaporation of cloud water with a saturation adjustment (cf. Sec. 3.2). Thus, only saturated layers are classified as cloud layers and the cloud coincides exactly with the saturated layers.
The cloud reaches a quasi-steady state during the first 24 hours of the simulation

which is a spin-up phase where all the variables have to adapt to each other and, thus, is not shown. When the stratus cloud has reached its quasi-steady state it exhibits a typical diurnal variation which is mainly driven by radiation (Bott, 2020; Bott et al., 1996; Ghonima et al., 2016; Wood, 2012, cf. Sec. 2.3). While the cloud top height is constant at about 980 m throughout the simulation, the cloud base varies between roughly 200 m in the afternoon and approximately 50–100 m at 6 UTC in the early morning before sunrise. The cloud obtains its largest vertical extent of roughly 880–930 m at 6 UTC.

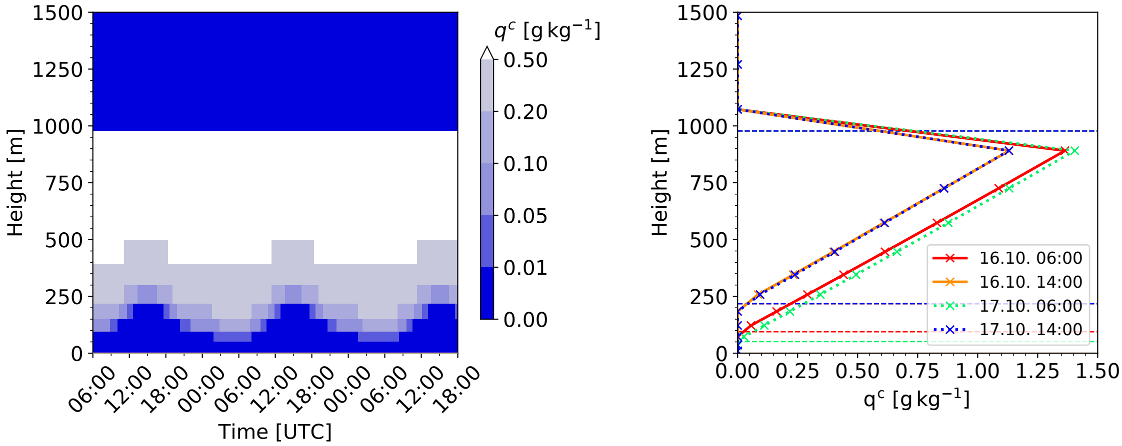

(a) (b)

Figure 4.4: (a) Cloud water content q^c [g kg^{-1}] as a function of time [UTC] and height [m] and (b) vertical profiles of the cloud water content at different times. Horizontal dashed lines indicate the layer where the cloud water content is larger than 0.01 g kg^{-1} for the respective time.

The profiles of cloud water content depicted in Figure 4.4 (b) for 6 UTC and 14 UTC on 16 and 17 October show that the maximum cloud water content ranges up to approximately 1.4 g kg^{-1} at 6 UTC before sunrise. During daytime the cloud water content decreases by 0.3 g kg^{-1}. In addition, the profiles of cloud water content show, that the cloud water content increases almost linearly with height as expected from observational studies (see Wood (2012) and references therein). The almost exact matching of the curves taken at the same time of the day highlights the quasi-stationary behaviour of the cloud.
The amount of cloud water content in the COSMO-LR simulation is unrealistically high. Typical values for the cloud water content of stratus and stratocumulus clouds are between 0.1–0.5 g m^{-3} (Pruppacher and Klett, 2010, cf. Sec. 2.3), which corresponds approximately to 0.1–0.5 g kg^{-1} assuming a density of moist air of 1.2 kg m^{-3} for saturated air at 15 °C. The unrealistically large values are very likely caused by the rather simple parametrisation of microphysical processes where no sink for cloud water due to sedimentation is considered. The importance of sedimentation for realistic fog simulations has recently been emphasised by Boutle et al. (2022), showing that models without a parametrisation of sedimentation simulate a too large water content. This hypothesis will be further analysed in the following in a simulation

where the microphysical parametrisation of PAFOG replaces the standard scheme of COSMO below 2000 m.

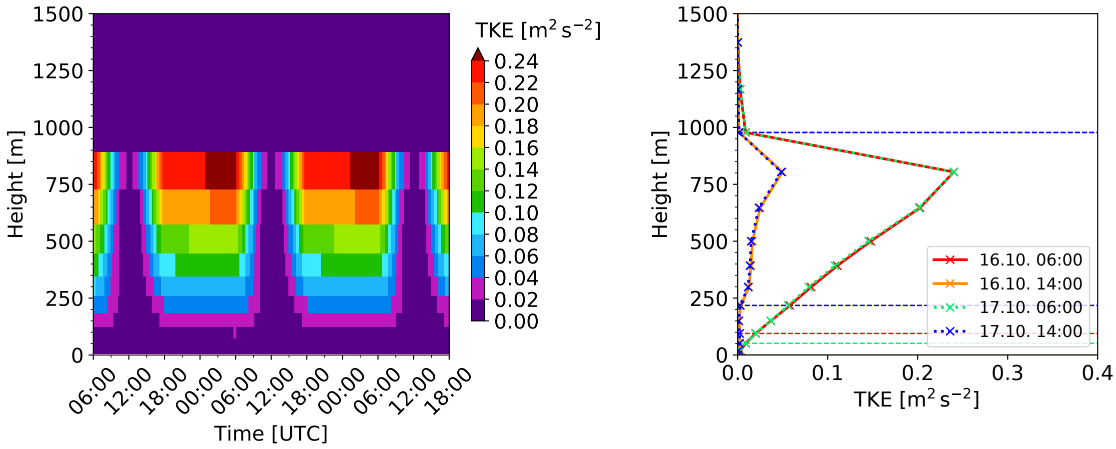

(a) **(b)**

Figure 4.5: As Figure 4.4, but for turbulent kinetic energy TKE [$\mathrm{m^2\,s^{-2}}$].

Figure 4.5 shows the TKE simulated by COSMO-LR as a function of time and height and its profiles at 6 and 14 UTC at 16 and 17 October. The COSMO model simulates a typical diurnal variation of turbulence with stronger turbulence in the cloud-topped MBL during the night than during daytime (cf. Sec. 2.3). The highest values of TKE occur during night in the upper part of the cloud. With insolation during daytime, TKE decreases. This results from the stronger radiative cooling at cloud top during night driving the turbulence in the cloud-topped MBL. At daytime the longwave radiative cooling is partly offset by the absorption of solar radiation in the upper regions of the cloud (Wood, 2012, cf. Sec. 2.3). The simulated turbulent structure of the boundary layer achieves a quasi-steady state with regular diurnal variations. This is confirmed by the profiles of TKE depicted in Figure 4.5 (b).

Despite of the unrealistically high cloud water content, the diurnal evolution of the cloud-topped MBL is reasonably simulated by the COSMO model. The diurnal variations are driven by solar insolation which is the only varying forcing. All other parameters driving the evolution of the cloud-topped MBL, e.g. the SST, are held constant throughout the simulation. Thus, the quasi-steady state is a logical consequence (Bott, 2020). From the analysis of the cloud and the turbulent structure of the cloud-topped MBL it can be expected that the local derivatives with respect to time of all prognostic variables vanish.
Figure 4.6 shows the tendencies of the temperature, specific humidity and cloud water content on 17 October at 6 UTC obtained from the MESSy submodel TENDENCY. In addition to the total tendencies, Figure 4.6 depicts the tendencies of several processes occurring in the corresponding prognostic equations of COSMO. As expected, the total tendencies of all variables are orders of magnitude smaller than for the various single processes. In the boundary layer the tendencies of the processes are partly quite large but all the single contributions balance each other

resulting in vanishing local time rates of change for each variable. This confirms the formation of a quasi-steady state in the cloud-topped boundary layer.

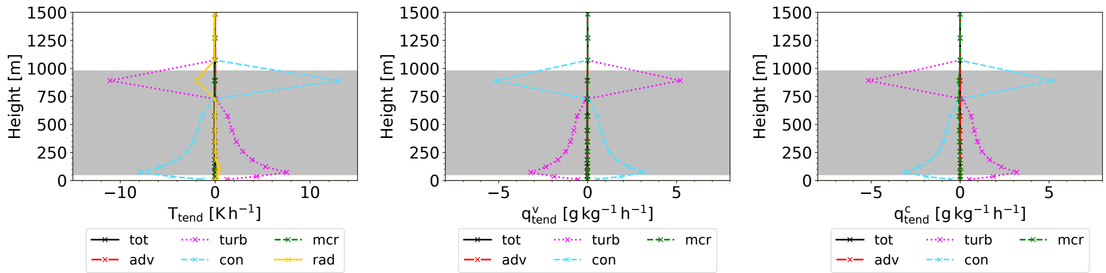

(a) **(b)** **(c)**

Figure 4.6: Vertical profiles of (a) temperature (T_{tend} [$K\,h^{-1}$]), (b) specific humidity (q^v_{tend} [$g\,kg^{-1}\,h^{-1}$]), and (c) cloud water content (q^c_{tend} [$g\,kg^{-1}\,h^{-1}$]) tendencies on 17 October, 6 UTC for COSMO-LR simulation; tot: total tendency, adv: advection, turb: turbulent mixing, con: condensation/evaporation, mcr: microphysical conversion rates other than condensation/evaporation, rad: radiation. Shaded grey areas indicate where the cloud water content is larger than $0.01\,g\,kg^{-1}$.

Figure 4.6 (a) displays the temperature tendencies. In the upper part of the saturated cloud layer strong positive temperature tendencies up to $13\,K\,h^{-1}$ occur due to the release of latent heat by condensation. This strong heating rate is balanced by radiative cooling of around $2\,K\,h^{-1}$ and cooling due to turbulent mixing of more than $10\,K\,h^{-1}$. Below 700 m, evaporative cooling occurs which is balanced by warming due to turbulent mixing. The maximum of approximately $8\,K\,h^{-1}$ occurs at cloud base. The temperature change due to radiative cooling around $2\,K\,h^{-1}$ appears unrealistically small since radiative cooling at cloud top typically causes temperature tendencies around $10\,K\,h^{-1}$ (Bott, 2020; Bott et al., 1996; Koračin et al., 2001; Roach et al., 1982; Wood, 2012). The infrared radiative cooling at cloud top is the main driver of turbulence in the cloud-topped MBL and condensation within the cloud (Bott et al., 1996; Ghonima et al., 2016; Lee, 2018; Zheng et al., 2018). Thus, the infrared cooling at cloud top is an important process to be accounted for which is not reasonably represented in this simulation.
The tendencies of specific humidity (Fig. 4.6 (b)) and cloud water content (Fig. 4.6 (c)) show the behaviour expected from the temperature tendencies. In the upper part of the cloud, cloud water is generated by condensation at the cost of specific humidity. In the lower part of the cloud, evaporation of cloud water increases specific humidity at the cost of cloud water. The evaporation in the lower part of the cloud is caused by turbulent mixing resulting in an upward transport of specific humidity and a downward transport of cloud water within the model timestep. Within the process calculation this leads to undersaturation and, thus, evaporation until saturation is reached again as long as cloud water is still present. The relative humidity of 100 % is calculated elsewhere later in the timestep and thus is just a diagnostic, which is relatively independent of the situation in the actual process calculation. As for the temperature, the tendencies due to turbulent mixing and condensation/evaporation

balance each other for specific humidity and cloud water. The cloud water tendencies due to microphysical conversion rates (e.g. autoconversion, accretion) other than condensation and evaporation are vanishingly small. Thus, the main sink of cloud water content in this simulation is evaporation. This agrees with a previous study of Boutle et al. (2022) who found that the COSMO model is not able to compensate for the missing sedimentation by autoconverting fog into precipitation.

The tendency profiles for the simulation with the COSMO microphysical parametrisation appear with sharp peaks. The upper cloud region where condensation takes place comprises only one model layer. At cloud base the tendency profiles exhibit a local maximum of evaporation and the turbulent counterpart. These patterns are supposed to be the result from the rather coarse vertical grid spacings and the simple microphysical parametrisation of the COSMO model. The latter hypothesis will be analysed step by step in the next sections starting with a simulation where the microphysical parametrisation of the PAFOG model replaces the standard scheme of the COSMO model below 2000 m while the vertical discretisation remains unchanged.

Results for the PAFOG microphysical parametrisation

Comparing the cloud water content profiles from simulations of COSMO-FOG-LR (Fig. 4.7) with those of COSMO-LR (Fig. 4.4) reveals that the development of the stratus in COSMO-LR and COSMO-FOG-LR is very similar concerning its time of formation, diurnal variation, and its cloud top height.

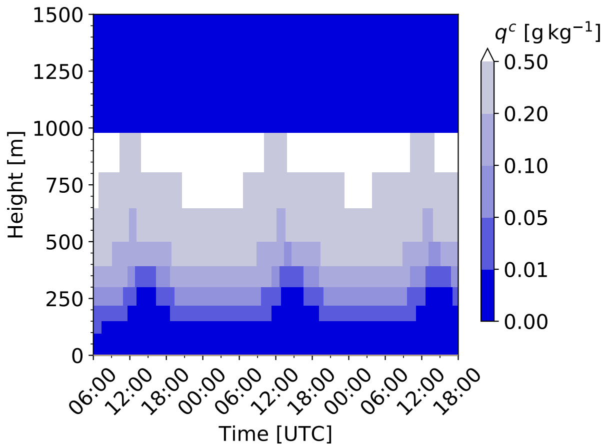

(a)

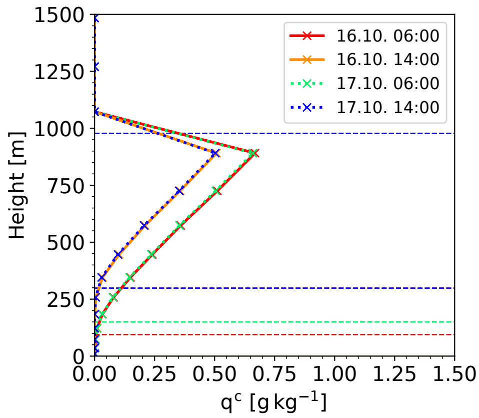

(b)

Figure 4.7: As Figure 4.4, but for the COSMO-FOG-LR simulation.

Like in COSMO-LR, a quasi-steady state is achieved for the cloud with constant cloud top height and slight diurnal variations. Again the cloud water content increases almost linearly with height. The vertical extent of the cloud layer is smaller with the cloud base at approximately 100–150 m in the early morning and 300 m at noon. The cloud top height is constant at roughly 980 m as for COSMO-LR. So in COSMO-FOG-LR the diurnal variation of cloud base height is slightly more

pronounced than in COSMO-LR.
However, comparison of Figure 4.4 and 4.7 reveals a crucial difference between the simulations. In the COSMO-FOG-LR simulation, the cloud water content is roughly $0.5\,\mathrm{g\,kg^{-1}}$ at 14 UTC and $0.65\,\mathrm{g\,kg^{-1}}$ at 6 UTC in the morning which is more realistic than the much higher cloud water content in the COSMO-LR simulation. Thus, the PAFOG microphysical scheme considerably improves this situation. This can very likely be explained by the more detailed description of microphysical processes including additional sinks for cloud water. In contrast to the COSMO microphysical parametrisation, where cloud water is a non-precipitating water category, the PAFOG microphysical scheme considers also gravitational settling of cloud droplets. A model intercomparison study by Boutle et al. (2022) has shown that including a parametrisation of cloud water sedimentation reduces an unrealistically high cloud water content. An additional difference to the COSMO-LR simulation, where all other cloud water sinks except for evaporation (e.g. due to autoconversion and accretion) were vanishingly small, is the simulation of cloud water loss due to drizzle formation by COSMO-FOG-LR. A model sensitivity study comprising simulations without drizzle or without sedimentation and without both parametrisations indicates that the formation of drizzle might be the more effective process to reduce the cloud water content in COSMO-FOG-LR[5].

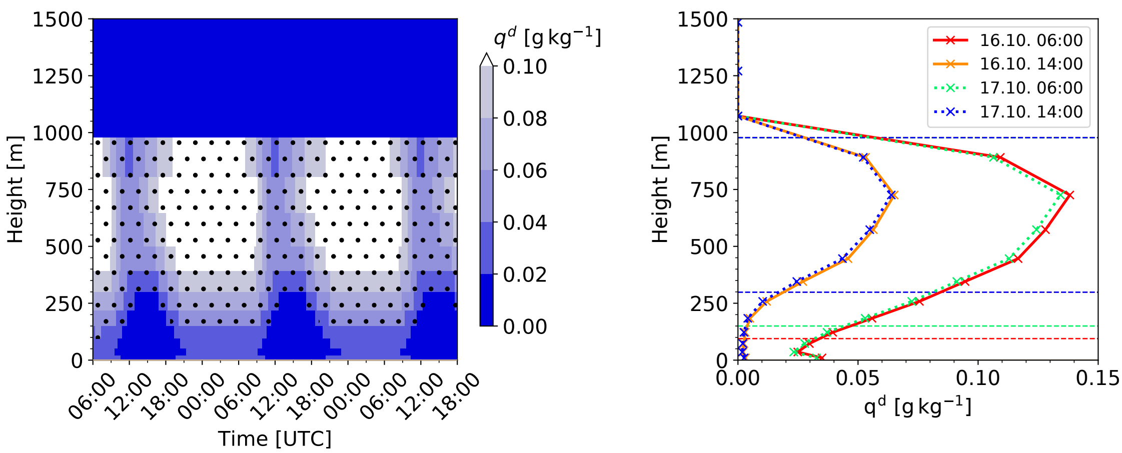

(a) (b)

Figure 4.8: (a) Drizzle water content q^d [$\mathrm{g\,kg^{-1}}$] as a function of time [UTC] and height [m]. Black dots mark the area where the cloud water content is larger than $0.01\,\mathrm{g\,kg^{-1}}$. (b) Vertical profiles of the drizzle water content at different times. Horizontal dashed lines indicate the layer where the cloud water content is larger than $0.01\,\mathrm{g\,kg^{-1}}$ for the respective time.

Figure 4.8 shows profiles of the drizzle water content as a function of time and height for the whole simulation duration and at selected times (6 UTC and 14 UTC). Unlike the cloud water content, whose maximum values occur at cloud top, the maximum

[5]An additional figure showing the cloud water content for simulations without drizzle, without sedimentation, and without both can be found in the appendix.

of the drizzle water content is located in the middle of the cloud. Bott (2020) explains this phenomenon as follows: Most of the drizzle is formed at cloud top where maximum cloud water values occur. But due to the larger assumed particle size of drizzle its terminal fall velocity is larger, so the drizzle quickly falls out. In the undersaturated part of the cloud, drizzle starts to evaporate. Due to its large fall velocity, only a portion of drizzle evaporates in the undersaturated region of the boundary layer. Thus drizzle occurs also between cloud base and the sea surface. The results for both, the drizzle water and the cloud water, agree qualitatively well with the results Bott (2020) presented for PAFOG, but the cloud water content is up to $0.15\,\mathrm{g\,kg^{-1}}$ larger and the drizzle water content is considerably larger in the simulation with COSMO-FOG-LR. The higher drizzle water content results most probably from the higher values of the cloud water content.

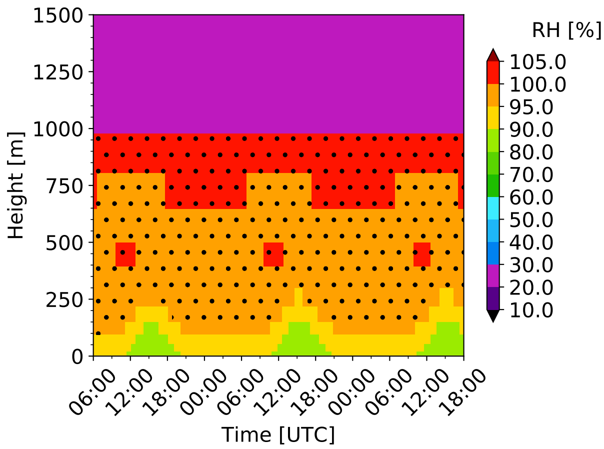

(a)

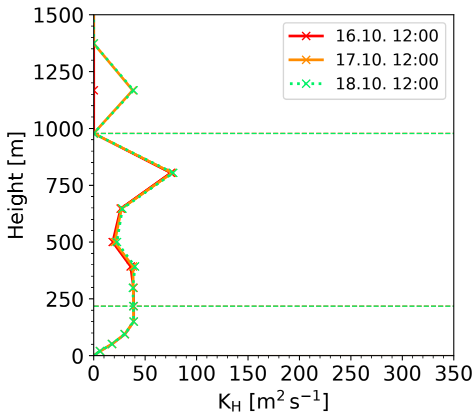

(b)

Figure 4.9: (a) Relative humidity [%] as a function of time [UTC] and height [m]. Black dots mark the area where the cloud water content is larger than $0.01\,\mathrm{g\,kg^{-1}}$. (b) Vertical profiles of the turbulent diffusion coefficient for scalars K_H $[\mathrm{m^2\,s^{-1}}]$ at different times. Horizontal dashed lines indicate the layer where the cloud water content is larger than $0.01\,\mathrm{g\,kg^{-1}}$ for the respective time.

The relative humidity (Fig. 4.9) indicates that only the upper part (upper third) of the cloud layer is saturated or supersaturated in COSMO-FOG-LR (red areas in Fig. 4.9). In contrast, the COSMO-LR simulation maintains saturation throughout the cloud region (see previous Sec.). Bott et al. (1996) showed that supersaturation can be removed within 10–20 seconds, which is in the range of the numerical time step used in this study. In contrast, the time scale for evaporation in undersaturated regions is one or two minutes. While the immediate removal of supersaturation within one model time step can be justified, the immediate dissolution of undersaturated areas in the cloud layer by the saturation adjustment of the COSMO model does not account for this different time scales. Figure 4.9 (a) confirms that the COSMO-FOG-LR simulation reproduces an undersaturated part of the cloud and is, thus, more realistic.

A striking feature in Figure 4.9 (a) is the increase of relative humidity between 400 and 500 m around noon. This is strongly related to a local minimum of the turbulent diffusion coefficient directly above the increase of relative humidity separating the MBL into a well-mixed layer below 400 m and a mixed cloud layer above 600 m. The lower part of the cloud layer is somehow decoupled from its upper part as the local minimum of the turbulent exchange coefficient at 500 m indicates (Fig. 4.9 (b)). The decoupling causes a reduction of the turbulent upward transport of specific humidity. Specific humidity accumulates below the local minimum of the turbulent exchange coefficient and, thus, increases the relative humidity there. In the upper cloud layers, the relative humidity decreases after sunrise until even an undersaturated region is established between 600 and 800 m since the upper cloud layers are decoupled from the surface moisture supply (cf. Sec. 2.3). These patterns occur regularly in the late morning around noon (cf. Fig. 4.9).
The evolution of relative humidity is an effect of the diurnal variation of solar irradiation (Bott et al., 1996). At daytime, solar warming partly compensates the cooling rate at cloud top, thus decreasing turbulent mixing during daytime. Between 600 and 800 m slight solar heating warms and stabilises the cloud layer. This causes the local minimum of the turbulent exchange coefficient slightly below and the undersaturated region between 600 and 800 m. Similar patterns of turbulent mixing and relative humidity have been reported for the simulation of a marine stratus by Bott et al. (1996).

Similar to the simulation with COSMO-LR a quasi-steady state develops. Thus, almost vanishing total tendencies are expected for all thermodynamic variables. Figure 4.10 shows exemplarily the vertical profiles of the tendencies of temperature, specific humidity, cloud water and drizzle water at 17 October, 6 UTC. As expected, the total tendencies of all variables are orders of magnitude smaller than for the various individual processes. The depicted profiles are representative of the whole night. As expected, the same processes balance each other as for the COSMO-LR simulation, e.g. at cloud top the latent heat release due to condensation is balanced by turbulent mixing and radiative cooling (see Fig. 4.10 (a)). The temperature tendency due to radiative cooling ($2\,\mathrm{K\,h^{-1}}$) is still unrealistically small. In the undersaturated cloud layer the temperature tendency due to evaporational cooling is balanced mainly by turbulent mixing. For the specific humidity and cloud water content the condensation/evaporation and turbulent mixing tendencies balance each other (see Fig. 4.10 (b)).
Although the balancing of the different process tendencies is similar to the COSMO-LR simulation, the tendencies differ in some respects. In the uppermost cloud level the condensation tendency of the cloud water content amounts up to $5\,\mathrm{g\,kg^{-1}\,h^{-1}}$ in COSMO-LR (see Fig. 4.6 (c)), while it is $4\,\mathrm{g\,kg^{-1}\,h^{-1}}$ in COSMO-FOG-LR (see Fig. 4.10 (c)). Additionally, the pronounced peak of $3\,\mathrm{g\,kg^{-1}\,h^{-1}}$ for evaporation at cloud base in COSMO-LR is in COSMO-FOG-LR reduced to $1\,\mathrm{g\,kg^{-1}\,h^{-1}}$ and appears approximately 100 m higher resulting in a smoother profile. The differences for condensation and evaporation result from the different parametrisations of these processes. In the COSMO-LR simulation, where condensation and evaporation are treated by a saturation adjustment, water vapour condenses until the supersatura-

tion is eroded. In contrast, the supersaturation is maintained in COSMO-FOG-LR, leading to a smaller condensation rate. The same holds for evaporation. In the COSMO-LR simulation, all the cloud water evaporates as long as no saturation occurs. In COSMO-FOG-LR, cloud water exists despite of undersaturation. The corresponding temperature tendency at cloud top differs by $2.5\,\mathrm{K\,h^{-1}}$ and at cloud base even $4\,\mathrm{K\,h^{-1}}$ (see Fig. 4.6 (a) and Fig. 4.10 (a)).

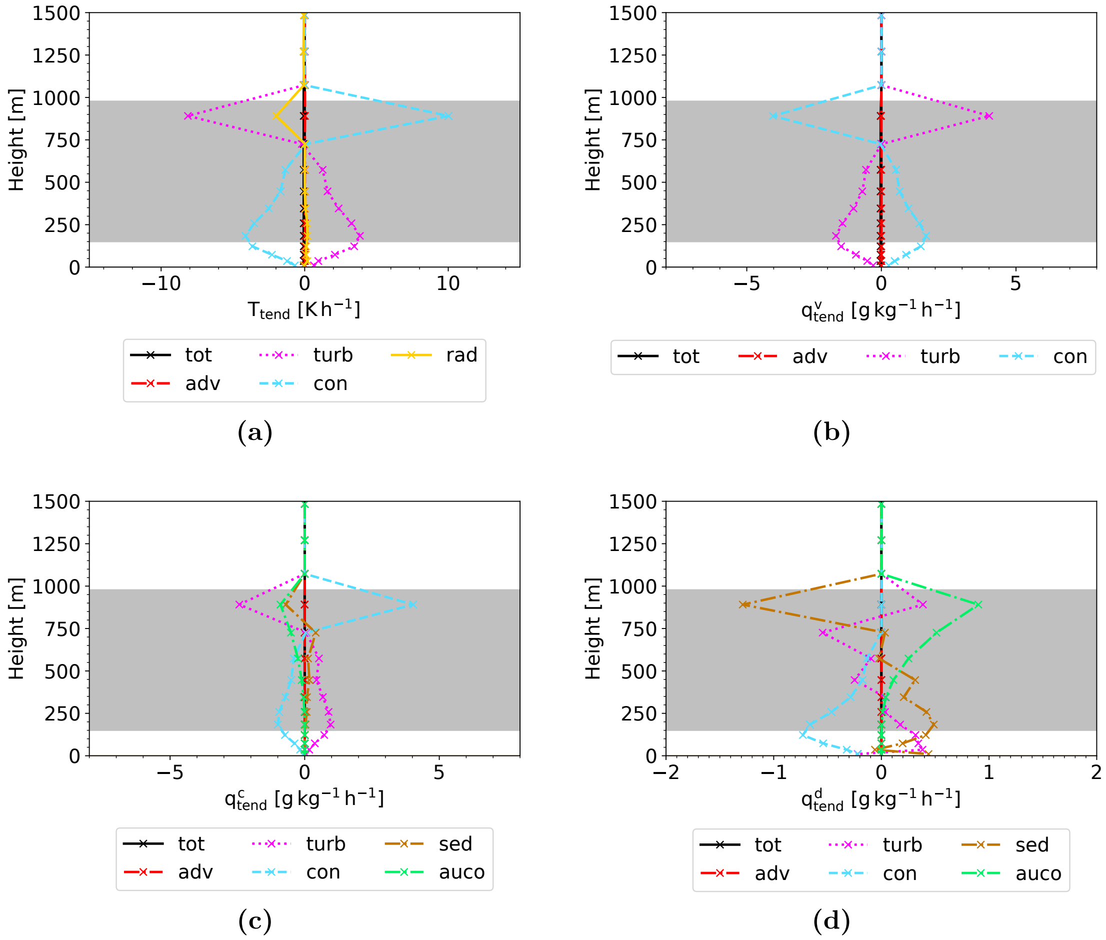

Figure 4.10: Vertical profiles of (a) temperature (T_{tend} [$\mathrm{K\,h^{-1}}$]), (b) specific humidity (q^{v}_{tend} [$\mathrm{g\,kg^{-1}\,h^{-1}}$]), (c) cloud water content (q^{c}_{tend} [$\mathrm{g\,kg^{-1}\,h^{-1}}$]), and (d) drizzle water content (q^{d}_{tend} [$\mathrm{g\,kg^{-1}\,h^{-1}}$]) tendencies on 17 October, 6 UTC for COSMO-FOG-LR simulation; tot: total tendency, adv: advection, turb: turbulent mixing, con: condensation/evaporation, rad: radiation, sed: sedimentation, auco: autoconversion. Shaded grey areas indicate where the cloud water content is larger than $0.01\,\mathrm{g\,kg^{-1}}$.

In COSMO-FOG-LR, two additional sink processes (sedimentation and autoconversion) appear for the cloud water content which did not become apparent in the COSMO-LR simulation (cf. Fig. 4.10 (c)). The negative tendency of cloud water due to drizzle formation is strongest in the uppermost cloud level and decreases to cloud base (Fig. 4.10 (c)). This is in accordance with the rate of drizzle formation

being a function of the cloud water content which is largest at cloud top. In addition to drizzle formation, the sedimentation transfers cloud water from the upper cloud layer to the lower parts of the cloud. In the uppermost cloud layer, the tendencies of gravitational settling and autoconversion have almost equal values.
For the tendencies of drizzle water content displayed in Figure 4.10 (d), the gravitational settling (sedimentation) is the most dominant process. Due to the large assumed droplet diameter the terminal fall velocity of the drizzle is high. The gravitational settling causes a large loss of drizzle water in the uppermost cloud layer and an increase at cloud base and below. In the saturated cloud region this tendency is compensated by turbulent mixing and the production of drizzle due to autoconversion. The gain of drizzle water in the undersaturated part of the cloud and below cloud base is compensated by the evaporation of drizzle which has its maximum directly below the cloud base.

While the simulation with COSMO-FOG-LR yields a more realistic cloud water content for the marine stratus cloud compared to the COSMO-LR simulation, a striking feature occurring in both simulations is the small radiative cooling at cloud top. The cooling rate is much smaller than expected from observations or modelling studies. This occurs independently of the microphysical parametrisation and despite strongly varying cloud water contents. The small cooling rate is very likely an effect of the large grid spacing of approximately 170 m at cloud top. This hypothesis will be investigated in the following by simulations with a different vertical discretisation.

4.3 Sensitivity to vertical discretisation

The simulations with COSMO and COSMO-FOG are repeated with the HR vertical grid. All other parameters defining the model setup are kept as in the previous section.

Results of the COSMO microphysical parametrisation

Figure 4.11 depicts the cloud water content as a function of time and height and its vertical profiles at the same times as in Figure 4.4 and Figure 4.7. In contrast to the LR simulations, in this HR simulation no quasi-steady state of the cloud is achieved.
The cloud top rises from approximately 980 m to more than 1300 m while the cloud base height rises by approximately 100 m resulting in an overall increase of geometrical cloud thickness (Fig. 4.11 (a)). As shown in the following, the vertical growth of the cloud can be explained by permanent cooling and moistening of the model layer directly above cloud top.
The cloud water content produced by COSMO-HR is still unrealistically high. The maximum cloud water content increases starting from roughly 1.2 g kg^{-1} on 16 October at 6 UTC and reaching a maximum of approximately 1.4 g kg^{-1} in the morning of 17 October (see Fig. 4.11 (b)). As in the previous simulations, the cloud exhibits a diurnal variation with lower cloud water content and higher cloud base height during the day compared to the night and early morning. Similar to the LR simulation,

the cloud water content increases almost linearly with height. However, the cloud top is defined by a much sharper gradient in cloud water content resulting from the smaller grid spacing.

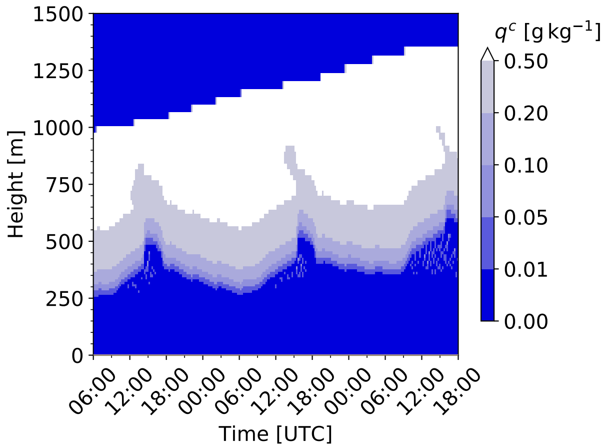

(a)

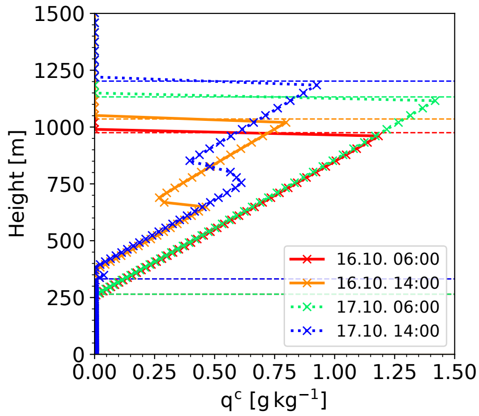

(b)

Figure 4.11: As Figure 4.4, but for the COSMO-HR simulation.

In his study dealing with the forecast of radiation fog, Masbou (2008) found that the turbulence parametrisation scheme of the precursor model of COSMO, named LM, was responsible for the occurrence of numerical instabilities for the small vertical grid spacings required for the forecast of radiation fog. These numerical instabilities were expressed by unphysical fluctuations and spurious peaks of the turbulent diffusion coefficient. A remarkable feature of this simulation with small vertical grid spacing is the smooth vertical structure of the turbulent diffusion coefficient without spurious peaks[6]. These smooth profiles of the turbulent diffusion coefficient do not hint at numerical instabilities. This indicates that the COSMO model is well capable of managing the simulation of the cloud-topped MBL for this vertical grid in a homogeneous setup.

Figure 4.12 shows exemplarily vertical profiles of the tendencies of temperature, specific humidity and cloud water on 17 October at 6 UTC. The displayed tendencies for the HR simulation are characterised by almost vanishing total tendencies although that is not representative for all other times. The phases around the vertical growth of the cloud are characterised by non-vanishing total tendencies.
Although the same processes compensate for each other as expected, the contributions of the different processes to the total tendencies differ considerably in magnitude compared to the LR simulation. The temperature tendencies (Fig. 4.12 (a)) reveal that for the COSMO-HR simulation a strong radiative cooling of approximately $10\,\mathrm{K\,h^{-1}}$ occurs at cloud top. This is $8\,\mathrm{K\,h^{-1}}$ more than in the COSMO-LR simulation. This confirms that the large vertical grid spacing causes the considerably weaker longwave cooling in the previous simulations.

[6]Additional figures of the turbulent diffusion coefficient can be found in the appendix.

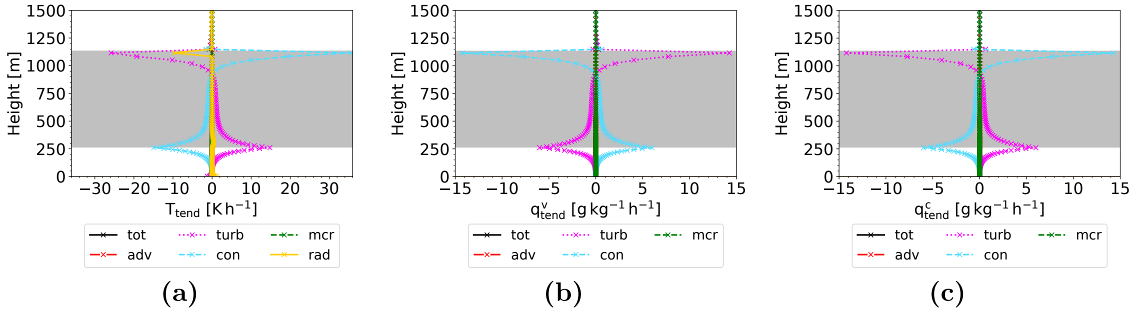

Figure 4.12: As Figure 4.6, but for the COSMO-HR simulation.

Since radiative cooling drives turbulent mixing and condensation in the cloud-topped MBL (see Sec. 2.3), the stronger radiative cooling likely causes the considerable increase of the condensation rate and turbulent tendencies. In the LR simulation the condensation creates cloud water and specific humidity tendencies of 5 g kg^{-1} h^{-1} (see Fig. 4.6 (b) and (c)), and around 14 g kg^{-1} h^{-1} for the HR simulation (see Fig. 4.12 (b) and (c)). The corresponding latent heat release amounts to $\sim$13 K h^{-1} for the LR simulation (see Fig. 4.6 (a)) and around 36 K h^{-1} for the HR simulation (Fig. 4.12 (a)). For both vertical grids, the parametrisation of the condensation/evaporation with the saturation adjustment yields a sharp peak in the tendencies at cloud base. The peak due to evaporation at cloud base is considerably more pronounced for the HR grid. For the LR grid, the evaporation tendency of the cloud water content amounts to roughly -3.5 g kg^{-1} h^{-1} (see Fig. 4.6 (c)), while it is around -6 g kg^{-1} h^{-1} for the HR grid spacing (Fig. 4.12 (c)). Accordingly the latent heat consumption changes from -8 K h^{-1} to -16 K h^{-1}.
This pronounced peak persists for both vertical grids and does not occur in the simulation with COSMO-FOG. Thus, it is very likely attributable to the microphysical parametrisation.
In general, the HR grid spacing yields tendency curves with more clearly defined patterns and a better representation of the local maxima and minima of the profiles. The supersaturated area of the cloud, where condensation takes place, comprises more than one model layer. The peaks and gradients become more pronounced and the transitions appear smoother representing the gradients and peaks more accurately than for the LR grid spacing. The smooth profiles of all analysed variables reveal that no numerical instabilities occur for the adapted grid spacing.

A remarkable feature of the HR simulation compared to the LR simulations is the vertical growth of the stratus cloud. The reasons of this behaviour can be analysed by means of the MESSy submodel TENDENCY. Figure 4.13 shows the tendencies of temperature, specific humidity and cloud water content in the model layer directly above cloud top as a function of time. Note, that the model layer above cloud top is replaced with the next layer at each time when the cloud increases by one model layer. This explains the strong peaks in the tendency curves.
In the model layer above cloud top, the total tendencies of temperature (specific humidity) are always negative (positive) (Fig. 4.13 (a) and (b)). As a result, the

model layer above cloud top is cooled and moistened, thus, increasing the relative humidity. The total temperature and specific humidity tendencies are largely explained by the sum of the tendencies from condensation/evaporation and turbulent diffusion (see congruence of black and green line in Fig. 4.13 (a) and (b)). The difference between the total temperature tendency and the sum of its contributions by turbulent diffusion and condensation/evaporation is due to radiation (Fig. 4.13 (a)).

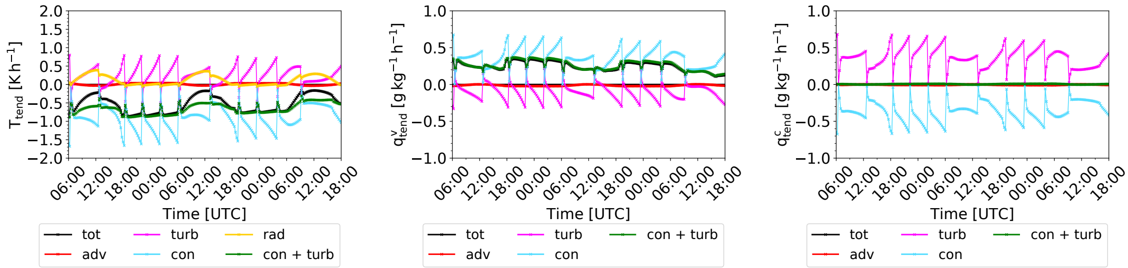

(a) **(b)** **(c)**

Figure 4.13: Time series of (a) temperature (T_{tend} [$K\,h^{-1}$]), (b) specific humidity (q^{v}_{tend} [$g\,kg^{-1}\,h^{-1}$]), and (c) cloud water content (q^{c}_{tend} [$g\,kg^{-1}\,h^{-1}$]) tendencies in the model layer directly above cloud top from 16 October, 6 UTC until 18 October, 18 UTC; tot: total tendency, adv: advection, turb: turbulent mixing, con: condensation/evaporation, rad: radiation, con + turb: sum of condensation/evaporation and turbulent mixing.

As can be seen from the tendencies of cloud water (Fig. 4.13 (c)), turbulent mixing transports a small amount of cloud water into the layer directly above cloud top. The cloud water is immediately evaporated by the saturation adjustment as long as this layer is undersaturated. The evaporation of the cloud water in turn increases specific humidity and cools the according layer causing an imbalance becoming evident by non-vanishing total tendencies of temperature and specific humidity (Fig. 4.13 (a) and (b)). This persistent behaviour moistens and cools the layer above cloud top until saturation is reached and the cloud water is not evaporated in the saturation adjustment any more. The cloud has grown by a further layer.

Despite the vertical growth of the cloud, some conclusions can be drawn. The smaller grid spacing enables a strong radiative cooling as known from other modelling studies or observations being realistic of a stratus cloud. This stronger cooling causes stronger condensation rates and turbulent mixing. However, the smaller grid spacing does not improve the unrealistically high cloud water content for the simulation with the COSMO model which, thus, is an effect of the microphysical parametrisation.

Results for the microphysical parametrisation of PAFOG

In the following, results obtained for the COSMO-FOG-HR simulation are analysed using the same vertical discretisation as in the previous section for the COSMO-HR simulation.

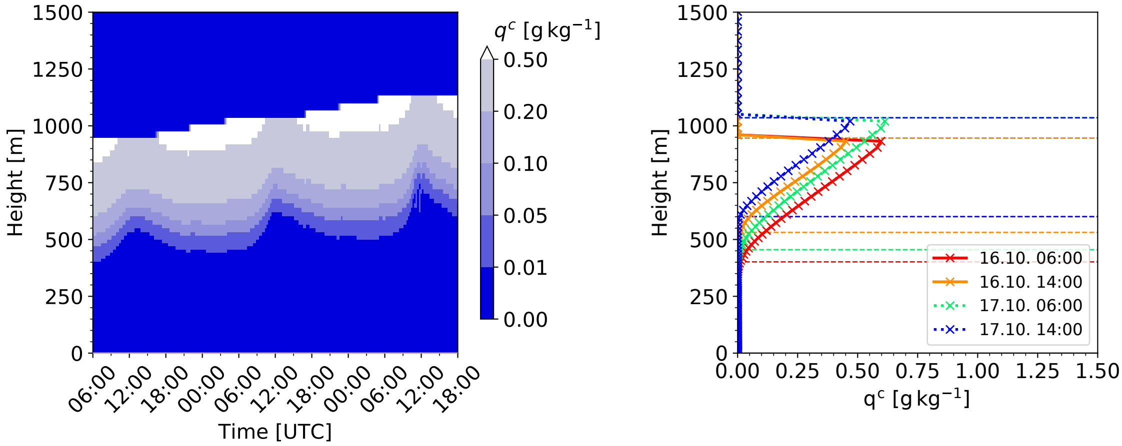

(a) **(b)**

Figure 4.14: As Figure 4.4, but for the COSMO-FOG-HR simulation.

Figure 4.14 illustrates the cloud water content as a function of time and height and its vertical profiles at the same times as in Figure 4.11. The comparison of the two figures yields in general a similar evolution of the cloud in time. On 16 October at 6 UTC, the cloud top is located at approximately 980 m increasing to roughly 1100 m in the end. The cloud base increases from 400 m to roughly 500 m (Fig. 4.14 (a)). As in the other simulations, the cloud exhibits a diurnal variation with lower cloud base and larger cloud water content at night than during daytime. The vertical extent of the cloud varies by approximately 100 to 150 m between 6 UTC before sunrise and 14 UTC. The cloud water content exhibits a diurnal variation with a minimum value around 0.5 g kg^{-1} at 14 UTC and a maximum of $\sim$0.6 g kg^{-1} at 6 UTC. Different from the COSMO-HR simulation, the cloud water content only slightly increases in total and never exceeds 0.65 g kg^{-1}. The gradient of cloud water content at cloud top is more pronounced with smaller vertical grid distances which is more in accordance with observations and other modelling studies (Bott, 2020; Bott et al., 1996; Duynkerke, 1989; Nicholls and Leighton, 1986). As in the COSMO-FOG-LR simulation, the inclusion of the PAFOG microphysical parametrisation considerably reduces the cloud water content which is in better accordance with other simulations and observations (Bott, 2020; Bott et al., 1996; Nicholls, 1984; Nicholls and Leighton, 1986; Wood, 2012).

Figure 4.15 depicts vertical profiles of the tendencies of temperature, specific humidity, and cloud water content for the COSMO-FOG-HR simulation. Due to the vertical growth of the cloud, the depicted tendency profiles with almost vanishing

total tendencies are not representative of all times during the simulation. The phases around the vertical growth of the cloud are characterised by non-vanishing total tendencies as for the simulation with COSMO-HR (cf. Sec. 4.3).
The compensating processes are the same as for all other simulations. In the uppermost supersaturated cloud layers the latent heat release by condensation is compensated by radiative cooling and turbulent mixing (Fig. 4.15 (a)). In the undersaturated cloud layer the temperature tendencies due to evaporation and turbulent mixing counteract with each other. For the specific humidity turbulent mixing and condensation/evaporation counteract (Fig. 4.15 (b)).
The cloud water tendency by condensation is compensated by sedimentation, drizzle formation and the turbulent transport of cloud water. The additional sinks of cloud water contribute to the lower cloud water content compared to the simulations with COSMO-LR and COSMO-HR.

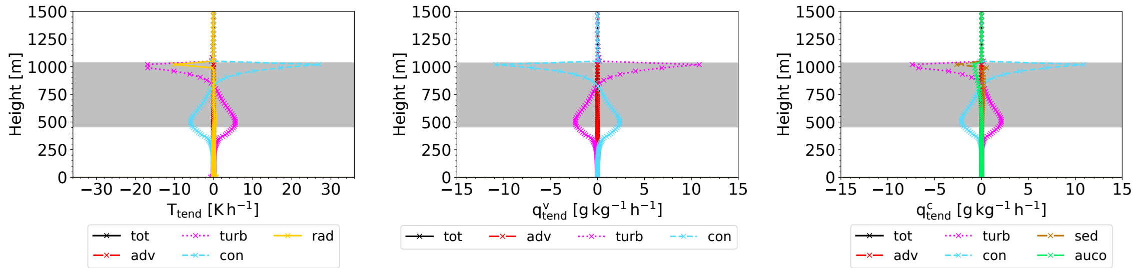

(a) **(b)** **(c)**

Figure 4.15: Vertical profiles of (a) temperature (T_{tend} [K h^{-1}]), (b) specific humidity (q^{v}_{tend} [g kg^{-1} h^{-1}]), and (c) cloud water content (q^{c}_{tend} [g kg^{-1} h^{-1}]) tendencies on 17 October, 6 UTC for COSMO-FOG-HR simulation; tot: total tendency, adv: advection, turb: turbulent mixing, con: condensation/evaporation, rad: radiation, sed: sedimentation, auco: autoconversion. Shaded grey areas indicate where the cloud water content is larger than 0.01 g kg^{-1}.

The comparison of the contributions of the different processes to the total tendencies reveals some differences to the simulations with COSMO-HR and COSMO-FOG-LR. The radiative cooling amounts up to 10 K h^{-1} as for the COSMO-HR simulation. These realistic cooling rates of 10 K h^{-1} occur for the HR simulations independent of the microphysical parametrisation but not for the LR simulations. Thus, radiative cooling at cloud top strongly depends on vertical grid distance as expected.
The condensation rate in the uppermost cloud layers is approximately 10 g kg^{-1} h^{-1} for the simulation with COSMO-FOG-HR (Fig. 4.15 (b) and (c)) which is smaller compared to COSMO-HR with around 14 g kg^{-1} h^{-1} (see Fig. 4.12 (b) and (c)). Compared to the simulation with COSMO-FOG-LR where the condensation rate amounted up to 4 g kg^{-1} h^{-1} (cf. Fig. 4.10 (c)), the condensation rate simulated by COSMO-FOG-HR is more than twice as large. This also feeds back on the corresponding temperature tendencies due to latent heat release. Compared to the COSMO-FOG-LR simulation, the temperature tendency due to latent heat release is nearly 20 K h^{-1} larger in the COSMO-FOG-HR simulation. The release of latent

heat by condensation is almost $10\,\mathrm{K\,h^{-1}}$ smaller for the COSMO-FOG-HR simulation than for the COSMO-HR simulation. The compensating tendency due to turbulent mixing is correspondingly smaller as well for the COSMO-FOG-HR simulation.
The differences of the tendencies between the COSMO-FOG-LR and COSMO-FOG-HR simulations confirm the result from the COSMO simulations, that the stronger radiative cooling at cloud top for the HR simulations triggers more condensation and turbulent mixing. The differences between the two HR simulations might probably be explained by the different parametrisation of the condensation/evaporation process. For the COSMO microphysical scheme the condensation rate might be larger, because all the excessive water vapour above the saturation water vapour is condensed into cloud water. In contrast to that, condensation for COSMO-FOG might be smaller since a supersaturation is possible so not all the water vapour above the saturation water vapour is transformed to cloud water.
A remarkable feature of all tendency profiles of the COSMO-FOG-HR simulation is their smooth and regular shape. As for the COSMO-HR simulation, the narrow supersaturated cloud region where condensation occurs extends over more than one model layer and is thus clearly defined. No more kinks or discontinuities occur. This holds especially for the peak of evaporation at cloud base which occurred in both configurations with the COSMO model. With COSMO-FOG-HR the evaporation at cloud base is smoother. As expected from the COSMO-HR simulation, also smaller peaks due to vertical discretisation are no more present.

The results agree qualitatively well with a previous study by Bott (2020). This is a promising result since only the microphysical parametrisation is almost identical (except for the size of the drizzle radius in the drizzle sedimentation) between the simulation performed by Bott (2020) and the simulation presented here while other processes like turbulence or radiation contributing to the fine balance in the cloud-topped MBL (cf. Sec. 2.3) are treated differently. A large-scale subsidence is not prescribed in COSMO-FOG which renders a quantitative agreement with the results of Bott (2020) impossible.

4.4 Finding a compromise

The previously presented sensitivity simulations with different model configurations have shown that a fine vertical grid is necessary in order to resolve sharp gradients of e.g. temperature, specific humidity and cloud water content at cloud top which are typical features of the cloud-topped MBL (Bott, 2020; Bott et al., 1996; Paluch and Lenschow, 1991; Wood, 2012). This applies especially for radiative cooling at cloud top driving condensation and turbulent mixing in the cloud layer (Bott et al., 1996; Duynkerke et al., 2004; Ghonima et al., 2016; Lee, 2018; Wood, 2012; Zheng et al., 2018).
However, the vertical discretisation with 188 model layers (HR) used in the latter two simulations is computationally too expensive for real case applications. In addition, the small grid distances close to the ground might violate assumptions of

the transfer scheme for a heterogeneous setup including orography and roughness elements larger than the lowest model layer at 1 m above the ground (Buzzi, 2008). Thus, a vertical grid is required, which still represents the important features of a cloud-topped MBL but which is numerically much more efficient (i.e. has a smaller number of vertical model levels) than the HR grid.

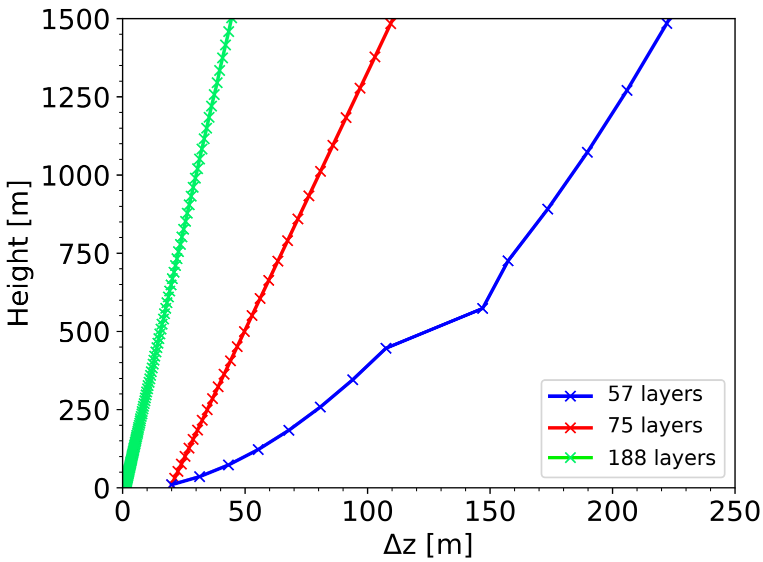

Figure 4.16: Vertical profiles of the model layer thickness Δz [m] for the LR configuration with 57 model layers (blue), the MR configuration with 75 model layers (red), and the HR configuration with 188 model layers (green).

Figure 4.16 illustrates the model layer thicknesses for the vertical grids used in Sections 4.2 and 4.3 and the vertical grid presented in the following. The vertical grid used in the remainder of this study comprises 75 layers from the surface up to 30 km height (medium resolution, MR). The lowest layer is 20 m thick. This corresponds to the layer thickness in the standard "COSMO tropical setup". The layer thickness increases slower than in the model configuration used in Section 4.2 (LR) reaching approximately 80 m in the inversion layer which is roughly half the grid spacing of the LR grid ($\sim$170 m)[7].
In the following, it is tested for an idealised COSMO-FOG simulation using this vertical grid with 75 layers (COSMO-FOG-MR), whether this configuration is capable to represent the features of the cloud-topped MBL and its diurnal cycle reasonably well compared to the simulations presented before.

Figure 4.17 displays the cloud water content as a function of time and height and its vertical profiles at 6 and 14 UTC on 16 and 17 October. As can be seen from Figure 4.17, the stratus cloud evolves similarly to the COSMO-FOG-LR simulation concerning its time of formation, diurnal variation and its cloud top and cloud base

[7] A table with the height of the model levels and layer thicknesses is provided in the appendix.

height. Similar to the COSMO-LR and COSMO-FOG-LR simulations, for COSMO-FOG-MR a quasi-steady state is achieved for the cloud with a constant cloud top height at 900 m. As in the COSMO-FOG-LR simulation, the cloud base height exhibits a typical diurnal variation. It varies between 200 m at 6 UTC in the early morning and roughly 400 m at 14 UTC. The largest vertical extent of the cloud occurs at 6 UTC before sunrise with the cloud top at 900 m and its base at 200 m yielding 700 m vertical extent. This is slightly less than in the COSMO-FOG-LR simulation.

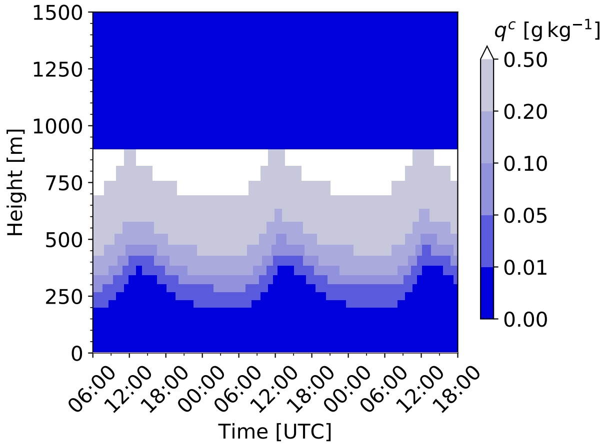

(a)

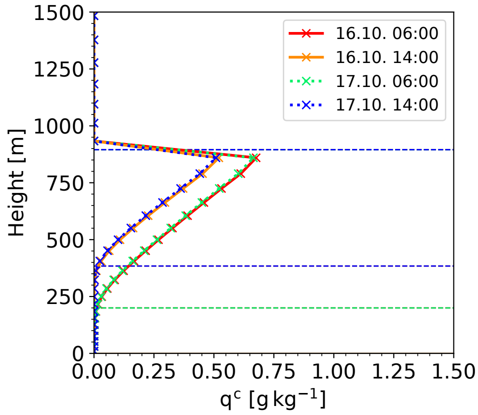

(b)

Figure 4.17: As Figure 4.4, but for the COSMO-FOG-MR simulation.

As in all other COSMO-FOG simulations, the cloud water content is considerably smaller than in the COSMO simulations. The maximum of the cloud water content is reached at 6 UTC in the early morning with approximately 0.65 g kg^{-1}. During daytime the cloud thins under the influence of solar radiation. The minimum cloud water content occurs at 14 UTC with 0.5 g kg^{-1}. These values are typical of stratus and stratocumulus clouds (Bott et al., 1996; Pruppacher and Klett, 2010; Wood, 2012). The quasi-steady state of the cloud is confirmed by the almost identical cloud top and base heights as well as by the almost identical profiles of the cloud water content for different days at a fixed time. As expected, the sharp gradient of cloud water content at cloud top is slightly worse represented for the MR simulation compared to the HR simulations but considerably better compared to the LR simulations.

The typical diurnal variation of the cloud is also evident for the drizzle water content. The vertical profiles of the drizzle water content depicted in Figure 4.18 are very similar to those obtained with COSMO-FOG-LR (cf. Fig. 4.8) whereby the MR configuration yields smaller values. The representation of the drizzle in the COSMO-FOG-MR simulation is much better than for the COSMO-FOG-LR simulation which yields a profile with some kinks. Although the values for the drizzle water content are larger than those obtained in the study by Bott (2020), the shape of the drizzle water profile resembles the results for the PAFOG model.

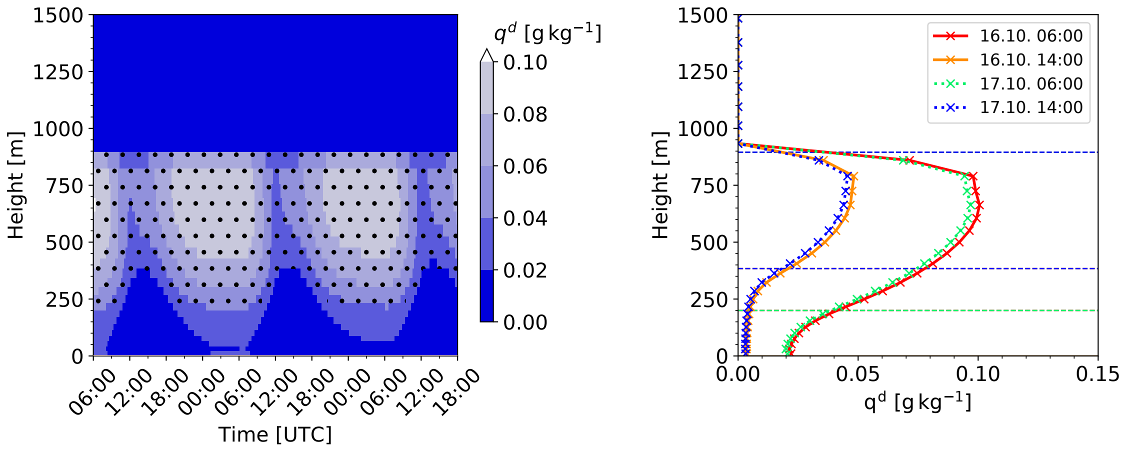

(a) **(b)**

Figure 4.18: As Figure 4.8, but for the COSMO-FOG-MR simulation.

The vertical structure and diurnal variation of the TKE and the turbulent diffusion coefficient in Figure 4.19 reveal that COSMO-FOG-MR simulates a typical diurnal variation of turbulence in the cloud-topped MBL. The maximum of the TKE and the diffusion coefficient occurs in the upper region of the cloud during night. This enhanced turbulence in the upper part of the boundary layer in presence of a cloud is driven mainly by radiative cooling at cloud top, especially during nighttime (Duynkerke et al., 2004; Ghonima et al., 2016; Paluch and Lenschow, 1991; Wood, 2012).

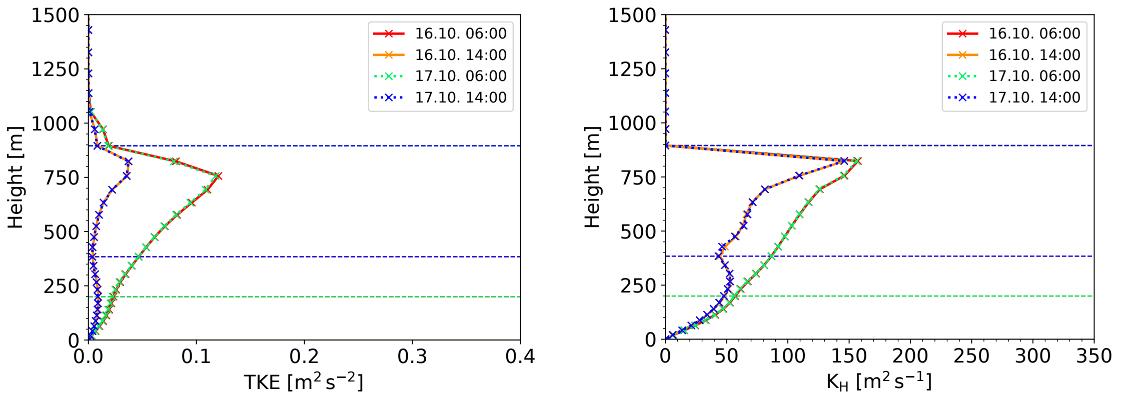

(a) **(b)**

Figure 4.19: Vertical profiles of (a) TKE [$m^2\,s^{-2}$] and (b) turbulent diffusion coefficient for scalars K_H [$m^2\,s^{-1}$] at different times. Horizontal dashed lines indicate the layer where the cloud water content is larger than $0.01\,g\,kg^{-1}$ for the respective time.

At daytime the TKE and the turbulent diffusion coefficient decrease and a minimum evolves due to the effect of shortwave radiative warming, thus, decoupling the cloud layer from surface moisture supply (Bott et al., 1996; Duynkerke et al., 2004;

Nicholls, 1984). This minimum of the TKE and the diffusion coefficient is considerably better represented in the MR (Fig. 4.19) and HR simulations compared to the LR simulations (cf. Fig. 4.5 (b)).
The profiles of the turbulent diffusion coefficient are characterised by a smooth shape without any sharp peaks or oscillations indicating, that the COSMO-FOG-MR simulation is numerically stable.

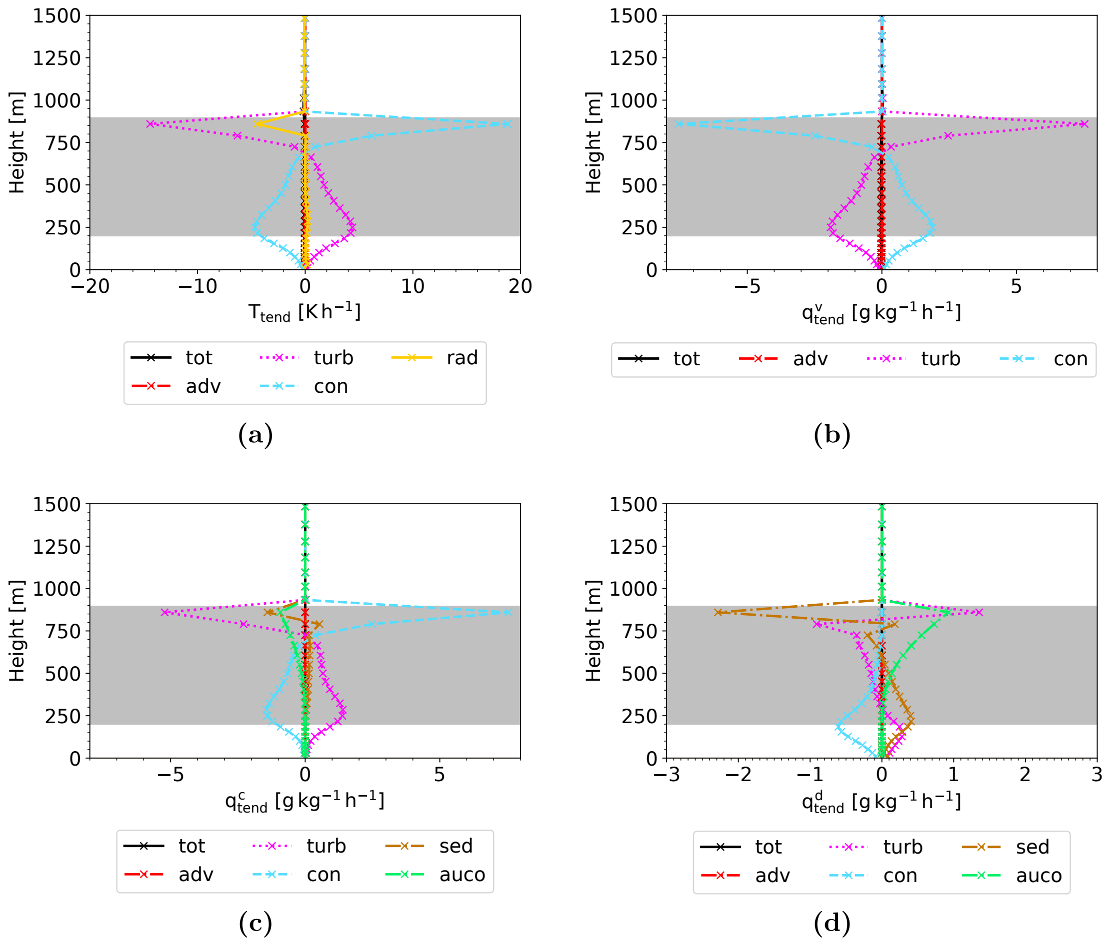

Figure 4.20: As Figure 4.10, but for the COSMO-FOG-MR simulation.

Figure 4.20 shows vertical profiles of the tendencies of temperature, specific humidity, cloud water content, and drizzle water content. As in the previously discussed simulations, the quasi-steady state of the cloud-topped MBL is reflected by almost vanishing total tendencies of thermodynamic variables. As expected, the compensating physical processes have the same importance as in the other model simulations. However, comparing the magnitudes of the different contributions to the total tendencies to those obtained with the other COSMO-FOG configurations some differences become evident.
The most striking difference is the smaller radiative cooling of $5\,\mathrm{K\,h^{-1}}$ at cloud top compared to $10\,\mathrm{K\,h^{-1}}$ for the COSMO-FOG-HR simulation. This difference can only be attributed to the differences in grid spacing. For the COSMO-FOG-HR simulation the corresponding layer at cloud top is $\sim 30\,\mathrm{m}$ thick while it is $\sim 70\,\mathrm{m}$ in the

MR configuration. The radiative cooling of $5\,\mathrm{K\,h^{-1}}$ is an improvement compared to the LR simulations with only $2\,\mathrm{K\,h^{-1}}$ where the model layer at cloud top is $\sim 170\,\mathrm{m}$ thick. A sensitivity study with 94 layers in total and a grid spacing of $\sim 60\,\mathrm{m}$ at cloud top shows no considerable improvement for radiative cooling (not shown).
Since the radiative cooling at cloud top is a main driver for the condensation this also explains the smaller condensation rate around $8\,\mathrm{g\,kg^{-1}\,h^{-1}}$ compared to the COSMO-FOG-HR simulation with $\sim 10\,\mathrm{g\,kg^{-1}\,h^{-1}}$ and larger condensation rate in comparison to the COSMO-FOG-LR simulation with only $4\,\mathrm{g\,kg^{-1}\,h^{-1}}$. The corresponding latent heating rates differ up to $10\,\mathrm{K\,h^{-1}}$ to the COSMO-FOG-HR and the COSMO-FOG-LR simulations.
As in the COSMO-FOG-LR simulation, for the large drizzle droplets, the tendencies of the drizzle water content are dominated by gravitational settling (sedimentation) resulting in a strong decrease at cloud top and an increase below. The tendency due to gravitational settling is compensated by turbulent mixing and the formation of drizzle due to autoconversion. Towards cloud base the gravitational settling is compensated by evaporation of drizzle water. Compared to the COSMO-FOG-LR simulation, the drizzle water content tendencies are considerably smoother. Except for the larger tendency due to autoconversion, the importance of the processes is similar to a previous study of Bott (2020).
An important feature of the MR configuration is, that the smooth shape of the tendency profiles, also occurring in the COSMO-FOG-HR simulations, is maintained for this coarser resolution.
In conclusion, the configuration with 75 vertical layers, which is only 18 additional vertical layers compared to the LR vertical discretisation, improves the results for the simulation of a horizontally homogeneous marine stratus cloud substantially. The vertical grid spacing is sufficient to represent gradients of temperature, specific humidity, cloud water content and especially radiative cooling at cloud top. With the COSMO-FOG-MR configuration a cloud water content being typical of stratus and stratocumulus clouds is simulated. It is possible to obtain reasonable results for the characteristics of the cloud-topped MBL with the COSMO-FOG-MR configuration. Therefore this model configuration will be used for the real case applications presented in the next chapter.

5 Diurnal cycle of fog and low stratiform clouds in the Namib Desert and its controlling processes

One of the main objectives of this study is to provide a comprehensive understanding of the local mechanisms controlling the occurrence and spatio-temporal evolution of FLCs in the hyper-arid Namib Desert. Using a meso-scale NWP model at a grid spacing of about 2.8 km, the present modelling study offers new insights into the development of spatio-temporal FLC patterns and the processes contributing to the FLC evolution in the Namib region during the advection of marine air masses. To the author's knowledge, no modelling study has been performed yet focusing on spatio-temporal patterns of FLCs and its contributing processes in the Namib region using a comparable grid resolution.
In this chapter, results are presented for the simulation of case studies in the central Namib Desert during the austral spring season in September/October 2017. In order to investigate the spatio-temporal patterns, diurnal life cycle phases, and contributing atmospheric processes of fog types in the Namib region, four **c**ase **s**tudies are performed with COSMO-FOG:

- CS1819: 18 to 19 September 2017
- CS2021: 20 to 21 September 2017
- CS2324: 23 to 24 September 2017
- CS2728: 27 to 28 September 2017.

The case studies were selected to illustrate on the one hand the similarity to climatology and on the other hand the variability and complexity of fog events in the central Namib.

The chapter starts with a description of the model setup and the model domain. Afterwards, the spatial patterns and temporal evolution of FLCs and the atmospheric conditions are analysed for the four case studies. In Section 5.2, CS1819 is exemplarily presented in detail and in Section 5.3, the other case studies are investigated with a focus on phenomena and processes that differ from the first case study. Finally, the model simulations are evaluated with surface-based measurements.

5.1 Model configuration

For the analysis of FLC patterns and the involved processes in the Namib region, COSMO-FOG-MR is used which has been tested in the idealised experiments (cf. Sec. 4.4) and will be called COSMO-FOG in the remainder of this thesis. The model simulations are performed with a horizontal grid spacing of 0.025°, i.e. roughly 2.8 km. The numerical time step in the simulations is set to 25 s.
The reference atmosphere, which is used in the dynamical core to build a reference state for all prognostic variables, is adapted to reflect subtropical conditions. This includes an increase of the temporally constant reference temperature on sea level from 288.15 K to 300 K. The temperature difference between sea level and the stratosphere is increased from 75 K to 90 K and the scale height from 10 000 to 12 000 m (Panitz et al., 2014). A similar setup has been applied for Africa by Panitz et al. (2014).
Apart from using the two-moment microphysical parametrisation from PAFOG instead of the standard microphysics scheme below 2000 m, the physical parametrisation schemes are mostly adopted from Baldauf et al. (2011). Departing from Baldauf et al. (2011), the parametrisation for subgrid-scale clouds is switched off at grid points where grid-scale clouds are present. Since neither lakes nor sea ice occur in the model domain, the lake model and the sea ice parametrisation are switched off. The parametrisation of the bare soil evaporation in the soil model TERRA-ML is based on a resistance formulation and the surface temperature is determined based on a skin temperature formulation (Schulz and Vogel, 2020). For the model simulations no data assimilation is performed.

For the analysis of the Namib fog life cycle the model domain is located around the central Namib Desert. Figure 5.1 (a) displays the model topography. The model domain ranges from 20.25 to 26 °S and 11 to 18 °E and covers a region of $784 \times 644\,\mathrm{km}^2$ (280×230 grid points). The model domain is approximately bisected by the coastline of Namibia. The regions of upwelling cold water of the Benguela Current are included in the model domain[1]. This allows for the simulation of weather situations when low stratiform clouds form above a low SST due to the upwelling of the Benguela Current (see Sec. 2.3) and are advected inland by westerly or north-westerly winds.
Onshore, the coastal Namib Desert, the Namibian part of the Great Escarpment with deeply incised river valleys (e. g. Kuiseb river, Omaruru, Khan, Swakop), and also areas of the inner plateau are included in the model domain (see Sec. 2.4 for further details). The inclusion of the Great Escarpment and the inner plateau in the model domain is a necessary prerequisite for the simulation of potentially evolving meso-scale circulations like e.g. the plain-mountain circulation which has frequently been observed (Seely and Henschel, 1998). North of a line Swakopmund – Windhoek the model domain covers the Escarpment Gap.

[1] A figure showing the SST is included in the appendix.

In Figure 5.1 (b) the FogNet measurement stations are marked which are used for the evaluation of the near-surface meteorological parameters (Sec. 5.4). The stations have been installed as part of the Southern African Science Service Centre for Climate Change and Adaptive Land Management (SASSCAL) initiative (Kaspar et al., 2015; Muche et al., 2018). The FogNet station network encompasses 11 automated meteorological stations (see Tab. 5.1) aligned in two transects (north to south from 22.97 to 23.92 °S and west to east from 14.46 to 15.31 °E) (Andersen et al., 2019).

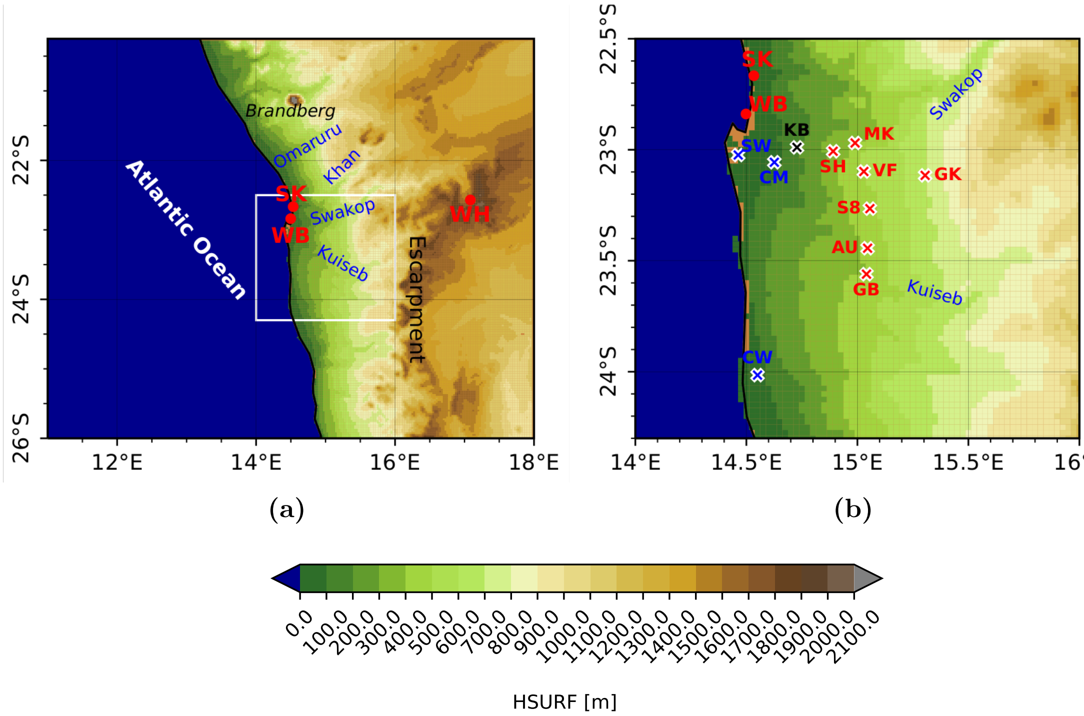

Figure 5.1: Topographic height of the surface $HSURF$ [m] in the COSMO-FOG model domain (left) as used in this study. The largest cities are Windhoek (WH), Swakopmund (SK) and Walvis Bay (WB). The largest ephemeral rivers are Omaruru, Khan, Swakop and Kuiseb. Enlargement of the white bordered area shows the FogNet stations (for explanation of the abbreviations see Table 5.1) (right). Stations are grouped into coastal stations (blue crosses), inland stations (red crosses) and a transition station (black cross).

According to their height above sea level, Andersen et al. (2019) grouped the stations into coastal stations (all stations located < 100 m a.s.l., blue crosses in Fig. 5.1) and inland stations (all stations located > 300 m a.s.l., red crosses in Fig. 5.1). The station in Kleinberg (KB, 185 m a.s.l., black cross in Fig. 5.1) is a transition station not belonging to either category (Andersen et al., 2019). During the NaFoLiCA-IOP tethered balloon sonde (TBS) and unmanned aerial vehicle (UAV) measurements have been performed for the sites in Gobabeb and Vogelfederberg (Spirig et al., 2019), respectively, which are used for the evaluation of the model results in Section 5.4.

Table 5.1: Name, abbreviation, latitude [°], longitude [°], elevation [m a.s.l.], and distance to the coast [km] of FogNet stations. According to their height above sea level, the stations are grouped into coastal stations (stations located < 100 m a.s.l.) and inland stations (stations located > 300 m a.s.l.). The station in Kleinberg is a transition station not belonging to either category. Adapted from Spirig et al. (2019).

Name	Abbr.	Lat	Lon	Elevation [m a.s.l.]	Distance to coast [km]
Saltworks	SW	–23.02	14.46	5	1
Conception Water	CW	–24.02	14.55	10	10
Coastal Met	CM	–23.06	14.63	94	17
Kleinberg	KB	–22.99	14.74	185	24
Sophies Hoogte	SH	–23.01	14.89	342	40
Marble Koppie	MK	–22.97	14.99	419	51
Vogelfederberg	VF	–23.10	15.03	515	58
Station 8	S8	–23.27	15.06	490	55
Aussinanis	AU	–23.44	15.05	444	55
Gobabeb	GB	–23.56	15.04	406	56
Garnet Koppie	GK	–23.12	15.31	733	85

As a limited-area regional weather prediction model, COSMO-FOG requires initial and lateral boundary conditions. At the lateral boundaries of the model domain, boundary values of all prognostic model variables are provided by a nesting simulation. Figure 5.2 depicts the model nesting domains. The COSMO-FOG simulation at 2.8 km resolution (model domain marked by solid square in Fig. 5.2) has been nested in a COSMO-FOG simulation with 7 km grid spacing (model domain marked by dashed square in Fig. 5.2). A sensitivity study for model initialisation has shown that results improve if the coarser nesting simulation is started 24 hours before the simulation with finer grid spacing to enable a spin-up phase. Table 5.2 summarises the start and end dates of the simulations[2].

Table 5.2: Start dates of the COSMO-FOG simulations with 7 km and 2.8 km horizontal grid spacing and simultaneous end dates of both simulations for the case studies.

Case study	Startdate 7 km	Startdate 2.8 km	Enddate
CS1819	2017/09/17 12 UTC	2017/09/18 12 UTC	2017/09/19 18 UTC
CS2021	2017/09/19 12 UTC	2017/09/20 12 UTC	2017/09/21 18 UTC
CS2324	2017/09/22 12 UTC	2017/09/23 12 UTC	2017/09/24 18 UTC
CS2728	2017/09/26 12 UTC	2017/09/27 12 UTC	2017/09/28 18 UTC

[2]Local time in Namibia is UTC+02:00.

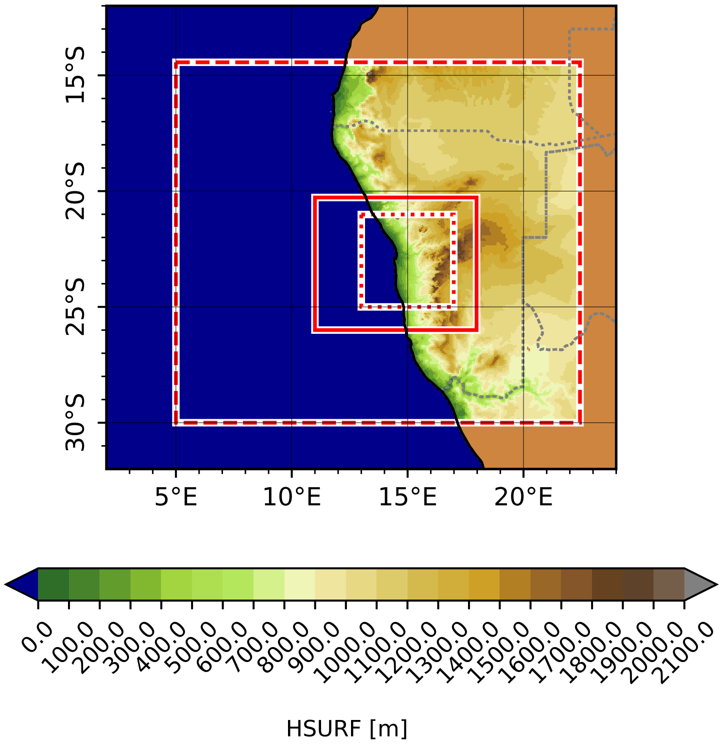

Figure 5.2: Topographic height of the surface $HSURF$ [m] in the model nesting domains of COSMO-FOG. The horizontal grid size of the nesting domain is 0.0625° (dashed square) covering 280x250 grid points. The horizontal grid size of the inner domain is 0.025° (solid square) covering 280x230 grid points. For a sensitivity study a simulation with a horizontal grid size of 0.01° and 400x400 grid points (dotted square) was nested into the inner domain.

The nesting simulation runs for 54 hours in total using ICON as initial and three-hourly lateral boundary conditions. After 24 hours of spin-up for the coarse resolution simulation, at 12 UTC, the atmospheric state of the nesting simulation is used to initialise the model simulation with a horizontal grid distance of 2.8 km which runs 30 hours and receives hourly lateral boundary conditions from the nesting simulation. For all simulations COSMO-FOG is used with 75 vertical levels. The external data (e.g. land use, roughness length,...) on both grids were provided by the Deutscher Wetterdienst (DWD, German Meteorological Service).

A sensitivity study was performed to investigate whether a horizontal grid spacing finer than 2.8 km improves the representation of FLCs. A COSMO-FOG simulation with approximately 1 km grid spacing was nested into the simulation with 2.8 km grid distance. The model domain of this simulation is depicted in Figure 5.2 (dotted square). The meteorological fields were compared for the overlapping areas of the domains yielding only small differences. This is illustrated in Figure 5.3 showing the vertically integrated cloud water content on 18 September 2017 at 22 UTC for all horizontal grid spacings. The integration takes part from the surface to a height of 1000 m above the surface. The resulting liquid water path is called LWP_{1000} in the remainder of this thesis. The simulated cloud cover and its spatial patterns resemble strongly for the three model simulations.

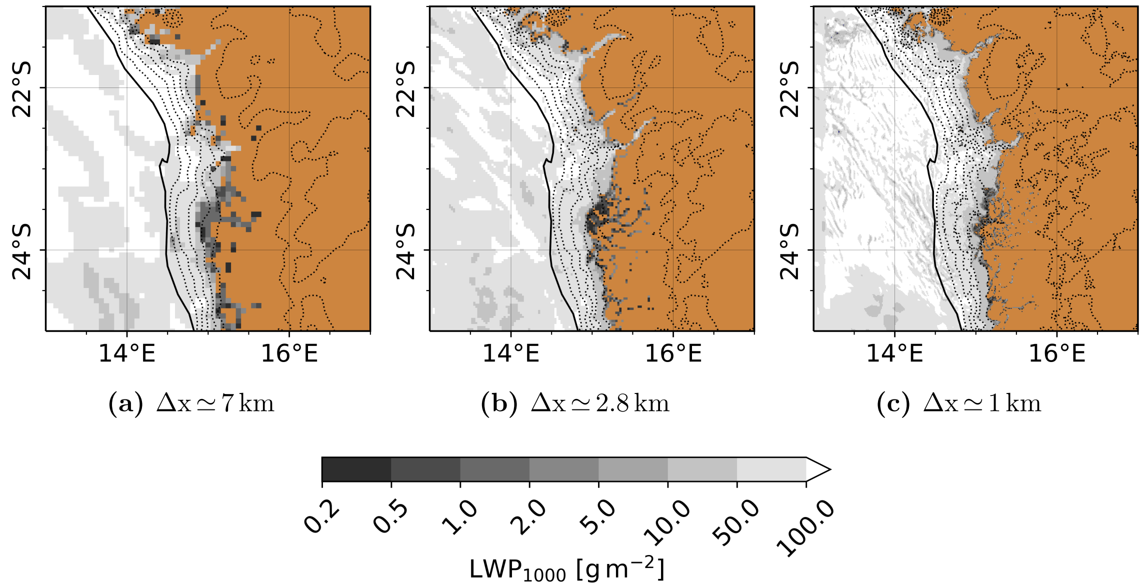

Figure 5.3: Vertically integrated cloud water content up to 1000 m (LWP_{1000} [g m^{-2}]) on 18 September 2017, 22 UTC simulated with COSMO-FOG for different horizontal grid spacings Δx. Dotted black lines mark terrain height (100, 200, 300, 400, 500, 1000, 1500, and 2000 m).

All model configurations simulate a cloud over the Atlantic Ocean reaching roughly 70–80 km inland. In some valleys the FLCs reach farther inland. These valleys are also evident for the simulation with 2.8 km grid spacing. This sensitivity study indicates that the horizontal grid spacing of 2.8 km is small enough to catch the essential processes for the simulation of FLCs in the Namib. This is quite clear from the investigated fog type and the topographic situation in the Namib. The investigated fog in the Namib is expected to be strongly related to the horizontally extensive fields of low-level marine stratiform clouds above the Atlantic Ocean intersecting the terrain at some distance from the coast (Andersen and Cermak, 2018; Andersen et al., 2019; Spirig et al., 2019). These clouds form in the shallow MBL above the cold Benguela Current capped by a strong temperature inversion under the influence of large-scale subsidence from the South Atlantic Anticyclone. Wind systems such as the sea breeze or the plain-mountain wind advect cold and moist maritime air masses. The subsidence and the Benguela Current are large-scale phenomena which are expected to be adequately accounted for at a horizontal grid spacing of 2.8 km. Heterogeneities in the Namib like the Great Escarpment, the coastline, some river valleys, even the Brandberg massif, are also evident in the simulation with 2.8 km grid spacing. This is small enough to catch e.g. the sea breeze or the plain-mountain wind. Thus, the horizontal grid spacing of 2.8 km is expected to be sufficient and is used for the model simulations of the analysed case studies.

5.2 Advection of low stratiform clouds - Case study 18 to 19 September 2017

In the night from 18 to 19 September 2017 the central Namib experienced a fog event. Stratiform clouds were already present at the coast from noon and extended inland in the evening and during the night. Before the spatial and temporal patterns of FLCs will be investigated in detail, the fog event is put into context focusing on the description of the large-scale weather patterns.

5.2.1 Synoptic conditions and meteorological situation

The Namib Desert is located in the subtropics where dry descending air masses in the subsiding branch of the Hadley cell circulation create semi-persistent surface anticyclones forming the subtropical high-pressure belt (cf. Sec. 2.4.2). On 18 September 2017 (CS1819), the subtropical anticyclones are established on both sides of the African continent[3]. The South Atlantic Anticyclone is located southwest off the Namibian coast and the Indian Ocean Anticyclone is located at the east coast of the African continent. The South Atlantic Anticyclone is characterised by a maximum surface pressure of 1034 hPa covering almost the entire area between South America and Africa. Generally, the large-scale subsidence within the subtropical high-pressure belt causes stable atmospheric conditions suppressing cloud development above the PBL. Thus, the whole southern African continent shows clear skies except for the eastern parts close to the Indian Ocean being influenced by a smaller-scale low-pressure system. The clear sky enables strong heating of the ground and near-surface air by solar radiation above southern Africa during daytime. In the northeast of Namibia, the near-surface temperature rises to more than 35 °C with the highest temperature around 40 °C. The near-surface heating by solar radiation causes low surface pressure extending over wide parts of southern Africa. The thermally induced low-pressure system is characterised by a minimum surface pressure of 1010 hPa extending from Namibia over Angola, the Democratic Republic of Congo, and Zambia.

Both, the thermally induced low-pressure system on the continent as well as the high-pressure system off the Namibian coast interact and govern the atmospheric flow which is modified by thermally and topographically induced wind systems (e.g. sea breeze and plain-mountain wind). At the eastern flank of the South Atlantic Anticyclone, southeasterly to southerly trade winds blow off the Namibian coast throughout the day (Fig. 5.4 (a)). A gentle to moderate southwesterly breeze blows in the coastal plain and a fresh southwesterly breeze on the mountain ridges of the Great Escarpment in the afternoon which result from the superposition of a sea breeze with the plain-mountain wind and the outflow from the high-pressure system off the Namibian coast. With the southwesterly wind cool and moist maritime air masses are advected inland (Fig. 5.4 (b, c)). The cold air advection by the southwesterly wind is counteracted by near-surface heating due to solar radiation and resultant heat fluxes from the ground. This causes a temperature gradient between

[3] Additional figures showing the synoptic situation on 18 September 2017 are provided in the appendix.

the coastal plain and the interior of Namibia. At daytime, the temperature is rather moderate and reaches 15–20 °C in the coastal area (Fig. 5.4 (b)). With increasing distance from the coast, the near-surface temperature gradually increases to more than 30 °C at the slopes of the Great Escarpment.
Specific humidity further illustrates the contrast between the coastal plain influenced by the advection of maritime air and the hot and dry inner plateau. Specific humidity reaches 9–11 g kg^{-1} in a stripe close to the coast and quickly decreases to 4 g kg^{-1} or even less further inland (Fig. 5.4 (c)).

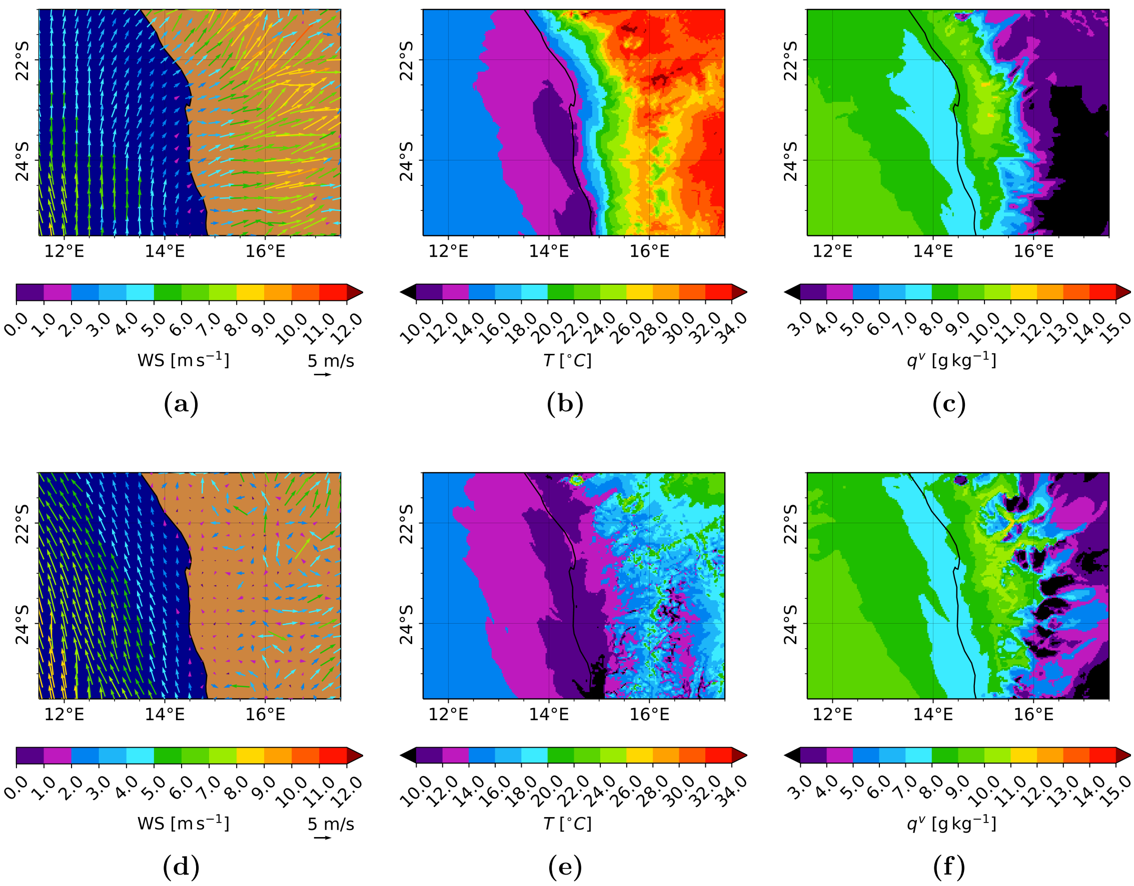

Figure 5.4: Spatial distribution of (a, d) horizontal wind WS [m s^{-1}], (b, e) temperature T [°C], and (c, f) specific humidity q^v [g kg^{-1}] in the lowest model layer at 14 UTC (top) and 21 UTC (bottom) for 18 September 2017.

As expected from temperature and specific humidity, near-surface relative humidity exhibits a strong gradient quickly decreasing from more than 80 % to below 50 % within roughly 60 km between the maritime air mass over the Atlantic Ocean and the warm air mass over land[4].
Towards sunset, the incoming solar radiation and, thus, heat fluxes decrease, so the temperature and its gradient decrease (Fig. 5.4 (e)). At night, a stably stratified

[4]Additional figures showing the weather situation of CS1819 can be found in the appendix.

nocturnal boundary layer develops over land due to longwave radiative cooling. The near-surface temperature widely drops to 10–15 °C. In the valleys of the Great Escarpment the coldest air aggregates leading even to temperatures below 10 °C. At the mountain ridges of the Great Escarpment and the Inselbergs, the temperature does not decrease below approximately 20 °C at night.
The moist air extends further inland but still being restricted to a distance 100–150 km from the coast (Fig. 5.4 (f)). In areas where the Great Escarpment is dissected by river valleys and no topographic lifting is required, moist air progresses farther inland as can be deduced from the spikes in Figure 5.4 (f). The shallow stably stratified boundary layer with accumulation of cold air and specific humidity in the coastal plain and in the river valleys of larger rivers such as Swakop, Khan and Omaruru allows for the existence of ground fog there.
A striking feature of the spatial patterns of specific humidity at 21 UTC is the development of isolated dry areas 100–150 km inland from the coast. These dry areas with specific humidity below 3–4 $g\,kg^{-1}$ spatially correlate with the Great Escarpment reaching around 2000 m. This is a hint that the mountain crests of the Great Escarpment peak into the dry free troposphere after the collapse of the PBL in the evening.
With the cooling at night, the thermal low weakens, as expected, while the anticyclone southwest of the Namibian coast extends eastwards on 19 September. Weaker pressure gradients due to the attenuated heat low and the stable boundary layer yield a near-surface wind pattern that is largely driven by mountain-valley circulations in the Great Escarpment and on the inner plateau at night. Close to the coast, the wind decreases to almost calm air (Fig. 5.4 (d)).
After sunrise (04:45 UTC), the near-surface temperature rises to about 20 °C, especially at the mountain peaks of the Great Escarpment and in the northeastern model domain. Closer to the coast the temperature only slightly increases and stays around 10–14 °C due to the maritime air masses and persisting clouds.

5.2.2 Spatial and temporal evolution of fog and low stratiform clouds

In this section, the spatial patterns and temporal evolution of FLCs simulated by COSMO-FOG are investigated.

Horizontal distribution and evolution of fog and low-level clouds

To analyse the spatial patterns and temporal evolution of FLCs in the COSMO-FOG simulation, Figure 5.5 displays the vertically integrated water content LWP_{1000}. Regions with ground fog are identified by visibility falling below 1000 m according to the definition of fog by the World Meteorological Organisation (WMO) (red dotted areas, cf. Sec. 2.2) or the cloud water content in the lowest model layer exceeding 0.01 $g\,kg^{-1}$ (blue dotted areas, see Bott (2020)). The visibility is determined by means of the empirical formulation according to Gultepe et al. (2006) (cf. Sec. 3.3).

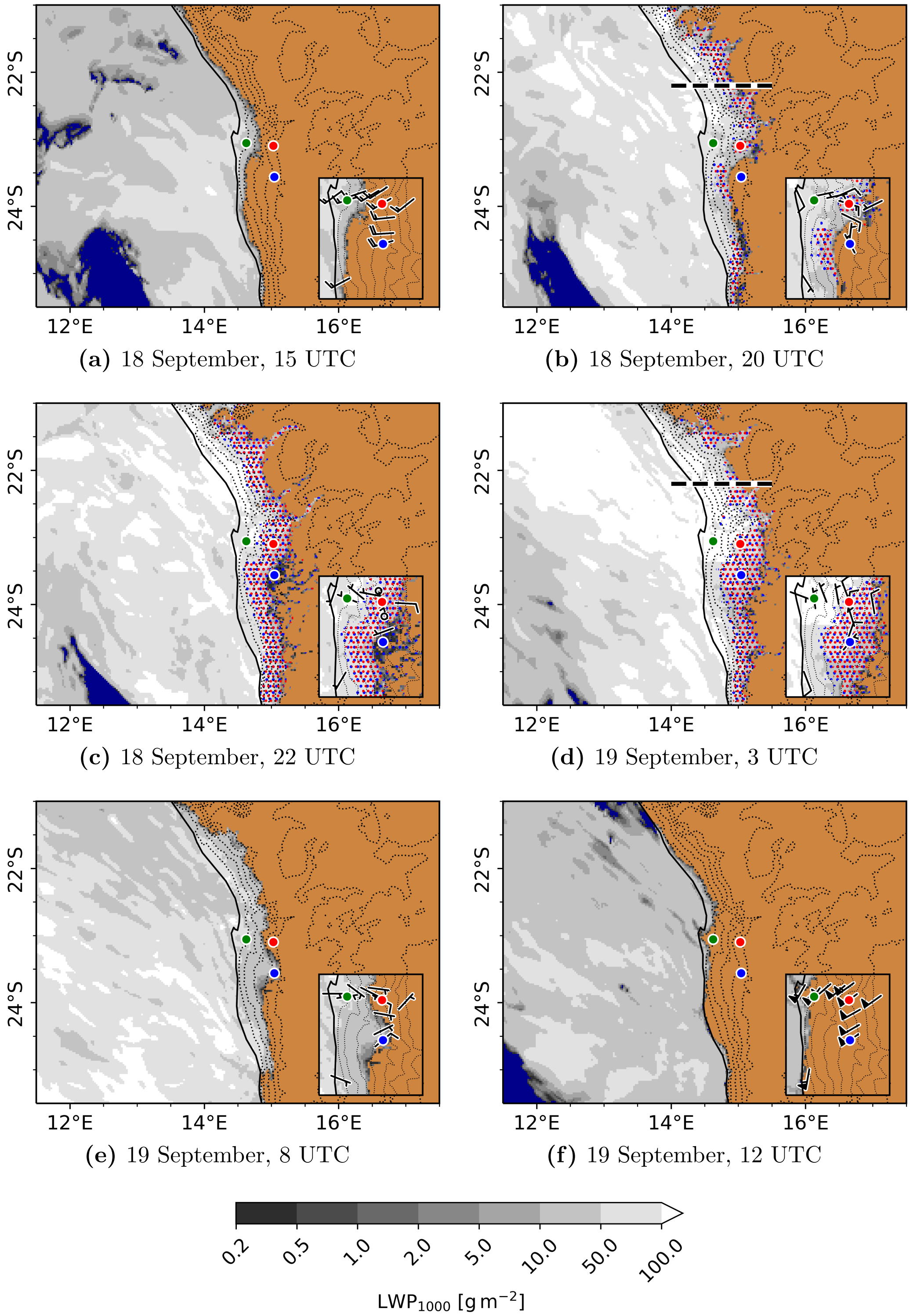

(a) 18 September, 15 UTC

(b) 18 September, 20 UTC

(c) 18 September, 22 UTC

(d) 19 September, 3 UTC

(e) 19 September, 8 UTC

(f) 19 September, 12 UTC

Figure 5.5: Spatial distribution of LWP$_{1000}$ [g m^{-2}] for CS1819 simulated with COSMO-FOG. Small blue and red dots mark the occurrence of ground fog. Dashed black lines mark terrain height (100, 200, 300, 400, 500, 1000, 1500, and 2000 m). Map inset shows enlargement of central Namib with simulated 10 m wind speed and direction at FogNet stations. Half line, full line, and flag indicate 1, 2, and 5 m s^{-1}. The cross sections shown in Figure 5.7 are indicated as dashed lines. Marked locations are Coastal Met (green), Vogelfederberg (red) and Gobabeb (blue).

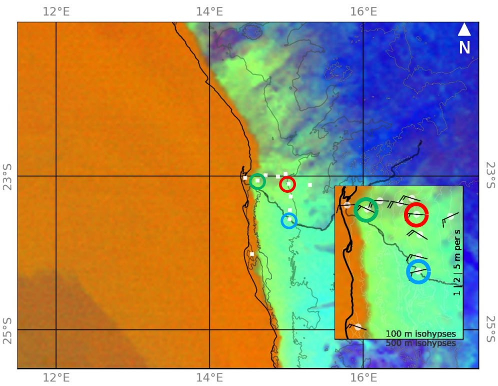

(a) 18 September, 15 UTC

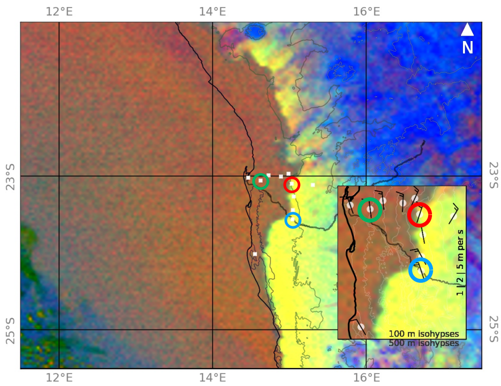

(b) 18 September, 20 UTC

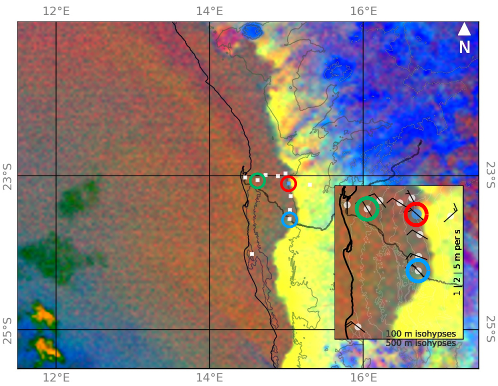

(c) 18 September, 22 UTC

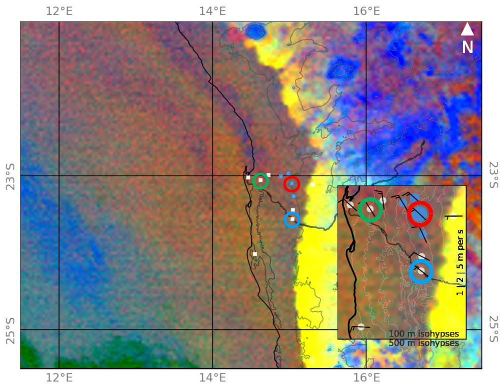

(d) 19 September, 3 UTC

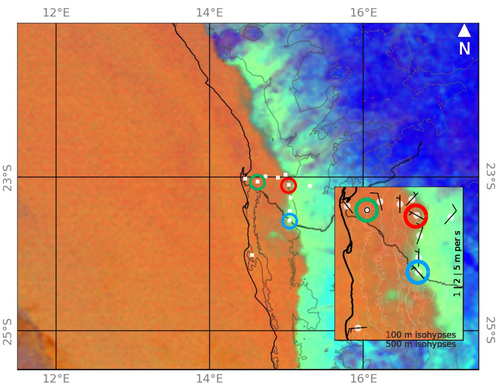

(e) 19 September, 8 UTC

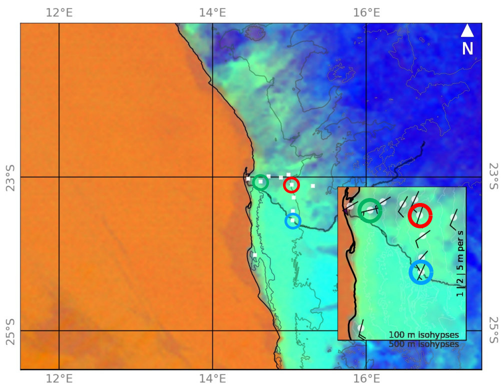

(f) 19 September, 12 UTC

Figure 5.6: Dust composite from Meteosat combined with FogNet data for CS1819. Orange (daytime) and darkorange/brownish (nighttime) colors mark FLCs. Wind barbs represent 15 minute averages of wind speed and direction at the FogNet stations. Half line, full line and triangle indicate 1, 2, and 5 $\mathrm{m\,s^{-1}}$. The FogNet stations are marked in blue if fog precipitation occured during the previous 15 minutes. Courtesy of Dr. Robert Spirig (Department of Environmental Sciences, University of Basel, now at Departement Umweltsystemwissenschaften, ETH Zürich). Marked locations are Coastal Met (green), Vogelfederberg (red) and Gobabeb (blue).

In order to evaluate if the model predicts FLCs reasonably, the simulated LWP_{1000} is visually compared to a RGB (Red, Green, Blue) composite based on the SEVIRI on board of the Meteosat Second Generation (MSG) satellite platform. The RGB composite combines data of the SEVIRI infra-red (IR) channels IR8.7, IR10.8 and IR12.0 (R: IR12.0-IR10.8, G: IR10.8-IR8.7, B: IR10.8) and is also referred to as dust composite (EUMETSAT, 2024; University of Basel, 2024). The dust composite allows to distinguish low clouds or fog from other clouds (Spirig et al., 2019) at daytime and nighttime over land and over ocean surfaces but it does not allow to discriminate between fog and low-level clouds. Therefore, the dust composite was combined with ground-based FogNet data by Spirig et al. (2019) which provide indications for the occurrence of ground fog. The occurrence of ground fog is determined by fog precipitation (i.e. fog deposition at a screen) (Spirig et al., 2019), which cannot be determined in the model simulation. Visibility, which is available in the model simulation, was only measured at the FogNet station in Gobabeb (Feigenwinter et al., 2020). On 18 September 2017 at 15 UTC in the late afternoon, a closed blanket of stratiform clouds covers the Atlantic Ocean offshore of the Namibian coast and reaches a few kilometres inland in the model simulation (cf. Fig. 5.5 (a)) which is in well accordance with satellite (orange (daytime) and darkorange/brownish (nighttime) areas) and ground-based observations (cf. Fig. 5.6 (a)).
Starting from 15 UTC, the simulated FLCs extend eastwards inland with a clear front-like boundary almost parallel to the shore (in the following also referred to as FLC front). A southwesterly sea breeze is simulated at that time. The simulated FLC front reaches the Namib Desert from the west with an estimated speed of 8 to 10 $\mathrm{km\,h^{-1}}$ covering the FogNet stations in the east-west transect successively with approximately one hour difference. Previous studies by Andersen and Cermak (2018) and Andersen et al. (2019) interpreted the simulated time lag in the arrival of the FLC front depending on the distance from the coast as a sign that the clouds are advected inland from the Atlantic Ocean. It is therefore likely that the clouds are advected in the model simulation.
During the eastward extension of the low stratiform clouds, the model simulates ground fog along the leading edge of the eastward progressing stratiform clouds from 18 UTC on as indicated by visibility below 1000 m and cloud water content above 0.01 $\mathrm{g\,kg^{-1}}$ in the lowest model layer (red and blue dotted area in Fig. 5.5 (b–d)). Figure 5.5 reveals, that both criteria for the occurrence of ground fog based on visibility and cloud water content yield very similar results which agree with measurements of fog precipitation for Coastal Met (no fog precipitation, white dots in Fig. 5.6 (c) and (d)) and Vogelfederberg (fog precipitation measured, large blue dot in Fig. 5.6 (c) and (d)). In Gobabeb, no fog precipitation is registered at 22 and 3 UTC, but ceilometer measurements reveal a ground fog from 21 UTC on, so the simulated ground fog seems reasonable[5].
At 22 UTC the FLCs extend up to 50–60 km inland. The horizontal distribution of FLCs in Figure 5.5 (b) and (c) shows that the inland progression of the FLCs is more pronounced north of the Kuiseb river in the gravel plains than south in the Namib Sand Sea. This pattern is confirmed by the satellite retrieval depicted in Figure 5.6 (b) and (c).

[5] Additional figures showing the ceilometer observations can be found in the appendix.

In the river valleys and canyons of larger rivers as Omaruru, Khan and Swakop the FLCs proceed further inland than in the surrounding between 20 and 22 UTC, which becomes obvious by the eastward spikes in Figure 5.5 (b–d). This feature cannot clearly be identified in the satellite retrieval depicted in Figure 5.6 (b–d), but has been found in a climatological satellite study by Olivier (1995) who found an eastward bulging of the isolines of fog frequency in the river valleys. So this model behaviour seems realistic. The FLCs in the river valleys do not persist during the whole night in all river valleys, but widely dissolve in the Swakop valley until 0 UTC. As this example shows, besides the distance from the coast, local topography affects the FLC occurrence and its spatial patterns.
Around 22 UTC, less dense (less LWP_{1000}) and rather patchy fog forms at the downstream eastern boundary of the FLCs. The satellite retrieval shows no hint for the occurrence of less dense fog before the arrival of the FLC front. This does not necessarily mean, that no shallow ground fog has been observed. Shallow thin fog has a similar cloud top temperature than the ground so the satellite retrieval based on cloud top temperature might not be able to distinguish fog from the ground.
Between 22 and 3 UTC, the dense fog further extends eastward especially south of the Kuiseb river in the model simulation thus overlapping the less dense fog. Between 2 and 3 UTC the simulated coverage with dense fog and stratiform clouds reaches its maximum horizontal extent. While the model simulates ground fog in Vogelfederberg and Gobabeb, fog precipitation has only been observed in Vogelfederberg, but the ceilometer measurements in Gobabeb show a ground fog. So the simulated ground fog seems reasonable.
Except for two coastal stations (Saltworks and Conception Water) where the southeasterly wind direction prevails, a near-surface wind from a northwesterly or northerly direction is simulated at all FogNet stations which is well in accordance with the observations (see Fig. 5.5 (d) and Fig. 5.6 (d)).
The dissolution of fog starts around 3 UTC while the cloud coverage stays still constant. In the Escarpment Gap north of Walvis Bay the fog lifts from the ground as indicated by visibility larger than 1000 m and cloud water content below $0.01\,\mathrm{g\,kg^{-1}}$ in the lowest model layer. The ground fog completely lifts until approximately 7 UTC. Similar to the eastward movement of the FLCs in the first half of the night, their dissolution progresses also like a front moving from the east westwards to the coast. From 6:30 UTC, the dissolution of the FLCs is strongly accelerated along its eastern boundary, which is in well accordance with the satellite observation (cf. Fig. 5.5 (e) and Fig. 5.6 (e)). The stratiform clouds widely disappear above land until the beginning of the sea breeze circulation around 9 UTC. The stations closest to the coast (Saltworks and Conception Water) are overcast for the longest time. The dissolution of the low stratiform clouds until 12 UTC corresponds well with the satellite observation (cf. Fig. 5.5 (f) and Fig. 5.6 (f)). With the complete dissolution of the low stratiform clouds over land until approximately 12 UTC, the life cycle begins anew.

The spatial patterns and temporal evolution of FLCs simulated by COSMO-FOG for 18 September 2017 are consistent with in-situ satellite observations and longer term climatological studies based on satellite retrievals (see e.g. Andersen et al., 2019;

Olivier, 1995). Analysing several years of satellite data, Andersen et al. (2019) showed that the FLC occurrence is highest along the coastline and the timing of fog occurrence depends on the distance from the coastline with later fog occurrence for larger distance from the coast which is also evident in the model simulation.

Vertical distribution and evolution of fog and low-level clouds

Figure 5.7 depicts a representative vertical cross section through the cloud water content reaching from [-22.2 °S,14.0 °E] to [-22.2 °S,15.5 °E] (dashed lines in Fig. 5.5 (b) and (d)). A spatially coherent low stratiform cloud reaching from the Atlantic Ocean onshore can be diagnosed. The cloud at the top of the MBL has a cloud top height slightly above 500 m and a cloud base height below 200 m a.s.l. Onshore, cloud top and base height increase in the PBL above the sloping terrain of the Great Escarpment. The cloud intersects with the ascending terrain of the Great Escarpment between 300 and 700 m a.s.l. at some distance from the coast forming ground fog there.

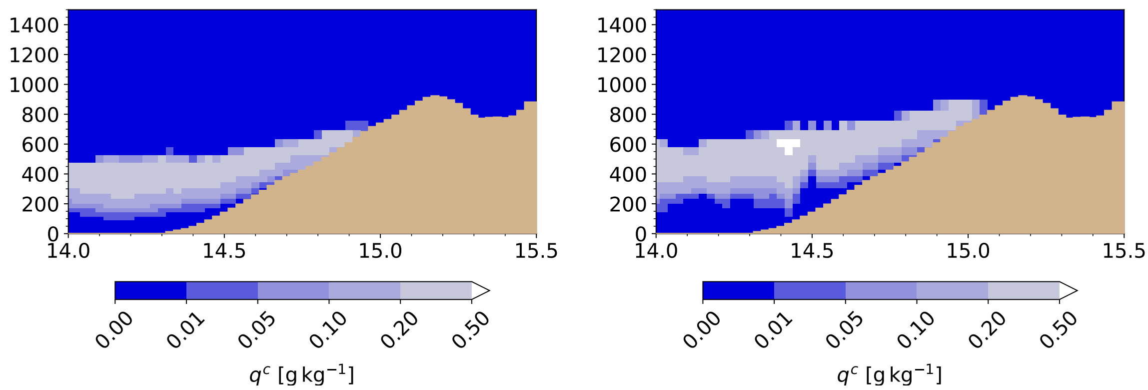

(a) 20 UTC **(b)** 3 UTC

Figure 5.7: Vertical cross sections of cloud water content q^c [g kg^{-1}] for CS1819 at (a) 20 UTC and (b) 3 UTC from [22.2 °S,14.0 °E] to [22.2 °S,15.5 °E] (dashed lines in Fig. 5.5 (b) and (d)). Brown areas mark the terrain height.

Between 20 and 3 UTC, the cloud rises in height and extends further onshore intersecting the terrain at higher altitude and farther onshore. This reveals that the eastward expansion of the FLCs comes along with the rise of the cloud top height. The cloud base height determines where the stratiform cloud first intercepts with the terrain and turns into fog while the cloud top height controls the maximum inland extension of the fog. So the ground fog simulated by the model results from the interception of the stratiform cloud with the terrain. This finding is in line with many past and recent studies linking the occurrence of the ground fog in the Namib to the stratus and stratocumulus clouds, (e.g. Andersen and Cermak, 2018; Andersen et al., 2019, 2020; Olivier, 1992; Spirig et al., 2019; Taljaard, 1979).

The vertical distribution of FLCs is analysed at selected locations in the central

Namib (Fig. 5.8). One profile is taken close to the coast (Coastal Met, Fig. 5.8 (a)), one in the area where less dense and patchy ground fog forms before the arrival of the FLC front (Gobabeb, Fig. 5.8 (b)), and one in a region where the FLC front arrives (Vogelfederberg, Fig. 5.8 (c)).
Close to the coast in Coastal Met, a low stratiform cloud is simulated with a cloud base around 300 m a.s.l. and cloud top height at approximately 550 m a.s.l. in the afternoon (Fig. 5.8 (a)). The cloud base height decreases to 200 m a.s.l. around sunset between 16 and 17 UTC (sunset: 16:45 UTC) and further lowers to 120 m a.s.l. between 21 and 23 UTC. This results in a geometrical thickening of the cloud and an increase of the cloud water content. This is further enhanced by the gradual increase of cloud top from 500 to 600 m between 22 and 3 UTC. From 0 UTC the cloud base gradually rises by roughly 50 m until the cloud dissolves around 10 UTC approximately six hours after sunrise at 04:45 UTC. The dissolution of the cloud is well met by COSMO-FOG, while the simulated cloud base is too low and no cloud was observed in the afternoon on 18 September[6].
At the inland station Gobabeb, a very shallow ground fog confined to the lowest model layer is simulated between 21 and 23 UTC (Fig. 5.8 (b)). Ceilometer measurements in Gobabeb reveal a ground fog from 21 UTC on, so the simulated ground fog seems reasonable. Around 23 UTC, a cloud is simulated at 550 m a.s.l. The cloud thickness quickly grows by more than 100 m in the next hour due to a rapid lowering cloud base. The rapid development of a thick ground fog by lowering cloud base coincides with an increase of LWP_{1000} and the arrival of the FLC front in Gobabeb (cf. Fig. 5.5 (c) and (d)). Thus, the sudden appearance of the thick ground fog by lowering cloud base height might probably suggest the arrival of the intercepting stratiform cloud in Gobabeb by an advective process. From 3 UTC on, the fog layer continues to grow gradually up to a thickness of 300 m. While still growing vertically, it starts to thin and lift from the ground around 4 UTC due to a slight warming by less than 1 °C which coincides with a shift of the wind direction to north and northeast. At 8 UTC the low stratiform cloud has completely dissipated in Gobabeb.

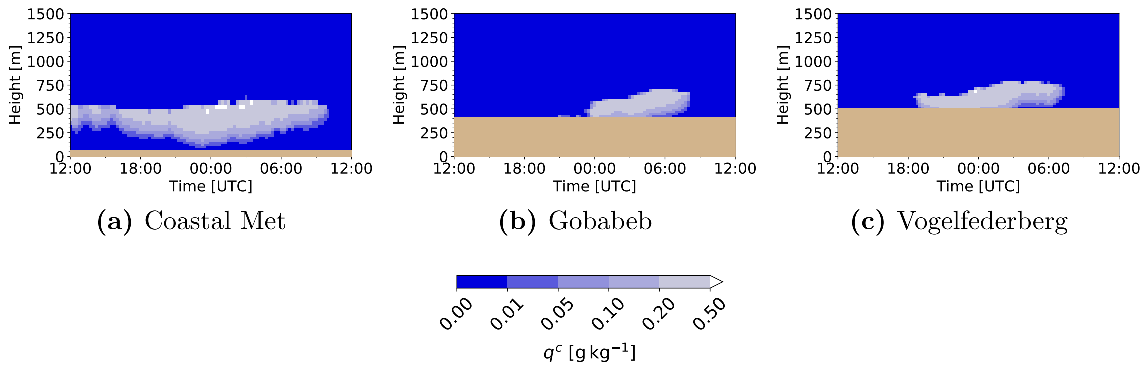

Figure 5.8: Time series of cloud water content q^c [g kg^{-1}] profiles at (a) a coastal and (b, c) two inland locations for CS1819. Brown areas mark the terrain height.

[6]Additional figures showing the ceilometer observations are displayed in the appendix.

At Vogelfederberg, the fog event starts abruptly with a cloud at approximately 600 m a.s.l. turning into a 150 m thick ground fog by rapid lowering of the cloud base between 18 and 19 UTC (Fig. 5.8 (c)). From 23 UTC until 2 UTC the fog top height gradually grows until the fog reaches its maximum vertical extent of 300 m around 3 UTC. Afterwards the fog lifts from the ground and dissolves around 7 UTC in the morning approximately two hours after sunset.
The spatio-temporal patterns at all selected locations have in common the increase of cloud top height after 22 UTC and the lifting of fog or cloud base height after 3 UTC. The vertical extent and LWP_{1000} of FLCs culminate between 3 and 5 UTC. The cloud already lifts from the ground while it still grows vertically. For the inland locations, the difference in cloud top height results from the increase of cloud top with the rising terrain of the Great Escarpment. The cloud water content of the FLCs is widely between 0.1 and 0.5 $\mathrm{g\,kg^{-1}}$ and does only rarely exceed 0.5 $\mathrm{g\,kg^{-1}}$.

Diurnal Cycle of fog and low stratiform clouds

Figure 5.9 illustrates the area covered by FLCs and the domain-averaged LWP_{1000} for the whole domain, ocean and land areas. A distinct life cycle of FLCs is evident from the total area covered with clouds and the LWP_{1000} averaged over the whole domain (black curves in Fig. 5.9). From the variation of the total area covered with clouds and the area covered with clouds over land, different life cycle phases of FLCs in the Namib Desert can be distinguished.

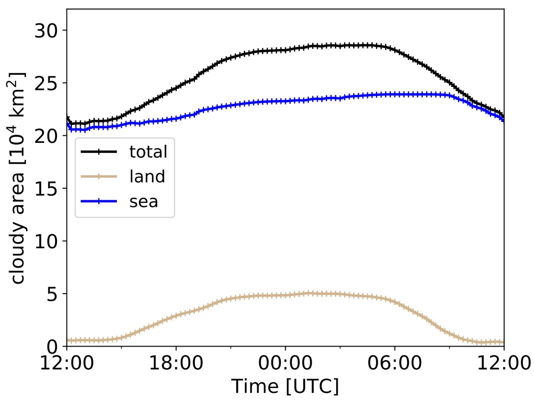

(a)

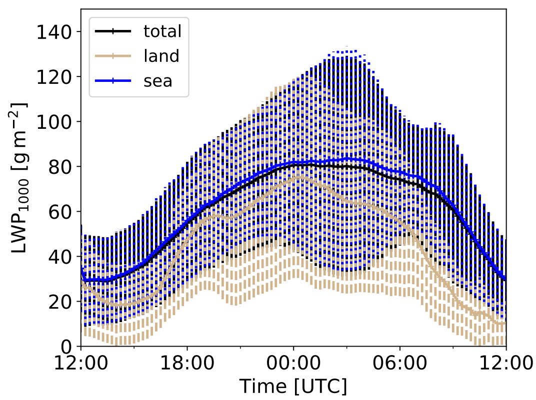

(b)

Figure 5.9: Time series of simulated (a) area covered by FLCs [$\mathrm{km^2}$] and (b) LWP_{1000} [$\mathrm{g\,m^{-2}}$] averaged over the model domain (b) for the whole domain and divided into land and ocean areas for CS1819. Dashed areas for LWP_{1000} represent the spatial variability of LWP_{1000}.

The cloud cover and mean LWP_{1000} for the whole domain are minimal in the cloud-free phase during daytime, when low stratiform clouds are for the most part confined to the Atlantic Ocean and hardly progress eastwards onshore. In the extension phase starting with lowering sun around 15 UTC, the total area covered with clouds increases almost linearly reaching its maximum during nighttime between 21 and 6

UTC. When the horizontal extension of FLCs slows down and the number of cloudy grid points stays nearly constant from 21 UTC on, the cloud and fog phase starts. The almost constant cloud coverage between 21 and 6 UTC along with the increase of mean LWP_{1000} until 0 UTC results from the vertical growth of the FLCs during night with only slight further horizontal extension. In the dissipation phase starting around 6 UTC after sunrise and lasting until approximately 10 UTC, cloud cover drops to the baseline of the day before.
Splitting the cloud coverage into land and ocean areas, it becomes clear that the cloud coverage is almost constant over the ocean while the diurnal cycle of total area covered with clouds is driven by the cloud coverage over land areas. FLCs extend onshore mainly from 15 UTC until 21 UTC and most of the clouds over land dissolve between 6 and 9 UTC after sunrise the next morning. Over land areas the mean LWP_{1000} is smaller than over the Atlantic Ocean and already starts to decrease after 0 UTC.
The diurnal cycle of FLCs simulated by COSMO-FOG is in line with a study by Warren et al. (2015), who found that the total cloud cover of all cloud types west of Namibia peaks at 4 UTC and reaches its minimum at 16 UTC. Warren et al. (2015) stated that low stratiform clouds are responsible for this diurnal cycle.

5.2.3 Atmospheric conditions and processes influencing fog and low stratiform clouds

The investigation of the spatio-temporal patterns of FLCs suggests various life cycle phases. To understand the evolution of FLCs in the life cycle phases, the atmospheric conditions and processes contributing to the development of FLCs and their properties are analysed in this section. This section provides an overview over the PBL conditions during different phases of the fog event.

Before the onset of fog and low-level clouds - the cloud-free and extension phase

The investigation of spatio-temporal FLC patterns in the previous section has shown that the eastward progression of FLCs starts towards sunset although a south-westerly wind advects cool and moist maritime air masses onshore and relative humidity increases already in the afternoon. Thus, the advection of cool maritime air masses with an onshore flow is not sufficient for the formation of FLCs onshore. In the following, it will be investigated which processes make the atmosphere favourable for the formation of FLCs until the cloud and fog phase starts.
Figure 5.10 illustrates the temporal and vertical evolution of the virtual potential temperature θ_v and relative humidity RH at two inland locations – namely in Gobabeb and Vogelfederberg (blue and red markers in Fig. 5.5). Figure 5.10 (a) and (b) reveal that at daytime the 200 m thick well-mixed boundary layer is topped by a strong temperature inversion. Until evening, the virtual potential temperature drops by approximately 10 °C in six hours in the entire PBL. The strongest cooling occurs around sunset (16:45 UTC) between 16 and 18 UTC when the solar surface warming and the sensible heat flux decrease. In Gobabeb, the cooling is stronger at

the surface resulting in the formation of a surface-based inversion and stabilisation of the boundary layer until 20 UTC. In Vogelfederberg, a well-mixed boundary layer of approximately 100 m depth persists for a longer time. Above 1000 m, the virtual potential temperature remains almost constant.

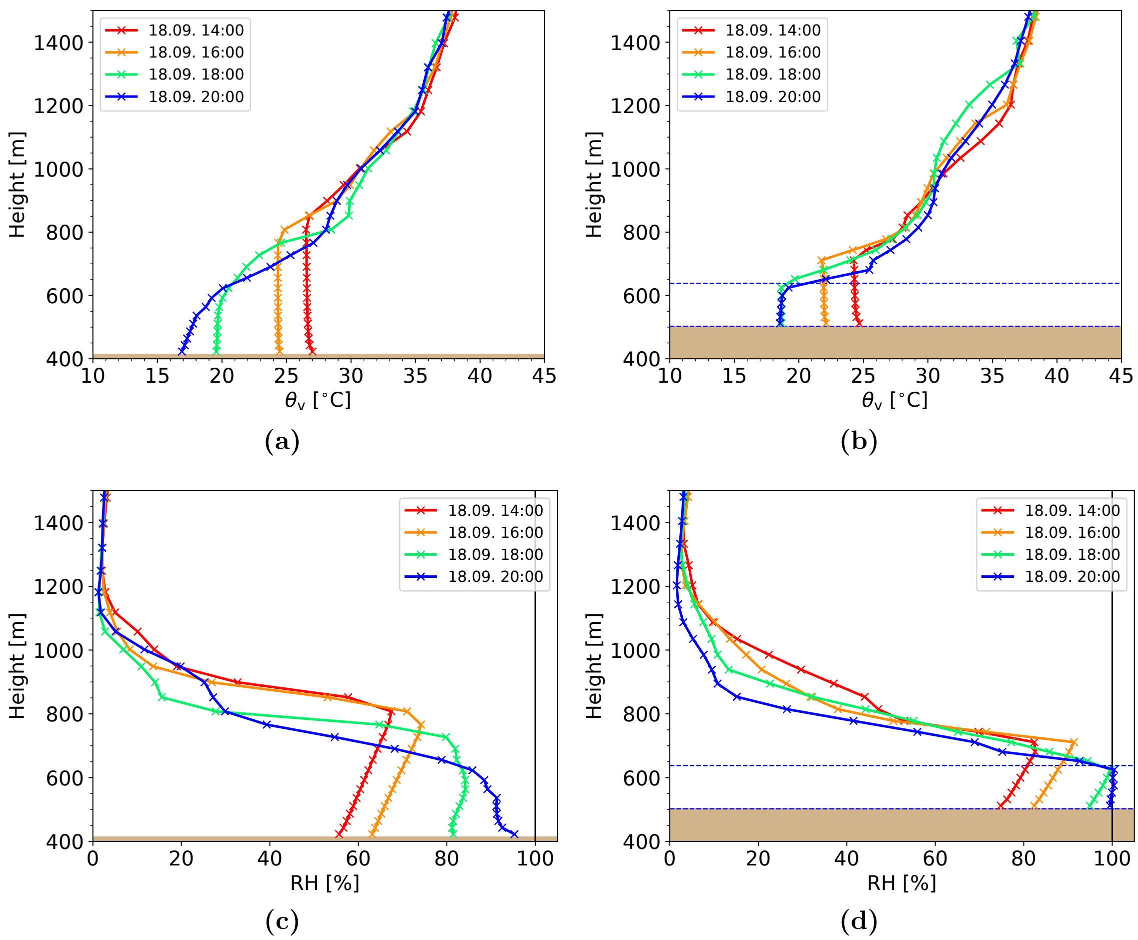

Figure 5.10: Vertical profiles of (a, b) virtual potential temperature θ_v [°C] and (c, d) relative humidity RH [%] in (a, c) Gobabeb and (b, d) Vogelfederberg (blue and red marker in Fig. 5.5) at different times of CS1819. Horizontal dashed lines indicate the layer where the cloud water content is larger than 0.01 g kg^{-1}. Brown areas mark the terrain height.

The relative humidity increases from beneath 50–70 % to more than 90 % from 14 UTC until 20 UTC in the PBL (Fig. 5.10 (c, d)). The strongest increase of the relative humidity happens along with the strongest cooling between 16 UTC and 18 UTC. As expected from the surface-based inversion in Gobabeb, a quicker increase of the relative humidity occurs in the lowest model layer above ground. Values of the relative humidity above 60 % are confined to the lowest 200–400 m above ground level. Above 1100 m, the atmosphere is very dry with a relative humidity below 10 %.

In order to understand whether the specific humidity or temperature change has a stronger influence on the relative humidity and thus fog formation, the contributions of temperature and specific humidity changes to the relative humidity changes are determined using equation 2.1. The changes of temperature and specific humidity are taken from the MESSy submodel TENDENCY and are averaged over the model output step.

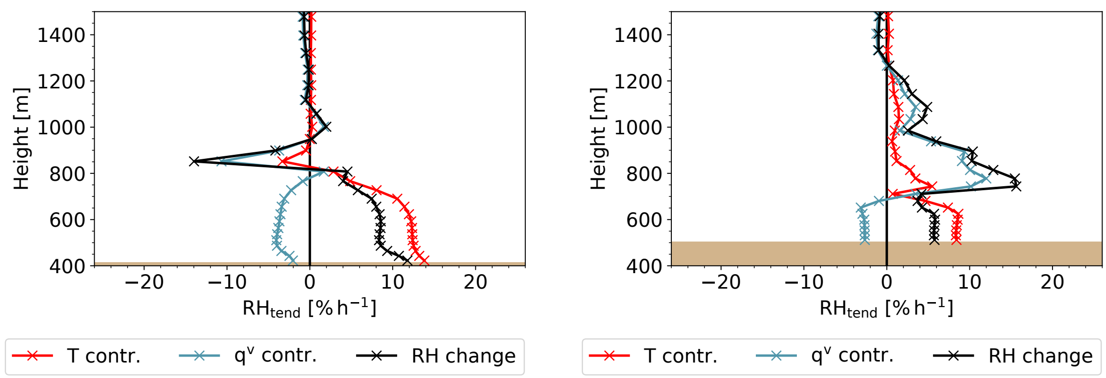

(a) **(b)**

Figure 5.11: Vertical profiles of relative humidity change [$\% \, h^{-1}$] and its individual contributions by temperature and specific humidity determined using Equation 2.1 in (a) Gobabeb and (b) Vogelfederberg on 18 September at 17 UTC. Brown areas mark the terrain height.

Figure 5.11 depicts vertical profiles of the relative humidity change and its individual contributions by temperature and specific humidity at 17 UTC when the increase of relative humidity is strongest. The strongest increase of relative humidity of 6–8 $\% \, h^{-1}$ occurs close to the ground up to approximately 600 m a.s.l. which is similar for both locations (Fig. 5.11). This relative humidity increase is caused by a relative humidity increase due to temperature around 8–12 $\% \, h^{-1}$ while specific humidity causes a smaller counteracting decrease of relative humidity by less than -5 $\% \, h^{-1}$. So the increase of relative humidity in the boundary layer, where low-level clouds and fog form, is for most driven by a temperature decrease while specific humidity changes play only a minor role or even counteract. Above the PBL the relative humidity tendencies are controlled by changes in specific humidity. These results are representative for the coastal plain of Namibia during the extension phase[7]. Since cooling is the key process leading to the saturation responsible for the formation of FLCs, the heat budget will be analysed with detail in the following.
From the model equation for temperature (Eq. 3.3), it follows that the total temperature tendency can be caused by dynamical processes, phase changes, radiation, subgrid-scale turbulent diffusion and subgrid-scale convection (cf. Sec. 3.1). The contributions of the different processes to the total temperature tendency and the total temperature tendency itself are provided by the MESSy submodel TENDENCY. Figure 5.12 shows vertical profiles of the temperature tendencies in Gobabeb and

[7] Additional figures showing the spatial distribution of the relative humidity changes in total and by temperature and specific humidity are displayed in the appendix

Vogelfederberg in the afternoon (14 UTC) and shortly after sunset (17 UTC) when cooling and the resulting increase of relative humidity are strongest. The temperature changes up to 750 m in the PBL are largely controlled by the interaction of cold air advection and turbulent diffusion. The contributions of all other processes are orders of magnitude smaller. At 14 UTC, in the cloud-free phase, the air cools by about 1 K h^{-1}. This cooling is caused by cold air advection with a southwesterly near-surface wind from the sea breeze and the upslope flow yielding an advective temperature tendency about -2.5 to -4 K h^{-1}. This negative advective temperature tendency is countered by a turbulent temperature tendency reaching approximately +1.5 to +3 K h^{-1} in the cloud-free phase.

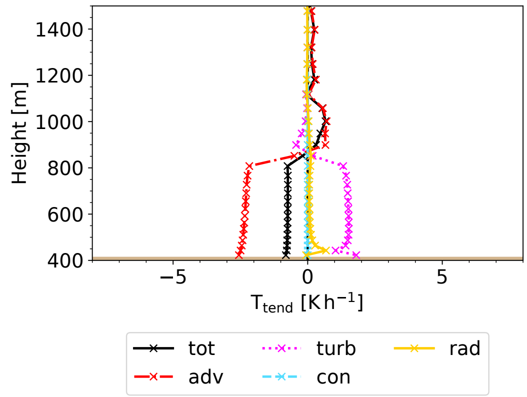

(a) Gobabeb (14 UTC)

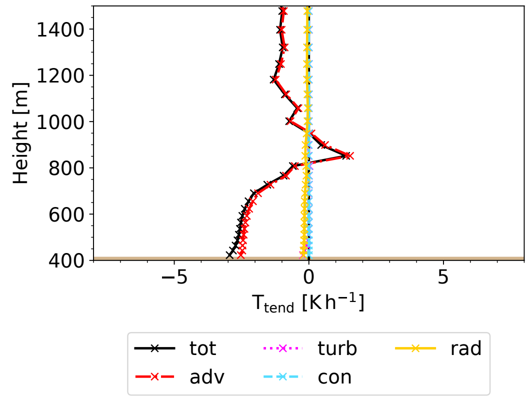

(b) Gobabeb (17 UTC)

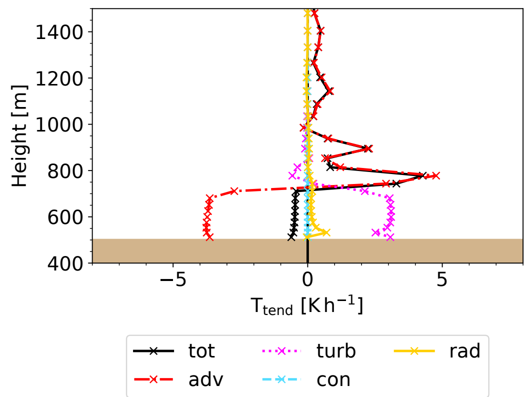

(c) Vogelfederberg (14 UTC)

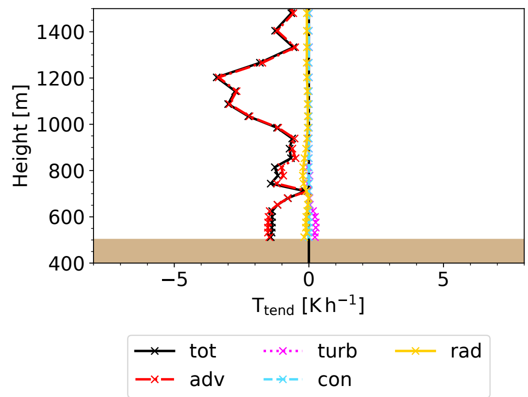

(d) Vogelfederberg (17 UTC)

Figure 5.12: Vertical profiles of temperature tendencies T_{tend} [K h^{-1}] in (a, b) Gobabeb and (c, d) Vogelfederberg on 18 September 2017 at (a, c) 14 UTC and (b, d) 17 UTC; tot: total tendency, adv: advection, turb: turbulent mixing, con: condensation/evaporation, rad: radiation. Brown areas mark the terrain height.

Around 17 UTC after sunset, the turbulent warming has nearly vanished while advective cooling around -1.5 to -3 K h^{-1} is still present. So during the extension phase the temperature changes in the boundary layer are almost exclusively caused by advection. Above the PBL the temperature tendencies are driven by advection.

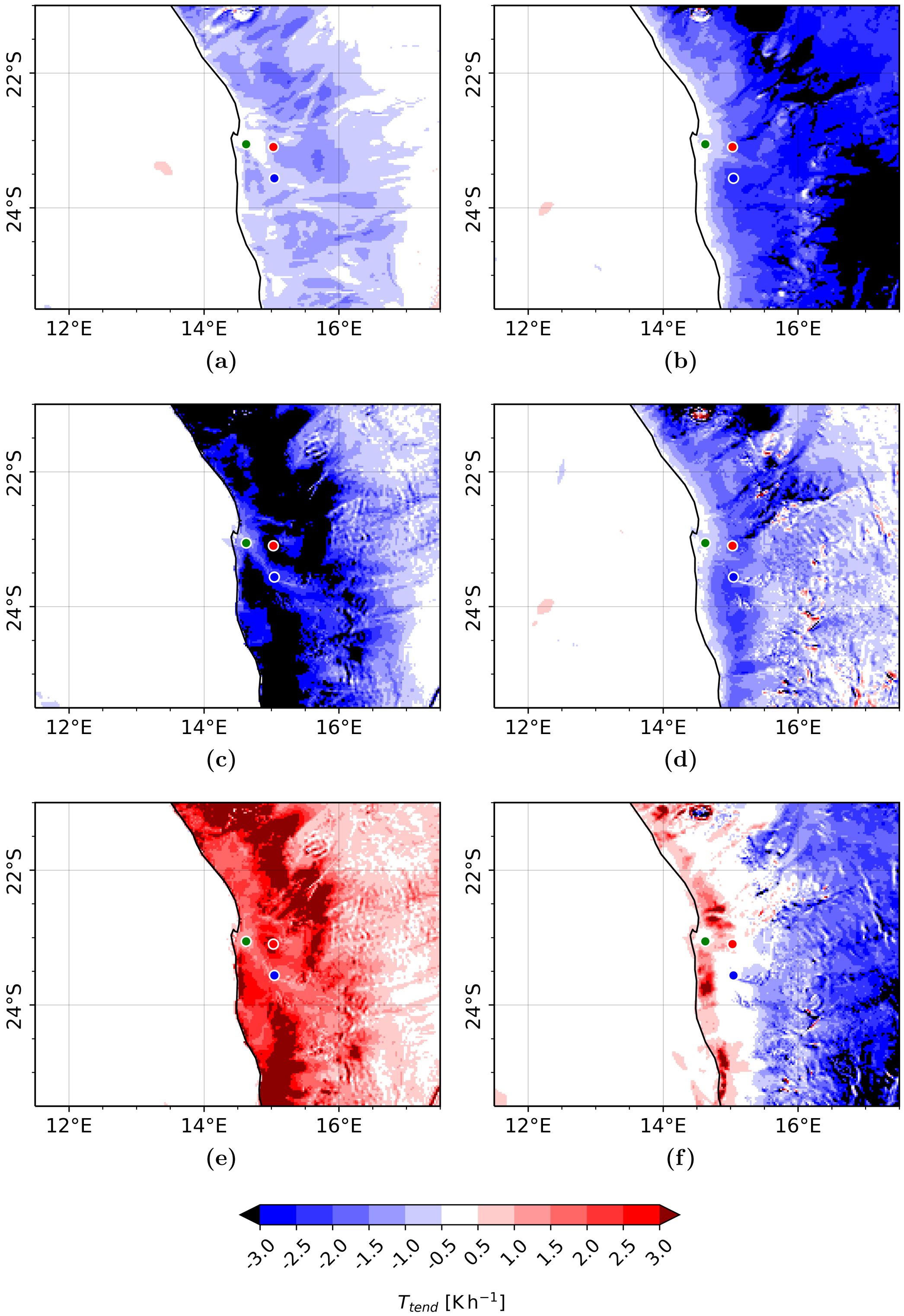

Figure 5.13: Spatial distribution of (a, b) total temperature tendency [K h^{-1}], temperature tendencies [K h^{-1}] due to (c, d) advection and (e, f) turbulent mixing on 18 September 2017 at 14 UTC (left) and 17 UTC (right), respectively. Marked locations are Coastal Met (green), Vogelfederberg (red) and Gobabeb (blue).

The results obtained for Gobabeb and Vogelfederberg are representative for large parts of the coastal plain as the spatial distribution of the temperature tendencies in total and due to turbulent diffusion and advection in the lowest model layer demonstrates (Fig. 5.13). In the cloud-free phase, the cooling takes place in a wide stripe almost parallel to the shore reaching approximately 200 km inland (Fig. 5.13 (a)). Almost the complete land areas in the model domain are affected by advective cooling which decreases with increasing distance from the coast due to the decreasing temperature gradient (Fig. 5.13 (c)). Where the cold air is advected over the warm land surface it is heated from below by the sensible heat flux causing turbulent mixing during daytime (Fig. 5.13 (e)).
After sunset, the turbulent warming has almost vanished in a stripe approximately 100 km from the coast while advective cooling still continues (Fig. 5.13 (d) and (f)). One has to note, that the positive turbulent temperature tendency close to the coast compensates evaporative cooling below the clouds.
Farther inland in the Great Escarpment and on the inner plateau turbulent diffusion cools the air close to the ground due to a negative sensible heat flux directed towards the ground. In these areas, cooling by turbulent diffusion explains the largest part of the total cooling. Despite of cooling, no saturation will be reached in the Great Escarpment and on the inner plateau due to the small values of relative humidity. In these regions, the boundary layer is too dry for fog to form. In the coastal plain, conditions are more favourable for the formation of FLCs due to the advection of cool and moist air during daytime.
The analysis of the contributions of individual processes to the total temperature tendency for the extension phase has shown, that the extension of FLCs is caused by cold air advection. Fog and cloud formation is related to the advection of maritime air masses supplying moisture in the coastal area of the Namib Desert. Also the occurrence of fog in the river valleys is related to the advection of moist maritime air.

The cloud and fog phase

From 21 UTC on, the FLCs extend only slightly further inland while the LWP_{1000} averaged over the model domain still increases (cf. Fig. 5.9) due to an increase of the cloud water content and a vertical growth of the cloud and fog layer (cf. Fig. 5.8). Figure 5.14 shows exemplarily the vertical profiles of virtual potential temperature, specific humidity and relative humidity at 21, 0, and 3 UTC in Gobabeb. In Vogelfederberg the results are very similar and will therefore be omitted in the following. The evolution of the virtual potential temperature profiles displayed in Figure 5.14 (a) illustrates the development of a $\sim$200 m deep well-mixed fog layer between 21 and 0 UTC. As the fog develops, the cooling in the fog layer decreases because the fog inhibits the radiative cooling of the surface and the station is surrounded by a rather homogeneous cool air mass.
The evolution of specific humidity reveals that specific humidity decreases in the fog layer, whereas it increases between 700 and 800 m (above fog top). Due to the increase above fog top a peak with values around 9.5 g kg^{-1} develops in the profile of specific humidity which is eroded once the fog grows into that layer.

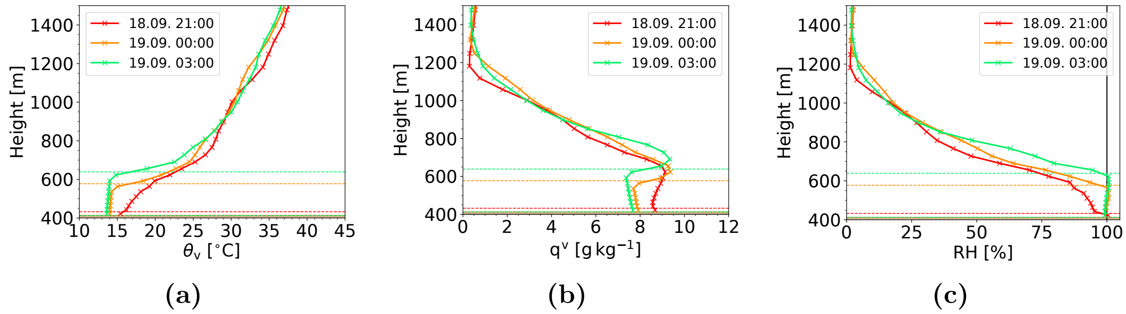

Figure 5.14: Vertical profiles of (a) virtual potential temperature θ_v [°C], (b) specific humidity q^v [g kg^{-1}], and (c) relative humidity RH [%] in Gobabeb (blue marker in Fig. 5.5) at different times in the cloud and fog phase for CS1819. Horizontal dashed lines indicate the layer where the cloud water content is larger than 0.01 g kg^{-1} for the respective time.

The maximum of the specific humidity profile is caused by the advection of moist air with an easterly wind (the affected layers are marked by a red rectangle in Fig. 5.15 (a)) which can be explained as follows: The specific humidity is advected inland during daytime in the PBL with a southwesterly sea breeze and plain-mountain wind. In the evening, the specific humidity is left in the boundary layer and is advected back to the coast with an easterly wind above the layer with maritime air masses (cf. Fig. 5.15 (a) and (b)). Later in the night, the wind turns to a southeasterly direction and specific humidity is advected alongshore. Note, that the largest changes of specific humidity occur **above** the maximum of specific humidity which is also evident from Figure 5.14 (b).

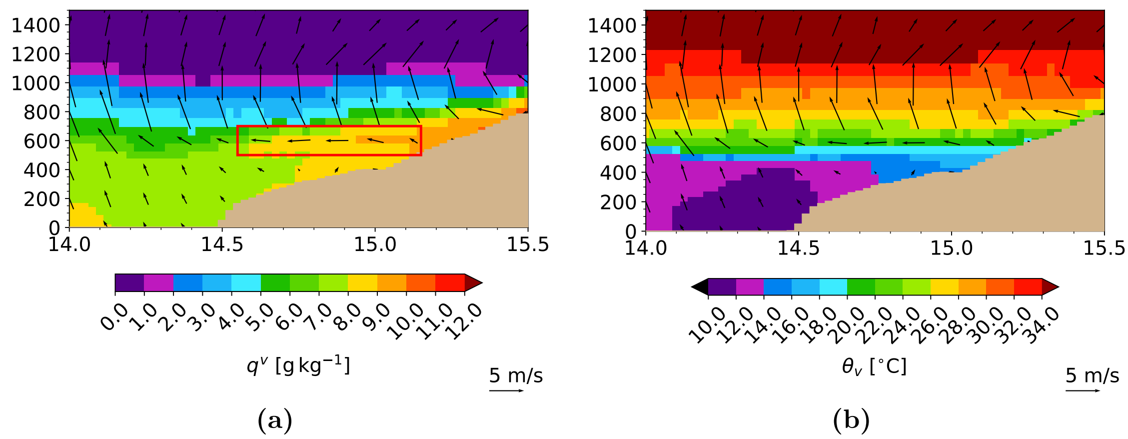

Figure 5.15: Vertical cross sections of (a) specific humidity q^v [g kg^{-1}] and (b) virtual potential temperature θ_v [°C] with **horizontal** wind (arrows) for CS1819 at 21 UTC from [23.56 °S, 14 °E] to [23.56 °S, 15.5 °E]. The red rectangle is referred to in the text. Brown areas mark the terrain height.

As expected from the surface-based inversion, the relative humidity profile in Gobabeb simulated by COSMO-FOG shows a very shallow saturated layer confined to the lowest model layer at 21 UTC. As a consequence, the fog phase starts with a very shallow ground fog in Gobabeb (cf. Fig. 5.8). During the night, an approximately 200 m deep saturated layer develops due to cooling which causes the strong increase of fog top height between 21 and 0 UTC (cf. Fig. 5.8). The increase of fog top height is not restricted to Gobabeb, but occurs at several locations. This explains the ongoing increase of the domain-averaged LWP_{1000} in the cloud and fog phase while the cloud coverage is nearly constant (cf. Fig. 5.9). As in the extension phase, the relative humidity stays constant at values below 10 % above 1200 m.

In order to get more insight into the processes contributing to the maintenance and growth of the FLCs, the tendencies resulting from the heat equation and the balance equation of specific humidity will be analysed.
Figure 5.16 displays the temperature and specific humidity tendencies in Gobabeb at 0 UTC. The processes from the heat equation and the balance equation for specific humidity occurring in the fog layer are the same as for the simulation of a homogeneous marine stratus (cf. Chap. 4). Departing from the simulation of a horizontally homogeneous marine stratus, an additional advective temperature tendency occurs which is not balanced (Fig. 5.16 (a)). Thus no quasi equilibrium is reached. In the undersaturated area of the fog, the evaporative cooling is slightly overcompensated by warming due to turbulent diffusion. Nevertheless, the total temperature tendency in that region is negative due to the advection of cold air with a southwesterly wind which turns to a southerly direction after 0 UTC when the South Atlantic Anticyclone approaches to the Namibian coast. In the saturated upper part of the cloud, the latent heat release due to condensation is overcompensated by the sum of turbulent diffusion and radiative cooling. An additional contribution by cold air advection further contributes to a negative total temperature tendency. The strongest cold air advection occurs at fog top with a southeasterly wind which, combined with longwave radiative cooling, causes strong cooling there (cf. Fig. 5.14). With roughly $7\,\mathrm{K\,h^{-1}}$ the tendency by radiative cooling at fog top is smaller than in the idealised case study. This is caused by the continuous growth of fog top and also occurred for the idealised cases when the cloud grew in the next layer (for the two simulations with high resolution). Above fog top, cold air advection occurs and causes a negative total temperature tendency.
As for temperature, an advective tendency occurs also for specific humidity. The advection of drier air in the boundary layer causes a decrease of specific humidity in most parts of the fog layer (Fig. 5.16 (b)). In the undersaturated area of the fog, the increase of specific humidity by evaporation is compensated by turbulent diffusion. In the uppermost part of the supersaturated region of the fog, the loss of specific humidity by condensation is not fully compensated by turbulent diffusion, resulting in a total decrease of specific humidity there. Between 700 and 1000 m, the advection of moist air with an easterly to southeasterly wind results in the increase of specific humidity discussed before (cf. Fig. 5.14 and 5.15).

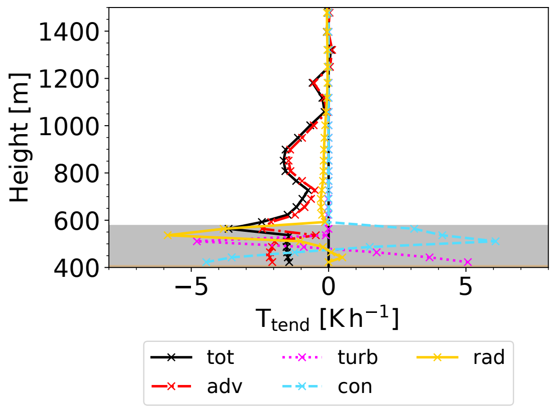

(a)

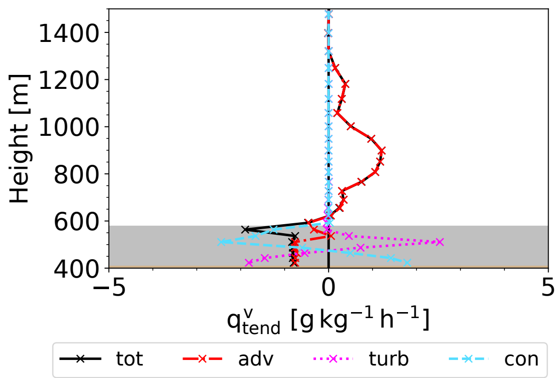

(b)

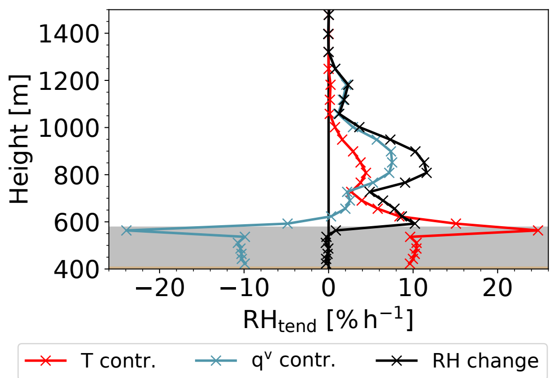

(c)

Figure 5.16: Vertical profiles of (a) temperature (T_{tend} [K h^{-1}]) and (b) specific humidity (q^v_{tend} [g kg^{-1} h^{-1}]) tendencies in Gobabeb on 19 September 2017, 0 UTC; tot: total tendency, adv: advection, turb: turbulent mixing, con: condensation/evaporation, rad: radiation. (c) Vertical profiles of relative humidity change [% h^{-1}] and its individual contributions by temperature and specific humidity determined using Equation 2.1 in Gobabeb. Shaded grey areas indicate where the cloud water content is larger than 0.01 g kg^{-1}.

Due to the decrease of temperature and specific humidity in the fog layer with competing effects on relative humidity, the inspection of relative humidity tendencies is especially interesting. As can be seen from Figure 5.16 (c), the negative relative humidity tendency due to the decrease of specific humidity and the positive relative humidity tendency due to cooling balance each other in most parts of the fog layer. Close to fog top, the negative relative humidity tendency by the decrease of specific humidity is overcompensated by the positive relative humidity tendency due to temperature yielding an increase of relative humidity by cooling.
So the analysis of the heat and moisture budget reveals that the increase of relative humidity around the cloud top is largely due to radiative cooling at the cloud top and the advection of cooler air. These processes cause the vertical growth and a slight eastward extension of the fog during the cloud and fog phase.

The dissipation phase

The profiles of the virtual potential temperature in Gobabeb depicted in Figure 5.17 (a) show the warming of the PBL after sunrise. In Gobabeb, the increase of the virtual potential temperature is not limited to the boundary layer but also occurs in the free troposphere. Other than expected, the boundary layer height decreases by about 100 m after sunrise. This hints at the contribution of additional dynamic processes besides heating by surface fluxes and turbulent diffusion.

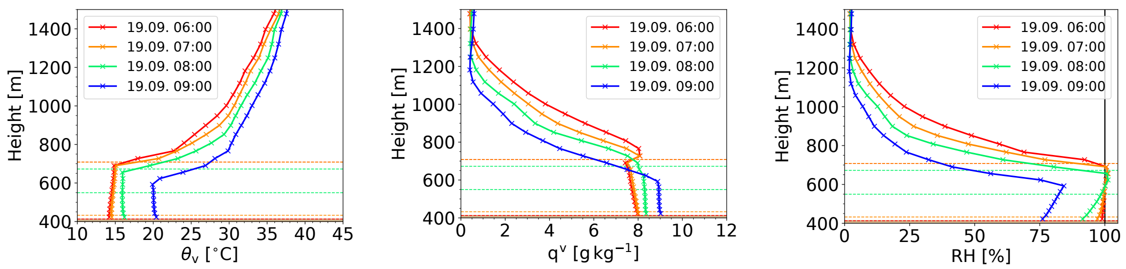

(a) (b) (c)

Figure 5.17: As Figure 5.14, but at different times in the dissipation phase for CS1819.

The specific humidity decreases between 600 and 1300 m from 6 to 9 UTC (Fig. 5.17 (b)) and increases in the PBL. The relative humidity decreases simultaneously at fog top and from fog base resulting in a lifting of fog base and a thinning of the fog. Between 7 and 8 UTC, the strongest decrease of relative humidity occurs from the bottom of the fog/cloud, so the fog dissipation mainly progresses from the ground upwards. Due to the warming, the relative humidity decreases by about 10 to 20 % and the cloud fully dissipates between 8 and 9 UTC in Gobabeb. As in the other phases, the relative humidity above 1200 m stays constant below 10 %.
In order to figure out the processes contributing to fog and cloud dissipation, the budgets of temperature and specific humidity are investigated. Figure 5.18 exemplarily displays the profiles of temperature and specific humidity tendencies in Gobabeb at 7:15 UTC, when the cloud already starts to thin and the processes are well es-

tablished. After sunrise, the absorption of incoming solar radiation at the surface starts convective surface fluxes driving turbulent mixing in the boundary layer. In Gobabeb, the temperature tendency due to turbulent mixing is around $5\,\mathrm{K\,h^{-1}}$ at the ground but is partly compensated by evaporative cooling (cf. Fig. 5.18 (a)). The warming enhances evaporation resulting in a decrease of cloud water content while specific humidity increases (cf. Fig. 5.18 (b)). The warming is further enhanced by slight warm air advection. An easterly wind advects air from inland areas where clouds already dissolved and heating of near-surface air by surface fluxes is stronger. The warming is further enhanced by dry adiabatic warming of the air flowing down the Great Escarpment. This warm air advection accelerates the fog dissipation.
The warming by advection and turbulent diffusion causes a decrease of the relative humidity by approximately 6–8 $\%\,\mathrm{h^{-1}}$ in the lower 200 m above ground level which is partly counteracted by the increase of specific humidity due to evaporation (cf. Fig. 5.18 (b, c)). The warming dominates resulting in a total decrease of the relative humidity by $6\,\%\,\mathrm{h^{-1}}$ at cloud base causing the lifting of the fog from the ground.
Ongoing sedimentation and evaporation result in an optically thinner cloud which gets more transparent for solar radiation. The optically thinner cloud and the intensifying sun increase the heating by shortwave solar radiation in the lower part of the cloud and at the ground. The feedbacks between these processes act together to rapidly dissipate the cloud after sunrise.
Normally, the increase of turbulence after sunrise would lead to an increase of cloud-top entrainment and of the inversion height. In contrast, the height of the inverion decreases by about 100 m between 6 and 9 UTC. Above the cloud-topped boundary layer, warm, dry air masses are advected between 700 and 1400 m height with an easterly and southeasterly wind. This is evident from the positive temperature tendency and the negative tendency of specific humidity by advection in Figure 5.18 (a) and (b). This advection of warmer and drier air at cloud top and above causes a strong decrease of the relative humidity up to $40\,\%\,\mathrm{h^{-1}}$.
Until 12 UTC, similar atmospheric conditions as on the previous day are obtained with maritime air masses being transported inland with a southwesterly breeze and heated from below by the land surface.

The analysis of the case study CS1819 reveals important processes controlling the life cycle of FLCs in the Namib Desert. The formation of FLCs is caused by the advection of cool and moist air masses interacting with turbulent mixing. The vertical growth and a slight eastward extension results from radiative cooling at fog/cloud top and the advection of cooler air. The dissipation of FLCs is caused by solar radiation initiating surface fluxes and, thus, turbulent mixing. The dissipation is enhanced by the advection of warm air.

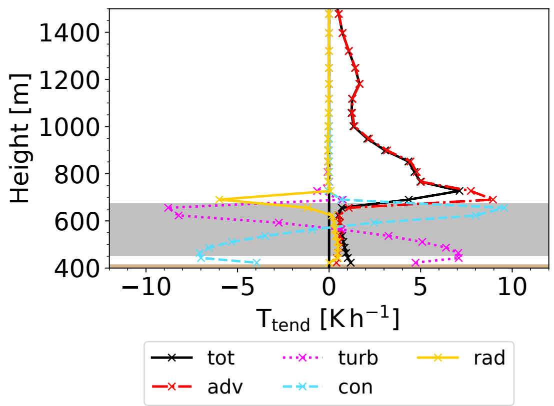

(a)

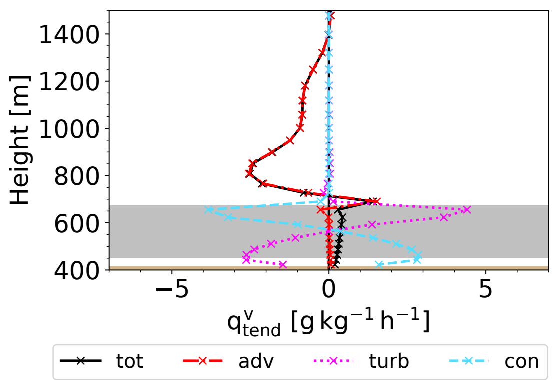

(b)

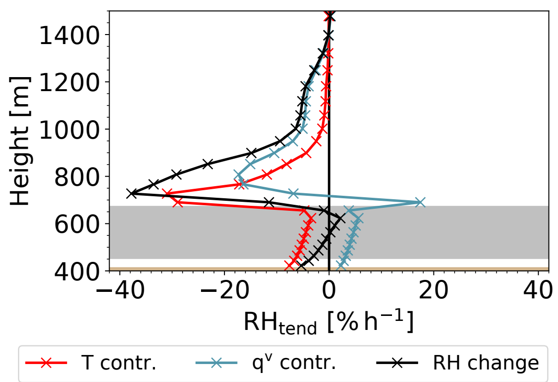

(c)

Figure 5.18: As Figure 5.16, but on 19 September 2017, 7:15 UTC.

5.3 Other factors influencing fog and low stratiform clouds

In the nights from 20 to 21, 23 to 24 and 27 to 28 September 2017 the central Namib experienced inland reaching fog events which reveal the role of processes contributing to the spatial patterns and temporal evolution of FLCs additional to the processes discussed in the previous section. Similar to the preceding case study, these fog events will be put into the large-scale synoptic context before the spatial and temporal patterns of FLCs and the contributing processes will be analysed.

5.3.1 Synoptic conditions and meteorological situation

On 20 and 23 September 2017, the large-scale subsidence within the subtropical high-pressure belt causes stable atmospheric conditions suppressing cloud development above the PBL as for 18 September. Thus, again the whole southern African continent shows clear skies except for the eastern parts close to the Indian Ocean being influenced by smaller-scale low-pressure systems on both days. The heating of near-surface air results in a thermally induced low surface pressure extending from the west coast of Namibia towards central Africa[8]. At the 500 hPa level, a high-pressure ridge is located over the southern African continent.
Both, on 20 and 23 September 2017, a surface high-pressure system of the subtropical high-pressure belt has shifted from the Atlantic Ocean to the east compared to 18 September. The eastward shift of the maximum in surface pressure results in a northeasterly flow over large parts of the southern African continent. This northeasterly flow causes warm air advection over the western and southern parts of Namibia and above the MBL over the Atlantic Ocean alongshore the Namibian coast. As a result of the warm air advection, the temperature at the 850 hPa level and the near-surface temperature in Namibia are higher compared to 18 September. The temperature at 850 hPa reaches more than 25 °C over the ocean along the Namibian coast. For CS2021 and CS2324, the soil temperature of 40 and 45 °C is approximately 10 °C higher than for the other two case studies with around 35 °C. The higher surface temperature causes stronger heating of the near-surface air by surface fluxes resulting in a stronger temperature increase with increasing distance from the coast than for CS1819. The near-surface temperature widely reaches around 30 to 35 °C in the Great Escarpment and in the interior of Namibia. Close to the coast, a thermally and topographically driven southwesterly wind advects cool and moist maritime air masses inland (Fig. 5.19 (a)).
After sunset, the temperature quickly decreases to 10–14 °C in a stripe of 60 km width alongshore while inland the near-surface temperature still widely reaches 25–30 °C. During night, the temperature at 850 hPa still reaches 25 °C and more at the Namibian coast. Due to the advection of warm air with the northeasterly wind and the cooling of inland areas during night, the highest temperature occurs in the western and southwestern part of Namibia rather than to the northeast at night. This relocation of the maximum heat results in a displacement of the thermally induced

[8] Additional figures showing the synoptic situation and the weather situation of CS2021, CS2324, and CS2728 are provided in the appendix.

low surface pressure. An extended zone of low surface pressure is located alongshore the Namibian coast during both nights, on 20 to 21 and 23 to 24 September. At the eastern flank of the relocated low surface pressure a northwesterly wind blows along the Namibian coast (Fig. 5.19 (b) and (c)) while an easterly wind blows in the Great Escarpment.
The maximum surface pressure of the South Atlantic Anticyclone decreases during night and the high-pressure ridge at 500 hPa attenuates.

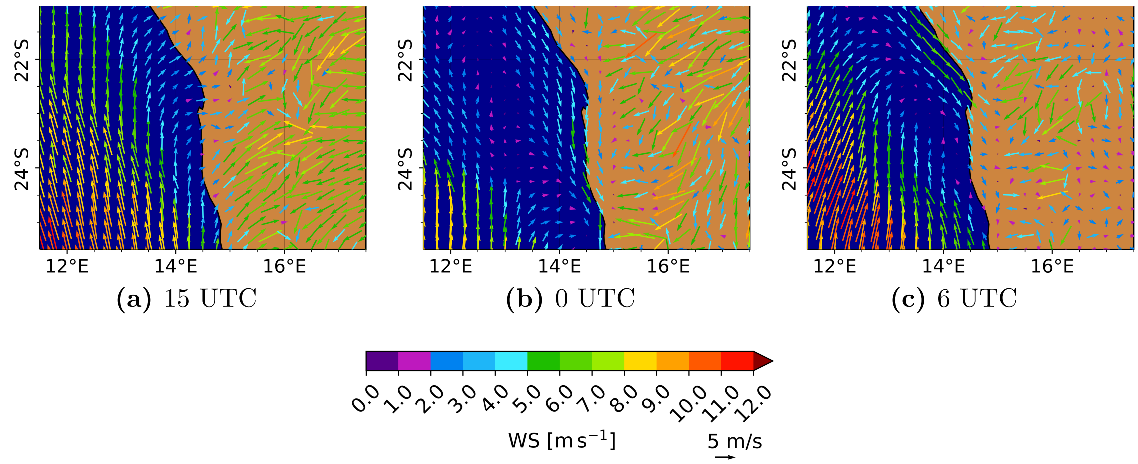

Figure 5.19: Spatial distribution of horizontal wind WS [m s^{-1}] in the lowest model layer for (a) 20 September, 15 UTC, (b) 21 September, 0 UTC, and (c) 24 September, 6 UTC.

On 24 September an upper level trough approaches the African continent which passes Cape Town on 25 and 26 September. With the passage of the trough, cold air is advected from southerly directions to the southern part of Namibia. The temperature at the 850 hPa pressure level decreases from around 30 °C for CS2021 and CS2324 to around 20 °C over southern Namibia for CS2728. This results in a lower temperature in the south of Namibia where the temperature rises to around 25–30 °C on 27 September. The highest temperature is reached in the northeast of Namibia as for 18 September raising to more than 30 °C. As for all case studies, a southwesterly and westerly wind blows in the coastal plain and a southwesterly wind in the Great Escarpment during daytime which advects maritime air masses onshore. Due to the lower temperature after the passage of the low, the diabatic heating of this maritime air masses is weaker than for 20 and 23 September. As a result the stripe with moderate near-surface temperature along the coastline is wider at daytime than for 20 and 23 September. During nighttime temperature decreases to 15–20 °C in wide parts of Namibia. In the coastal area the temperature decreases to 10–14 °C.

5.3.2 Spatial and temporal evolution of fog and low stratiform clouds

As for CS1819, the spatial patterns and temporal evolution of FLCs simulated by COSMO-FOG are analysed by means of the LWP_{1000}. In order to estimate the quality of the model simulation with respect to the spatial distribution of FLCs, the simulated cloud cover is visually compared to the RGB composite combined with FogNet measurements as for 18 September.

Horizontal distribution of fog and low-level clouds

Similarly to Figure 5.5, Figure 5.20 displays the LWP_{1000} below 1000 m and the RGB composite combined with FogNet measurements. Figure 5.20 shows the time with maximum horizontal extent of FLCs for CS2021, the significantly smaller extent of FLCs for CS2324 at a similar time, and a time where COSMO-FOG underestimates the cloud cover for CS2728.

The spatial distribution of fog and low-level clouds on 20 and 21 September 2017 is very similar to 18 September 2017. On 21 September at 3 UTC, FLCs are located above the Atlantic Ocean and reach 50 to 60 km inland (Fig. 5.20(a)). The FLCs do not reach as far inland as for CS1819. They scarcely reach the FogNet stations on 21 September at 3 UTC (see red and blue point in Fig. 5.20(a)). Finally, the low stratiform clouds intersect with the land surface at a height of 200 m a.s.l. which is lower than for CS1819. The eastward extension stops when the fog reaches approximately 500 m a.s.l. In the south of the model domain, there is a stripe of sea fog above the Atlantic Ocean in the vicinity of the coast.

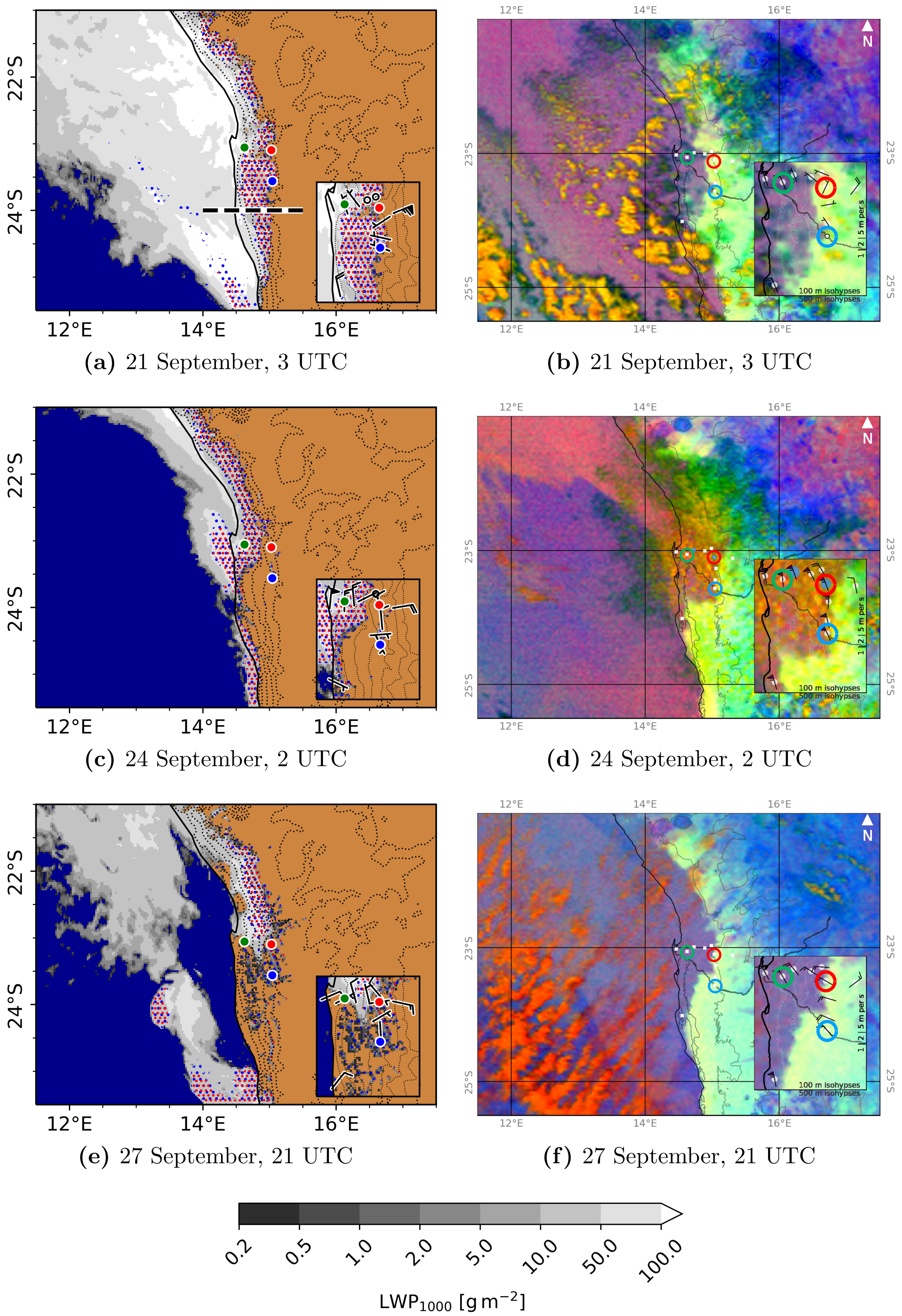

(a) 21 September, 3 UTC **(b)** 21 September, 3 UTC

(c) 24 September, 2 UTC **(d)** 24 September, 2 UTC

(e) 27 September, 21 UTC **(f)** 27 September, 21 UTC

Figure 5.20: Left: as Figure 5.5, right: as Figure 5.6, but for (a, b) CS2021, (c, d) CS2324, and (e, f) CS2728. Dark magenta (b, d) and violet (f) colors mark FLCs. Courtesy of Dr. Robert Spirig (Department of Environmental Sciences, University of Basel, now at Departement Umweltsystemwissenschaften, ETH Zürich). The cross sections shown in Figure 5.21 are indicated as dashed line.

The vertical cross section of the cloud water content depicted in Figure 5.21 reveals that the cloud base and top height are smaller compared to CS1819 leading to a lower intercept of the stratiform cloud with the terrain than in CS1819.

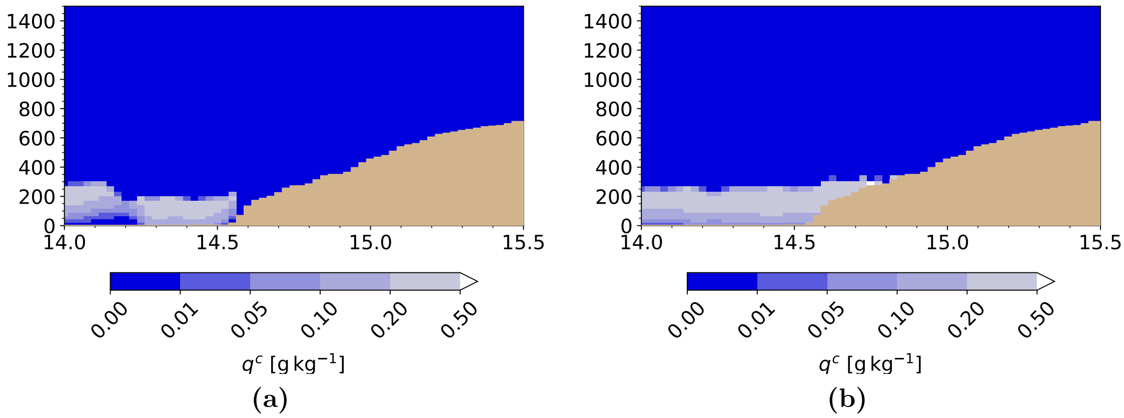

Figure 5.21: Vertical cross sections of cloud water content q^c [g kg^{-1}] for 20 September 2017 at (a) 18 UTC and (b) 22 UTC from [24 °S,14.0 °E] to [24 °S,15.5 °E] (dashed line in Fig. 5.20 (a)). Brown areas mark the terrain height.

The cloud base height simulated by COSMO-FOG is lower than in reality[9].
Figure 5.20(b) displays the RGB composite combined with FogNet measurements for 21 September at 3 UTC. In contrast to CS1819, some mid level clouds (yellow areas) above the Atlantic Ocean slightly hinder the satellite observations of FLCs (purple areas). The eastward extension of the simulated FLCs is in good accordance with the satellite retrieval.
On 23 and 24 September 2017, the model simulates a stripe of FLCs which follows the coastline at 2 UTC (Fig. 5.20(c)) and is considerable smaller than the cloud blanket on 19 and 21 September. Furthermore, ground fog is simulated from a height of 100 m a.s.l. on, while in the other case studies it started much higher. The lower interception of the cloud with the terrain of the Great Escarpment and the occurrence of sea fog along the coast south of Walvis Bay hints at a lower cloud base compared to the other case studies. The simulated stripe of FLCs is in well accordance with the satellite observation displayed in Figure 5.20(d), although the extent of the fog and cloud cover is underestimated in the central Namib Desert and above the Atlantic Ocean north of 22 °S.
On 27 September 2017 around 21 UTC, an almost cloud free gap stays between the clouds above the ocean and onshore (Fig. 5.20(e)). The clouds start to intercept with the terrain above 200–300 m a.s.l. and the eastward extension of the fog and clouds stops at approximately 500 m a.s.l. Similar to CS1819, patchy and rather thin ground fog forms in the coastal area of the Namib Desert independent of the large areas with FLCs.
Although some mid-level clouds (red areas) hinder the observation of FLCs (purple areas) by satellite, the visual comparison of the model results to the satellite image

[9]Additional figures showing ceilometer measurements can be found in the appendix.

displayed in Figure 5.20(f) shows that the model strongly underestimates the cloud cover over ocean areas. The extent of FLCs over land areas simulated by COSMO-FOG is in rather well agreement with the satellite observation.

Diurnal cycle of fog and low-level clouds

Figure 5.22 illustrates the area covered by FLCs in total and divided into ocean and land areas for the three case studies. The total area covered by clouds is minimal between 15 and 18 UTC. For CS2324 and CS2728, it decreases due to the cloud dissolution over the ocean until 18 UTC. After 18 UTC, the area covered by clouds over the ocean and in total increases until the next morning for all three case studies. For CS2728 the increase of the area covered by clouds is strongest. Until 6 UTC it increases by a factor of five. Between 6 and 9 UTC the total cloud area decreases due to the dissipation over land areas. The decrease is accelerated if the cloud area over the ocean decreases as well.

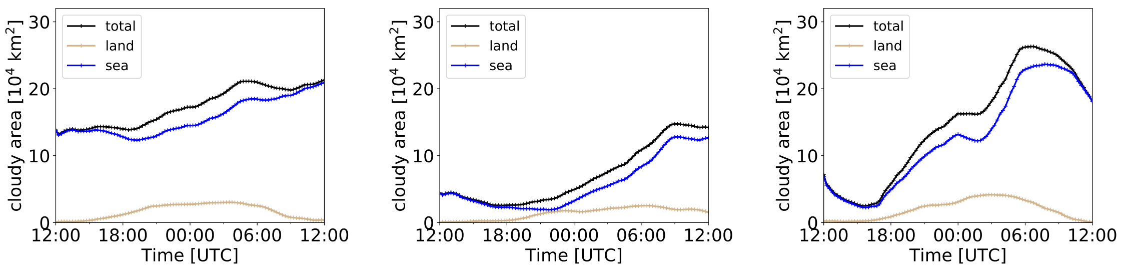

(a) 20 and 21 September **(b)** 23 and 24 September **(c)** 27 and 28 September

Figure 5.22: Time series of simulated area covered by FLCs [km^2] for the whole domain and divided into land and ocean areas for (a) CS2021, (b) CS2324, and (c) CS2728.

A distinct life cycle of FLCs is evident over land areas. The temporal development of the FLC area over land is quite similar to CS1819 for all case studies, but especially for CS2021. On 20 September 2017, the area covered by FLCs over land is minimal in the afternoon when the low-level clouds are confined to the ocean and starts to increase when the clouds proceed eastwards inland like a front around 15 UTC (cf. Fig. 5.22(a)). The extension of clouds lasts until around 21 UTC (extension phase). Between 21 and 4 UTC the cloud cover is almost constant (cloud and fog phase). The dissolution is also similar to CS1819. Starting from 4 UTC the fog lifts from the ground before the stratiform clouds break up. The lifting of the ground fog has almost no effect on the area covered by fog and clouds over land since the area covered by FLCs does not distinguish between fog and low clouds. After 5 UTC the cloud area decreases more rapidly when the dissolution gradually starts and accelerates further after 6 UTC (dissipation phase). Until 11 UTC the stratiform clouds widely dissolve and the cloud area reaches the baseline of the day before. So the general life cycle of FLCs, i.e. the cloud-free phase, the extension phase, the cloud and fog phase and the dissipation phase, is identical to CS1819.
However, the area covered by FLCs over land and ocean is overall smaller. This is

due to the smaller extension of the cloud blanket over the ocean compared to CS1819 until the clouds spread during the night. In addition, the FLCs do not reach as far inland to the east as for CS1819.
The visual comparison of model results to the satellite images reveals that the model captures the diurnal cycle of FLCs quite well for CS2021 although COSMO-FOG slightly underestimates the horizontal extension of FLCs for that case study in the first half of the night. In Gobabeb, e.g., COSMO-FOG simulates a ground fog from 0 UTC on, while ground fog was observed already from 21 UTC on[10,11].

For CS2324, the cloudy area over land stays almost constant until 18 UTC (cf. Fig. 5.22(b)). Its increase in the extension phase starts three hours later than for CS1819 and CS2021. First clouds form in a small stripe in the flat coastal area of the Namib Desert north of Walvis Bay in direct vicinity to the Atlantic Ocean. Until 23 UTC FLCs spread eastward farther onshore and southwards. This increase of cloud coverage onshore dominates the total cloud coverage until 23 UTC while the cloud coverage over ocean areas is nearly constant at its minimum. This is because the cloud in the model simulation is restricted to the coastal area north of Walvis Bay while almost no clouds have formed over the Atlantic Ocean. The formation of FLCs only over land areas has not been observed but results from an underestimation of the cloud cover over the ocean by COSMO-FOG in the first half of the night.
In the cloud and fog phase after 23 UTC, the cloud coverage over land increases slightly until it reaches its maximum around 7 UTC. As for CS2021 the maximum eastward extension is smaller than for CS1819. The maximum inland extent of FLCs is slightly underestimated by the model simulation. During the cloud and fog phase, clouds form over the Atlantic Ocean in the second half of the night and the cloud cover over the ocean is in agreement with satellite observations.
In the dissipation phase, the cloud coverage decreases between 8 and 12 UTC but in contrast to CS1819 and CS2021, the cloudy area over land does not reach the level of the day before. This results from an approximately 20–40 km wide stripe of persistent clouds in the vicinity of the coast which cannot be confirmed by the satellite observation.
On 27 September 2017 at 15 UTC, the area covered by clouds is very similar to CS2324 (cf. Fig. 5.22(b) and Fig. 5.22(c)). Cloud formation in the model starts spatially independent over the ocean and in the coastal area north of Walvis Bay around 16 UTC. Departing from the other case studies the extension phase is twofold for CS2728. Between 15 and 18 UTC, FLCs start to extend onshore. This first extension phase lasts until 21 UTC. Between 21 and 0 UTC, the FLC area over land is almost constant. During that time shallow ground fog thickens which does not impact on the area covered by clouds since ground fog is already included in the cloudy area. Until 0 UTC, rather coherent and thick FLCs are simulated onshore. The extension of FLCs continues after 0 UTC until approximately 2 UTC. During that time, the FLCs spread slightly further eastward. The FLCs do not penetrate eastwards as far as for CS1819 but wider than for CS2021 and CS2324 as can be

[10] Additional figures displaying ceilometer measurements for CS2021 are shown in the appendix.
[11] Supplementary figures of this subsection showing simulated and observed cloud cover can be found in the appendix.

seen from the land area covered by FLCs being smaller (larger) than for CS1819 (CS2021 and CS2324). Until 4 UTC, the land area covered by FLCs stays more or less constant (cloud and fog phase), before the dissipation phase starts with the decrease of the cloud covered land area. Until 12 UTC all the clouds over land dissolve and the land area covered by FLCs reaches the baseline of the day before as for CS1819 and CS2021. The cloud deck over the Atlantic Ocean thins and appears more patchy as the decrease of the area covered by FLCs over the ocean shows.
The visual comparison of the model results to satellite images shows that the model underestimates the cloud cover over the ocean until 4 UTC, while the extent of FLCs over land areas simulated by COSMO-FOG is in rather well agreement with the satellite observation.
The investigated case studies confirm the general life cycle of FLCs, i.e. the cloud-free phase, the extension phase, the cloud and fog phase and the dissipation phase, which has been identified for CS1819.

5.3.3 Atmospheric conditions and processes influencing fog and low stratiform clouds

The processes contributing to the formation of FLCs in the coastal area of Namibia for the second to fourth test case are very similar to CS1819 (cf. Sec. 5.2.3). Therefore, the following analysis will focus only on the differences between the second to fourth test case and CS1819.

In the previous section it has been shown that the eastward inland extent of the FLCs is smaller for CS2021 and CS2324 compared to CS1819. The atmospheric conditions leading to these differences are analysed in the following.

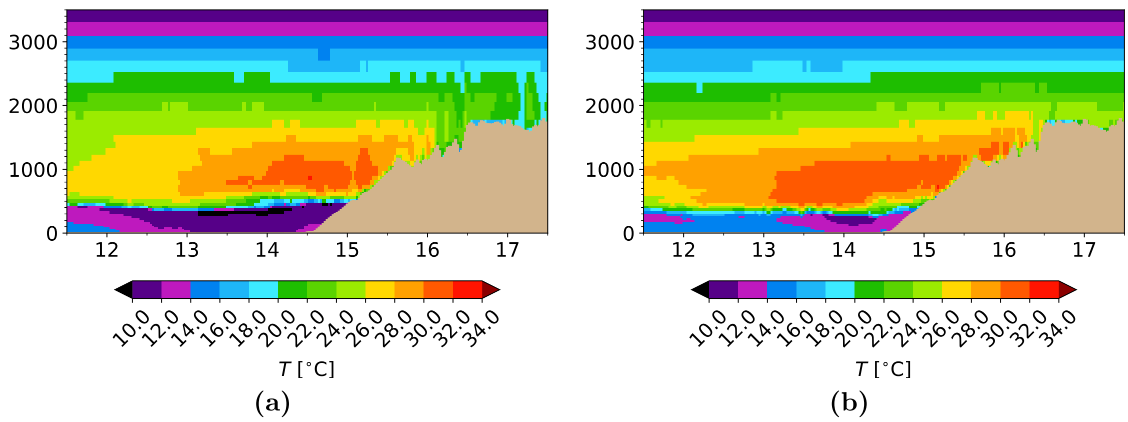

Figure 5.23: Vertical cross sections of temperature T [°C] for (a) 21 September 2017 at 3 UTC and (b) 24 September 2017 at 3 UTC from [23 °S, 11.5 °E] to [23 °S, 17.5 °E]. Brown areas mark the terrain height.

Figure 5.23 displays cross sections of the temperature field in the central Namib at 23 °S on 21 and 24 September at 3 UTC. Air masses with a temperature up to 32 °C are located between 500 and 1500 m a.s.l. This is about 10 °C warmer than for

CS1819[12]. The higher temperature above 500 m compared to 19 September results from the advection of warm air from the African continent with a northeasterly flow (see Sec. 5.3.1). The warm air is further advected alongshore with the southeasterly trade winds. The warm air masses stabilise the boundary layer and result in a strong inversion at 500 m (CS2021) and 300 m (CS2324) a.s.l. The inversion is further enhanced by large-scale subsidence in the subtropical high-pressure belt, especially for CS2324 where the influence of the high-pressure ridge at 500 hPa is stronger than for CS2021. Inland, where the warm air intersects the terrain of the Great Escarpment, COSMO-FOG simulates a strong surface-based inversion (cf. Fig. 5.24).

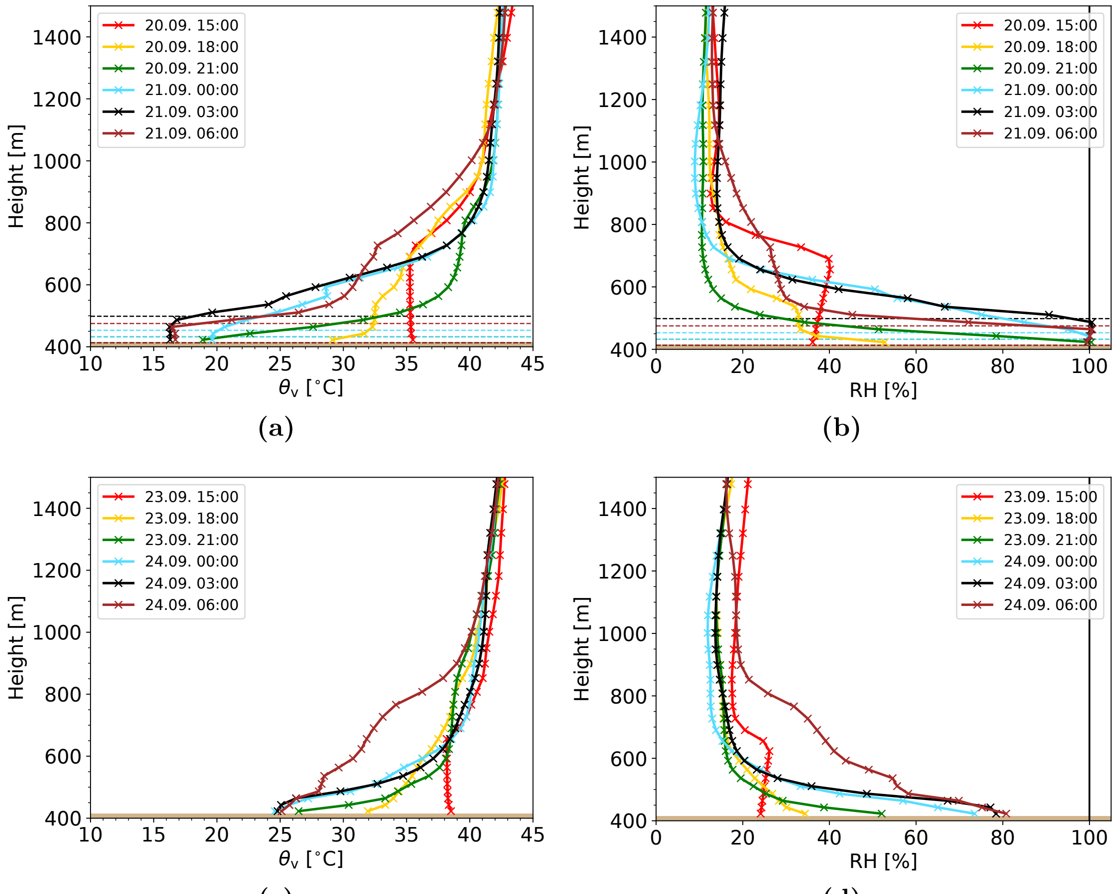

Figure 5.24: Vertical profiles of (a, c) virtual potential temperature θ_v [°C] and (b, d) relative humidity [%] in Gobabeb at different times of CS2021 (top) and CS2324 (bottom). Horizontal dashed lines indicate the layer where the cloud water content is larger than 0.01 g kg^{-1} for the respective time. Brown areas mark the terrain height.

Figure 5.24 shows the profiles of the virtual potential temperature and relative humidity for CS2021 and CS2324 at Gobabeb at approximately 15 °E where the warm air intersects the terrain of the Great Escarpment. In the night from 20 to 21

[12]An additional figure showing a cross section for CS1819 is displayed in the appendix.

September, a strong surface inversion with a temperature jump of more than 20 °C across the first 200 m above the surface develops after the collapse of the roughly 300 m deep well-mixed boundary layer (cf. Fig. 5.24(a)). Until 20 UTC, the cooling of the lowermost model level is due to longwave radiation of the ground, afterwards cold air advection dominates the cooling. Between 400 and 800 m a.s.l., the virtual potential temperature increases until 21 UTC due to large-scale subsidence which is related to the intensifying high-pressure ridge at 500 hPa. Due to the cooling near the surface, the relative humidity reaches saturation in the lowermost model layer (cf. Fig. 5.24(b)). Until 0 UTC, the temperature decreases up to 700 m a.s.l. by cold air advection which decreases the stability in the lowermost part of the atmosphere. In the following hours a flat well-mixed fog layer of 100 m depth develops. The strong increase of temperature in the inversion layer results in a quick decrease of relative humidity to less than 20 % above the boundary layer as can be seen in the profiles of relative humidity (Fig. 5.24(b)).

On 23 September, the virtual potential temperature (around 38 °C) in the 200 m deep well-mixed boundary layer is higher than for 20 September (around 33 °C), while above the inversion layer the virtual potential temperature is with around 40 °C about equal in these two cases (cf. Fig. 5.24(a) and Fig. 5.24(c)). At daytime, this results in a weaker inversion for CS2324. After sunset a strong near-surface inversion develops with a temperature jump slightly less than 20 °C across the lower 200 m of the atmosphere above the ground. Close to the surface, the relative humidity reaches no more than about 80 % (Fig. 5.24(d))

The stable stratification for CS2021 and CS2324 suppresses topographically forced lifting for inland advection and, thus, hinders further extension of cool and moist maritime air masses during night. Figure 5.25 shows the temperature and specific humidity in the lowermost model level at 3 UTC for 21 and 24 September. The cool maritime air is restricted to a small stripe along the coast and a sharp gradient in near-surface temperature and specific humidity occurs where the top of the MBL intersects with the terrain of the Great Escarpment (cf. Fig. 5.23). This sharp gradient marks the boundary between the continental air and the maritime air at the slope of the Great Escarpment where the cool maritime air is trapped below the strong temperature inversion. For CS2021, the temperature is too high and the specific humidity too low for fog to exist or form further east where, due to the mountainous terrain, the lowest model layer is located higher than the trade wind boundary layer height. For CS2324 the near-surface temperature is the limiting factor for fog formation since specific humidity is still available from the advection with a southwesterly wind during daytime.

So the shallow boundary layer with maritime air topped by a strong temperature inversion results in the low cloud height and low cloud interception with the terrain and explains the smaller horizontal extent of FLCs for CS2021 and CS2324. The shallow MBL is caused by the advection of warm air masses from the continent and by large-scale subsidence due to a high-pressure ridge. That way, the large-scale circulation feeds back on the spatial patterns of FLCs in the Namib Desert.

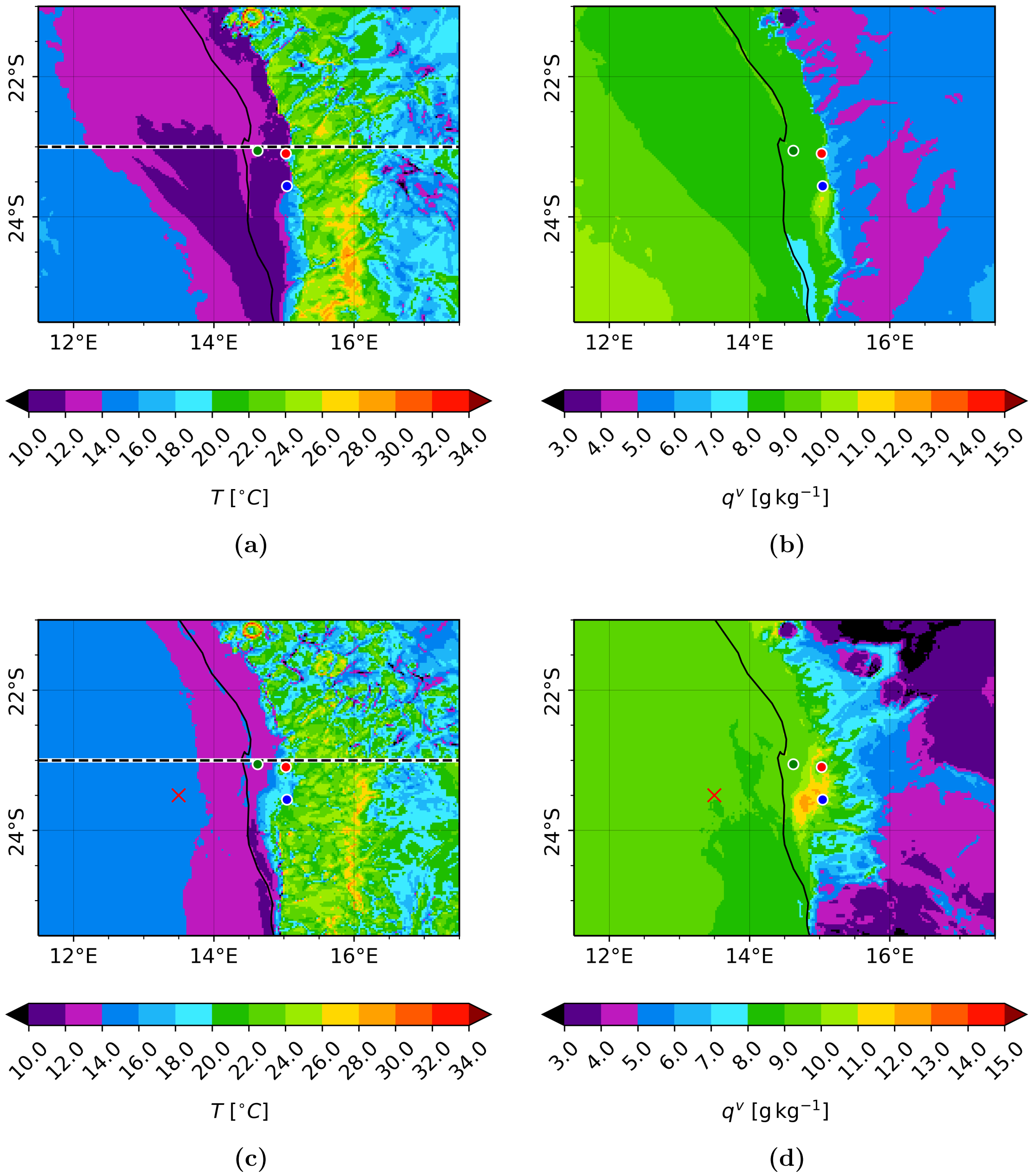

Figure 5.25: Spatial distribution of (a, c) temperature T [°C] and (b, d) specific humidity q^v [g kg^{-1}] in the lowest model layer at 3 UTC for 21 (top) and 24 (bottom) September 2017. The location of the tendency profiles shown in Figure 5.26 is marked by a red x. The cross sections shown in Figure 5.23 are indicated as dashed lines. Marked locations are Coastal Met (green), Vogelfederberg (red) and Gobabeb (blue).

Another difference between CS2324 and CS1819 is the smaller extent of clouds and the cloud formation in the second half of the night above the Atlantic Ocean for CS2324. Due to the eastward shift of the surface high pressure and the resulting northeasterly flow (see Sec. 5.3.1) warm air masses have been advected above the

MBL. Large-scale subsidence further enhances the strong inversion. As a result, the boundary layer is topped by a strong temperature inversion and even more shallow as for CS2021. This inhibits cloud formation over the ocean because for CS2324 the lifting condensation level over the Atlantic Ocean exceeds the height of the inversion base, thus, preventing cloud formation over the ocean. In the second half of the night, clouds start to form over ocean areas.

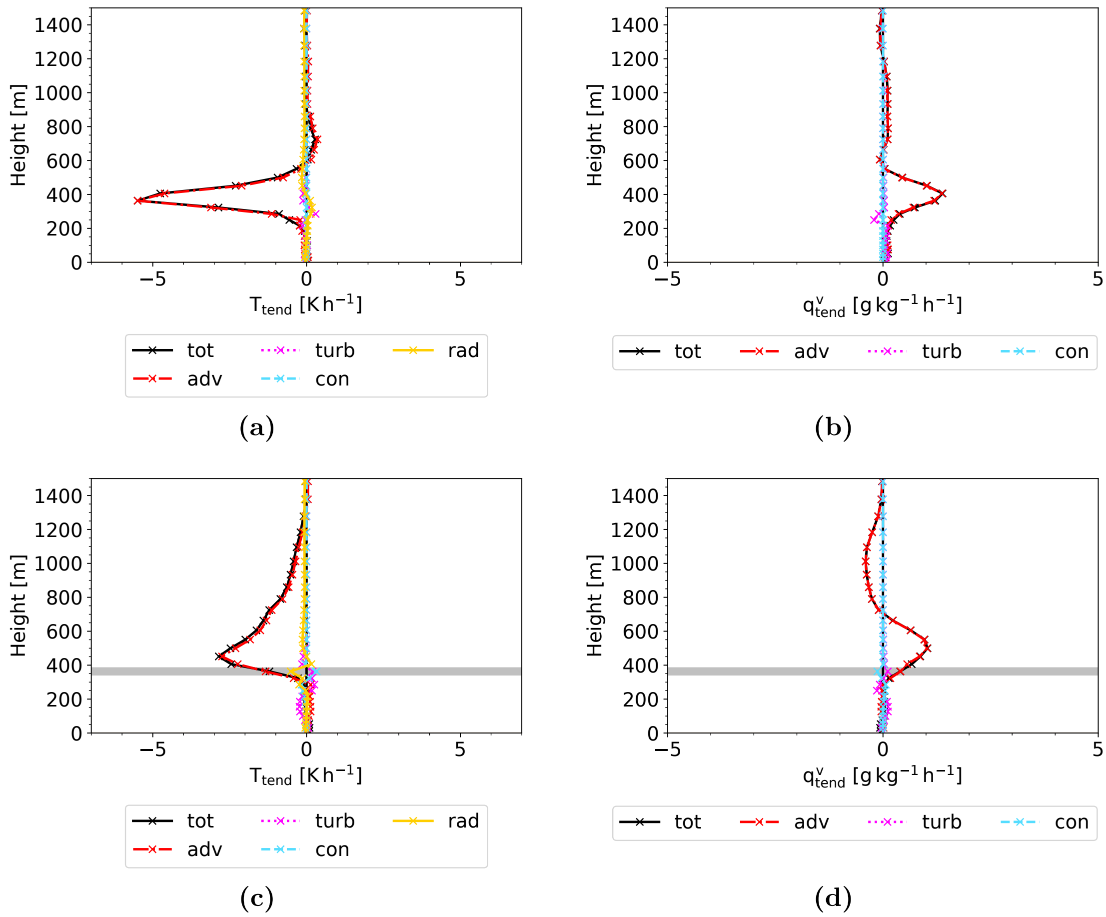

Figure 5.26: Vertical profiles of (a, c) temperature (T_{tend} [K h^{-1}]) and (b, d) specific humidity (q^{v}_{tend} [g kg^{-1} h^{-1}]) tendencies at 23.5 °S, 13.5 °E on 24 September 2017 at (a, b) 5 UTC and (c, d) 6:30 UTC; tot: total tendency, adv: advection, turb: turbulent mixing, con: condensation/evaporation, rad: radiation. Shaded grey areas indicate where the cloud water content is larger than 0.01 g kg^{-1}.

Figure 5.26 depicts the tendencies of temperature and specific humidity at 5 and 6:30 UTC for a point over the Atlantic Ocean (see red crosses in Figure 5.25 (c, d)) in order to analyse what makes the atmosphere over the ocean favourable for cloud formation. From around 1 UTC during night, colder and moister air masses are advected with a southeasterly trade wind between 250 and 600 m height a.s.l. The cold air advection destabilises the MBL and results in an increase of the boundary layer height. This is further supported by the decrease of large-scale subsidence due

to a weakening of the high-pressure ridge at 500 hPa. Due to the advection of cold and moist air, a cloud forms at ~380 m a.s.l. at 6:30 UTC.
Further north, the cold air advection starts already before 0 UTC with a northwesterly wind and clouds form correspondingly earlier. This northwesterly wind along the Namibian coast results from the relocation of the thermally induced surface low-pressure system onto the Atlantic Ocean due to the advection of warm air from the continent (see Sec. 5.3.1). At the eastern flank of the relocated surface low-pressure system a northwesterly wind blows along the Namibian coast north of Walvis Bay causing the cold air advection. So the cloud formation over the Atlantic Ocean, which occurs for most parts in the second half of the night, results from the advection of cool and moist air resulting from feedbacks with the large-scale circulation. The northwesterly wind along the Namibian coast is another example how the large-scale circulation feeds back on FLC patterns in the Namib region.

The case studies CS2021 and CS2324 reveal important processes for the occurrence and evolution of FLCs in the Namib Desert. The advection of warm continental air masses with an easterly wind due to an eastward shift of a surface high-pressure maximum causes lower cloud heights or even hinders the onshore movement of FLCs. The influence of high-pressure ridges and related large-scale subsidence enhances these effects. In cases where the heat maximum is advected to the Namibian coast and the thermally induced low surface pressure is relocated onto the Atlantic Ocean, a northwesterly wind at its eastern flank causes the onshore advection of maritime air masses which is important for FLC formation.

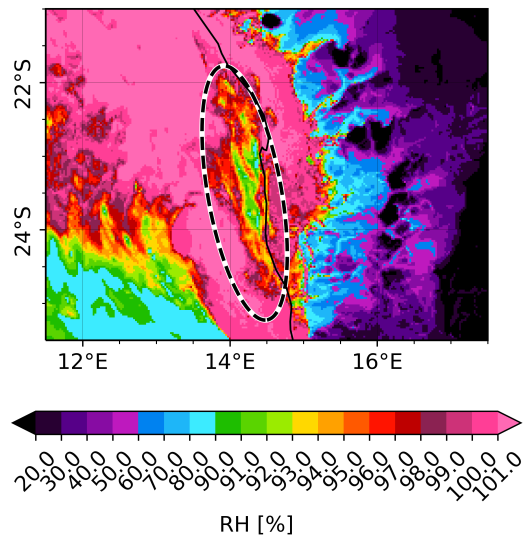

Figure 5.27: Spatial distribution of relative humidity RH [%] in the model layer where relative humidity is at its maximum on 27 September 2017 at 21 UTC. The maximum is determined between the surface and a height of 2500 m a.s.l. The dashed ellipse marks the region where the model misses the observed clouds.

For CS2728, the model simulation temporarily underestimates the low cloud cover over the ocean, e.g. at 21 UTC (see previous section). Figure 5.27 displays the maximum relative humidity in each grid column. FLCs can only form, where the relative humidity exceeds 100 %. Figure 5.27 reveals that the areas, where the model misses the observed clouds (dashed ellipse), have a relative humidity larger than 90 %, often even larger than 95 %. To answer the question, why in the simulation the relative humidity does not reach the 100 % required for cloud formation, the dew point spread is analysed. The dew point spread is the difference between temperature and dew point temperature. A larger (smaller) dew point spread means smaller (larger) relative humidity, respectively. If the dew point spread is equal to zero, saturation is reached and relative humidity is equal to 100 %.

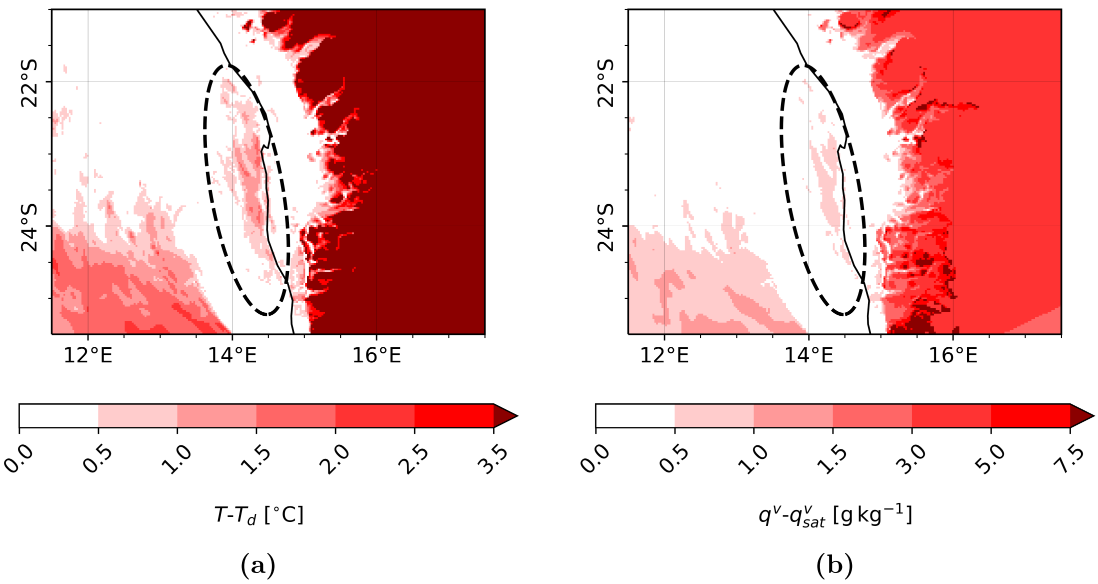

Figure 5.28: Spatial distribution of (a) dew point spread [°C] and (b) difference between specific humidity q^v and specific humidity at saturation q^v_{sat} [g kg^{-1}] on 27 September 2017 at 21 UTC in the model layer where relative humidity is at its maximum (see Fig. 5.27). The dashed ellipse marks the region where the model misses the observed clouds.

Figure 5.28 (a) shows a map of the dew point spread in the layer where the relative humidity is maximal. The dew point spread is between 0.5 and 1.5 °C for the large areas along the Namibian coast where the model misses the clouds observed in the satellite retrieval. The difference of specific humidity and specific humidity at saturation for the actual temperature, shown in Figure 5.28 (b), reveals that the specific humidity is too low by 0–1 g kg^{-1} for clouds. Already a small change of temperature or specific humidity would lead to the required cloud cover.
Small temperature or specific humidity changes can be easily obtained in the model by initialisation, dynamic processes, or parametrisations, and the feedbacks among all of them decide if a cloud forms or not. This example highlights the difficulties in modelling clouds. A wrongly simulated cloud cover can have large feedback effects.

Stratiform clouds reflect incoming downward solar radiation efficiently and play a major role in the global energy budget. In a region where baroclinicity is weak and for most part given by thermal contrasts, e.g. land-sea contrast, a wrongly simulated cloud cover can also impact on the circulation.

5.4 Evaluation of model simulations with observations

The simulated spatial and temporal patterns of FLCs have already been shown to agree quite well with satellite images. The horizontal extent of FLCs is temporarily underestimated if warm continental air masses are advected to the Namibian coast with an easterly wind.

To further check, if the atmospheric conditions are simulated correctly by COSMO-FOG, a comparison to measurements at ground-based FogNet stations is performed in the following. Due to the scarcity of the observational data this is not an objective model evaluation, but for the case studies analysed in this thesis it provides the best way for evaluation.

The 2 m temperature and relative humidity are compared to measurements at FogNet stations. The root mean square error (RMSE) and the correlation coefficient (R^2) are calculated. The FogNet station in Gobabeb is equipped with a CS215 Temperature and Relative Humidity Probe[13] measuring air temperature and relative humidity (Spirig et al., 2019). This device has an accuracy of $\pm 0.9\,°C$ for temperature and $\pm 4\,\%$ for relative humidity (Campbell Scientific, 2018). In the absence of measurement accuracies for the other FogNet stations, it is assumed that the accuracies for the station in Gobabeb also apply to the other stations.

The measurement data available every minute is averaged to the model output frequency of 15 minutes. To obtain representative simulation results accounting for the effective model resolution of about 5 to $7\Delta x$ (Skamarock, 2004), model results are averaged over a square with the grid box containing the station measurement in the centre and its three neighbours at each side thus yielding 7 x 7 grid points. This corresponds to an edge length of ~ 19.6 km for $\Delta x \simeq 2.8$ km.

On 18 and 19 September the 2 m temperature is simulated realistically (RMSE= 1.65 °C, R^2=0.94), so COSMO-FOG captures the spatial distribution of near-surface temperature in the central Namib Desert reasonably well. As an example, Figure 5.29 displays observed and simulated 2 m temperature at a coastal station (Coastal Met (a)) and two inland stations (Gobabeb (b) and Vogelfederberg (c)) for 18 and 19 September. The simulated 2 m temperature is widely in the error range of the observations. In Coastal Met the daytime maximum temperature is underestimated due to a wrongly simulated cloud blocking incoming solar radiation. In Gobabeb and Vogelfederberg, the maximum temperature is well captured, but slightly too early. The observations at the FogNet stations Gobabeb and Vogelfederberg in Figure 5.29 (b) and (c) confirm the simulated cooling by about 10 °C between 15 and 18 UTC near the surface. The minimum temperature of ~ 10 °C is met by the model simulation in Coastal Met and Gobabeb.

[13]Temperature and relative humidity probe CS215, Campbell Scientific

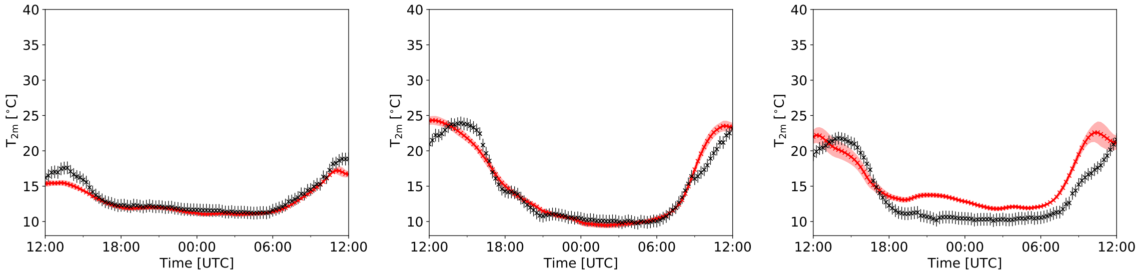

(a) Coastal Met **(b)** Gobabeb **(c)** Vogelfederberg

Figure 5.29: Time series of observed (black) and simulated (red) 2 m temperature [°C] at (a) a coastal and (b, c) two inland stations for CS1819. The shaded bands represent the standard deviation of the simulation values over the averaging area. Error bars represent accuracies of the observations.

The near-constant temperature evolution during night is in well accordance with the FogNet observations of 2 m temperature for Coastal Met and Gobabeb. A light warm bias arises, since the model simulates fog earlier than observed at some stations and longwave radiative cooling is blocked by FLCs, e.g. in Vogelfederberg the nighttime temperature minimum is overestimated by COSMO-FOG.

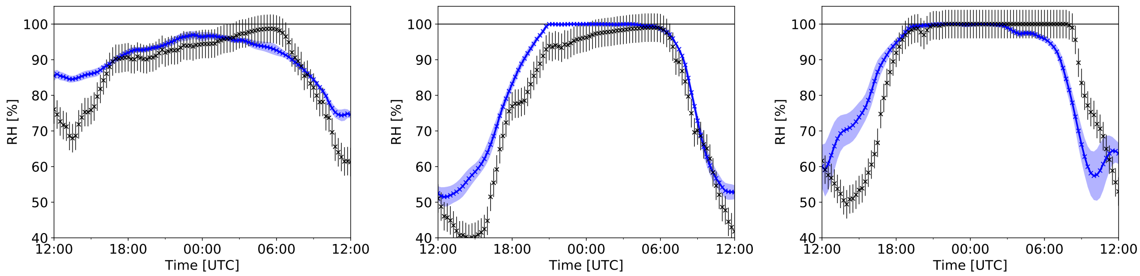

(a) Coastal Met **(b)** Gobabeb **(c)** Vogelfederberg

Figure 5.30: As Figure 5.29, but for observed (black) and simulated (blue) 2 m relative humidity [%].

The temporal evolution of near-surface relative humidity (Fig. 5.30) reveals that the simulated relative humidity is in rather well agreement with the FogNet observations, especially between 17 and 3 UTC, i.e. in the phase where clouds and fog form and occur. In Gobabeb the timing of fog occurrence is well captured by the model (Fig. 5.30 (b)) while in Coastal Met (Fig. 5.30 (a)) and Vogelfederberg (Fig. 5.30 (c)) the decrease of relative humidity starts earlier in the model compared to the observation resulting in an underestimation of near-surface relative humidity by the model in the morning. In the afternoon the model overestimates the relative humidity causing a rather large RMSE for relative humidity (RMSE=9.35 %, R^2=0.93). In accordance with the observations, the simulated near-surface relative humidity is approximately 30 % higher closer to the coast than inland in the afternoon.

The simulation of the fog event and the meteorological conditions and, thus, the underlying processes, appear reasonable for 18 and 19 September.

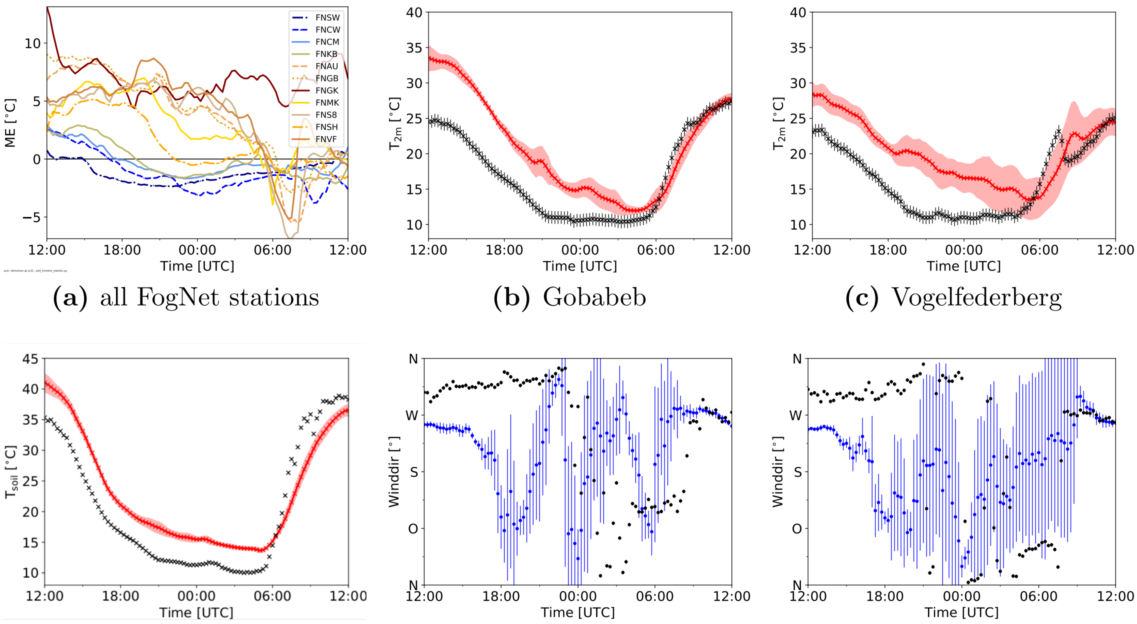

(a) all FogNet stations **(b)** Gobabeb **(c)** Vogelfederberg

(d) Gobabeb **(e)** Gobabeb **(f)** Vogelfederberg

Figure 5.31: Time series of (a) mean error of 2 m temperature [°C] at all FogNet stations, (b, c) observed (black) and simulated (red) 2 m temperature [°C] at two inland stations, (d) observed (black) and simulated (red) surface temperature [°C] at an inland station, (e, f) observed (black) and simulated (blue) wind direction [°] at two inland stations for CS2021. The shaded bands (and error bars for wind direction) represent the standard deviation of the simulation values over the averaging area. Error bars represent accuracies of the observations.

In contrast to CS1819, the simulated 2 m temperature deviates from the observations for CS2021 (RMSE=3.78 °C, R^2=0.83) and CS2324 (RMSE=3.29 °C, R^2=0.87). For CS2021, the 2 m temperature fits well to the observations for coastal stations with a bias around 2 °C (blue lines in Fig. 5.31 (a)) but is largely overestimated at inland stations (orange and red lines in Fig. 5.31 (a)). The large warm bias at inland stations in the first 10 hours of the simulation period causes the large RMSE for CS2021. At most inland stations the warm bias in the first ten hours is around 5 °C (Fig. 5.31 (a)). At the location of some inland stations the model is initialised warm biased by ∼8–18 °C (see Fig. 5.31 (a) and examples in Fig. 5.31 (b) and (c)). The overestimated 2 m temperature from the beginning of the simulation on results very likely from an overestimation of the surface temperature[14] (measurements only available in Gobabeb, see Fig. 5.31 (d)). Due to the warmer surface, the marine air advected inland is heated more strongly by heat fluxes from the surface.

[14]Infra-red Remote Temperature Sensor IR120, Campbell Scientific, accuracy ±0.2 °C (Campbell Scientific, 2019)

A sensitivity simulation initialised 24 hours earlier (at 19 September 2017, 12 UTC) develops equally large errors as the simulation initialised at 20 September, 12 UTC although started with a very small error (not shown). It is most likely that COSMO-FOG overestimates the advection of warm air with a northeasterly wind causing the higher simulated surface and 2 m temperature.
During night, COSMO-FOG simulates a southerly to easterly surface wind while a northwesterly wind direction[15] has been observed (see examples in Fig. 5.31 (e) and (f)). As a result, the model misses the maritime influence in the first half of the night. The large spatial variability of the simulated wind direction (large error bars) results from the weak pressure gradients at night, so the wind direction is strongly dominated by local effects. It seems, that the zone with thermally induced low surface pressure causing a northwesterly wind at its eastern flank is not correctly simulated. When the northwesterly wind direction is correctly simulated from approximately 21 UTC on, the bias of the 2 m temperature subsequently decreases at all stations except for the easternmost (Fig. 5.31 (a)). The observed southeasterly wind in Gobabeb between 3 and 6 UTC blows parallel to the valley of the Kuiseb river and, thus, can be due to local effects.
In order to exclude that a too small model domain is the cause for the misrepresentation of the circulations, a sensitivity simulation was performed with a domain ranging from 15 to 35 °S and 5 to 40 °E covering a region of $2\,240 \times 3\,920\,\mathrm{km}^2$. This simulation does not improve the results. So the choice of the model domain is not responsible for the wrong wind direction and the large bias.
In the morning of 21 September 2017, a cold bias occurs at most inland stations. The model simulates wind from westerly directions advecting cool maritime air masses, while an easterly land breeze is observed after sunrise advecting warm air which causes a peak of 2 m temperature at some stations until the westerly sea breeze sets in and results in cooling (see e.g. Fig. 5.31 (c)). The model misses the easterly wind and warm air advection resulting in the temperature difference. On 21 September, the temperature fits again well with the observations from 9 UTC on and the bias is around 2 °C for most of the stations.
Despite the large temperature bias, a fog event is simulated for the FogNet station in Gobabeb (Fig. 5.32 (a)). Although the temperature is overestimated by up to 7 °C at the beginning of the night, the relative humidity is in quite well accordance with the observations during the night. This is most likely caused by an overestimation of specific humidity by the model. A comparison of specific humidity to the FogNet measurements is not possible in Gobabeb since no pressure measurements are available in Gobabeb to calculate specific humidity from relative humidity. In contrast, no fog is simulated at the FogNet station in Vogelfederberg (Fig. 5.32 (b)), where the relative humidity is underestimated by up to 30 % during night (Fig. 5.32 (c)). Overall, the simulated relative humidity is slightly worse represented than for CS1819 (RMSE=9.94 %, R^2=0.88).

For 20 and 21 September, the 2 m temperature is not simulated realistically at inland stations, partly leading to missing fog in the model simulation.

[15]Wind Monitor, R.M. Young, Campbell Scientific, accuracy ±3°(Campbell Scientific, 2012)

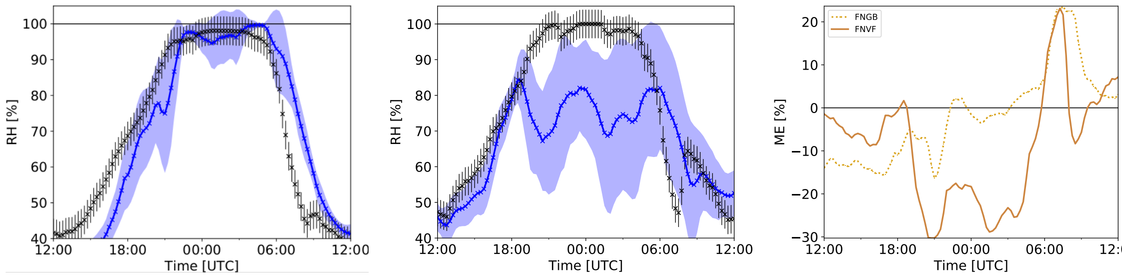

(a) Gobabeb **(b)** Vogelfederberg **(c)** Gobabeb and Vogelfederberg

Figure 5.32: Time series of observed (black) and simulated (blue) 2 m relative humidity [%] in (a) Gobabeb and (b) Vogelfederberg, (c) mean error of 2 m relative humidity [%] in Gobabeb (FNGB) and Vogelfederberg (FNVF) for CS2021. The shaded bands represent the standard deviation of the simulation values over the averaging area. Error bars represent accuracies of the observations.

On 23 September COSMO-FOG simulates the 2 m temperature quite realistic at the coastal stations (see example in Fig. 5.33 (a)). On 24 September the daytime maximum temperature is underestimated by COSMO-FOG due to a wrongly simulated cloud along the coastline.
For 23 September, the daytime temperature is simulated rather well at the inland stations until 18 UTC (see examples in Fig. 5.33 (b) and (c)). The above mentioned large RMSE for this case study is caused by a warm bias of more than 5 °C at all inland stations during night (orange and red lines in Fig. 5.33 (d)). This is due to underrepresented cooling after sunset in the model simulation.
The overestimation of temperature during night results likely from a wrongly simulated wind direction. The model simulates an easterly land breeze during night, while from 18 and 21 UTC on, respectively, a northwesterly wind was observed (Fig. 5.33 (e) and (f)). The northwesterly wind at the eastern flank of the surface low pressure is not at all simulated by COSMO-FOG for the inland stations. As a result, the model misses the maritime influence. This can be further enhanced by an underestimation of the MBL height due to large-scale subsidence under the influence of the high-pressure ridge at the 500 hPa level.
The overestimation of the near-surface temperature at inland stations during night causes a strong underestimation of relative humidity, e.g. in Vogelfederberg where the observed fog event is not reproduced by COSMO-FOG (not shown). The underestimation during night at inland stations causes a larger deviation and a smaller correlation between observed and simulated relative humidity for CS2324 (RMSE=11.58, R^2=0.85). This results in the underestimation of the fog extent above land areas.
Although the model does not simulate the atmospheric conditions and the fog event correctly for 20 and 23 September, these simulations have revealed important processes for the occurrence and evolution of FLCs in the Namib Desert. The advection of warm continental air masses with an easterly wind due to an eastward shift of a surface high-pressure maximum causes lower cloud heights or even hinders the

onshore movement of FLCs. If the heat maximum is advected to the Namibian coast and the thermally induced low surface pressure is relocated onto the Atlantic Ocean, a northwesterly wind at its eastern flank supports the onshore advection of maritime air masses supporting FLC formation.

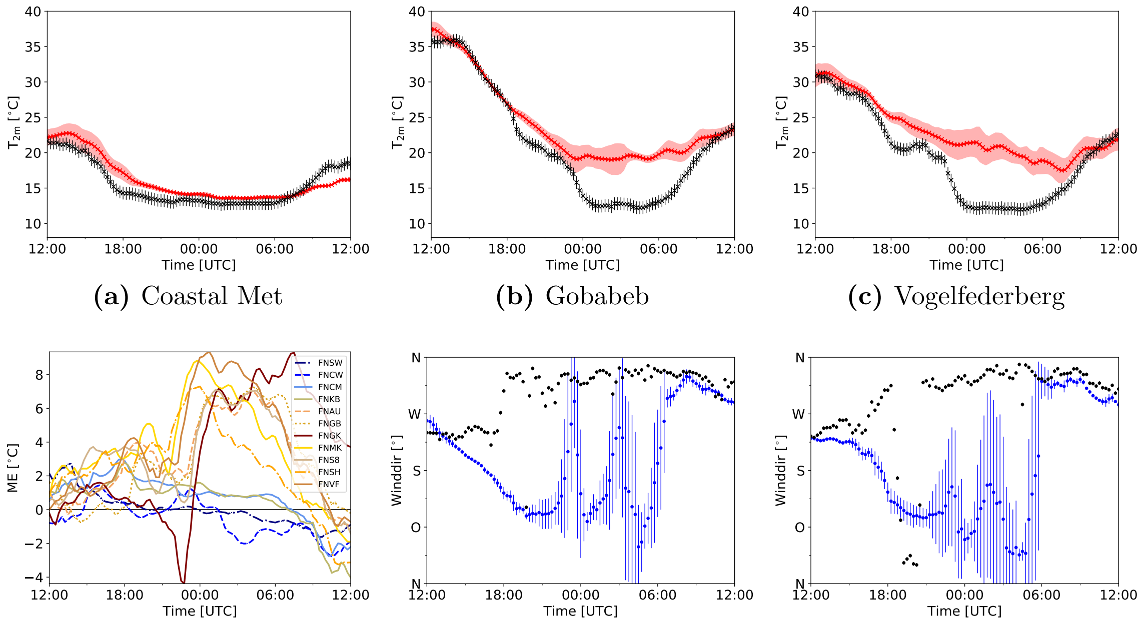

(a) Coastal Met **(b)** Gobabeb **(c)** Vogelfederberg

(d) all FogNet stations **(e)** Gobabeb **(f)** Vogelfederberg

Figure 5.33: Time series of observed (black) and simulated (red) 2 m temperature [°C] at (a) a coastal and (b, c) two inland stations, (d) mean error of 2 m temperature [°C] at all FogNet stations, (e, f) observed (black) and simulated (blue) wind direction [°] at two inland stations for CS2324. The shaded bands (and error bars for wind direction) represent the standard deviation of the simulation values over the averaging area. Error bars represent accuracies of the observations.

On 27 September 2017 the 2 m temperature agrees rather well with the observations (RMSE=2.11, R^2=0.95). As for 18 September 2017, the model captures the near-surface temperature evolution very well at the coastal station except for an underestimation of the daytime maximum at 28 September 2017 (Fig. 5.34 (a)). At inland stations the simulated near-surface temperature matches the observation well until the simulated cooling stops around 19 UTC which is some hours earlier than observed (see examples in Fig. 5.34 (b) and (c)). As a result the nighttime temperature is overestimated. The overestimation of the near-surface temperature during night is caused by the formation of the first fog two to three hours earlier than observed. Inspection of the relative humidity reveals that the end of the cooling at the inland stations coincides with the relative humidity reaching 100 % and thus the occurrence of fog some hours earlier than observed (cf. Fig. 5.35 (b) and (c)). That way, the cooling of the ground by longwave radiation is reduced or even completely inhibited resulting in the 2 m temperature bias.

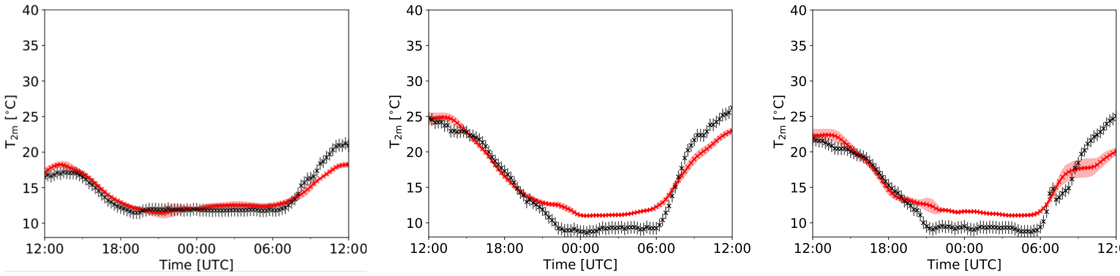

(a) Coastal Met **(b)** Gobabeb **(c)** Vogelfederberg

Figure 5.34: Time series of observed (black) and simulated (red) 2 m temperature [°C] at (a) a coastal and (b, c) two inland stations for CS2728. The shaded bands represent the standard deviation of the simulation values over the averaging area. Error bars represent accuracies of the observations.

At Coastal Met the simulated relative humidity fits quite well to the observation for the night between 27 and 28 September (Fig. 5.35 (a)). At the inland stations the model captures the temporal evolution of relative humidity but shifted by approximately one to three hours (Fig. 5.35 (b) and (c)). This results in an overestimation of the relative humidity and fog formation earlier than observed causing the aforementioned temperature bias. The temporal shift and overestimation of the relative humidity also feeds back on the RMSE for relative humidity which is larger than for all other case studies (RMSE=14.81). Nevertheless, the observed and simulated relative humidity are quite well correlated (R^2=0.92). In Gobabeb the simulated relative humidity is equal to 100 % departing from the observation staying slightly below 100 %.

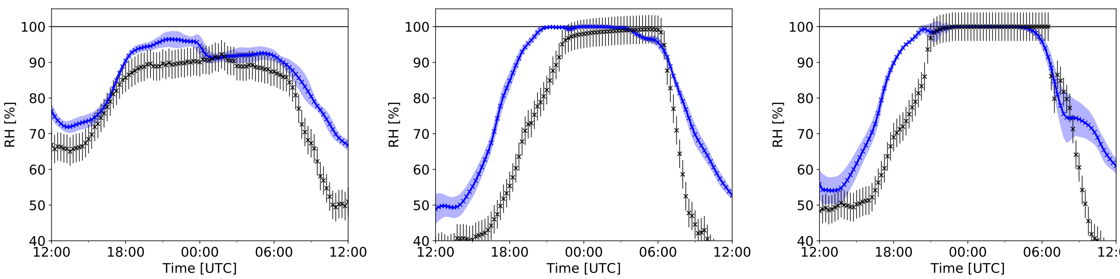

(a) Coastal Met **(b)** Gobabeb **(c)** Vogelfederberg

Figure 5.35: As Figure 5.34, but for observed (black) and simulated (blue) 2 m relative humidity [%].

The analysis of the case studies has revealed the importance of the inversion height and strength for spatial fog and low cloud patterns. To estimate if the inversion is reasonably represented in the model simulations, simulated temperature profiles are compared to manually operated profile measurements. At the site in Gobabeb, a Graw radiosonde is used (TBS) and in Vogelfederberg the measurement device is

self-constructed (UAV, Spirig et al. (2019), cf. Sec. 5.1). The Graw radiosonde has an accuracy of ±0.2 °C for temperature and ±0.3 hPa for pressure (GRAW Radiosondes, 2018). It is assumed that these accuracies also apply to the self-constructed device.
For the profile measurements data are available for the ascent and the descent. These measurements differ frequently. This can either be due to memory effects of the devices or the time passed between ascent and descent. In order to get representative data for the comparison with the model simulation the data from ascent and descent are averaged.
The model data have to be chosen representative and fitting to the measurements. In the time taken for an ascent and a descent several model outputs are available. To get a value representative for the time span of the measurements the model output is averaged over the time slot taken for ascent and descent. The model output is also averaged spatially over 7×7 grid points to account for the effective model resolution.

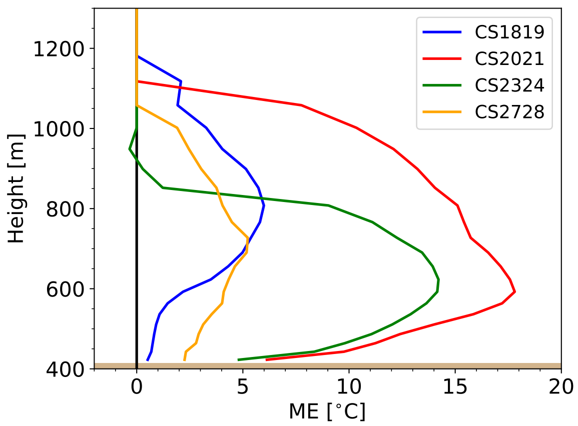

(a) Gobabeb

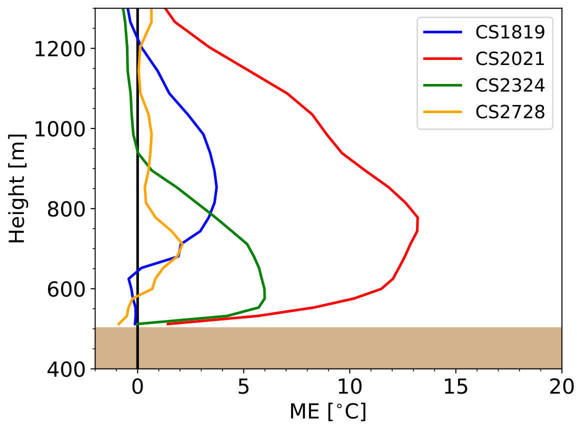

(b) Vogelfederberg

Figure 5.36: Vertical profiles of mean error (ME, bias) of the potential temperature for (a) Gobabeb and (b) Vogelfederberg for the analysed case studies. Brown areas mark the terrain height.

Figure 5.36 displays the mean error of potential temperature averaged over all time slots with available observations for each case study. As expected from the results for near-surface temperature, the bias of potential temperature (around 6 °C) is smaller for 18 September and 27 September than for the remaining two case studies with a bias larger than 10 °C (up to 18 °C). For all case studies the largest deviations occur between 600 and 900 m a.s.l.
In order to get an idea how these errors arise, some examples of profiles of potential temperature are displayed in Figure 5.37.
On 18 September at 21 UTC, COSMO-FOG simulates a ground-based inversion which has not been observed (Fig. 5.37 (a)). In contrast to the model, the TBS sounding shows a 200 m deep well-mixed layer already at 21 UTC. Close to the ground the potential temperature of the sounding is well captured by the model which is in agreement with the FogNet station comparison. The simulated potential

temperature increases too strongly causing a difference between model and observation of approximately 5 °C. Around 1200 m the simulated and observed potential temperature converge again. In the fog layer at 4 UTC, the potential temperature simulated with COSMO-FOG fits very well to the TBS sounding. But the vertical extent of the fog layer is underrepresented in the model simulation. Especially between 600 and 900 m a.s.l. the model simulation overestimates the potential temperature by up to 10 °C. However, the shape of the observed potential temperature profile (as far as available) is represented rather well by COSMO-FOG.

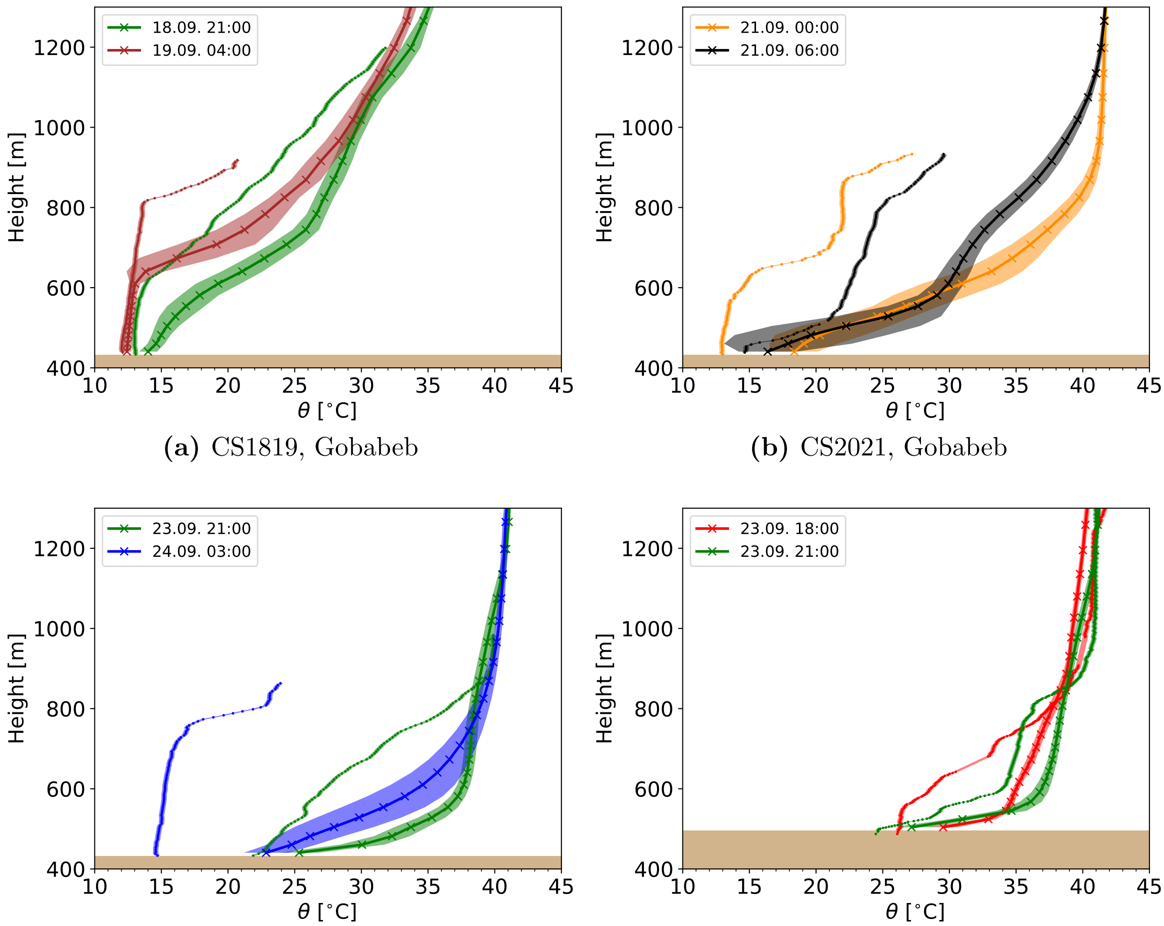

(a) CS1819, Gobabeb **(b)** CS2021, Gobabeb

(c) CS2324, Gobabeb **(d)** CS2324, Vogelfederberg

Figure 5.37: Vertical profiles of simulated (lines with crosses) and observed (dots) potential temperature θ [°C] at different times for (a) CS1819, (b) CS2021, (c) and (d) CS2324 in (a–c) Gobabeb and (d) Vogelfederberg. The shaded bands represent the standard deviation of the simulation values over the averaging area. For observations, shaded bands represent errors obtained from error propagation. Brown areas mark the terrain height.

So on 18 September 2017 the differences between model simulation and observations are caused by a stronger inversion in the model simulation. The overestimation of the potential temperature by the model results in an underestimation of relative humidity by up to 30 % (not shown).

For CS2021 and CS2324, COSMO-FOG simulates a strong surface inversion at night, which is not confirmed by the observations in Gobabeb. For CS2021, a roughly 150 m deep well-mixed layer was observed during the night (from 21 to 3 UTC) with an elevated mixed layer above (Fig. 5.37 (b)). Neither the elevated mixed layer nor the well-mixed layer close to the surface are captured by the model wich simulates a strong surface inversion. This leads to a strong overestimation of the potential temperature by $\sim 20\,°C$ by COSMO-FOG. In the morning, the simulated strong inversion is in better accordance with the observation due to a decrease of the height of the observed well-mixed layer to less than 500 m a.s.l. Above 500 m a.s.l., the model still overestimates the potential temperature by more than 5 °C.

On 23 September, the observations show a surface inversion at 21 UTC in Gobabeb, but COSMO-FOG strongly overestimates the strength of the inversion (Fig. 5.37 (c)). At 21 UTC, a potential temperature jump of 20 °C between 400 and 800 m a.s.l. was observed, while the model simulates a similar potential temperature jump between 400 and 600 m a.s.l. Afterwards, the formation of a ~ 350 m deep well-mixed fog layer was observed which is completely missed by the model simulation. In Vogelfederberg, the potential temperature simulated by COSMO-FOG fits better to the observations although the surface inversion forms too early in the model simulation. At 18 UTC the simulated temperature deviates by less than 5 °C from the observation close to the surface (Fig. 5.37 (d)). The model misses a less than 100 m deep well-mixed layer causing a temperature difference between model and observation of 5–10 °C. Around 800 m a.s.l. the simulated and observed temperature converge again. At 21 UTC, the model simulates a surface inversion which was observed. The deviation of the model simulation from the observation is smaller than 5 °C, especially between 600 and 800 m and above 1200 m. The differences of model errors between Gobabeb and Vogelfederberg show that the model quality is also influenced by regional effects.

In summary, the evaluation of the model simulations with ground-based observations shows that COSMO-FOG simulates the atmospheric conditions well at coastal stations. At inland stations COSMO-FOG predicts the atmospheric conditions quite well, but the model experiences some difficulties dependent on synoptic patterns. The situations with an advection of continental air masses seem difficult to predict for the model, because these situations are dependent on the exact position of the low surface pressure. If the low surface pressure minimum is slightly differently located, this results in a completely different wind direction. This impacts on the temperature and relative humidity and, thus, FLC occurrence. Also the height of the inversion capping the MBL might impact on the model results at inland stations. If the height of the MBL in the model simulation is lower than observed this causes higher temperatures at inland stations. The dominating processes controlling the height of the inversion layer are turbulent mixing in the boundary layer and subsidence in the lower troposphere. Stronger mixing increases the height of the boundary layer and rises the inversion. Large-scale subsidence over low SSTs creates a shallow MBL capped by a strong temperature inversion. This above analysis shows, that the model deficiencies result mainly from the dynamical and not the microphysical representation in the model. The dynamical core (advection) as well as the turbulent mixing likely exhibit the largest impact on the analysed deficiencies in the model simulation. A further investigation of these deficiencies is beyond the scope of this study.

6 Conclusion and Outlook

6.1 Summary and concluding remarks

The Namib Desert located at the southern west coast of the African continent in the proximity of the cold Benguela current is a typical coastal desert. Scarce precipitation makes the Namib Desert one of the driest places on earth. Fog occurs regularly along the coast. Water input by fog often exceeds rainfall and thus fog water deposition is a major source of water for the ecosystem and could be a supplementary source of water for human settlements. Little is still known about the processes which control the formation and spatio-temporal patterns of fog and low stratiform clouds (FLCs) in the Namib Desert, despite their importance.
By means of numerical simulations, this study investigates spatial patterns and diurnal variations of FLCs as well as the processes which control these variations in the hyper-arid Namib Desert. In the present thesis, the following scientific questions have been answered:

Q1 Is the three-dimensional fog model COSMO-FOG able to reasonably simulate the time evolution of the cloud-topped marine boundary layer?

Q2 What are the temporal and spatial patterns of coastal fog occurrence in the Namib region?

Q3 What are typical life cycle phases of Namib region fog?

Q4 What factors determine the development, persistence and properties of the fog?

For this purpose, the two-moment microphysical parametrisation of the one-dimensional fog and boundary layer model PAFOG has been implemented into the numerical weather prediction model COSMO including the Modular Earth Submodel System, forming the three-dimensional fog model COSMO-FOG. The one-moment bulk microphysical parametrisation scheme of COSMO has been replaced by the microphysics scheme from PAFOG below 2000 m. Above 2000 m, the microphysical parametrisation of the COSMO model remained unchanged. Additionally, a visibility parametrisation based on the prognostic variables cloud water content and droplet number concentration has been implemented into COSMO.
The model behaviour of COSMO-FOG has been investigated in a highly idealised environment for a horizontally homogeneous marine stratus to check if the three-dimensional fog model is able to reasonably well simulate the time evolution of the cloud-topped MBL (scientific question **Q1**). A sensitivity study for both microphysical parametrisation schemes (standard COSMO model and COSMO-FOG) and different vertical model grids has been performed.
This sensitivity study revealed that COSMO-FOG yields more realistic cloud water

contents for the marine stratus compared to the COSMO model which produces an unrealistically high cloud water content. Additional sinks for cloud water by gravitational settling and autoconversion in the simulations with COSMO-FOG reduced the cloud water content, thus, highlighting the importance of these processes for realistic cloud simulations. This finding is in agreement with a previous study by Boutle et al. (2022).
The sensitivity simulations with different vertical grids have shown that a fine vertical grid is necessary to resolve sharp gradients of e.g. temperature, specific humidity, and cloud water content at cloud top. Especially the radiative cooling at cloud top is not reasonably well represented in the simulations using a vertical grid typical of meso-scale models. A vertical grid has been defined which combines an as accurate as possible representation of the important features of the cloud-topped MBL with computational efficiency and starts with a grid spacing typical of meso-scale models for the lowest layer above the surface. This vertical discretisation improves the representation of radiative cooling at cloud top. A fine tuning of the turbulent diffusion coefficients in the turbulence parametrisation further improves the model results for the marine stratus by maintaining the strong gradients across the inversion layer. With the resulting model configuration, COSMO-FOG is capable of reasonably well simulating the diurnal evolution and processes in the cloud-topped MBL. This configuration is used for real case applications in the Namib region.

In order to investigate the spatio-temporal patterns, diurnal life cycle phases and contributing atmospheric processes of FLCs in the Namib Desert, individual case studies in the austral spring season in September 2017 have been simulated with COSMO-FOG for a model domain located around the central Namib Desert.
The analysis of the case studies revealed spatial and temporal patterns of FLCs which allow to distinguish life cycle phases of FLCs in the Namib region (scientific questions **Q2** and **Q3**). During daytime, low stratiform clouds are mostly confined to the Atlantic Ocean. In this cloud-free phase cloud coverage above land is almost constant at its minimum. In the extension phase starting around sunset, the clouds extend eastward in a front-like structure almost parallel to the coastline inducing an increase of cloud area coverage above land areas. When the clouds intercept with the ascending terrain of the Great Escarpment at some distance from the coast, fog forms. In the cloud and fog phase the cloud coverage is at its maximum and nearly constant. When the fog thins and lifts from the ground the next morning, the dissipation phase starts. In the following hours during the dissipation phase, the stratiform clouds dissolve resulting in a decreasing cloud covered area. Occasionally, a narrow stripe of clouds persists along the coast during the day. After the dissipation of FLCs over land areas the life cycle starts again.
In order to estimate the quality of the model simulation with respect to the spatial distribution of clouds, the simulated cloud cover has been visually compared to RGB composites combined with ground measurements of fog occurrence. For most of the case studies, the horizontal extension of FLCs is in rather well accordance with the satellite observations. For one case study, COSMO-FOG strongly underestimates the cloud cover above ocean areas at times during night, while the extent of FLCs above land areas simulated by COSMO-FOG matches quite well with the satellite

observation. The cloud layer above the ocean did not form in the model due to small deviations from saturation. This highlights the difficulty in modelling clouds.
The spatial patterns and temporal evolution of FLCs simulated by the model above land areas are consistent with satellite observations of the exact dates. Although the dataset of four case studies is small, the consistency with longer term satellite retrievals indicates that the spatio-temporal patterns simulated with COSMO-FOG are typical for the Namib region.

In order to get insights into the processes contributing to the FLC patterns in the various life cycle phases (scientific question **Q4**), the temperature and specific humidity budget was analysed using the MESSy submodel TENDENCY.
In the cloud-free phase, thermally and topographically induced wind systems advect cool and moist air onshore resulting in a front-like boundary in temperature and specific humidity at some distance from the coast. Sensible heat fluxes from the surface and turbulent mixing counter the cold air advection thus preventing clouds to proceed eastwards.
In the extension phase, the sensible heat flux and turbulent mixing decrease around sunset, so cooling by advection is no longer compensated resulting in a strong cooling of the PBL around sunset. This cooling makes the atmosphere favourable for fog and cloud formation enabling their onshore progression. The analysis of the contributions of temperature and specific humidity to relative humidity changes revealed that the increase of relative humidity before the onset of fog or low clouds is mostly caused by cooling while the specific humidity changes play a minor role.
In the cloud and fog phase, the FLCs grow vertically by longwave radiative cooling and the advection of cold air at cloud top. This vertical growth supports slightly further eastward extension above land areas.
In the dissipation phase, the absorption of solar radiation warms the land surface leading to an increase of the sensible heat flux. The resulting warming causes evaporation at the bottom of the fog layer. Due to the evaporation, the fog and cloud layer becomes increasingly transparent for solar radiation, thus, enhancing the heating of the ground and fog dissipation. That way the fog lifts from the ground. Advection of warm air with an easterly wind from the interior of Namibia contributes to fog and cloud dissipation.
The spatial and temporal patterns of FLCs are further modified by large-scale synoptic patterns. Due to an eastward shift of a surface high-pressure maximum, warm continental air masses are advected towards the Namibian coast with an easterly wind. This results in a shallow MBL capped by a strong inversion and, thus, lower cloud height. The strong inversion suppresses topographically forced lifting for inland advection and, thus, hinders the onshore movement of FLCs. For the case studies with an advection of warm continental air masses towards the Namibian coast, the extent of FLCs is smaller. In extreme, even cloud formation above the Atlantic Ocean is inhibited, if the inversion layer above the ocean is located below the lifting condensation level. The influence of high-pressure ridges and related large-scale subsidence enhances these effects.
If the heat maximum is advected to the Namibian coast and the thermally induced low surface pressure is relocated onto the Atlantic Ocean, a northwesterly wind at

its eastern flank supports the onshore advection of maritime air masses supporting FLC formation.

Finally the simulation results obtained with COSMO-FOG have been compared to ground-based measurements performed in the central Namib Desert. The evaluation of the model simulations with ground-based observations has shown that COSMO-FOG simulates the atmospheric conditions quite well. At inland stations COSMO-FOG exhibits some weaknesses for the weather situations with advection of continental air masses where the temperature is overestimated causing an underestimation of the FLC extent. The correct simulation of FLCs in these weather situations depends on a fine balance between the position of the thermally induced low surface pressure, large-scale subsidence and turbulence in the MBL. The inclusion of the PAFOG microphysics improves the microphysical representation of the FLCs, but can not compensate other deficiencies in the model. Since other physical parametrisations than the microphysical parametrisation are tuned with the standard microphysical scheme of COSMO, this is a notable result. Improving these deficiencies is an important next step on the way to a reliable FLC prediction. Although the model did not simulate the atmospheric conditions and the fog events correctly for the case studies with an advection of continental air masses, these simulations revealed important processes for the occurrence and evolution of FLCs in the Namib Desert.

The findings of this study for the processes contributing to the development, persistence and properties of the fog demonstrated the importance of advection processes which is in agreement with many previous studies (e.g. Andersen and Cermak, 2018; Andersen et al., 2019, 2020; Lancaster et al., 1984; Olivier, 1992, 1995; Spirig et al., 2019; Taljaard, 1979). Especially in the extension phase and in the cloud and fog phase, the advection of cold and moist air masses is decisive for the occurrence and persistence of fog. These findings oppose the hypothesis for the occurrence of radiation fog (Kaseke et al., 2017).

The application of COSMO-FOG in this study presented new insights into the processes controlling fog occurrence and its spatial and temporal patterns in the Namib region. Key factors influencing the onshore movement of low clouds that intercept higher elevation terrain could be simulated and identified with COSMO-FOG. Increasing the knowledge about these processes involved in the fog formation is of crucial importance for future water resources in the Namib Desert. Montecinos et al. (2018) reported that no fog water was collected if the cloud water content was below $0.045\,\mathrm{g\,m^{-3}}$. The cloud water content in the fog simulated with COSMO-FOG would be sufficient for fog water harvesting. However, further factors like wind speed, duration of fog events, orientation of the mesh relative to fog movement, and the properties of the mesh influence water yields (Eckardt et al., 2013; Montecinos et al., 2018).

The regions most suitable to establish fog water harvesting are those locations where low stratiform clouds intersect with ascending terrain (called landfall regions in the following). These locations are determined by the cloud base and the cloud top height and the terrain height. The cloud base height determines the westernmost location of landfall while the cloud top height decides how far the fog reaches eastwards onshore. The cloud top height is in turn dependent on the height and strength of the inversion and the cloud base height depends on the lifting condensation level. Previous studies based on satellite and ground-based observations revealed, that the regions of frequent ground fog occurrence vary considerably (Andersen et al., 2019; Spirig et al., 2019). Andersen et al. (2019) found seasonal patterns in cloud base altitude with lower cloud base height between April and June shifting the landfall region closer to the coast. A recommendation of regions favourable for fog formation and thus suitable for water harvesting would require long-term model simulations over several years combined with observations which is beyond the scope of the present project.

6.2 Outlook

In the investigated case studies, COSMO-FOG yielded promising results for the analysis of regional FLC occurrence and controlling processes in the Namib region. However, there is room for model improvements to produce even more realistic results.

Future model development could be directed towards the microphysical parametrisation. Up to now, the drizzle parametrisation in COSMO-FOG is a bulk parametrisation with assumptions for the drizzle radius and the condensation and evaporation process. The drizzle parametrisation could be extended to a two-moment scheme assuming a droplet size distribution for drizzle and treating the drizzle drop concentration as a prognostic variable. This would improve the parametrisation of the condensation/evaporation process for drizzle since it could be formulated based on the change of the drop number concentration and mean drizzle diameter, so smaller drizzle drops could evaporate first.

The effect of autoconversion on the cloud droplet number concentration is not yet accounted for. Including autoconversion as a sink for the cloud droplets which becomes larger with increasing size of drizzle drops could yield a more realistic treatment of cloud processes.

For the activation of cloud droplets a temporally and spatially constant number concentration of dry aerosol as cloud condensation nuclei is assumed. This is a strong assumption since the number concentration of dry aerosol varies between ocean and continental regions and is transported with local and large-scale circulations. For three-dimensional applications, a prognostic treatment of dry aerosol would improve the activation process. This would also allow to consider the effect of activation on dry aerosol. The concentration of dry aerosol particles is important because it influences processes and properties of stratiform clouds. A higher aerosol concentration favours more and smaller cloud droplets yielding higher albedo, more evaporation, less drizzle and less sedimentation due to a decreased droplet radius.

Further improving the microphysical scheme by a two-moment drizzle parametrisation and prognostic aerosol is important e.g. to analyse the life cycle of microphysical properties like droplet number concentration and cloud or drizzle droplet diameter.

Systematical tests and an objective model evaluation for real case applications with COSMO-FOG in the Namib region would be an important next step. This could be realised by performing a series of daily re-forecasts with COSMO-FOG and a statistical evaluation of the model results against satellite data and the few available ground measurements. An objective calibration of tuning parameters in COSMO-FOG would be another important step to further improve the model results.

Although there is still room for further model improvement as mentioned above, COSMO-FOG is ready for worldwide use cases. Further applications of COSMO-FOG in coastal Namibia could be directed towards simulations over longer time periods to get new insights into the seasonal variability of key factors for fog occurrence. Model simulations over several years are also needed in order to better assess those regions most suitable for fog water harvesting. These findings are important not only for the construction of fog water collectors but also to understand the ecosystems living from fog water input. For the long-term future, simulations with a regional climate model suggested a significant warming and a decrease of rainfall to about 50 % of today's rainfall amount in the Namib Desert while the number of fog days is expected to increase in the coastal areas (Haensler et al., 2011). In a warmer climate with less precipitation, fog could become an even more essential water source for ecosystems in the Namib region in the future. In sensitivity studies, the role of factors like the Benguela Current or the Great Escarpment could be further investigated with COSMO-FOG. The impact of the cold Benguela Current on the fog occurrence in coastal Namibia is e.g. important to understand how global warming might impact on FLC patterns.
The application of COSMO-FOG is not restricted to Namibia. COSMO-FOG can be applied in other parts of the world with similar environmental and meteorological conditions to gain new knowledge concerning coastal fog occurrence, e.g. in the Desert at the Pacific coast of Baja California and in the Atacama Desert.

A Supplementary figures and tables

A.1 Model description

In the COSMO three-category ice scheme the following transfer rates $S^{l,f}$ between the liquid and frozen hydrometeor categories are considered:

S_c	condensation and evaporation of cloud water
S_{au}^c	autoconversion of cloud water to form rain
S_{ac}	accretion of cloud water by raindrops
S_{ev}	evaporation of rain water
S_{nuc}	heterogeneous nucleation of cloud ice
S_{frz}^c	nucleation of cloud ice due to homogeneous freezing of cloud water
S_{dep}^i	deposition growth and sublimation of cloud ice
S_{melt}^i	melting of cloud ice to form cloud water
S_{au}^i	autoconversion of cloud ice to form snow due to aggregation
S_{aud}	autoconversion of cloud ice to form snow due to deposition
S_{agg}^s	collection of cloud ice by snow (aggregation)
S_{agg}^g	collection of cloud ice by graupel (aggregation)
S_{rim}^s	collection of cloud water by snow (riming)
S_{rim}^g	collection of cloud water by graupel (riming)
S_{shed}^s	collection of cloud water by wet snow to form rain (shedding)
S_{shed}^g	collection of cloud water by wet graupel to form rain (shedding)
S_{cri}^i	collection of cloud ice by rain to form graupel
S_{cri}^r	freezing of rain due to collection of cloud ice to form graupel
S_{frz}^r	freezing of rain to form graupel
S_{dep}^s	deposition growth and sublimation of snow
S_{dep}^g	deposition growth and sublimation of graupel
S_{melt}^s	melting of snow to form rain water
S_{melt}^g	melting of graupel to form rain water
S_{csg}	conversion of snow to graupel due to riming

A.2 Idealised simulations

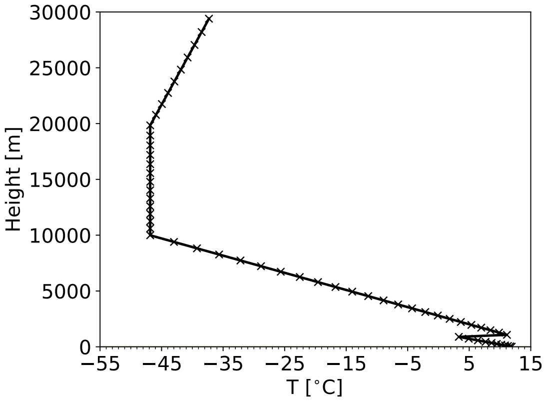

(a)

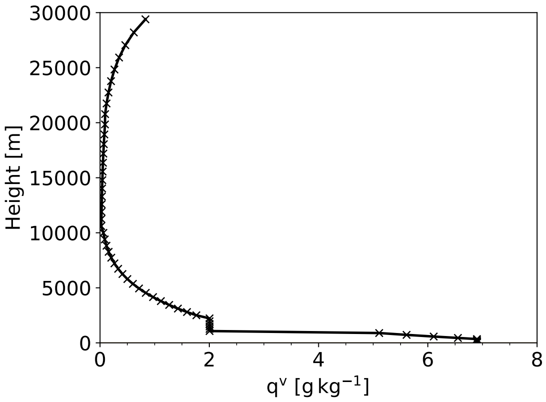

(b)

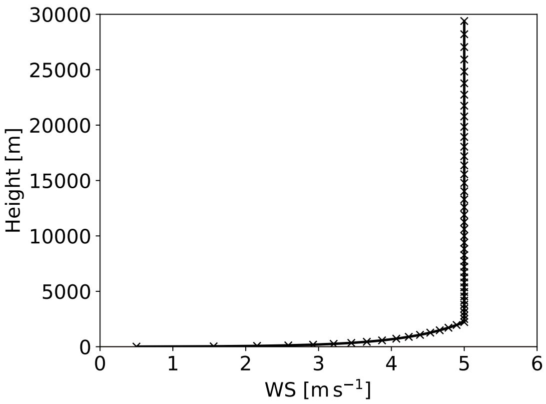

(c)

Figure A.1: Initial profiles of (a) temperature T [°C], (b) specific humidity q^v [$\mathrm{g\,kg^{-1}}$], and (c) horizontal wind velocity WS [$\mathrm{m\,s^{-1}}$] on 15 October, 6 UTC.

k	z [m]	Δz [m]
1	29395.10	1209.80
2	28202.94	1174.52
3	27045.56	1140.24
4	25922.00	1106.89
5	24831.34	1074.43
6	23772.71	1042.82
7	22745.29	1012.02
8	21748.28	982.00
9	20780.91	952.74
10	19842.45	924.18
11	18932.21	896.31
12	18049.51	869.09
13	17193.71	842.50
14	16364.21	816.50
15	15560.41	791.10
16	14781.75	766.23
17	14027.67	741.91
18	13297.67	718.09
19	12591.25	694.76
20	11907.92	671.90
21	11247.22	649.49
22	10608.72	627.51
23	9991.99	605.95
24	9396.62	584.79
25	8822.23	564.00
26	8268.44	543.58
27	7734.90	523.51
28	7221.25	503.78
29	6727.17	484.37
30	6252.36	465.27
31	5796.50	446.45
32	5359.31	427.92
33	4940.53	409.65
34	4539.88	391.64
35	4157.13	373.85
36	3792.06	356.30
37	3444.44	338.95
38	3114.06	321.80
39	2800.74	304.84
40	2504.31	288.03
41	2224.60	271.38
42	1961.48	254.85
43	1714.83	238.46
44	1484.53	222.14
45	1270.51	205.90

k	z [m]	Δz [m]
46	1072.71	189.71
47	891.08	173.53
48	725.65	157.35
49	573.48	146.97
50	446.25	107.50
51	345.54	93.93
52	258.21	80.71
53	183.93	67.86
54	122.32	55.36
55	73.04	43.21
56	35.72	31.43
57	10.00	20.00

Table A.1: Height z [m] a.s.l. of model layers (main levels) k and model layer thicknesses Δz [m] of the LR configuration

k	z [m]	Δz [m]
1	29395.10	1209.80
2	28202.94	1174.52
3	27045.56	1140.24
4	25922.00	1106.89
5	24831.34	1074.43
6	23772.71	1042.82
7	22745.29	1012.02
8	21748.28	982.00
9	20780.91	952.74
10	19842.45	924.18
11	18932.21	896.31
12	18049.51	869.09
13	17193.71	842.50
14	16364.21	816.50
15	15560.41	791.10
16	14781.75	766.23
17	14027.67	741.91
18	13297.67	718.09
19	12591.25	694.76
20	11907.92	671.90
21	11247.22	649.49
22	10608.72	627.51
23	9991.99	605.95
24	9396.62	584.79
25	8822.23	564.00
26	8268.44	543.58
27	7734.90	523.51
28	7221.25	503.78

k	z [m]	Δz [m]
29	6727.17	484.37
30	6252.36	465.27
31	5796.50	446.45
32	5359.31	427.92
33	4940.53	409.65
34	4539.88	391.64
35	4157.13	373.85
36	3792.06	356.30
37	3444.44	338.95
38	3114.06	321.80
39	2800.74	304.84
40	2546.16	204.32
41	2408.65	70.70
42	2338.90	68.80
43	2271.10	66.80
44	2205.25	64.90
45	2141.30	63.00
46	2079.20	61.20
47	2018.85	59.50
48	1960.20	57.80
49	1903.25	56.10
50	1847.95	54.50
51	1794.20	53.00
52	1741.95	51.50
53	1691.20	50.00
54	1641.95	48.50
55	1594.10	47.20
56	1547.60	45.80
57	1502.45	44.50
58	1458.55	43.30
59	1415.90	42.00
60	1374.50	40.80
61	1334.30	39.60
62	1295.20	38.60
63	1257.20	37.40
64	1220.35	36.30
65	1184.55	35.30
66	1149.75	34.30
67	1115.95	33.30
68	1083.10	32.40
69	1051.20	31.40
70	1020.20	30.60
71	990.05	29.70
72	960.80	28.80
73	932.40	28.00

k	z [m]	Δz [m]
74	904.80	27.20
75	878.00	26.40
76	851.95	25.70
77	826.65	24.90
78	802.10	24.20
79	778.20	23.60
80	755.00	22.80
81	732.50	22.20
82	710.60	21.60
83	689.30	21.00
84	668.65	20.30
85	648.60	19.80
86	629.10	19.20
87	610.15	18.70
88	591.75	18.10
89	573.90	17.60
90	556.55	17.10
91	539.65	16.70
92	523.25	16.10
93	507.35	15.70
94	491.90	15.20
95	476.90	14.80
96	462.30	14.40
97	448.10	14.00
98	434.30	13.60
99	420.95	13.10
100	408.00	12.80
101	395.35	12.50
102	383.05	12.10
103	371.15	11.70
104	359.60	11.40
105	348.35	11.10
106	337.40	10.80
107	326.80	10.40
108	316.50	10.20
109	306.50	9.80
110	296.80	9.60
111	287.35	9.30
112	278.15	9.10
113	269.20	8.80
114	260.55	8.50
115	252.15	8.30
116	244.00	8.00
117	236.05	7.90
118	228.30	7.60

k	z [m]	Δz [m]
119	220.85	7.30
120	213.60	7.20
121	206.50	7.00
122	199.60	6.80
123	192.95	6.50
124	186.50	6.40
125	180.20	6.20
126	174.05	6.10
127	168.10	5.80
128	162.35	5.70
129	156.75	5.50
130	151.30	5.40
131	146.00	5.20
132	140.85	5.10
133	135.85	4.90
134	131.00	4.80
135	126.30	4.60
136	121.75	4.50
137	117.30	4.40
138	112.95	4.30
139	108.75	4.10
140	104.70	4.00
141	100.75	3.90
142	96.90	3.80
143	93.15	3.70
144	89.50	3.60
145	85.95	3.50
146	82.55	3.30
147	79.25	3.30
148	76.00	3.20
149	72.85	3.10
150	69.80	3.00
151	66.85	2.90
152	63.95	2.90
153	61.15	2.70
154	58.45	2.70
155	55.80	2.60
156	53.25	2.50
157	50.75	2.50
158	48.30	2.40
159	45.95	2.30
160	43.65	2.30
161	41.45	2.20
162	39.30	2.20
163	37.20	2.00

k	z [m]	Δz [m]
164	35.20	2.00
165	33.20	2.00
166	31.25	1.90
167	29.40	1.80
168	27.60	1.80
169	25.85	1.70
170	24.15	1.70
171	22.50	1.60
172	20.90	1.60
173	19.30	1.60
174	17.75	1.50
175	16.30	1.50
176	14.85	1.50
177	13.45	1.40
178	12.10	1.40
179	10.75	1.30
180	9.50	1.30
181	8.25	1.30
182	7.05	1.20
183	5.90	1.20
184	4.75	1.10
185	3.65	1.10
186	2.55	1.10
187	1.50	1.00
188	0.50	1.00

Table A.2: Height z [m] a.s.l. of model layers (main levels) k and model layer thicknesses Δz [m] of the HR configuration

k	z [m]	Δz [m]
1	29107.17	1785.66
2	27374.09	1680.50
3	25743.08	1581.52
4	24208.13	1488.38
5	22763.58	1400.72
6	21404.11	1318.23
7	20124.70	1240.59
8	18920.64	1167.52
9	17787.50	1098.77
10	16721.08	1034.05
11	15717.48	973.16
12	14772.98	915.84
13	13884.11	861.90
14	13047.59	811.14
15	12260.33	763.37

k	z [m]	Δz [m]
16	11519.45	718.41
17	10822.19	676.10
18	10166.00	636.28
19	9548.46	598.81
20	8967.28	563.54
21	8420.33	530.35
22	7905.60	499.12
23	7421.18	469.72
24	6965.29	442.06
25	6536.25	416.02
26	6132.48	391.52
27	5752.49	368.47
28	5394.87	346.76
29	5058.32	326.34
30	4741.59	307.12
31	4443.51	289.03
32	4163.00	272.01
33	3899.00	255.99
34	3650.54	240.91
35	3416.73	226.73
36	3196.68	213.37
37	2989.58	200.81
38	2794.69	188.98
39	2611.27	177.85
40	2438.67	167.37
41	2276.22	157.52
42	2123.34	148.24
43	1979.46	139.51
44	1844.06	131.29
45	1716.64	123.57
46	1596.71	116.28
47	1483.85	109.43
48	1377.64	103.00
49	1277.68	96.92
50	1183.61	91.22
51	1095.08	85.84
52	1011.77	80.79
53	933.35	76.03
54	859.57	71.55
55	790.12	67.34
56	724.77	63.37
57	663.26	59.65
58	605.37	56.12
59	550.90	52.83
60	499.62	49.71

k	z [m]	Δz [m]
61	451.38	46.78
62	405.97	44.03
63	363.24	41.43
64	323.03	39.00
65	285.18	36.70
66	249.57	34.53
67	216.04	32.51
68	184.49	30.59
69	154.81	28.78
70	126.87	27.10
71	100.57	25.49
72	75.83	24.00
73	52.54	22.58
74	30.62	21.25
75	10.00	20.00

Table A.3: Height z [m] a.s.l. of model layers (main levels) k and model layer thicknesses Δz [m] of the MR configuration

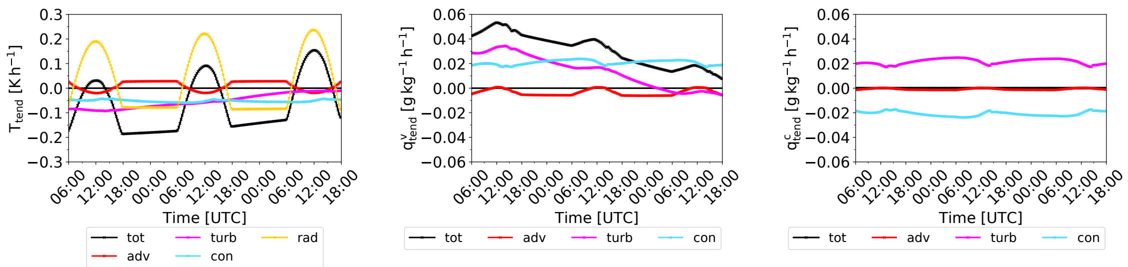

(a) **(b)** **(c)**

Figure A.2: Time series of (a) temperature (T_{tend} [K h^{-1}]), (b) specific humidity (q^v_{tend} [g kg^{-1} h^{-1}]), and (c) cloud water content (q^c_{tend} [g kg^{-1} h^{-1}]) tendencies in the model layer directly above cloud top from 16 October, 6 UTC until 18 October, 18 UTC for $K = 0.75\,\mathrm{m}^2\,s^{-1}$; tot: total tendency, adv: advection, turb: turbulent mixing, con: condensation/evaporation, rad: radiation.

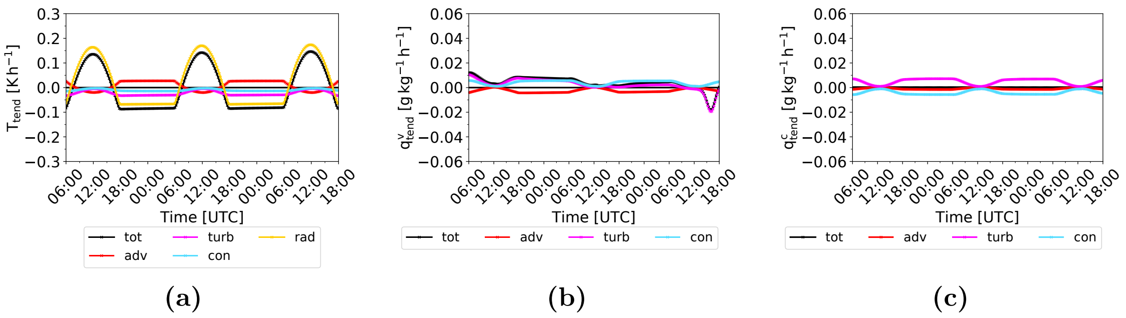

Figure A.3: Time series of (a) temperature ($\mathrm{T_{tend}}$ [$\mathrm{K\,h^{-1}}$]), (b) specific humidity ($\mathrm{q^{v}_{tend}}$ [$\mathrm{g\,kg^{-1}\,h^{-1}}$]), and (c) cloud water content ($\mathrm{q^{c}_{tend}}$ [$\mathrm{g\,kg^{-1}\,h^{-1}}$]) tendencies in the model layer directly above cloud top from 16 October, 6 UTC until 18 October, 18 UTC for $K = 0.01\,\mathrm{m}^2\,s^{-1}$; tot: total tendency, adv: advection, turb: turbulent mixing, con: condensation/evaporation, rad: radiation.

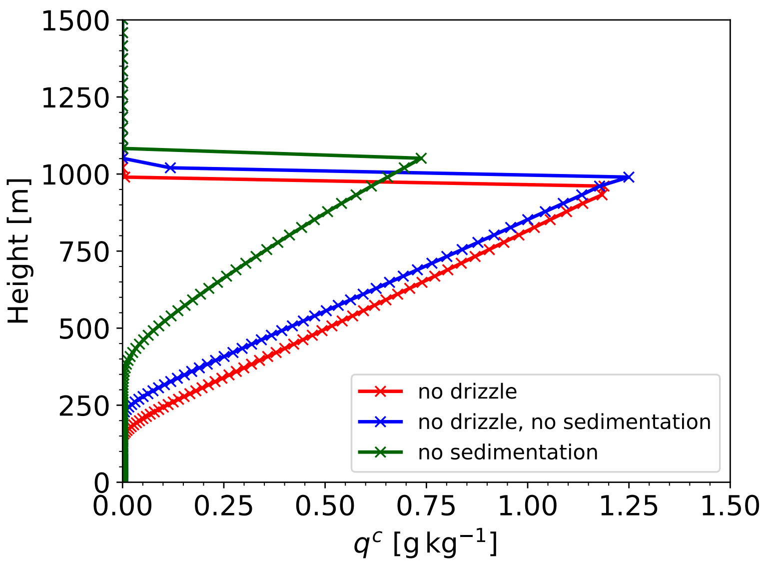

Figure A.4: Vertical profiles of the cloud water content q^c [$\mathrm{g\,kg^{-1}}$] for simulations with sedimentation and without drizzle (red), without sedimentation and without drizzle (blue), with drizzle and without sedimentation (green) at 16 October, 6 UTC

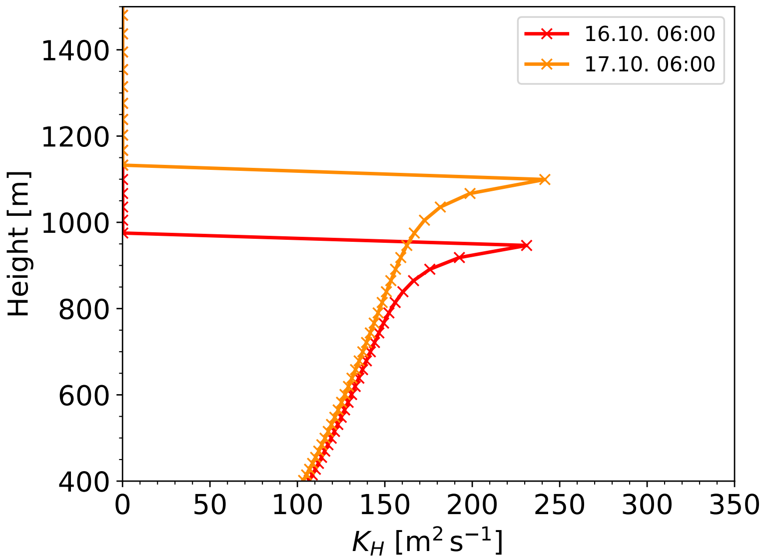

Figure A.5: Vertical profiles of the turbulent diffusion coefficient for scalars K_H [$\mathrm{m^2\,s^{-1}}$] at different times for COSMO-HR.

A.3 CS1819

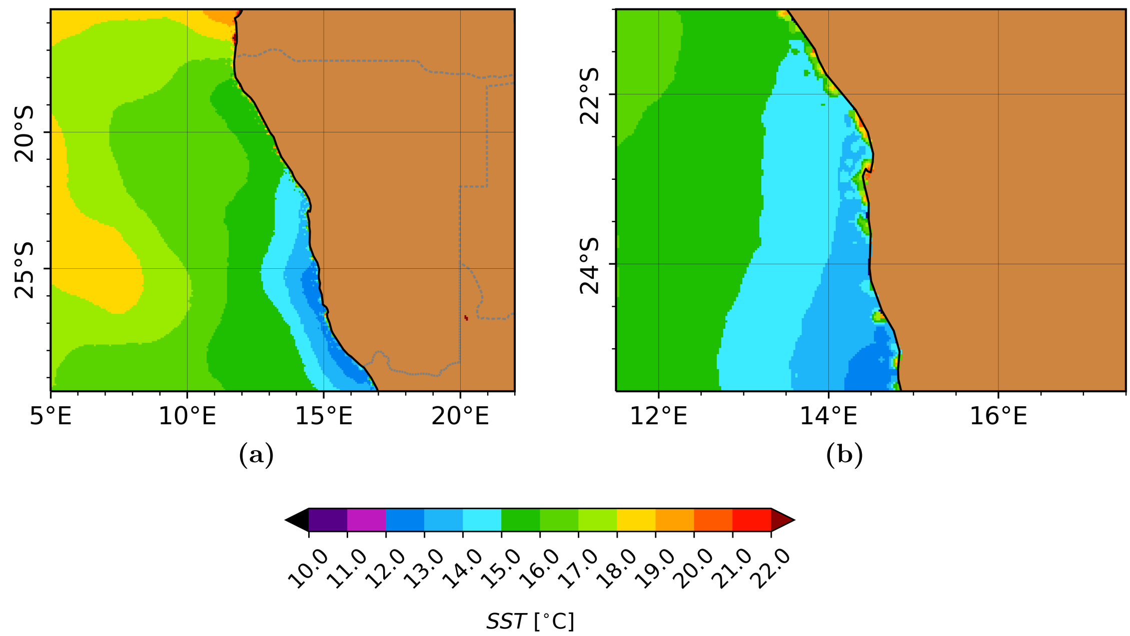

Figure A.6: Spatial distribution of sea surface temperature SST [°C] for (a) the nesting domain and (b) the inner domain of COSMO-FOG.

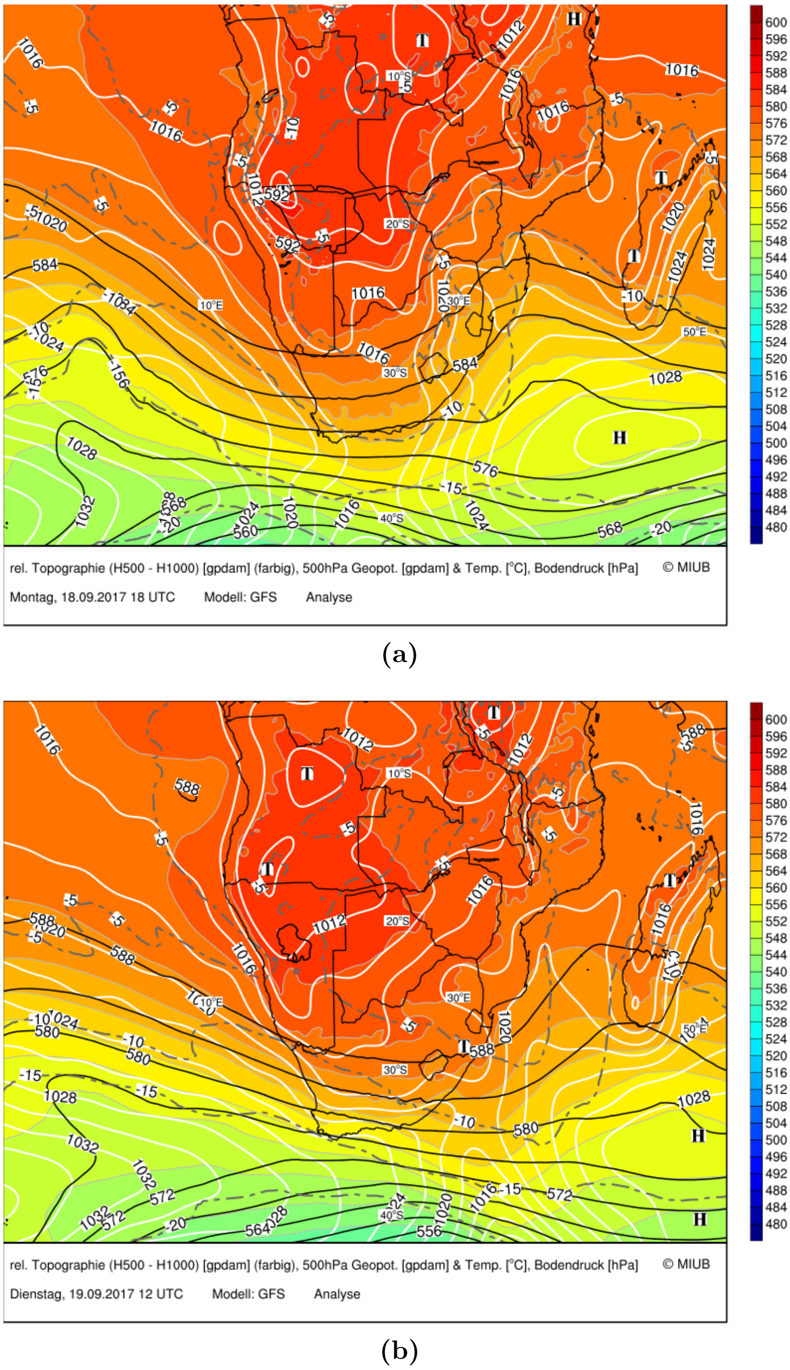

Figure A.7: Synoptic situation on 18 and 19 September 2017, Courtesy of Andre Demers (Institute of Geosciences, Section Meteorology, University of Bonn) and Dr. Michael Langguth (Institute of Geosciences, Section Meteorology, University of Bonn, now at Forschungszentrum Jülich)

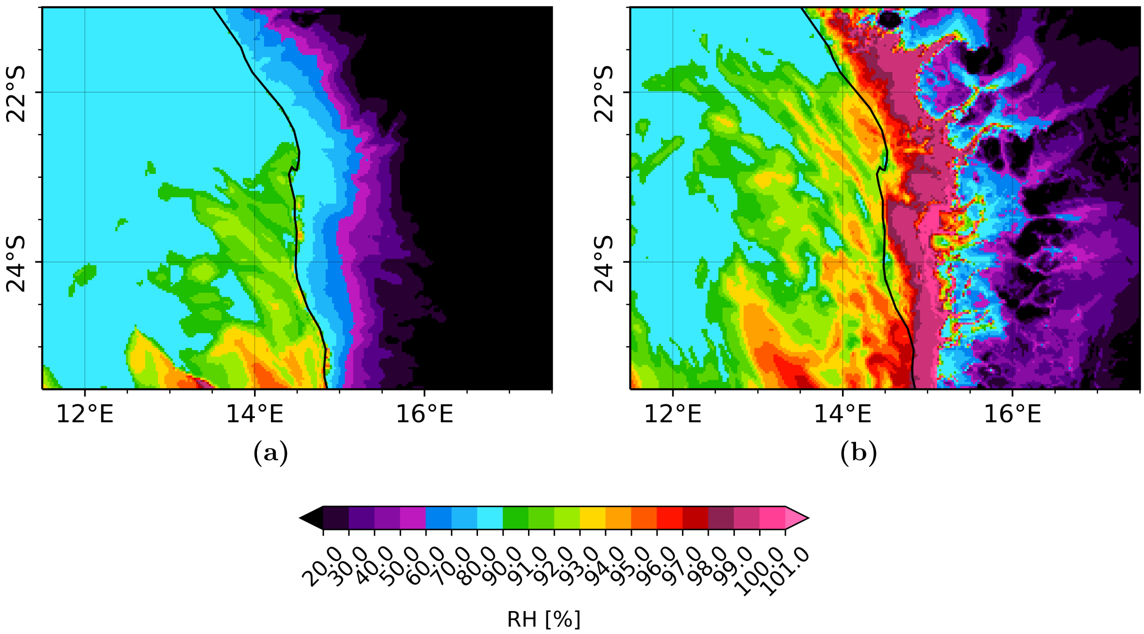

Figure A.8: Spatial distribution of relative humidity *RH* [%] at 14 UTC (a) and 21 UTC (b) for 18 September 2017

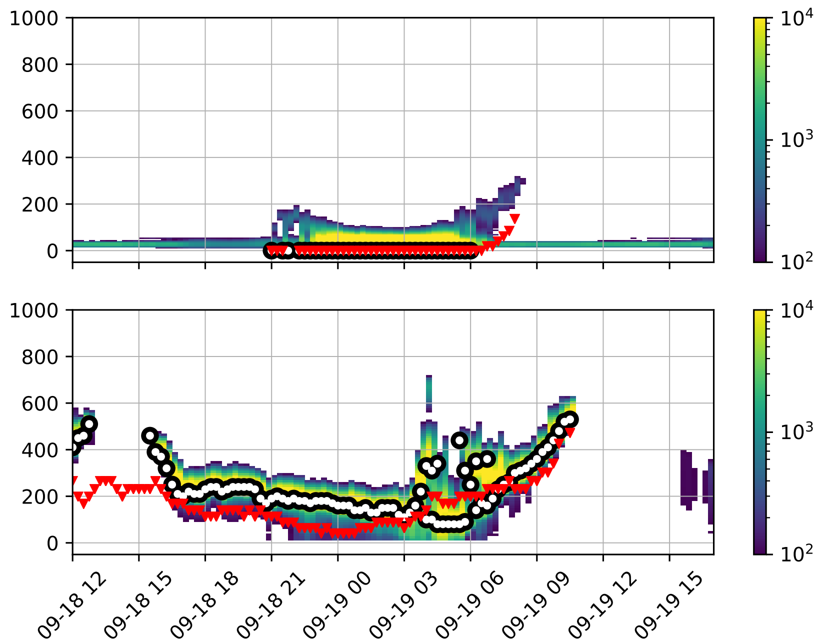

Figure A.9: Ceilometer measurements of cloud base height (black circles) and simulated cloud base height (red triangles) for Gobabeb (top) and Coastal Met (bottom) for CS1819. Courtesy of Dr. Robert Spirig (Department of Environmental Sciences, University of Basel, now at Departement Umweltsystemwissenschaften, ETH Zürich).

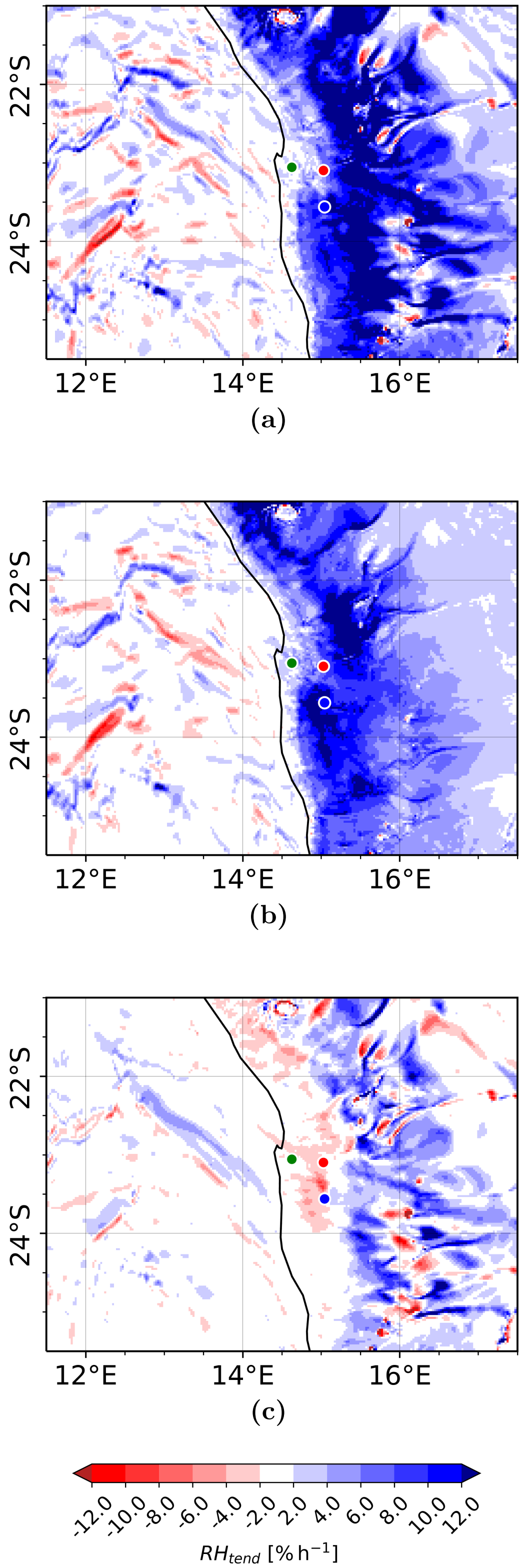

Figure A.10: Spatial distribution of (a) relative humidity change [$\% \, h^{-1}$] and its individual contributions by (b) temperature and (c) specific humidity on 18 September 2017 at 17 UTC determined using Equation 2.1.

A.4 CS2021, CS2324 and CS2728

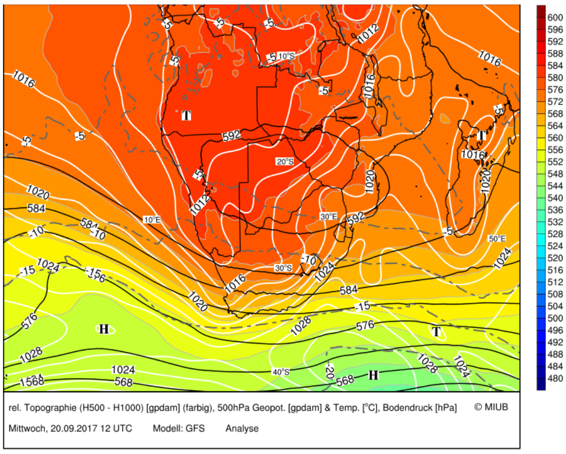

(a)

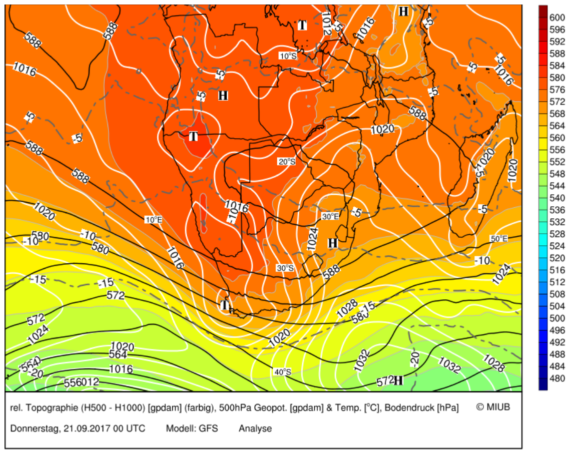

(b)

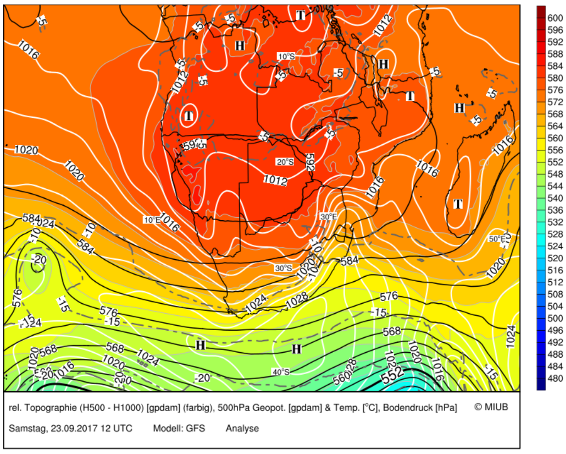

(c)

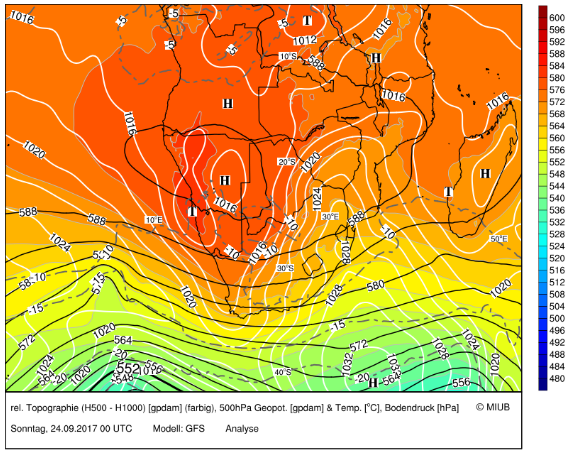

(d)

Figure A.11: Synoptic situation on 20–21 September 2017 (top) and on 23–24 September 2017 (bottom), Courtesy of Andre Demers (Institute of Geosciences, Section Meteorology, University of Bonn) and Dr. Michael Langguth (Institute of Geosciences, Section Meteorology, University of Bonn, now at Forschungszentrum Jülich)

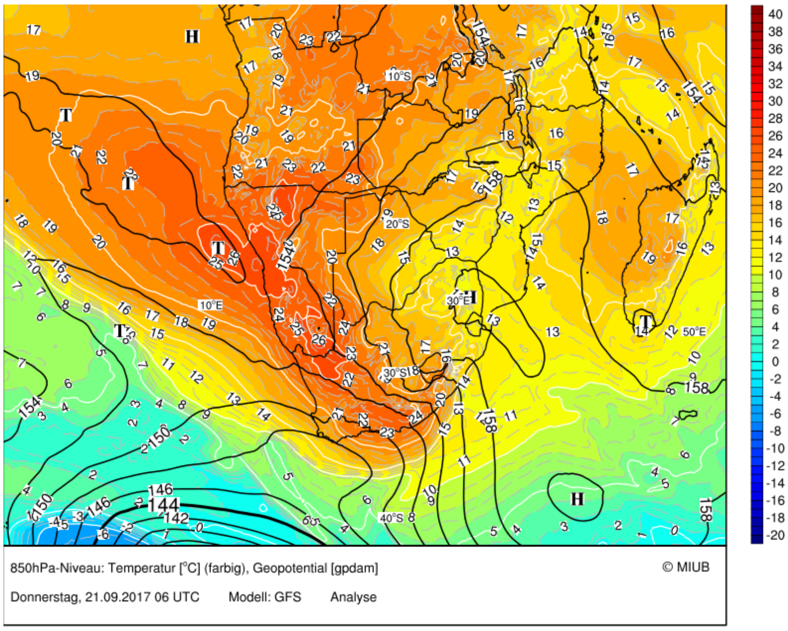

(a)

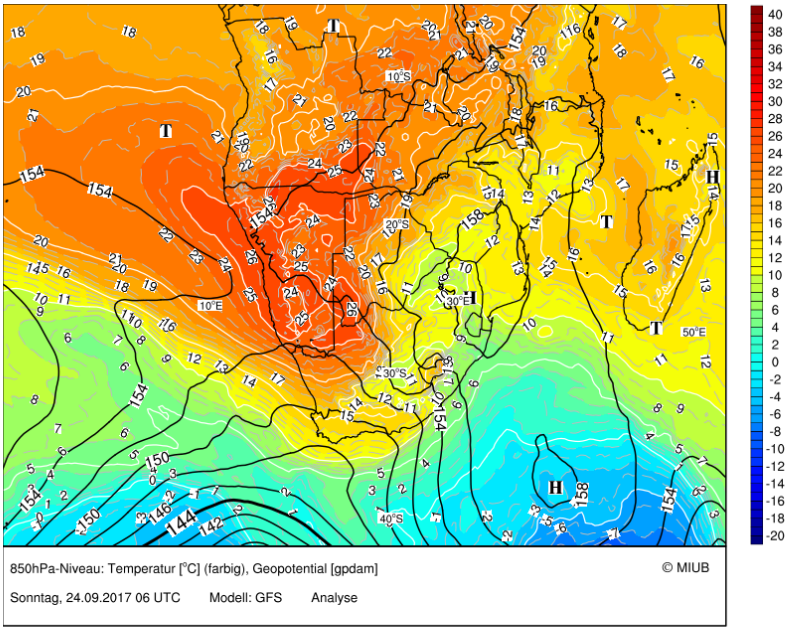

(b)

Figure A.12: Temperature at 850 hPa level on 21 September 2017 (top) and on 24 September 2017 (bottom) at 6 UTC, Courtesy of Andre Demers (Institute of Geosciences, Section Meteorology, University of Bonn) and Dr. Michael Langguth (Institute of Geosciences, Section Meteorology, University of Bonn, now at Forschungszentrum Jülich)

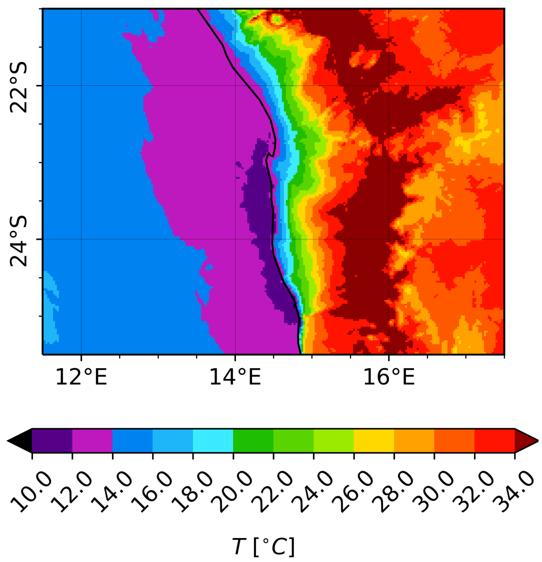

(a) 15 UTC

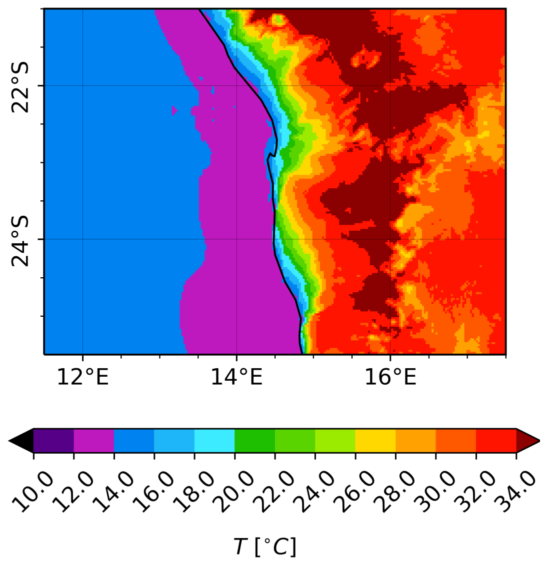

(b) 15 UTC

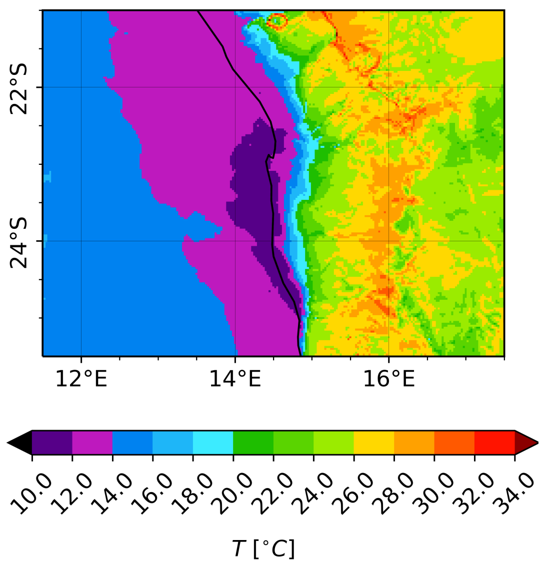

(c) 18 UTC

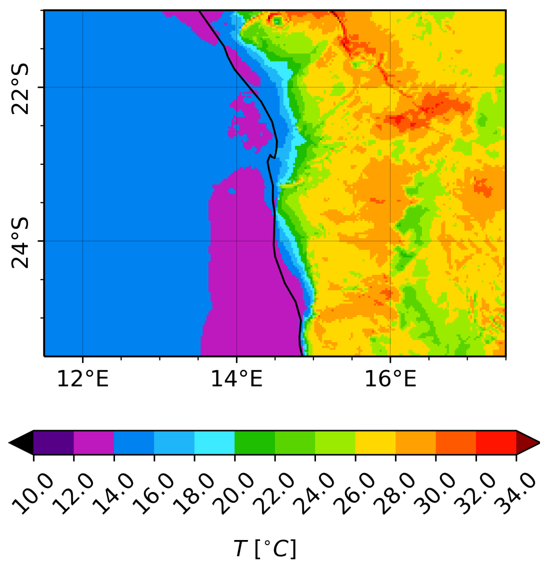

(d) 18 UTC

Figure A.13: Spatial distribution of temperature T [°C] in the lowest model layer on (a, c) 20 September and (b, d) 23 September 2017 at 15 UTC (top) and 18 UTC (bottom).

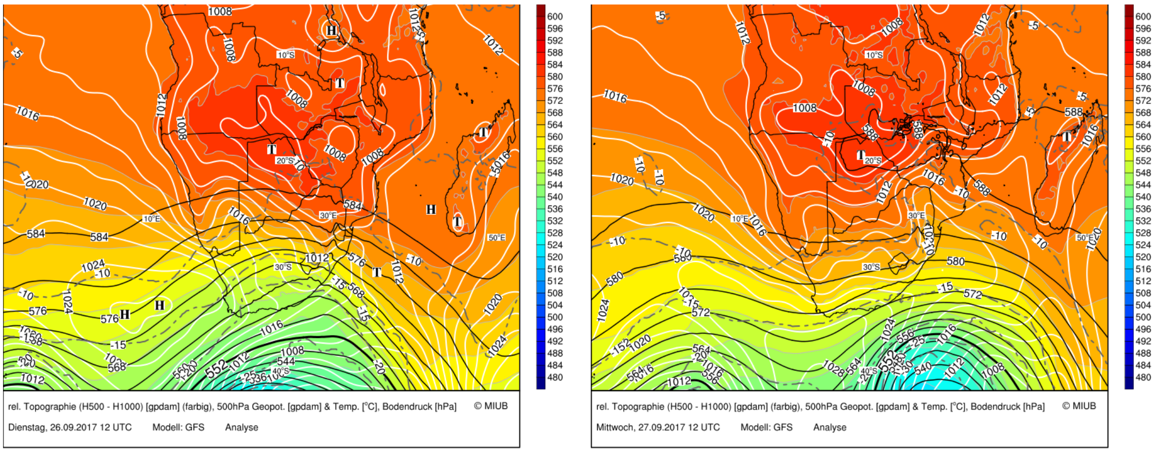

(a) a **(b)** b

Figure A.14: Synoptic situation on 27 and 28 September 2017, Courtesy of Andre Demers (Institute of Geosciences, Section Meteorology, University of Bonn) and Dr. Michael Langguth (Institute of Geosciences, Section Meteorology, University of Bonn, now at Forschungszentrum Jülich)

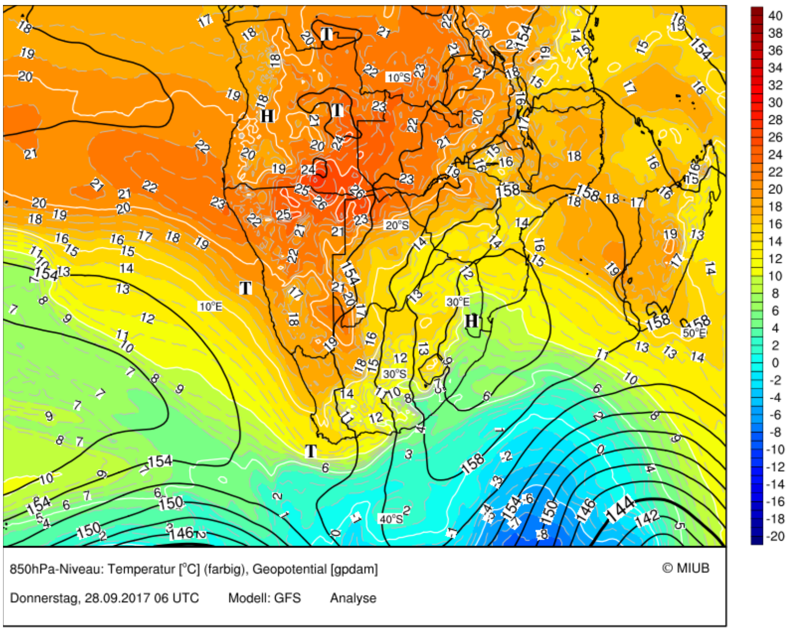

Figure A.15: Temperature at 850 hPa level on 28 September 2017 at 6 UTC, Courtesy of Andre Demers (Institute of Geosciences, Section Meteorology, University of Bonn) and Dr. Michael Langguth (Institute of Geosciences, Section Meteorology, University of Bonn, now at Forschungszentrum Jülich)

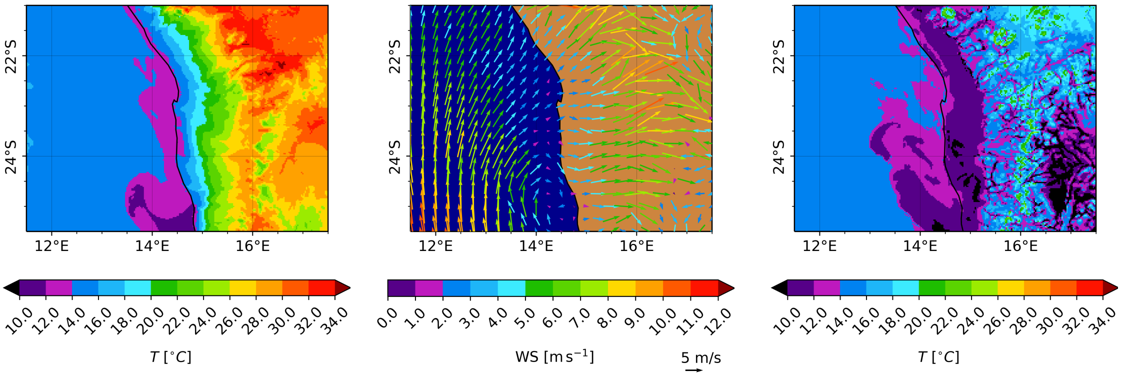

(a) 15 UTC **(b)** 15 UTC **(c)** 1 UTC

Figure A.16: Spatial distribution of (a, c) temperature T [°C] and (b) horizontal wind WS [$\mathrm{m\,s^{-1}}$] in the lowest model layer on 27 and 28 September 2017 at different times.

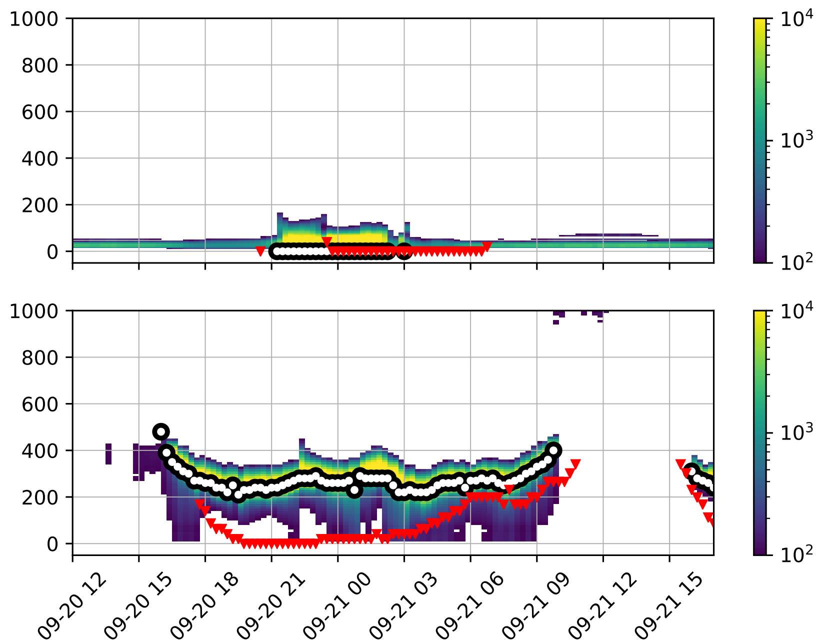

Figure A.17: Ceilometer measurements of cloud base height (black circles) and simulated cloud base height (red triangles) for Gobabeb (top) and Coastal Met (bottom) for CS2021. Courtesy of Dr. Robert Spirig (Department of Environmental Sciences, University of Basel, now at Departement Umweltsystemwissenschaften, ETH Zürich).

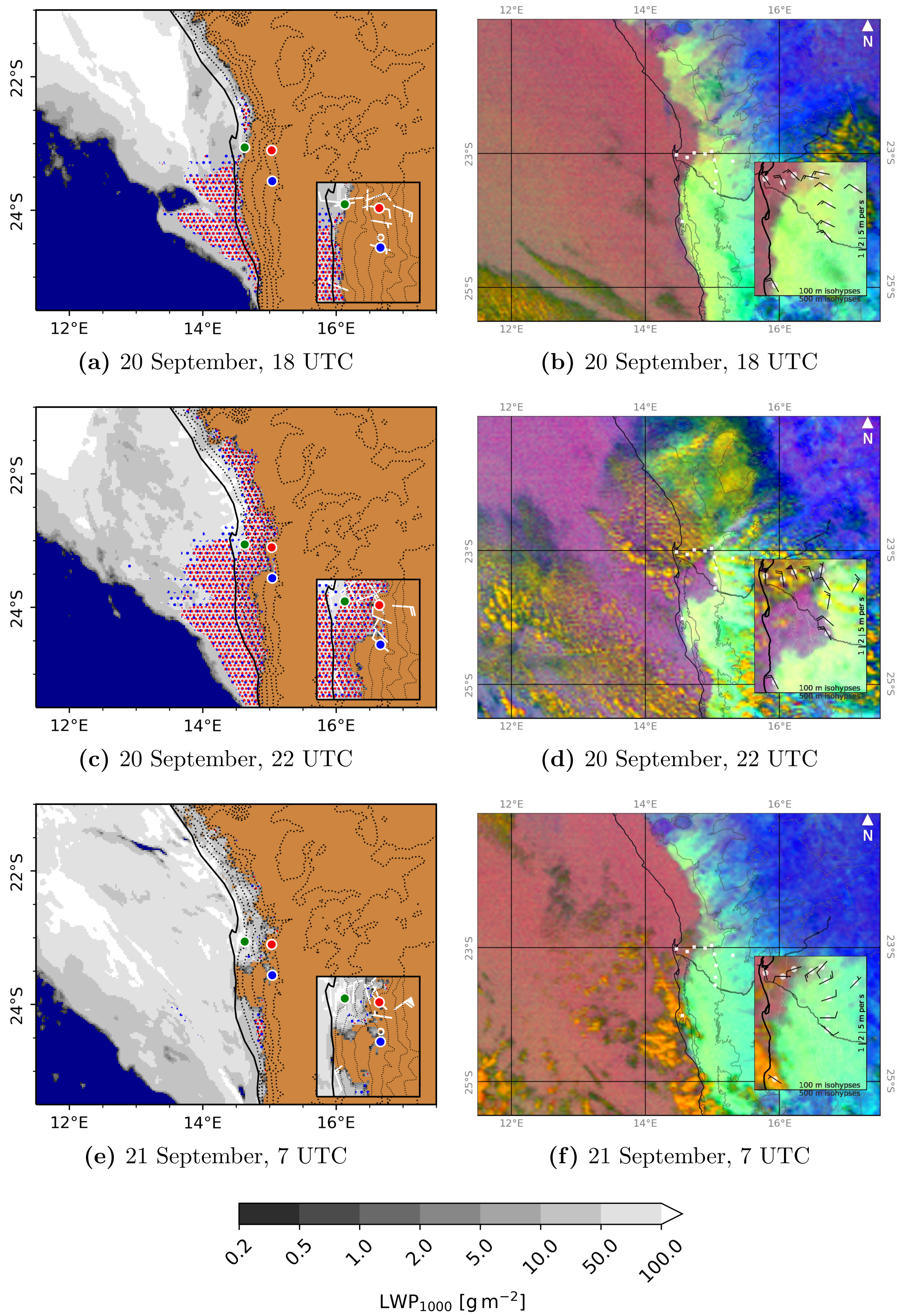

Figure A.18: Left: LWP_{1000} [$\mathrm{g\,m^{-2}}$] for CS2021 simulated with COSMO-FOG. Small blue and red dots mark the occurrence of ground fog. Coastal Met (green), Vogelfederberg (red) and Gobabeb (blue). Right: Dust composite from Meteosat with FogNet data for CS2021. Dark magenta colors mark FLCs. Wind barbs represent 15 minute averages of wind speed and direction at the FogNet stations. Courtesy of Dr. Robert Spirig (Department of Environmental Sciences, University of Basel, now at Departement Umweltsystemwissenschaften, ETH Zürich).

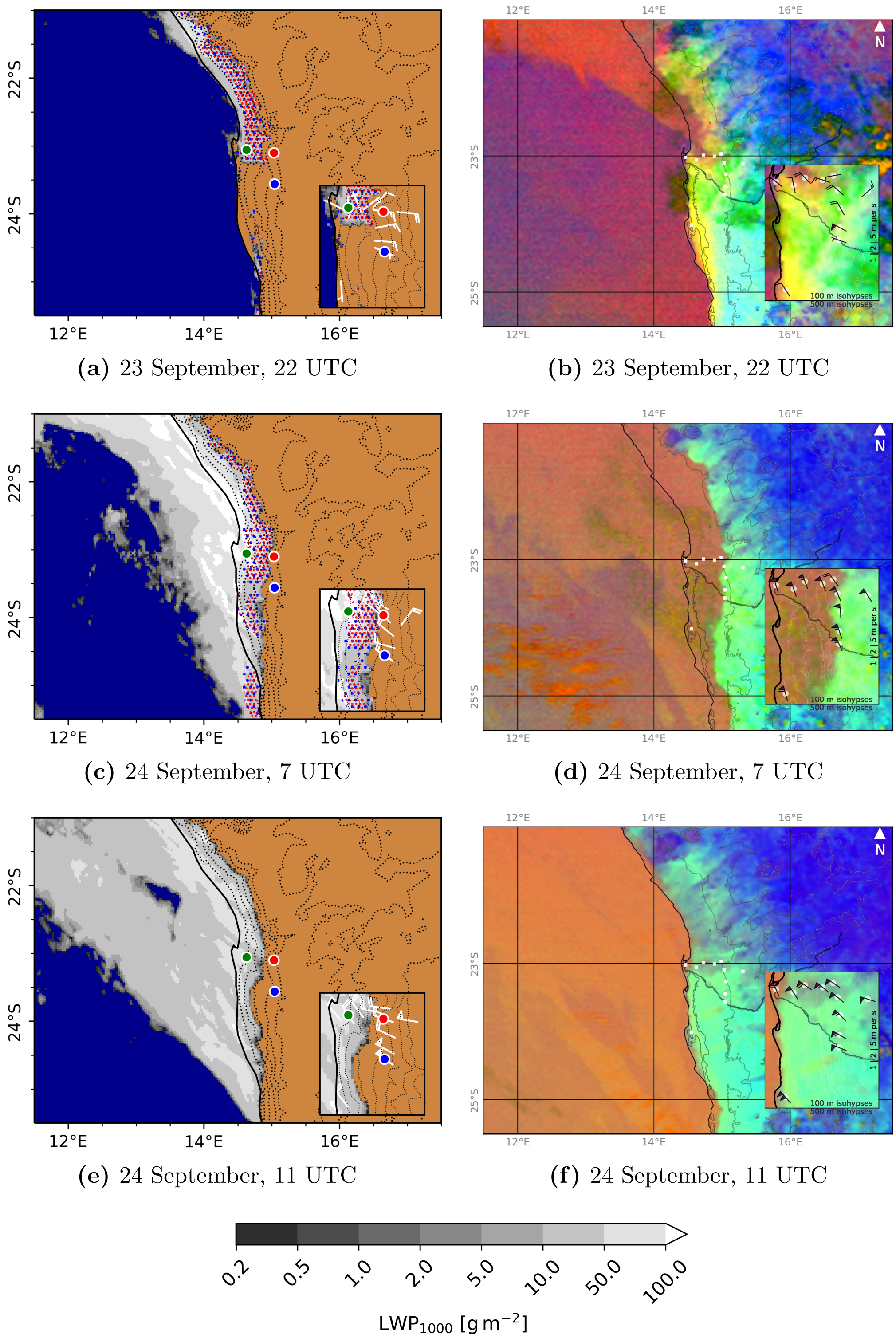

(a) 23 September, 22 UTC

(b) 23 September, 22 UTC

(c) 24 September, 7 UTC

(d) 24 September, 7 UTC

(e) 24 September, 11 UTC

(f) 24 September, 11 UTC

Figure A.19: Left: LWP_{1000} [$\mathrm{g\,m^{-2}}$] for CS2324 simulated with COSMO-FOG. Small blue and red dots mark the occurrence of ground fog. Coastal Met (green), Vogelfederberg (red) and Gobabeb (blue). Right: Dust composite from Meteosat with FogNet data for CS2324. Ochre colors mark FLCs. Wind barbs represent 15 minute averages of wind speed and direction at the FogNet stations. Courtesy of Dr. Robert Spirig (Department of Environmental Sciences, University of Basel, now at Departement Umweltsystemwissenschaften, ETH Zürich).

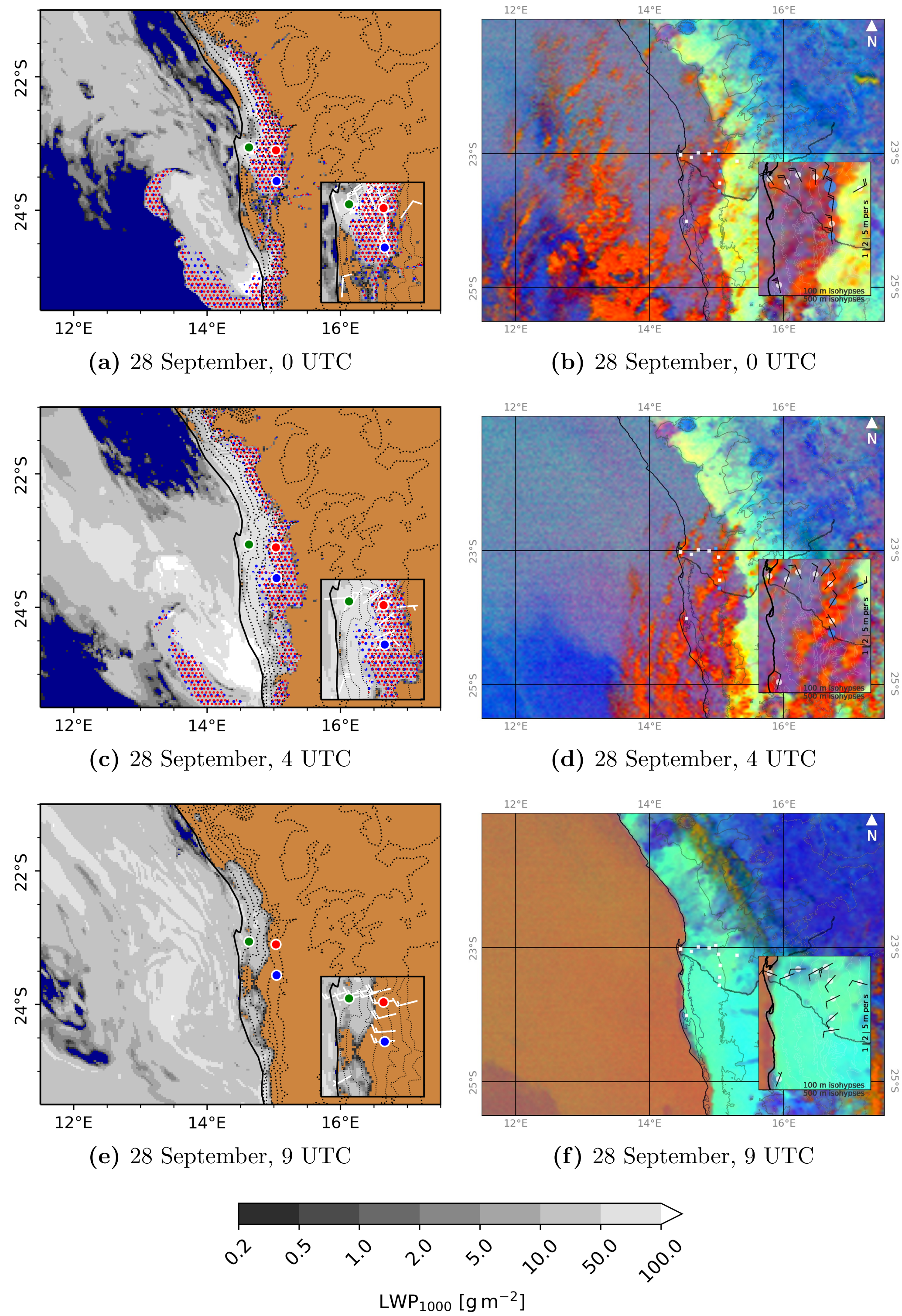

(a) 28 September, 0 UTC

(b) 28 September, 0 UTC

(c) 28 September, 4 UTC

(d) 28 September, 4 UTC

(e) 28 September, 9 UTC

(f) 28 September, 9 UTC

Figure A.20: Left: LWP$_{1000}$ [g m^{-2}] for CS2728 simulated with COSMO-FOG. Small blue and red dots mark the occurrence of ground fog. Coastal Met (green), Vogelfederberg (red) and Gobabeb (blue). Right: Dust composite from Meteosat with FogNet data for CS2728. Violet (b,d) and ochre (f) colors mark FLCs. Wind barbs represent 15 minute averages of wind speed and direction at the FogNet stations. Courtesy of Dr. Robert Spirig (Department of Environmental Sciences, University of Basel, now at Departement Umweltsystemwissenschaften, ETH Zürich).

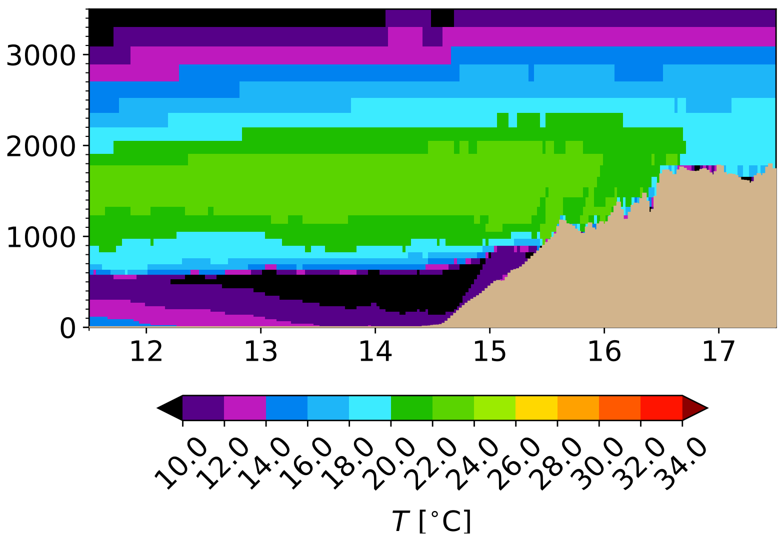

(a)

Figure A.21: Vertical cross section of temperature [°C] for 19 September 2017 at 3 UTC from 11.5 to 17.5 °E at 23 °S. Brown areas mark terrain height.

List of symbols and abbreviations

Symbols

C	empirical constant in the Twomey relation	$[\mathrm{m}^{-3}]$
c_p/c_v	specific heat at constant pressure/volume	$[\mathrm{J\,kg^{-1}\,K^{-1}}]$
D	cloud droplet diametre	$[\mu\mathrm{m}]$
D_0	mean cloud droplet diametre	$[\mu\mathrm{m}]$
$D_{c,eva}$	critical diametre of the largest evaporating droplet	$[\mu\mathrm{m}]$
D_v	water vapour diffusivity	$[\mathrm{m^2\,s^{-1}}]$
e	water vapour pressure	[Pa]
e_{sat}	saturation vapour pressure over plane water surface	[Pa]
$\mathbf{F}^{l/f}$	turbulent flux of liquid/frozen water	$[\mathrm{kg\,m^{-2}\,s^{-1}}]$
$\mathbf{F}^{v}$	turbulent flux of water vapour	$[\mathrm{kg\,m^{-2}\,s^{-1}}]$
$\mathbf{g}$	acceleration of gravity	$[\mathrm{m\,s^{-2}}]$
$\mathbf{H}$	heat flux vector	$[\mathrm{W\,m^{-2}}]$
$I^{l/f}$	phase transition rate of liquid/frozen water	$[\mathrm{kg\,m^{-3}\,s^{-1}}]$
k	empirical constant (exponent) in the Twomey relation	[1]
K	thermal conductivity	$[\mathrm{W\,m^{-1}\,K^{-1}}]$
$L_{v/s}$	latent heat of vaporisation/sublimation	$[\mathrm{m^2\,s^{-2}}]$
N^a	number of dry aerosol particles	$[\mathrm{m}^{-3}]$
N_{act}	number of activated condensation nuclei	$[\mathrm{m}^{-3}]$
N^c	total number concentration of cloud droplets	$[\mathrm{m}^{-3}]$
p	atmospheric pressure	[Pa]
$\mathbf{P}^{l/f}$	diffusion flux of liquid/frozen water	$[\mathrm{kg\,m^{-2}\,s^{-1}}]$
q^c	(mass) specific content of cloud water	$[\mathrm{kg\,kg^{-1}}]$
q^d	(mass) specific content of drizzle	$[\mathrm{kg\,kg^{-1}}]$
q^g	(mass) specific content of graupel	$[\mathrm{kg\,kg^{-1}}]$
q^i	(mass) specific content of ice	$[\mathrm{kg\,kg^{-1}}]$
$q^{l/f}$	(mass) specific content of liquid/frozen water	$[\mathrm{kg\,kg^{-1}}]$
q^r	(mass) specific content of rain	$[\mathrm{kg\,kg^{-1}}]$
q^s	(mass) specific content of snow	$[\mathrm{kg\,kg^{-1}}]$
q^t	(mass) specific total water content	$[\mathrm{kg\,kg^{-1}}]$
q^v	(mass) specific content of water vapour	$[\mathrm{kg\,kg^{-1}}]$
q^v_{sat}	saturation specific water vapor content	$[\mathrm{kg\,kg^{-1}}]$
$\mathbf{R}$	radiative net flux	$[\mathrm{W\,m^{-2}}]$
R_d	gas constant of dry air	$[\mathrm{m^2\,s^{-2}}]$
Re	Reynolds number	[1]
RH	relative humidity	[1]
R_v	gas constant for water vapour	$[\mathrm{m^2\,s^{-2}}]$

r^v_{sat}	saturation mixing ratio of water	$[\mathrm{kg\,kg^{-1}}]$
S	supersaturation	[1]
$\overline{S}$	average supersaturation	[1]
T	temperature	[K,°C]
$\underline{\mathbf{T}}$	general stress tensor	$[\mathrm{kg\,m^{-1}\,s^{-2}}]$
t	time	[s]
v	settling velocity of the droplets	$[\mathrm{m\,s^{-1}}]$
$\mathbf{v}^{l,f}_T$	mean terminal fall velocities of particles	$[\mathrm{m\,s^{-1}}]$
VIS	visibility	[m]
z	height (position in vertical direction)	[m]
ζ	generalised terrain-following height coordinate	[1]
θ	potential temperature	[K,°C]
θ_e	equivalent potential temperature	[K,°C]
θ_v	virtual potential temperature	[K,°C]
ρ	air density	$[\mathrm{kg\,m^{-3}}]$
ρ_w	density of water	$[\mathrm{kg\,m^{-3}}]$
σ_c	dispersion parameter of the log-normal distribution	[1]
$\mathbf{\Omega}$	angular velocity of the earth	$[\mathrm{s^{-1}}]$

Abbreviations

AEROCLO-sA	Aerosol, Radiation and Clouds in southern Africa	
a.s.l.	above sea level	[m]
CCN	cloud condensation nuclei	
COSMO	Consortium for Small-scale Modeling	
COSMO-DE	former operational model configuration	
COSMO-FOG	COSMO including microphysical parametrisation from PAFOG	
DWD	Deutscher Wetterdienst (German Meteorological Service)	
ETH	Eidgenössische Technische Hochschule	
FLC	fog and low stratiform cloud	
HR	high resolution	
ICON	Icosahedral non-hydrostatic	
IOP	intensive observation period	
IR	infra-red	
LM	Lokal Modell	
LR	low resolution	
LÜ	Lüderitz	
LWP	liquid water path	$[\mathrm{g\,m^{-2}}]$
LWP_1000	liquid water path integrated between surface and 1000 m	$[\mathrm{g\,m^{-2}}]$
MBL	marine boundary layer	
ME	mean error	
MESSy	Modular Earth Submodel System	
MR	medium resolution	
MSG	Meteosat Second Generation	
NaFoLiCA	Namib Fog Life Cycle Analysis	
Nml	namelist	

NWP	numerical weather prediction	
PBL	planetary boundary layer	
R^2	correlation coefficient	
RGB	red, green, blue	
RH	relative humidity	[%]
RMSE	root mean square error	
SASSCAL	Southern African Science Service Centre for Climate Change	
SEVIRI	Spinning Enhanced Visible and Infrared Imager	
SFC	Standard Fog Collector	
SK	Swakopmund	
SST	sea surface temperature	[°C]
TBS	tethered balloon sonde	
TERRA-ML	multi-layer soil model	
TKE	turbulent kinetic energy	[$m^2\,s^{-2}$]
UAV	unmanned aerial vehicle	
UM	Unified Model	
WB	Walvis Bay	
WH	Windhoek	
WMO	World Meteorological Organisation	
WRF	Weather Research and Forecasting	
WRF-NMM	WRF non-hydrostatic meso-scale model	

Bibliography

Albrecht, B. A. et al. (1995). "The Atlantic Stratocumulus Transition Experiment – ASTEX". In: *Bulletin of the American Meteorological Society* 76.6, pp. 889–904. DOI: https://doi.org/10.1175/1520-0477(1995)076<0889:TASTE>2.0.CO;2. URL: https://journals.ametsoc.org/view/journals/bams/76/6/1520-0477_1995_076_0889_taste_2_0_co_2.xml.

Allan, S. S., S. G. Gaddy, and J. E. Evans (2001). *Delay Causality and Reduction at the New York City Airports Using Terminal Weather Information Systems.* Tech. rep. Massachusetts Institute of Technology, Lincoln Laboratory.

American Meteorological Society (2024). *Glossary of Meteorology.* URL: https://glossary.ametsoc.org/wiki/Fog (visited on 05/19/2024).

Andersen, H. and J. Cermak (2018). "First fully diurnal fog and low cloud satellite detection reveals life cycle in the Namib". In: *Atmospheric Measurement Techniques* 11.10.

Andersen, H. et al. (2019). "Spatiotemporal dynamics of fog and low clouds in the Namib unveiled with ground-and space-based observations". In: *Atmospheric Chemistry and Physics* 19.7, pp. 4383–4392.

Andersen, H. et al. (2020). "Synoptic-scale controls of fog and low-cloud variability in the Namib Desert". In: *Atmospheric Chemistry and Physics* 20.6, pp. 3415–3438.

Andersen, H. et al. (2022). "Attribution of Observed Recent Decrease in Low Clouds Over the Northeastern Pacific to Cloud-Controlling Factors". In: *Geophysical Research Letters* 49.3, e2021GL096498. DOI: https://doi.org/10.1029/2021GL096498. eprint: https://agupubs.onlinelibrary.wiley.com/doi/pdf/10.1029/2021GL096498. URL: https://agupubs.onlinelibrary.wiley.com/doi/abs/10.1029/2021GL096498.

Babić, K. et al. (2019). "The observed diurnal cycle of low-level stratus clouds over southern West Africa: a case study". In: *Atmospheric Chemistry and Physics* 19.2, pp. 1281–1299. DOI: 10.5194/acp-19-1281-2019. URL: https://acp.copernicus.org/articles/19/1281/2019/.

Baldauf, M. et al. (2011). "Operational Convective-Scale Numerical Weather Prediction with the COSMO Model: Description and Sensitivities". In: *Mon. Wea. Rev.* 139, pp. 3887–3905.

Ballard, S. P., B. W. Golding, and R. N. B. Smith (1991). "Mesoscale Model Experimental Forecasts of the Haar of Northeast Scotland". In: *Monthly Weather Review* 119.9, pp. 2107–2123.

Bartok, J., A. Bott, and M. Gera (2012). "Fog Prediction for Road Traffic Safety in a Coastal Desert Region". In: *Boundary-Layer Meteorol.* 145, pp. 485–506.

Bauer, P., A. Thorpe, and G. Brunet (2015). “The quiet revolution of numerical weather prediction”. In: *Nature* 525.7567, pp. 47–55. DOI: https://doi.org/10.1038/nature14956.

Bendix, J., W. Eugster, and O. Klemm (2011). “FOG—BOON OR BANE?” In: *Erdkunde*, pp. 229–232.

Bergot, T. et al. (2007). “Intercomparison of single-column numerical models for the prediction of radiation fog”. In: *Journal of Applied Meteorology and Climatology* 46.4, pp. 504–521.

Berry, E. and M. Pranger (1974). “Equations for Calculating the Terminal Velocities of Water Drops”. In: *Journal of Applied Meteorology* 13, pp. 108–113.

Blahak, U. (2015). *Simulating idealized cases with the COSMO-model.* (also available at www.cosmo-model.org). Consortium for small scale modelling. Deutscher Wetterdienst. Offenbach, Germany.

Böhm, C. (2020). “Atmospheric water supply to the Atacama Desert from newly developed satellite remote sensing techniques and reanalysis”. PhD thesis. Universität zu Köln.

Bollmeyer, C. et al. (2015). “A high-resolution regional reanalysis for the European CORDEX region”. In: *EGUGA*, p. 11209.

Boss, G. (1941). “Niederschlagsmenge und Salzgehalt des Nebelwassers an der Küste Deutsch-Südwestafrikas”. In: *Bioklimatische Beiblätter der Meteorologischen Zeitschrift* 8. Ed. by Prof. Dr. Franz Linke and Dr. Ferdinand Steinhauser.

Bott, A (1989). “A Positive Definite Advection Scheme Obtained by Nonlinear Renormalization of the Advective Fluxes”. In: *Monthly Weather Review* 117, pp. 1006–1015.

— (2016). *Synoptische Meteorologie. Methoden der Wetteranalyse und -prognose.* 2nd edition. Heidelberg, Germany: Springer. 534 pp. DOI: 10.1007/978-3-662-48195-0.

— (2020). “Comparison of a Spectral Microphysics and a Two-Moment Cloud Scheme: Numerical Simulations of the Cloud-Topped Marine Boundary Layer”. In: *Bound. Layer Meteor.* 175, pp. 153–178.

— (2021). “Comparison of a spectral microphysics and a two-moment cloud scheme: Numerical simulation of a radiation fog event”. In: *Atmospheric Research* 262, p. 105787. ISSN: 0169-8095. DOI: https://doi.org/10.1016/j.atmosres.2021.105787. URL: https://www.sciencedirect.com/science/article/pii/S0169809521003434.

Bott, A., U. Sievers, and W. Zdunkowski (1990). “A Radiation Fog Model with a Detailed Treatment of the Interaction between Radiative Transfer and Fog Microphysics”. In: *J. Atmos. Sci.* 47, pp. 2153–2166.

Bott, A. and T. Trautmann (1997). *Entwicklung eines Nebelvorhersagemodells mit parametrisierter Tropfenmikrophysik - Dokumentation von PAFOG.* Tech. rep. Institut für Physik der Atmosphäre Johannes Gutenberg-Universität Mainz.

— (2002). “PAFOG - a new efficient forecast model of radiation fog and low-level stratiform clouds”. In: *Atmos. Res.* 64, pp. 191–203.

Bott, A., T. Trautmann, and W. Zdunkowski (1996). “A numerical model of the cloud-topped planetary boundary-layer: Radiation, turbulence and spectral microphysics in marine stratus". In: *Quart. J. Roy. Meteor. Soc.* 122, pp. 635–667.

Boutle, I. et al. (2022). "Demistify: a large-eddy simulation (LES) and single-column model (SCM) intercomparison of radiation fog". In: *Atmospheric Chemistry and Physics* 22.1, pp. 319–333.

Boutle, I. A. and S. J. Abel (2012). "Microphysical controls on the stratocumulus topped boundary-layer structure during VOCALS-REx". In: *Atmospheric Chemistry and Physics* 12.6, pp. 2849–2863.

Boutle, I. A. et al. (2016). "The London Model: forecasting fog at 333 m resolution". In: *Quarterly Journal of the Royal Meteorological Society* 142.694, pp. 360–371.

Broza, M. (1979). "Dew, fog and hygroscopic food as a source of water for desert arthropods". In: *Journal of Arid Environments* 2.1, pp. 43–49.

Bruijnzeel, L. A. S., W. Eugster, and R. Burkard (2006). "Fog as a Hydrologic input". In: *Encyclopedia of hydrological sciences.*

Buzzi, M. (2008). "Challenges in Operational Numerical Weather Prediction at High Resolution in Complex Terrain." PhD thesis. Swiss Federal Institute of Technology (ETH) Zürich.

Buzzi, M. et al. (2011). "Evaluation of the COSMO-SC turbulence scheme in a shear-driven stable boundary layer". In: *Meteorologische Zeitschrift (Berlin)* 20.

Campbell Scientific (2012). *Wind Monitors (05103/05103LM, 05305, 05106 and 05103-45), User Guide.* Campbell Scientific Ltd. Shepshed, Loughborough, UK.

— (2018). *CS215 Temperature and Relative Humidity Probe.* Campbell Scientific (Canada) Corp. Edmonton, Canada.

— (2019). *IR100/IR120 Infra-red Remote Temperature Sensor.* Campbell Scientific Ltd. Shepshed, Loughborough, UK.

Carvajal, D. et al. (2022). "Assessing fog water collection in the coastal mountain range of Antofagasta, Chile". In: *Journal of Arid Environments* 198, p. 104679. ISSN: 0140-1963. DOI: `https://doi.org/10.1016/j.jaridenv.2021.104679`. URL: `https://www.sciencedirect.com/science/article/pii/S0140196321002457`.

Cereceda, P. et al. (2002). "Advective, orographic and radiation fog in the Tarapacá region, Chile". In: *Atmospheric Research* 64.1-4, pp. 261–271.

Cerenzia, I., F. Tampieri, and M. S. Tesini (2014). "Diagnosis of turbulence schema in stable atmospheric conditions and sensitivity tests". In: *Cosmo Newsletter* 14, pp. 1–11.

Cermak, J. (2012). "Low clouds and fog along the South-Western African coast – Satellite-based retrieval and spatial patterns". In: *Atmospheric Research* 116, pp. 15–21.

Chaumerliac, N. et al. (1987). "Sulfur scavenging in a mesoscale model with quasi-spectral microphysics: Two-dimensional results for continental and maritime clouds". In: *J. Geophys. Res.* 92, pp. 3114–3126.

Chen, C. et al. (2021). "A Case Study: Evaluation of PAFOG One-D Model With Advection in Simulations of Fog/Stratus From C-FOG Experiment". In: *Journal of Geophysical Research: Atmospheres* 126.20. e2021JD034812 2021JD034812, e2021JD034812. DOI: `https://doi.org/10.1029/2021JD034812`. URL: `https://agupubs.onlinelibrary.wiley.com/doi/abs/10.1029/2021JD034812`.

Doms, G. and M. Baldauf (2018). *A Description of the Nonhydrostatic Regional COSMO-Model. Part I: Dynamics and Numerics.* Ed. by Ulrich Schättler. (also available at www.cosmo-model.org). Consortium for small scale modelling. Deutscher Wetterdienst. Offenbach, Germany: Deutscher Wetterdienst. DOI: 10.5676/DWD_pub/nwv/cosmo-doc_5.05_I.

Doms, G. et al. (2018). *A Description of the Nonhydrostatic Regional COSMO-Model. Part II: Physical Parameterizations.* Ed. by Ulrich Schättler. (also available at www.cosmo-model.org). Consortium for small scale modelling. Deutscher Wetterdienst. Offenbach, Germany: Deutscher Wetterdienst. DOI: 10.5676/DWD_pub/nwv/cosmo-doc_5.05_II.

Ducongé, L. et al. (2020). "Fog in heterogeneous environments: the relative importance of local and non-local processes on radiative-advective fog formation". In: *Quarterly Journal of the Royal Meteorological Society* 146.731, pp. 2522–2546. DOI: https://doi.org/10.1002/qj.3783. eprint: https://rmets.onlinelibrary.wiley.com/doi/pdf/10.1002/qj.3783. URL: https://rmets.onlinelibrary.wiley.com/doi/abs/10.1002/qj.3783.

Duynkerke, P. G. (1989). "The Diurnal Variation of a Marine Stratocumulus Layer: A Model Sensitivity Study". In: *Monthly Weather Review* 117.8, pp. 1710–1725. DOI: https://doi.org/10.1175/1520-0493(1989)117<1710:TDVOAM>2.0.CO;2. URL: https://journals.ametsoc.org/view/journals/mwre/117/8/1520-0493_1989_117_1710_tdvoam_2_0_co_2.xml.

— (1991). "Radiation Fog: A Comparison of Model Simulation with Detailed Observations". In: *Monthly Weather Review* 119, pp. 324–341.

Duynkerke, P. G. et al. (2004). "Observations and numerical simulations of the diurnal cycle of the EUROCS stratocumulus case". In: *Quarterly Journal of the Royal Meteorological Society* 130.604, pp. 3269–3296. DOI: https://doi.org/10.1256/qj.03.139. eprint: https://rmets.onlinelibrary.wiley.com/doi/pdf/10.1256/qj.03.139. URL: https://rmets.onlinelibrary.wiley.com/doi/abs/10.1256/qj.03.139.

Ebner, M., T. Miranda, and A. Roth-Nebelsick (2011). "Efficient fog harvesting by Stipagrostis sabulicola (Namib dune bushman grass)". In: *Journal of arid environments* 75.6, pp. 524–531.

Eckardt, F. D. et al. (2013). "The nature of moisture at Gobabeb, in the central Namib Desert". In: *Journal of arid environments* 93, pp. 7–19.

Egli, S., B. Thies, and J. Bendix (2018). "A Hybrid Approach for Fog Retrieval Based on a Combination of Satellite and Ground Truth Data". In: *Remote Sensing* 10.4, p. 628.

Eichinger, R. and P. Jöckel (2014). "The generic MESSy submodel TENDENCY (v1.0) for process-based analyses in Earth system models". In: *Geosci. Model Dev.* 7.4, pp. 1573–1582. DOI: 10.5194/gmd-7-1573-2014. URL: https://www.ingentaconnect.com/content/doaj/1991959x/2014/00000007/00000004/art00019.

EUMETSAT (2024). *Meteosat 0 degree RGB Composites.* URL: https://eumetview.eumetsat.int/static-images/MSG/RGB/ (visited on 05/01/2024).

Farnum, R. L. (2022). "Fog Harvesting". In: *Unconventional Water Resources.* Ed. by M. Qadir et al. Cham, Switzerland: Springer Nature Switzerland AG, pp. 51–

71. ISBN: 978-3-030-90146-2. DOI: 10.1007/978-3-030-90145-5. URL: https://doi.org/10.1007/978-3-030-90146-2.

Feigenwinter, C. et al. (2020). “On the performance of microlysimeters to measure non-rainfall water input in a hyper-arid environment with focus on fog contribution”. In: *Journal of Arid Environments* 182, p. 104260.

Feingold, G. et al. (1998). “Simulations of marine stratocumulus using a new microphysical parameterization scheme”. In: *Atmospheric research* 47, pp. 505–528.

Ferrier, B. S. (1994). “A Double-Moment Multiple-Phase Four-Class Bulk Ice Scheme. Part I: Description”. In: *Journal of Atmospheric Sciences* 51.2, pp. 249–280. DOI: https://doi.org/10.1175/1520-0469(1994)051<0249:ADMMPF>2.0.CO;2. URL: https://journals.ametsoc.org/view/journals/atsc/51/2/1520-0469_1994_051_0249_admmpf_2_0_co_2.xml.

Fessehaye, M. et al. (2014). “Fog-water collection for community use”. In: *Renewable and Sustainable Energy Reviews* 29, pp. 52–62.

Formenti, P. et al. (2019). “The Aerosols, Radiation and Clouds in Southern Africa Field Campaign in Namibia: Overview, Illustrative Observations, and Way Forward”. In: *Bulletin of the American Meteorological Society* 100.7, pp. 1277–1298. DOI: https://doi.org/10.1175/BAMS-D-17-0278.1. URL: https://journals.ametsoc.org/view/journals/bams/100/7/bams-d-17-0278.1.xml.

Ghonima, M. S. et al. (2016). “Factors Controlling Stratocumulus Cloud Lifetime over Coastal Land”. In: *Journal of the Atmospheric Sciences* 73.8, pp. 2961–2983. DOI: https://doi.org/10.1175/JAS-D-15-0228.1. URL: https://journals.ametsoc.org/view/journals/atsc/73/8/jas-d-15-0228.1.xml.

Gottlieb, T. R. et al. (2019). “The contribution of fog to water and nutrient supply to Arthraerua leubnitziae in the central Namib Desert, Namibia”. In: *Journal of Arid Environments* 161, pp. 35–46.

Goudie, A. and H. Viles (2015). *Landscapes and Landforms of Namibia*. 1st ed. World Geomorphological Landscapes. Springer Netherlands. 173 pp.

Grabowski, W. W. et al. (2019). “Modeling of Cloud Microphysics: Can We Do Better?” In: *Bulletin of the American Meteorological Society* 100.4, pp. 655–672.

GRAW Radiosondes (2018). *DFM-09 Datenblatt*. GRAW Radiosondes GmbH & Co. KG. Nürnberg, Germany.

Gultepe, I., M. D. Müller, and Z. Boybeyi (2006). “A New Visibility Parameterization for Warm-Fog Applications in Numerical Weather Prediction Models”. In: *Journal of Applied Meteorology and Climatology* 45, pp. 1469–1480. DOI: 10.1175/JAM2423.1.

Gultepe, I. et al. (2007). “Fog Research: A Review of Past Achievements and Future Perspectives”. In: *Pure and Applied Geophysics* 164, pp. 1121–1159.

Hachfeld, B., N. Jürgens, et al. (2000). “Climate patterns and their impact on the vegetation in a fog driven desert: the Central Namib Desert in Namibia.” In: *Phytocoenologia* 30.3/4, pp. 567–589.

Haensler, A. et al. (2011). “Will the southern African west coast fog be affected by future climate change? Results of an initial fog projection using a regional climate model”. In: *Erdkunde*, pp. 261–275.

Hamilton, W. J. and M. K. Seely (1976). "Fog basking by the Namib Desert beetle, Onymacris unguicularis". In: *Nature* 262.5566, pp. 284–285.

Haywood, J. M. et al. (2021). "The CLoud–Aerosol–Radiation Interaction and Forcing: Year 2017 (CLARIFY-2017) measurement campaign". In: *Atmospheric Chemistry and Physics* 21.2, pp. 1049–1084. DOI: 10.5194/acp-21-1049-2021. URL: https://acp.copernicus.org/articles/21/1049/2021/.

Henschel, J., M. Seely, and S. E. Shanyengana (1998). "Namfog: Namibian Applications of Fog-Collecting Systems: Phase 1. Evaluation of Fog-Water Harvesting". In: *Occasional paper No 8, DRFN* 1, pp. 1–82.

Henschel, J. R. and M. K. Seely (2008). "Ecophysiology of atmospheric moisture in the Namib Desert". In: *Atmospheric Research* 87.3-4, pp. 362–368.

Hesse, R. (2012). "Spatial distribution of and topographic controls on Tillandsia fog vegetation in coastal southern Peru: Remote sensing and modelling". In: *Journal of Arid Environments* 78, pp. 33–40. ISSN: 0140-1963. DOI: https://doi.org/10.1016/j.jaridenv.2011.11.006. URL: https://www.sciencedirect.com/science/article/pii/S0140196311003405.

Holmes, R., J. de Dios Rivera, and E. de la Jara (2015). "Large fog collectors: New strategies for collection efficiency and structural response to wind pressure". In: *Atmospheric Research* 151. Sixth International Conference on Fog, Fog Collection and Dew, pp. 236–249. ISSN: 0169-8095. DOI: https://doi.org/10.1016/j.atmosres.2014.06.005. URL: https://www.sciencedirect.com/science/article/pii/S0169809514002415.

Holtslag, M. C., G. J. Steeneveld, and A. A. M. Holtslag (2010). "Fog forecasting: "old fashioned" semi-empirical methods from radio sounding observations versus "modern" numerical models". In: *Proceedings of the 5th International Conference on Fog Collection and Dew*.

Hong, S., J. Dudhia, and S. Chen (2004). "A Revised Approach to Ice Microphysical Processes for the Bulk Parameterization of Clouds and Precipitation". In: *Monthly Weather Review* 132.1, pp. 103–120. DOI: https://doi.org/10.1175/1520-0493(2004)132<0103:ARATIM>2.0.CO;2. URL: https://journals.ametsoc.org/view/journals/mwre/132/1/1520-0493_2004_132_0103_aratim_2.0.co_2.xml.

Houze, R. (2014). *Cloud Dynamics*. 2nd. Vol. 104. International geophysics series. Academic Press. 496 pp.

Iguchi, T. et al. (2012). "Numerical analysis using WRF-SBM for the cloud microphysical structures in the C3VP field campaign: Impacts of supercooled droplets and resultant riming on snow microphysics". In: *Journal of Geophysical Research: Atmospheres* 117.D23. DOI: https://doi.org/10.1029/2012JD018101. eprint: https://agupubs.onlinelibrary.wiley.com/doi/pdf/10.1029/2012JD018101. URL: https://agupubs.onlinelibrary.wiley.com/doi/abs/10.1029/2012JD018101.

Jayakumar, A. et al. (2018). "An operational fog prediction system for Delhi using the 330 m Unified Model". In: *Atmospheric Science Letters* 19.1, e796. DOI: https://doi.org/10.1002/asl.796.

Jöckel, P. et al. (2005). "Technical Note: The Modular Earth Submodel System (MESSy) - a new approach towards Earth System Modeling". In: *Atmos. Chem.*

Phys. 5.2, pp. 433–444. URL: https://www.ingentaconnect.com/content/doaj/16807316/2005/00000005/00000002/art00013.

Jöckel, P. et al. (2010). "Development cycle 2 of the Modular Earth Submodel System (MESSy2)". In: *Geosci. Model Dev.* 3.2, pp. 717–752. DOI: 10.5194/gmd-3-717-2010. URL: https://www.ingentaconnect.com/content/doaj/1991959x/2010/00000003/00000002/art00023.

Jung, G., M. Prange, and M. Schulz (2014). "Uplift of Africa as a potential cause for Neogene intensification of the Benguela upwelling system". In: *Nature Geoscience* 7.10, pp. 741–747.

Kaseke, K. F., L. Wang, and M. K. Seely (2017). "Nonrainfall water origins and formation mechanisms". In: *Science Advances* 3.3, e1603131.

Kaseke, K. F. et al. (2018). "Fog Spatial Distributions over the Central Namib Desert-An Isotope Approach". In: *Aerosol and Air Quality Research* 18, pp. 49–61. DOI: doi:10.4209/aaqr.2017.01.0062.

Kaspar, F. et al. (2015). "The SASSCAL contribution to climate observation, climate data management and data rescue in Southern Africa". In: *Advances in science and research* 12.1, pp. 171–177.

Kerkweg, A. and P. Jöckel (2012). "The 1-way on-line coupled atmospheric chemistry model system MECO(n)-Part 1: Description of the limited-area atmospheric chemistry model COSMO/MESSy". In: *Geosci. Model Dev.* 5.1, pp. 87–110. DOI: 10.5194/gmd-5-87-2012. URL: https://www.ingentaconnect.com/content/doaj/1991959x/2012/00000005/00000001/art00006.

Kessler, E. (1969). "On the distribution and continuity of water substance in atmospheric circulations". In: *On the Distribution and Continuity of Water Substance in Atmospheric Circulations*. Vol. 32. Meteorology monographs. Boston, MA: American Meteorological Society, pp. 1–84. ISBN: 978-1-935704-36-2. DOI: 10.1007/978-1-935704-36-2_1.

Khain, A. et al. (2004). "Simulation of Effects of Atmospheric Aerosols on Deep Turbulent Convective Clouds Using a Spectral Microphysics Mixed-Phase Cumulus Cloud Model. Part I: Model Description and Possible Applications". In: *Journal of the Atmospheric Sciences* 61.24, pp. 2963–2982. DOI: https://doi.org/10.1175/JAS-3350.1. URL: https://journals.ametsoc.org/view/journals/atsc/61/24/jas-3350.1.xml.

Khain, A. P. et al. (2015). "Representation of microphysical processes in cloud-resolving models: Spectral (bin) microphysics versus bulk parameterization". In: *Reviews of Geophysics* 53.2, pp. 247–322. DOI: https://doi.org/10.1002/2014RG000468.

Kim, W., S. S. Yum, and C. K. Kim (2020a). "Numerical Simulation of Sea Fog over the Yellow Sea: Comparison between UM+ PAFOG and WRF+ PAFOG Coupled Systems". In: *Asia-Pacific Journal of Atmospheric Sciences* 56, pp. 89–105. DOI: https://doi.org/10.1007/s13143-019-00134-9.

Kim, W. et al. (2020b). "Improvement of Fog Simulation by the Nudging of Meteorological Tower Data in the WRF and PAFOG Coupled Model". In: *Atmosphere* 11.3. ISSN: 2073-4433. DOI: 10.3390/atmos11030311. URL: https://www.mdpi.com/2073-4433/11/3/311.

Klein, S. A. and D. L. Hartmann (1993). “The Seasonal Cycle of Low Stratiform Clouds”. In: *Journal of Climate* 6.8, pp. 1587–1606. DOI: https://doi.org/10.1175/1520-0442(1993)006<1587:TSCOLS>2.0.CO;2. URL: https://journals.ametsoc.org/view/journals/clim/6/8/1520-0442_1993_006_1587_tscols_2_0_co_2.xml.

Kogan, Y. L. (1991). “The Simulation of a Convective Cloud in a 3-D Model With Explicit Microphysics. Part I: Model Description and Sensitivity Experiments”. In: *Journal of the Atmospheric Sciences* 48.9, pp. 1160–1189. DOI: https://doi.org/10.1175/1520-0469(1991)048%3C1160:TSOACC%3E2.0.CO;2.

Köhler, C. et al. (Feb. 2017). “Critical weather situations for renewable energies – Part B: Low stratus risk for solar power”. In: *Renewable Energy* 101, pp. 794–803. DOI: 10.1016/j.renene.2016.09.002. URL: https://www.sciencedirect.com/science/article/pii/S0960148116307844.

Koračin, D. (2017). “Modeling and Forecasting Marine Fog”. In: *Marine Fog: Challenges and Advancements in Observations, Modeling, and Forecasting*. Ed. by D. Koračin and C. E. Dorman. Cham, Switzerland: Springer Nature Switzerland AG, pp. 425–475. ISBN: 978-3-319-45229-6. DOI: 10.1007/978-3-319-45229-6_9. URL: https://doi.org/10.1007/978-3-319-45229-6_9.

Koračin, D. et al. (2001). “Transition of Stratus into Fog along the California Coast: Observations and Modeling”. In: *Journal of the Atmospheric Sciences* 58.13, pp. 1714–1731. DOI: https://doi.org/10.1175/1520-0469(2001)058<1714:TOSIFA>2.0.CO;2. URL: https://journals.ametsoc.org/view/journals/atsc/58/13/1520-0469_2001_058_1714_tosifa_2.0.co_2.xml.

Kraus, H. (2004). *Die Atmosphäre der Erde. Eine Einführung in die Meteorologie.* Heidelberg, Germany: Springer. 427 pp. DOI: 10.1007/3-540-35017-9.

— (2008). *Grundlagen der Grenzschicht-Meteorologie. Einführung in die Physik der Atmosphärischen Grenzschicht und in die Mikrometeorologie.* Heidelberg, Germany: Springer. 211 pp.

Lancaster, J., N. Lancaster, and M. K. Seely (1984). “Climate of the central Namib Desert”. In: *Madoqua* 14.1, pp. 5–61.

Lang, S. E. et al. (2014). “Benefits of a Fourth Ice Class in the Simulated Radar Reflectivities of Convective Systems Using a Bulk Microphysics Scheme”. In: *Journal of the Atmospheric Sciences* 71.10, pp. 3583–3612. DOI: https://doi.org/10.1175/JAS-D-13-0330.1. URL: https://journals.ametsoc.org/view/journals/atsc/71/10/jas-d-13-0330.1.xml.

Lee, X. (2018). *Fundamentals of Boundary-Layer Meteorology.* Springer Cham. 256 pp. DOI: 10.1007/978-3-319-60853-2.

Lilly, D. K. (1968). “Models of cloud-topped mixed layers under a strong inversion”. In: *Q. J. R. Meteorol. Soc.* 94, pp. 292–309.

Lim, K. S. and S. Hong (2010). “Development of an Effective Double-Moment Cloud Microphysics Scheme with Prognostic Cloud Condensation Nuclei (CCN) for Weather and Climate Models”. In: *Monthly Weather Review* 138.5, pp. 1587–1612. DOI: https://doi.org/10.1175/2009MWR2968.1. URL: https://journals.ametsoc.org/view/journals/mwre/138/5/2009mwr2968.1.xml.

Lin, C. et al. (2017). “Numerical simulations of an advection fog event over Shanghai Pudong International Airport with the WRF model”. In: *Journal of Meteoro-*

logical Research 31.5, pp. 874–889. DOI: https://doi.org/10.1007/s13351-017-6187-2.

Lin, Y.-L., R. D. Farley, and H. D. Orville (1983). "Bulk Parameterization of the Snow Field in a Cloud Model". In: *Journal of Applied Meteorology and climatology* 22.6, pp. 1065–1092. DOI: 10.1175/1520-0450(1983)022<1065:BPOTSF>2.0.CO;2.

Lindesay, J. A. and P. D. Tyson (1990a). "Thermo-topographically induced boundary layer oscillations over the central Namib, southern Africa". In: *International Journal of Climatology* 10.1, pp. 63–77. DOI: https://doi.org/10.1002/joc.3370100108. eprint: https://rmets.onlinelibrary.wiley.com/doi/pdf/10.1002/joc.3370100108. URL: https://rmets.onlinelibrary.wiley.com/doi/abs/10.1002/joc.3370100108.

— (1990b). "Climate and Near-surface Airflow Over the Central Namib". In: *Namib ecology* 25, pp. 27–37.

Logan, R. F. (1968). "Causes, climates and distribution of deserts". In: *Desert biology: special topics on the physical and biological aspects of arid regions.* Vol. 1. Academic Press, Inc New York (NY), pp. 21–50.

Luccini, E. and M. Rivas (2021). "Kinematics and dynamics of the stratocumulus average diurnal dissipation process at Atacama Desert". In: *Atmospheric Research* 255, p. 105523. ISSN: 0169-8095. DOI: https://doi.org/10.1016/j.atmosres.2021.105523. URL: https://www.sciencedirect.com/science/article/pii/S0169809521000752.

Lynn, B. H. et al. (2005). "Spectral (Bin) Microphysics Coupled with a Mesoscale Model (MM5). Part I: Model Description and First Results". In: *Monthly Weather Review* 133.1, pp. 44–58. DOI: https://doi.org/10.1175/MWR-2840.1.

Makuti, O. et al. (2004). "Testing Fog Collectors in the Namib Desert". In: *Proceedings of the Third International Conference on Fog, Fog Collection and Dew*, pp. 11–15.

Masbou, M. (2008). "LM-PAFOG - a new three-dimensional fog forecast model with parametrised microphysics". PhD thesis. Meteorologisches Institut der Universität Bonn, Germany, and Laboratoire de Météorologie Physique, Université Blaise Pascal, Clermont-ferrand, France.

Mellor, G. L. and T. Yamada (1974). "A Hierarchy of Turbulence Closure Models for Planetary Boundary Layers". In: *Journal of the Atmospheric Sciences* 31, pp. 1791–1806.

— (1982). "Development of a turbulence closure model for geophysical fluid problems". In: *Rev. Geophys. Space Phys.* 20, pp. 851–875.

Mendelsohn, J. et al. (2002). *Atlas of Namibia. A portrait of the land and its people.* New Africa Books (Pty) Ltd. 200 pp.

Mitchell, D. et al. (2020). "Fog and fauna of the Namib Desert: past and future". In: *Ecosphere* 11.1, e02996.

Mohr, C. (2009). "Nebelvorhersage am Flughafen München: Klimatologie und Modellentwicklung". MA thesis. Meteorologisches Institut der Universität Bonn.

Mölders, N. and G. Kramm (2014). *Lectures in Meteorology.* Springer International Publishing Switzerland. 591 pp. ISBN: 978-3-319-02143-0. DOI: 10.1007/978-3-319-02144-7.

Montecinos, S. et al. (2018). "Collection efficiency of fog events". In: *Atmospheric Research* 209, pp. 163–169.

Muche, G. et al. (2018). "SASSCAL WeatherNet: present state, challenges, and achievements of the regional climatic observation network and database". In: *Climate change and adaptive land management in southern Africa – assessments, changes, challenges, and solutions*. Ed. by R. Revermann et al. Vol. 6. Göttingen and Windhoek: Klaus Hess, pp. 34–43.

Müller, M. D., M. Masbou, and A. Bott (2010). "Three-dimensional fog forecasting in complex terrain". In: *Q. J. R. Meteorol. Soc.* 136, pp. 2189–2202.

Nagel, J. F. (1959). "Fog precipitation at Swakopmund". In: *Weather Bureau Newsletter* 125, pp. 1–9.

Nakanishi, M. (2000). "Large-Eddy Simulation Of Radiation Fog". In: *Boundary-layer meteorology* 94, pp. 461–493.

Nicholls, S. (1984). "The dynamics of stratocumulus: Aircraft observations and comparisons with a mixed layer model". In: *Quarterly Journal of the Royal Meteorological Society* 110.466, pp. 783–820. DOI: https://doi.org/10.1002/qj.49711046603. eprint: https://rmets.onlinelibrary.wiley.com/doi/pdf/10.1002/qj.49711046603. URL: https://rmets.onlinelibrary.wiley.com/doi/abs/10.1002/qj.49711046603.

Nicholls, S. and J. Leighton (1986). "An observational study of the structure of stratiform cloud sheets: Part I. Structure". In: *Quarterly Journal of the Royal Meteorological Society* 112.472, pp. 431–460. DOI: https://doi.org/10.1002/qj.49711247209. eprint: https://rmets.onlinelibrary.wiley.com/doi/pdf/10.1002/qj.49711247209. URL: https://rmets.onlinelibrary.wiley.com/doi/abs/10.1002/qj.49711247209.

Nicholls, S. and J. D. Turton (1986). "An observational study of the structure of stratiform cloud sheets: Part II. Entrainment". In: *Quarterly Journal of the Royal Meteorological Society* 112.472, pp. 461–480. DOI: https://doi.org/10.1002/qj.49711247210. eprint: https://rmets.onlinelibrary.wiley.com/doi/pdf/10.1002/qj.49711247210. URL: https://rmets.onlinelibrary.wiley.com/doi/abs/10.1002/qj.49711247210.

Nickerson, E. et al. (1986). "The numerical simulation of clouds, rain, and airflow over the Vosges and Black Forest Mountains: A meso-beta model with parameterized microphysics". In: *Mon. Wea. Rev.* 114, pp. 398–414.

Nørgaard, T., M. Ebner, and M. Dacke (2012). "Animal Or Plant: Which Is The Better Fog Water Collector?" In: *PloS one* 7.4, e34603. DOI: https://doi.org/10.1371/journal.pone.0034603.

Olivier, J. (1992). "Some spatial and temporal distribution of fog in the Namib". In: *S. Afr. Geogr* 119.1/2, pp. 107–127.

— (1995). "Spatial distribution of fog in the Namib". In: *Journal of Arid Environments* 29.2, pp. 129–138.

Olivier, J. and P. L. Stockton (1989). "The influence of upwelling extent upon fog incidence at Lüderitz, southern Africa". In: *International Journal of Climatology* 9.1, pp. 69–75.

Pagowski, M., I. Gultepe, and P. King (2004). "Analysis and Modeling of an Extremely Dense Fog Event in Southern Ontario". In: *Journal of Applied Mete-*

orology 43.1, pp. 3–16. DOI: https://doi.org/10.1175/1520-0450(2004)043<0003:AAMOAE>2.0.CO;2. URL: https://journals.ametsoc.org/view/journals/apme/43/1/1520-0450_2004_043_0003_aamoae_2.0.co_2.xml.

Paluch, I. R. and D. H. Lenschow (1991). “Stratiform Cloud Formation in the Marine Boundary Layer”. In: *Journal of Atmospheric Sciences* 48.19, pp. 2141–2158.

Paluch, I. R. et al. (1994). “Evolution of the Subtropical Marine Boundary Layer: Comparison of Soundings over the Eastern Pacific from FIRE and HaRP”. In: *Journal of Atmospheric Sciences* 51.11, pp. 1465–1479.

Panitz, H.-J. et al. (2014). “COSMO-CLM (CCLM) climate simulations over CORDEX – Africa domain: analysis of the ERA-Interim driven simulations at 0.44 and 0.22 resolution”. In: *Climate dynamics* 42, pp. 3015–3038.

Park, J. K. and S. Kim (2019). “Three-Dimensionally Structured Flexible Fog Harvesting Surfaces Inspired by Namib Desert Beetles”. In: *Micromachines* 10.3, p. 201. DOI: https://doi.org/10.3390/mi10030201.

Pawlowska, H. and J.-L. Brenguier (2003). “An observational study of drizzle formation in stratocumulus clouds for general circulation model (GCM) parameterizations”. In: *Journal of Geophysical Research: Atmospheres* 108.D15. DOI: https://doi.org/10.1029/2002JD002679. eprint: https://agupubs.onlinelibrary.wiley.com/doi/pdf/10.1029/2002JD002679. URL: https://agupubs.onlinelibrary.wiley.com/doi/abs/10.1029/2002JD002679.

Philip, A. et al. (2016). “The Impact of Vertical Resolution on Fog Forecasting in the Kilometric-Scale Model AROME: A Case Study and Statistics”. In: *Weather and Forecasting* 31.5, pp. 1655–1671. DOI: https://doi.org/10.1175/WAF-D-16-0074.1.

Pietruszka, R. D. and M. K. Seely (1985). “Predictability of two moisture sources in the Namib Desert.” In: *South African journal of science* 81.11, pp. 682–685.

Pilié, R. J. et al. (1979). “The Formation of Marine Fog and the Development of Fog-Stratus Systems along the California Coast”. In: *Journal of Applied Meteorology and Climatology* 18.10, pp. 1275–1286. DOI: https://doi.org/10.1175/1520-0450(1979)018<1275:TFOMFA>2.0.CO;2. URL: https://journals.ametsoc.org/view/journals/apme/18/10/1520-0450_1979_018_1275_tfomfa_2_0_co_2.xml.

Price, J. D. et al. (2018). “LANFEX: A Field and Modeling Study to Improve Our Understanding and Forecasting of Radiation Fog”. In: *Bulletin of the American Meteorological Society* 99.10, pp. 2061–2077. DOI: https://doi.org/10.1175/BAMS-D-16-0299.1. URL: https://journals.ametsoc.org/view/journals/bams/99/10/bams-d-16-0299.1.xml.

Price, J.D. (2019). “On the Formation and Development of Radiation Fog: An Observational Study”. In: *Boundary-Layer Meteorology* 172.2, pp. 167–197.

Pruppacher, H. R. and J. D. Klett (2010). *Microphysics of Clouds and Precipitation. Second revised and expanded editionwith an introduction tocloud chemistry and cloud electricity.* 2nd ed. Atmospheric and Oceanographic Sciences Library 18. Dordrecht, Holland: Springer Dordrecht. 954 pp. DOI: https://doi.org/10.1007/978-0-306-48100-0.

Randall, D. A. and M. J. Suarez (1984). “On the Dynamics of Stratocumulus Formation and Dissipation”. In: *Journal of Atmospheric Sciences* 41.20, pp. 3052–

3057. DOI: https://doi.org/10.1175/1520-0469(1984)041<3052:OTDOSF>2.0.CO;2. URL: https://journals.ametsoc.org/view/journals/atsc/41/20/1520-0469_1984_041_3052_otdosf_2_0_co_2.xml.

Randall, D. A. et al. (1984). "Outlook for Research on Subtropical Marine Stratiform Clouds". In: *Bulletin of the American Meteorological Society* 65.12, pp. 1290–1301. ISSN: 00030007, 15200477. URL: http://www.jstor.org/stable/26224283 (visited on 11/20/2023).

Rangno, A. L. (2015). "CLOUDS AND FOG — Classification of Clouds". In: *Encyclopedia of Atmospheric Sciences*, pp. 141–160. DOI: 10.1016/B978-0-12-382225-3.00112-2.

Redemann, J. et al. (2021). "An overview of the ORACLES (ObseRvations of Aerosols above CLouds and their intEractionS) project: aerosol–cloud–radiation interactions in the southeast Atlantic basin". In: *Atmospheric Chemistry and Physics* 21.3, pp. 1507–1563. DOI: 10.5194/acp-21-1507-2021. URL: https://acp.copernicus.org/articles/21/1507/2021/.

Reinhardt, T. and A. Seifert (2006). "A Three-Category Ice cheme for LMK". In: *COSMO Newsletter*. Vol. 6, pp. 115–120.

Riehl, H. et al. (1951). "The north-east trade of the Pacific Ocean". In: *Quarterly Journal of the Royal Meteorological Society* 77.334, pp. 598–626. DOI: https://doi.org/10.1002/qj.49707733405. eprint: https://rmets.onlinelibrary.wiley.com/doi/pdf/10.1002/qj.49707733405. URL: https://rmets.onlinelibrary.wiley.com/doi/abs/10.1002/qj.49707733405.

Ritter, B. and J.-F. Geleyn (1992). "A Comprehensive Radiation Scheme for Numerical Weather Prediction Models with Potential Applications in Climate Simulations". In: *Mon. Weather Rev.* 120, pp. 303–325.

Roach, W. T. (1994). "Back to basics: Fog: Part 1-Definitions and basic physics". In: *WEATHER-LONDON-* 49, pp. 411–411.

— (1995). "Back to basics: Fog: Part 2 - The formation and dissipation of land fog". In: *Weather* 50, pp. 7–11.

Roach, W. T. et al. (1982). "A field study of nocturnal stratocumulus: I. Mean structure and budgets". In: *Quarterly Journal of the Royal Meteorological Society* 108.455, pp. 103–123. DOI: https://doi.org/10.1002/qj.49710845507. eprint: https://rmets.onlinelibrary.wiley.com/doi/pdf/10.1002/qj.49710845507. URL: https://rmets.onlinelibrary.wiley.com/doi/abs/10.1002/qj.49710845507.

Rockel, B., A. Will, and A. Hense (2008). "The Regional Climate Model COSMO-CLM (CCLM)". In: *Meteorologische Zeitschrift* 17.4, pp. 347–348. DOI: 10.1127/0941-2948/2008/0309. URL: https://www.ingentaconnect.com/content/schweiz/mz/2008/00000017/00000004/art00001.

Roth-Nebelsick, A. et al. (2012). "Leaf surface structures enable the endemic Namib desert grass Stipagrostis sabulicola to irrigate itself with fog water". In: *J. R. Soc. Interface* 9, pp. 1965–1974. DOI: https://doi.org/10.1098/rsif.2011.0847.

Sakakibara, H. (1979). "A Scheme for Stable Numerical Computation of the Condensation Process with a Large Time Step". In: *Journal of the Meteorological Society of Japan. Ser. II* 57.4, pp. 349–353.

Schättler, U., G. Doms, and C. Schraff (2018). *A Description of the Nonhydrostatic Regional COSMO-Model. Part VII: User's Guide.* Ed. by Ulrich Schättler. (also available at www.cosmo-model.org). Consortium for small scale modelling. Deutscher Wetterdienst. Offenbach, Germany: Deutscher Wetterdienst. DOI: 10.5676/DWD_pub/nwv/cosmo-doc_5.05_VII.

Schemenauer, R. S. and P. Cereceda (1994). "A Proposed Standard Fog Collector for Use in High-Elevation Regions". In: *Journal of Applied Meteorology and Climatology* 33.11, pp. 1313–1322.

Schulz, J.-P. and G. Vogel (2020). "Improving the Processes in the Land Surface Scheme TERRA: Bare Soil Evaporation and Skin Temperature". In: *Atmosphere* 11.5. ISSN: 2073-4433. DOI: 10.3390/atmos11050513feigenwinter. URL: https://www.mdpi.com/2073-4433/11/5/513.

Seely, M. and J. R. Henschel (1998). "The climatology of Namib fog". In: *Proceedings of the First International Conference on Fog and Fog Collection*, pp. 19–24.

Seely, M. K. (1978). "Standing crop as an index of precipitation in the Central Namib grassland". In: *Madoqua* 1978.v11i1, pp. 61–68.

— (1979). "Irregular fog as a water source for desert dune beetles". In: *Oecologia* 42.2, pp. 213–227.

Seely, M. K. and W. J. Hamilton (1976). "Fog Catchment Sand Trenches Constructed by Tenebrionid Beetles, Lepidochora, from the Namib Desert". In: *Science* 193.4252, pp. 484–486.

Seifert, A. and K. D. Beheng (2001). "A double-moment parameterization for simulating autoconversion, accretion and selfcollection". In: *Atmospheric research* 59, pp. 265–281. DOI: https://doi.org/10.1016/S0169-8095(01)00126-0.

— (2006). "A two-moment cloud microphysics parameterization for mixed-phase clouds. Part 1: Model description". In: *Meteorol. Atmos. Phys.* 92, pp. 45–66. DOI: https://doi.org/10.1007/s00703-005-0112-4.

Shanyengana, E. S. et al. (2002). "Exploring fog as a supplementary water source in Namibia". In: *Atmospheric Research* 64.1-4, pp. 251–259.

Skamarock, W. C. (2004). "Evaluating Mesoscale NWP Models Using Kinetic Energy Spectra". In: *Mon. Wea. Rev.* 132, pp. 3019–3032.

Smith, D. K. E. et al. (2018). "Numerical modelling of the evolution of the boundary layer during a radiation fog event". In: *Weather* 73.10, pp. 310–316.

Soderberg, K. S. (2010). "The role of fog in the ecohydrology and biogeochemistry of the Namib Desert". PhD thesis. University of Virginia Charlottesville, Virginia, USA.

Southgate, R. I., P. Masters, and M. K. Seely (1996). "Precipitation and biomass changes in the Namib Desert dune ecosystem". In: *Journal of Arid Environments* 33.3, pp. 267–280. ISSN: 0140-1963. DOI: https://doi.org/10.1006/jare.1996.0064. URL: https://www.sciencedirect.com/science/article/pii/S0140196396900646.

Spirig, R. (Nov. 17, 2020). "Fog in the Namib - Occurrence Dynamics Properties". PhD thesis. Universität Basel.

Spirig, R. et al. (2019). "Probing the Fog life Cycles in the Namib Desert". In: *Bulletin of the American Meteorological Society* 100.12, pp. 2491–2507.

Steeneveld, G. J., R. J. Ronda, and A. A. M. Holtslag (2015). “The Challenge of Forecasting the Onset and Development of Radiation Fog Using Mesoscale Atmospheric Models”. In: *Boundary-Layer Meteorology* 154, pp. 265–289. DOI: https://doi.org/10.1007/s10546-014-9973-8.

Steppeler, J. et al. (2003). “Meso-gamma scale forecasts using the nonhydrostatic model LM”. In: *Meteorology and Atmospheric Physics* 82.1, pp. 75–96. URL: https://www.ingentaconnect.com/content/ssam/01777971/2003/00000082/00000001/art00004.

Stevens, B. et al. (1996). “Elements of the Microphysical Structure of Numerically Simulated Nonprecipitating Stratocumulus”. In: *Journal of Atmospheric Sciences* 53.7, pp. 980–1006. DOI: https://doi.org/10.1175/1520-0469(1996)053<0980:EOTMSO>2.0.CO;2. URL: https://journals.ametsoc.org/view/journals/atsc/53/7/1520-0469_1996_053_0980_eotmso_2_0_co_2.xml.

Stolaki, S., I. Pytharoulis, and T. Karacostas (2012). “A Study of Fog Characteristics Using a Coupled WRF–COBEL Model Over Thessaloniki Airport, Greece”. In: *Pure and applied geophysics* 169.5-6, pp. 961–981. DOI: 10.1007/s00024-011-0393-0.

Taljaard, J. J. (1979). “Low-level atmospheric circulation over the Namib”. In: *Newsletter (South African Weather Bureau) Pretoria. Weather Bureau Department of Transport*, pp. 65–67.

Tardif, R. (2007). “The Impact of Vertical Resolution in the Explicit Numerical Forecasting of Radiation Fog: A Case Study”. In: *Pure and Applied Geophysics* 164, pp. 1221–1240.

Tardif, R. and R. M. Rasmussen (2007). “Event-Based Climatology and Typology of Fog in the New York City Region”. In: *Journal of applied meteorology and climatology* 46.8, pp. 1141–1168.

Tiedtke, M. (1989). “A Comprehensive Mass Flux Scheme for Cumulus Parameterization in Large Scale Models”. In: *Mon. Wea. Rev.* 117, pp. 1779–1800.

Twomey, S. (1959). “The nuclei of natural cloud formation. Part ll: The supersaturation in natural Clouds and the variation of Cloud Droplet concentration”. In: *Pure and Applied Geophysics* 43, pp. 243–249.

Tyson, P. D. and M. K. Seely (1980). “Local winds over the central Namib”. In: *South African Geographical Journal* 62.2, pp. 135–150.

United Nations (2011). *Global Drylands: A UN system-wide response*. Tech. rep. United Nations Environment Management Group.

University of Basel (2024). “Visualising remote sensed weather phenomena with ground measurements in Namibia”.

VanZanten, M. C. et al. (2005). “Observations of Drizzle in Nocturnal Marine Stratocumulus”. In: *Journal of the atmospheric sciences* 62.1, pp. 88–106.

Verbrugghe, N. and A. Z. Khan (Mar. 2023). “Water harvesting through fog collectors: a review of conceptual, experimental and operational aspects”. In: *International Journal of Low-Carbon Technologies* 18, pp. 392–403. ISSN: 1748-1317. DOI: 10.1093/ijlct/ctac129. eprint: https://academic.oup.com/ijlct/article-pdf/doi/10.1093/ijlct/ctac129/50083430/ctac129.pdf. URL: https://doi.org/10.1093/ijlct/ctac129.

Wahl, S. et al. (2017). "A novel convective-scale regional reanalysis COSMO-REA2: Improving the representation of precipitation". In: *Meteorologische Zeitschrift* 26.4, pp. 345–361. DOI: 10.1127/metz/2017/0824. URL: https://www.ingentaconnect.com/content/doaj/09412948/2017/00000026/00000004/art00001.

Warner, T. T. (2004). *Desert Meteorology.* Cambridge University Press. 595 pp. DOI: 10.1017/CBO9780511535789.

Warren, S., R. Eastman, and C. J. Hahn (2015). "Clouds and Fog— Climatology". In: *Encyclopedia of Atmospheric Sciences.*

Weiss, S. (Dec. 20, 2014). *Kondenswasser-Nutzung in Chile: Die Nebelfänger der Atacama-Wüste.* Ed. by Tagesspiegel. URL: https://www.tagesspiegel.de/gesellschaft/panorama/die-nebelfanger-der-atacama-wuste-8470948.html (visited on 06/12/2023).

Westberg, M. and K. Westberg (2013). "The Oldest Desert in the World". In: *National Geographic.* URL: https://www.nationalgeographic.com/travel/article/the-oldest-desert-in-the-world.

Whiteman, C. D. (Aug. 24, 2000). *Mountain Meteorology: Fundamentals and Applications.* Oxford University Press. 368 pp. ISBN: 9780195132717. DOI: 10.1093/oso/9780195132717.001.0001.

Wood, R. (2012). "Stratocumulus clouds." In: *Mon. Wea. Rev.* 140, pp. 2373–2423.

— (Dec. 2015). "Clouds and Fog — Stratus and Stratocumulus". In: *Encyclopedia of Atmospheric Sciences*, pp. 196–200. DOI: 10.1016/B978-0-12-382225-3.00396-0. URL: https://www.sciencedirect.com/science/article/pii/B9780123822253003960.

Wood, R., C. S. Bretherton, and D. L. Hartmann (2002). "Diurnal cycle of liquid water path over the subtropical and tropical oceans". In: *Geophysical Research Letters* 29.23, pp. 7–1.

World Meteorological Organization (2017). *International Cloud Atlas.* URL: https://cloudatlas.wmo.int/en/fog.html (visited on 06/25/2023).

Yu, Z. et al. (2021). "Namib desert beetle inspired special patterned fabric with programmable and gradient wettability for efficient fog harvesting". In: *Journal of Materials Science & Technology* 61, pp. 85–92. ISSN: 1005-0302. DOI: https://doi.org/10.1016/j.jmst.2020.05.054. URL: https://www.sciencedirect.com/science/article/pii/S1005030220305879.

Zdunkowski, W. and B. Nielsen (1969). "A preliminary prediction analysis of radiation fog". In: *Pure and Applied Geophysics* 19, pp. 45–66.

Zdunkowski, W. G. and A. E. Barr (1972). "A radiative-conductive model for the prediction of radiation fog". In: *Boundary-Layer Meteorology* 3, pp. 152–177.

Zhang, W. et al. (2024). "The impact of aerosol-cloud interaction on mesoscale numerical weather prediction when low-cloud and haze coexist in winter over major polluted regions of China". In: *Atmospheric Environment* 319, p. 120270. ISSN: 1352-2310. DOI: https://doi.org/10.1016/j.atmosenv.2023.120270. URL: https://www.sciencedirect.com/science/article/pii/S1352231023006969.

Zheng, Y., D. Rosenfeld, and Z. Li (2018). "The Relationships Between Cloud Top Radiative Cooling Rates, Surface Latent Heat Fluxes, and Cloud-Base Heights in Marine Stratocumulus”. In: *Journal of Geophysical Research: Atmospheres* 123.20, pp. 11, 678–11, 690. DOI: https://doi.org/10.1029/2018JD028579. eprint: https://agupubs.onlinelibrary.wiley.com/doi/pdf/10.1029/2018JD028579. URL: https://agupubs.onlinelibrary.wiley.com/doi/abs/10.1029/2018JD028579.

BONNER METEOROLOGISCHE ABHANDLUNGEN

Herausgegeben vom Institut für Geowissenschaften der Universität Bonn, Abteilung Meteorologie, durch Prof. Dr. H. FLOHN (Hefte 1-25), Prof. Dr. M. HANTEL (Hefte 26-35), Prof. Dr. H.-D. SCHILLING (Hefte 36-39), Prof. Dr. H. KRAUS (Hefte 40-49), ab Heft 50 durch Prof. Dr. A. HENSE.

Heft 1-79: siehe `https://www.ifgeo.uni-bonn.de/de/abteilungen/meteorologie/bibliothek/bibliothek-meteorologie#BMA`

80-97: open access, verfügbar unter `https://bonndoc.ulb.uni-bonn.de/xmlui/handle/20.500.11811/1627`

Heft 80: ***Tanja Zerenner***: Atmospheric downscaling using multi-objective genetic programming, 2016, [erschienen] 2017, X, 191 S.

Heft 81: ***Sophie Stolzenberger***: On the probabilistic evaluation of decadal and paleoclimate model predictions, 2017, IV, 122 S.

Heft 82: ***Insa Thiele-Eich***: Flooding in Dhaka, Bangladesh, and the challenge of climate change, 2017, V, 158 S.

Heft 83: ***Liselotte Bach***: Towards a probabilistic regional reanalysis for Europe, 2017 [erschienen] 2018, VI, 114 S.

Heft 84: ***Yen-Sen Lu***: Propagation of land surface model uncertainties in terrestrial system states, 2017, [erschienen] 2018, X, 120 S.

Heft 85: ***Rüdiger Hewer***: Stochastic physical models for wind fields and precipitation extremes, 2018, 99 S.

Heft 86: ***Sebastian Knist***: Land-atmosphere interactions in multiscale regional climate change simulations over Europe, 2018, VIII, 147 S.

Heft 87: ***Jessica Keune***: Integrated terrestrial simulations at the continental scale: Impact of groundwater dynamics and human water use on groundwater-to-atmosphere feedbacks during the European heatwave in 2003, 2019, IX, 172 S.

Heft 88: ***Christoph Beekmans***: 3-D Cloud Morphology and Evolution Derived from Hemispheric Stereo Cameras, 2019, [erschienen] 2020, VIII, 118 S.

Heft 89: ***Nils Weitzel***: Climate field reconstructions from pollen and macrofossil syntheses using Bayesian hierarchical models, 2019, [erschienen] 2020, XII, 153 S.

Heft 90: ***Alexander Kelbch***: Investigations to quantify individual exposure to solar ultraviolet erythemal radiation including cloud meteorological impact, 2020, III, 107 S.

Heft 91: ***Mari L. Schmidt***: Improvement of hail detection and nowcasting by synergistic combination of information from polarimetric radar, model predictions, and in-situ observations, 2020, VI, 136 S.

Heft 92: ***Sebastian Brune***: Der Wavelet-basierte Organisationsindex als Maß der konvektiven Organisation über Deutschland und dem tropischen Atlantik, 2021, IV, 121 S.

Heft 93: ***Sebastian Buschow***: Spatial Verification with Wavelets, 2022, V, 195 S.

Heft 94: ***Michael Langguth***: Representation of deep convection at gray-zone resolutions - Implementing and testing the HYbrid MAss flux Convection Scheme (HYMACS) in the ICON model, 2022, VI, 173 S.

Heft 95: ***Timon Netzel***: Quantitative paleoclimate reconstructions in the European region based on multiple proxies, 2023, VI, 179 S.

Heft 96: ***Lukas Hubert Leufen***: Time Filter Assisted Deep Learning to Predict Air Pollution, 2023, IV, 156 S.

Heft 97: ***Maike Hacker***: Modelling Fog and Low Stratiform Clouds in the Namib Desert with COSMO-FOG, 2024, VIII, 176 S.

Institut für Geowissenschaften
Abteilung Meteorologie
Mathematisch Naturwissenschaftliche Fakultät
Universität Bonn